

**Synthesis of various shaped cyano-bridged
coordination polymers under controlled
crystallization**

様々な形態を有するシアン架橋型配位高分子結晶
の創製

February 2019

Azhar salman m ALOWASHEEIR

アルオウエシィール アズハール

**Synthesis of various shaped cyano-bridged
coordination polymers under controlled
crystallization**

様々な形態を有するシアン架橋型配位高分子結晶
の創製

February 2019

Waseda University

**Graduate School of Advanced Science and
Engineering**

Department of Nanoscience and Nanoengineering

Research on Synthetic Chemistry of Nanomaterials

Azhar salman m ALOWASHEEIR

アルオウエシール アズハール

Preface

Coordination compounds are an emerging class of molecular solids that have promising properties including selective adsorption and high proton conductivity. Bulk coordination crystals have generated enormous insight in the field of molecular and crystal engineering, but in recent years scientists have begun to manipulate their mesoscale and nanoscale structures. This work is part of an emerging field called 'nanoarchitectonics' which brings together chemists, physicists and materials scientists to bridge the gap between molecules and materials to create new kinds of coordination compounds with unusual properties. Cyano-bridged coordination polymers (CPs) support a rich array of physical/chemical properties that enable a multi-functional platform for various applications including sensing, batteries, biomedicine, imaging and water purification. Prussian blue (PB) is a classic example of cyano-bridged CPs. The general composition of PB is $A_mM_x[M'(CN)_6]_y \cdot nH_2O$ where M and M' represent different transition metal ions, and the A components are alkali-metal ions.

This thesis describes the synthesis of various shaped cyano-bridged CPs under strictly controlled crystallization conditions. Significant changes in their chemical and physical properties is observed by changing the size of the crystals and their nanoscale morphologies. These results demonstrate that the properties of coordination compounds can depend on their morphology.

Chapter 1 introduces recent advances on various cyano-bridged CP nanoarchitectures and explains different synthetic methods reported previously. In particular, this chapter emphasizes the development of several techniques for controlling crystal growth of cyano-bridged CPs. Thermal conversion of these compounds to metal oxides and other related materials is also mentioned.

Chapter 2 describes the synthesis of cyano-bridged CP single crystals. Creating single crystals of CPs were necessary to carefully study the chemical and physical properties of these

materials. Here crystals of two-dimensional (2D) cyano-bridged CPs containing Ni and Mn ions were prepared by a slow diffusion method. Through detailed structural analysis, it was found that the as-synthesized crystals of $[\text{Mn}(\text{H}_2\text{O})_2\text{Ni}(\text{CN})_4] \cdot 3\text{H}_2\text{O}$ transformed into another crystalline phase of $[\text{Mn}(\text{H}_2\text{O})_2\text{Ni}(\text{CN})_4] \cdot \text{H}_2\text{O}$ upon dehydration via a topotactic route. Water molecules play a key role in this structural transformation upon dehydration/hydration in the 2D cyano-bridged CPs because such frameworks respond to changes in humidity. This information is highly useful for applications of these cyano-bridged CPs in adsorption applications and solid-state ionics.

Chapter 3 extends the slow diffusion method described in **Chapter 2** to generate another cyano-bridged CP system consisting of Ni and Co($[\text{Co}(\text{H}_2\text{O})_2\text{Ni}(\text{CN})_4] \cdot 4\text{H}_2\text{O}$). However, the obtained sample was made of many aggregated crystals, and its surface was very rough. To overcome this issue, a chelating agent called trisodium citrate (TSCD) was added to decelerate the crystallization process and generate high-quality single crystals. We hypothesized that citrate ions could chelate with Co^{+2} and modify the kinetics of the coordination reaction between Co^{+2} and $[\text{Ni}(\text{CN})_4]^{-2}$. UV/Vis spectra showed that the addition of TSCD caused the maximum absorption peak of $\text{Co}(\text{NO}_3)_2$ to significantly increase. Addition of TSCD will be useful in the preparation of other kinds of cyano-bridged CPs.

Chapter 4 describes the nanoscale crystal growth of cyano-bridged CPs under controlled conditions to introduce new nanostructures. Hollow Prussian blue analogue (CoFe PBA) nanocubes were successfully synthesized using spherical silica particles as sacrificial templates. In the first step, silica cores were coated by CoFe PBA shell and then removed by etching using hydrofluoric acid (HF). Interestingly, the cubic shape of CoFe PBA was well-retained even after the removal of silica cores, resulting in the formation of hollow CoFe PBA cubes. The resulting hollow architecture offered a larger interfacial area between the electrolyte and the electrode, leading to the improvement of the storage capacity of sodium ions with stable

cycle performance compared to the solid CoFe PBA nanocubes. This strategy can be applied in the future for the developing PBAs with hollow interiors toward a wide range of applications.

Nanocomposite materials have a wider range of potential applications because they cooperatively combine the properties/advantages of two (or more) individual components. **Chapter 5** describes a simple approach to hybridize NiCo oxide flakes with graphene (G) sheets. Positively charged cyano-bridged CoNi CP flakes (CoNi-CP) were mixed with negatively charged graphene surfaces. Due to effective electrostatic forces, the materials hybridized to form a nanocomposite composed of CoNi-CP/G. The as-prepared CoNi-CP/G composite was thermally treated in air to remove the C-N components, which did not affect the integrity of the parent graphene sheets. During the thermal treatment, the CoNi-CP flakes deposited onto graphene sheets were successfully converted to NiCo oxide, resulting in a new composite consisting of NiCo oxide flakes and graphene sheets (NiCo-oxide/G). Cyclic voltammetry (CV) measurements using a three electrode setup showed that the NiCo-oxide/G nanocomposite had a high specific capacitance (199 F g^{-1} at 5 mV s^{-1}) and featured good capacitance retention of ca. 68 % (135 F g^{-1} at 100 mV s^{-1}). This strategy will be useful in the future for the synthesis of nanocomposites with dual characters for the application in energy-related systems.

Chapter 6 demonstrates a novel synthetic strategy to deposit cyano-bridged CuNi CPs on the surface of graphene oxide (GO) sheets. This method allows precise control of the resulting lamellar nanoarchitectures via in-situ crystallization. The GO sheets serve as nucleation sites to promote optimal crystal growth of cyano-bridged CuNi CPs. The self-assembled GO sheets with cyano-bridged CuNi CPs were stabilized as ordered lamellar structures. Thermal treatment in air yielded CuNi-oxide/G composite structures with a similar morphology to the starting material. During the formation of CuNi oxide within the graphene sheets, the CN units were removed. The CuNi-oxide/G hybrid materials could be calcined at

an optimal temperature to generate a high surface area ($144.5 \text{ m}^2 \text{ g}^{-1}$), which was much higher than the individual CuNi oxide ($11.1 \text{ m}^2 \text{ g}^{-1}$) and graphene sheet ($34.9 \text{ m}^2 \text{ g}^{-1}$) starting materials. This synthetic pathway is a very promising approach which can be applied in the synthesis of other functional nanocomposites using in-situ crystallization of various PBAs.

Chapter 7 summarizes this thesis and future prospects. This thesis emphasizes a significant role of controlled crystallization of cyano-bridged CPs to prepare various architectures such as single crystals, hollow and nanocomposite structures, *etc.* High quality single crystals can be prepared by adding a chelating agent to slow the speed of the crystallization process. With a reaction rate much slower, the synthetic conditions become optimal to trigger an oriented crystal growth. We have realized various cyano-bridged CP nanostructures with different compositions, which can serve as excellent precursors for the synthesis of many nanoporous metal oxides and their nanocomposite materials. In the future, this strategy can be extended for the synthesis of other tailor-made cyano-bridged CPs with their potential applications for the desired nanoporous inorganic materials.

Table of Contents

CHAPTER 1	1
GENERAL INTRODUCTION.....	1
1.1. SINGLE-CRYSTAL ENGINEERING	2
1.1.1. <i>Three-dimensional (3D) single-crystal system</i>	2
1.1.2. <i>Two-dimensional (2D) single-crystal system</i>	5
1.1.3. <i>Crystal-growth approaches - Advantages of the vapor diffusion method (slow diffusion method)</i>	7
1.1.4. <i>Applications</i>	7
1.2. NANOSTRUCTURED PB AND PB ANALOGUES	9
1.2.1. <i>0D nanostructured PB and PB analogues (nanoparticles)</i>	9
1.2.2. <i>1D nanostructured PB and PB analogues (nanowires and nanorods)</i>	15
1.2.3. <i>2D nanostructured PB and PB analogues</i>	16
1.2.4. <i>Hybridized nanostructures</i>	18
1.3. MATERIALS DERIVED FROM PB AND PBAS.....	21
1.3.1. <i>PB- and PBA-derived metal oxide nanostructures</i>	21
1.3.2. <i>PB-derived metal carbides and alloys</i>	39
1.3.3. <i>PB-derived metal sulfides and selenides</i>	50
1.3.4. <i>PB-derived metal phosphides</i>	59
1.4. PERSPECTIVE.....	65
REFERENCES	65
CHAPTER 2	83
TWO-DIMENSIONAL CYANO-BRIDGED COORDINATION POLYMER OF MN(H ₂ O) ₂ NI(CN) ₄ : STRUCTURAL ANALYSIS AND PROTON CONDUCTIVITY MEASUREMENTS UPON DEHYDRATION AND REHYDRATION	83
2.1. INTRODUCTION.....	84
2.2. EXPERIMENTAL SECTIONS.....	86
2.2.1. <i>Synthesis</i>	86
2.2.3. <i>Water adsorption/desorption isotherms</i>	88
2.2.4. <i>Proton conductivity measurements of single-crystal</i>	88
2.2.4. <i>Other measurements</i>	88

2.3. RESULTS AND DISCUSSION	89
2.4. CONCLUSION	107
REFERENCES	108
2.5. APPENDIX.....	112
REFERENCES	114
CHAPTER 3	116
SINGLE CRYSTAL GROWTH OF TWO-DIMENSIONAL CYANO-BRIDGED	
COORDINATION POLYMER OF [CO(H₂O)₂NI(CN)₄]·4H₂O USING TRISODIUM CITRATE	
DIHYDRATE	116
3.1. INTRODUCTION.....	117
3.2. EXPERIMENTAL SECTIONS.....	118
<i>3.2.1. Single-crystal X-ray diffraction (SC-XRD)</i>	118
<i>3.2.3. Water adsorption/desorption isotherms.</i>	119
3.3. RESULTS AND DISCUSSION	119
3.4. CONCLUSION	128
REFERENCES	128
CHAPTER 4	130
GRAPHENE-WRAPPED NANOPOROUS NICKEL-COBALT OXIDE FLAKES FOR	
ELECTROCHEMICAL SUPERCAPACITORS	130
4.1. INTRODUCTION.....	131
4.2. EXPERIMENTAL SECTIONS.....	132
<i>4.2.1. Chemicals</i>	132
<i>4.2.2. Preparation of cyano-bridged CoNi-CP flakes.</i>	132
<i>4.2.3. Preparation of graphene sheets.</i>	133
<i>4.2.4. Preparation of NiCo-oxide/G composite.</i>	133
<i>4.2.5. Characterization.</i>	133
<i>4.2.6. Electrode preparation and electrochemical measurements.</i>	134
4.3. RESULTS AND DISCUSSION	135
4.4. CONCLUSION	146
REFERENCES	147
CHAPTER 5	149

SYNTHESIS OF HOLLOW CO-FE PRUSSIAN BLUE ANALOGUE CUBES BY USING SILICA SPHERES AS A SACRIFICIAL TEMPLATE	149
5.1. INTRODUCTION.....	150
5.2. EXPERIMENTAL SECTIONS.....	151
<i>5.2.1. Chemicals</i>	<i>151</i>
<i>5.2.2. Synthesis of Hollow CoFe-PBA.....</i>	<i>152</i>
<i>5.2.3. Synthesis of Hollow CoFe-PBA.....</i>	<i>152</i>
<i>5.2.4. Structural Characterization Afield-emission</i>	<i>153</i>
<i>5.2.5. Electrochemical Measurements.....</i>	<i>153</i>
5.3. RESULTS AND DISCUSSION	154
5.4. CONCLUSION	161
REFERENCES	161
CHAPTER 6-1	164
CYANO-BRIDGED CU-NI COORDINATION POLYMER NANOFLAKES AND THEIR THERMAL CONVERSION TO MIXED CU-NI OXIDES	164
6-1.1. INTRODUCTION.....	165
6-1.2. EXPERIMENTAL SECTIONS	166
<i>6-1.2.1. Chemicals.....</i>	<i>166</i>
<i>6-1.2.2. Synthesis of 2D Cu-Ni CP flakes.....</i>	<i>166</i>
<i>6-1.2.3. Thermal conversion from 2D Cu-Ni nanoflakes to mixed metal oxides.....</i>	<i>167</i>
<i>6-1.2.4. Characterization.....</i>	<i>167</i>
<i>6-1.2.5. Electrochemical measurements.....</i>	<i>168</i>
6-1.3. RESULTS AND DISCUSSION.....	169
6-1.4. CONCLUSION	179
REFERENCES	180
CHAPTER 6-2	183
IN-SITU FORMATION OF CU-NI CYANO-BRIDGED COORDINATION POLYMER ON GRAPHENE OXIDE NANOSHEETS AND THEIR THERMAL CONVERSION	183
6-2.1. INTRODUCTION.....	184
6-2.2. EXPERIMENTAL SECTIONS	185
<i>6-2.2.1. Chemicals.....</i>	<i>185</i>
<i>6-2.2.2. Synthesis of GO nanosheets.....</i>	<i>185</i>

6-2.2.3. <i>Synthesis of Cu-Ni cyano-bridged CP.</i>	185
6-2.2.3. <i>In situ formation of Cu-Ni cyano-bridged CP on GO nanosheets.</i>	186
6-2.2.3. <i>Characterization.</i>	186
6-1.3. RESULTS AND DISCUSSION	187
6-2.4. CONCLUSION	196
REFERENCES	196
CHAPTER 7	199
GENERAL CONCLUSIONS	199
8.1. OVERVIEW OF THE ACHIEVEMENTS.....	200
(I) <i>Two-dimensional cyano-bridged coordination polymer of Mn(H₂O)₂[Ni(CN)₄]: structural analysis and proton conductivity measurements upon dehydration and rehydration (Chapter 2).</i> ..	201
(II) <i>Single Crystal Growth of Two-Dimensional Cyano-Bridged Coordination Polymer of [Co(H₂O)₂Ni(CN)₄].4H₂O Using Trisodium Citrate Dihydrate (Chapter 3).</i>	202
(III) <i>Synthesis of Hollow Co-Fe Prussian Blue Analogue Cubes by using Silica Spheres as a Sacrificial Template (Chapter 4)</i>	202
(IV) <i>Graphene-Wrapped Nanoporous Nickel-Cobalt Oxide Flakes for Electrochemical Supercapacitors (Chapter 5)</i>	202
(V) <i>Cyano-Bridged Cu-Ni Coordination Polymer Nanoflakes and Their Thermal Conversion to Mixed Cu-Ni Oxides (Chapter 6)</i>	203
LIST OF ACHIEVEMENTS LIST	204
ACKNOWLEDGMENT.....	207

Chapter 1

General Introduction

1.1. Single-crystal engineering

In the last few decades, there has been interest in crystal growth processes, particularly in the increasing demand for materials with technological applications.[1,2] Although it is more difficult to prepare a single crystal than a polycrystalline material, several efforts have been made because of the outstanding advantages of single crystals.[3] The high-quality single crystal of coordination polymers (CPs) is necessary to study the physics of correlated materials,[4] tune the properties of existing materials by growing related analogues, and discover new systems that will lead to understanding of the chemistry and physics of materials that will impact technology.[5–6] Such polymers are generally insoluble, retaining their original framework in solvents. Recrystallization which is the most common crystallization method, is not available because many physical properties are obscured or complicated by the effects of grain boundaries.

1.1.1. Three-dimensional (3D) single-crystal system

As one of the oldest coordination polymers, PB ($\text{Fe}_4[\text{Fe}(\text{CN})_6]_3 \cdot 14\text{H}_2\text{O}$) has attracted scientists for many centuries.[7] The first structure was originally proven by Keggin and Miles,[8] who proposed the occurrence of interstitial metal ions within the face-centered cubic unit cell in order to achieve electroneutrality via X-ray powder patterns.[9–10] This sample unit cell, $Fm\bar{3}m (O_h^5)$, where alternating Fe(II) and Fe(III) located on the face centered cubic lattice, the Fe(III) are surrounded octahedrally by nitrogen atoms, and Fe(II) are surrounded by carbon atoms, in unit cell dimensions is 10.2 Å.[8–10] However, because of the small particle size and the analytical uncertainties, the structure was not conclusively determined. In 1977, Buser *et al.* grew single crystals of PB, $\text{Fe}_4[\text{Fe}(\text{CN})_6]_3 \cdot x\text{H}_2\text{O}$ ($x = 14–16$), by the very slow diffusion of water vapor into a solution of Fe^{3+} and $\text{Fe}(\text{CN})_6^{4-}$ in concentrated hydrochloric acid solution[11] and presented the prototype structural model as space group symmetry $Fm\bar{3}m$ for cubic cyanides. A 12 cm of single crystal grew without potassium contamination after ion exchange column with $\text{K}_4\text{Fe}(\text{CN})_6$ to $\text{H}_4\text{Fe}(\text{CN})_6$. Franz *et al.* prepared $\text{Mn}(\text{II})[\text{Mn}(\text{III})(\text{CN})_6]_{2/3} \cdot (6\text{H}_2\text{O})_{1/3}, y\text{H}_2\text{O}$ using slow diffusion, but with a similar unit cell occupancy ($Fm\bar{3}m$).[12] The Ludi group studied the $\text{Fe}_4[\text{Fe}(\text{CN})_6]$ crystal using single-crystal

X-ray and neutron diffraction during a hydration/dehydration process. The X-ray study showed that PB is a face-centered cubic system.[13] However, Widmann and co-worker preferred a unit cell similar to that of Keggin and Miles, suggesting that the Ludi's structure is an alkali-free compound.[14]

Rubidium manganese hexacyanoferrates $\text{Rb}_x\text{Mn}[\text{Fe}(\text{CN})_6]_y \cdot z\text{H}_2\text{O}$ have received attention because they show many functionalities such as a charge transfer phase transition,[15–16] a pressure-induced magnetic pole inversion,[17] and a photomagnetic effect.[18] Additionally, the dehydrated $\text{RbMnFe}(\text{CN})_6$ is a suitable material to investigate the electronic structure. Tokoro and co-worker prepared a dark brown single crystal of rubidium manganese hexacyanoferrate, $\text{Rb}_{0.61}\text{Mn}[\text{Fe}(\text{CN})_6]_{0.87} \cdot 1.7\text{H}_2\text{O}$, using the slow diffusion method.[19] The results of X-ray crystallography show that $\text{Rb}_{0.61}\text{Mn}[\text{Fe}(\text{CN})_6]_{0.87} \cdot 1.7\text{H}_2\text{O}$ belongs to the face-centered cubic lattice $Fm\bar{3}m$ with lattice constants of $a = b = c = 10.5354(4)$ Å. Vertelman *et al.*[20] obtained $\text{Rb}(\text{H}_2\text{O})\text{FeMn}(\text{CN})_6$ using a modified version of the crystallization method developed by Kepert *et al.*[21] The obtained structural model belongs to the cubic space group $F\bar{4}3m$ with lattice constants of $a = b = c = 10.521(2)$ Å. When the electron transfer occurs, $\text{Rb}_{0.61}\text{Mn}[\text{Fe}(\text{CN})_6]_{0.87} \cdot 1.7\text{H}_2\text{O}$ become inactive, possibly because of the unbalanced redox potentials of the individual metal sites, which are a consequence of the unfavorable stoichiometry involving $\text{Fe}(\text{CN})_6$ vacancies and an associated number of water molecules.[20,22]

Dong *et al.* successfully synthesized and characterized a PB ferrimagnetic $\text{Na}[\text{MnCr}(\text{CN})_6]$ PBA with a strictly face-centered cubic system. In this system, each unit cell contains four $\text{Na}[\text{MnCr}(\text{CN})_6]$ molecules. The $[\text{Cr}(\text{CN})_6]^{3-}$ connects to six Mn atoms through CN bridges, and each Mn atom connects to the six nitrogen atoms of the six cyanide bridges. A face-centered cubic framework ($Fm\bar{3}m$, $a = b = c = 10.8159(12)$ Å) of $\text{Cr}-\text{C}\equiv\text{N}-\text{Mn}$ and both Mn and Cr atoms are six-coordinated with octahedral geometry.[23] Julie and co-worker designed new single-molecule magnets to explore synthetic routes to metal cyanide clusters by reactions between $[(\text{Me}_3\text{tacn})\text{Cr}(\text{CN})_3]$ ($\text{Me}_3\text{tacn}=\text{N},\text{N}',\text{N}''$ -trimethyl-1,4,7-triazacyclononane) and selected manganese(II) salts. The reaction between the perchlorate salt and AClO_4 ($\text{A}=\text{Na}$,

K) forms $A[(Me_3tacn)_6MnCr_6(CN)_{18}](ClO_4)_3$, where the center Mn(II) ion is surrounded by six $[(Me_3tacn)Cr(CN)_3]$ units. The Mn coordination geometry is similar to a trigonal prism, with triangular faces twisted away from an eclipsed position at an angle of 12.83° and 11.33° for $A = Na$ and K , respectively.[24]

The octahedral compounds with high valence cluster complexes with terminal cyano groups, which can be form 2D and 3D of coordination polymer like a mononuclear cyano complexes, were found in 1998.[25] In 2001, Bennett and co-worker were the first to form PB cyano cluster-based compounds from the general formula $M_4[Re_6X_8(CN)_6]_3 \cdot xH_2O$ ($M = Ga^{3+}$, Fe^{3+} , $X = Se, Te$).[26] They succeeded in “direct expansion of Prussian blue” and kept the PB structure unchanged by replacing a small $[Fe(CN)_6]^{4-}$ node with a large $[Re_6X_8(CN)_6]^{4-}$, benefiting from the long distances between metal and metal.

Some materials’ dimensions increase with heating, and by using the enhanced negative thermal expansion (NTE) or thermal expansivities to develop and design materials for some specific applications. It is required to understand and study the chemical composition and structure after NTE or thermal expansion. The effects of NTE on cyanide-based molecular framework materials including PB have been reported.[21, 27,28] Chapman and co-worker[21] reported the growth of a single crystal of PBA via the slow diffusion method and studied the effects of systematic variation of the divalent metal ion (MII) site in $M^{II}Pt^{IV}(CN)_6$ ($M = Mn, Fe, Co, Ni, Cu, Zn, Cd$) by NTE. They suggest that the NTE behavior in the sample was influenced by the vibrational flexibility of the metal-cyanide binding interaction and that for more flexible framework, the NTE behavior should be enhanced.

The first $Ag_3[Co(CN)_6]$ structure was studied using X-ray powder in 1967 by Ludi and co-workers,[29] but it was validated by Pauling and Pauling when they reevaluated the structure in 1968 because of some deflections in the structure, such as the large amount of triple bond of C-N in cyanide and the position of H and Ag ions.[30] They studied the structure using modern X-ray and neutron diffraction[31,32] and described the structure as a 3D framework formed by $Co-CN-Ag-NC-Co$ linkages. Each Co^{3+} ion in the center position connects to six other Co atoms by cyano linkages to form a cubic framework like the PB with an extended

covalent framework. The distance between the cube edges (Co–CN–Ag–NC–Co) are long, and other two additional identical framework lattices can accommodate within the open cavities of the first framework to form trip interpenetrating (**Figure 1.1c**). The thermal expansion behavior of $\text{Ag}_3[\text{Co}(\text{CN})_6]$ was studied in 2008, and the results show that thermal expansion in cell dimensions takes place with minimal distortion of the $\text{Co}(\text{CN})_6$ coordination polyhedra, but with involves flexing of the Co–CN–Ag–NC–Co linkages.[33]

For the first time, Pan *et al.*[34] successfully prepared a fabrication of micron-size single-crystalline PB nanosheets using a simple hydrothermal process (**Figure 1.1d**). X-ray diffraction results show that the nanosheets have a face-centered cubic (fcc) structure of $\text{Fe}_4[\text{Fe}(\text{CN})_6]_3$ with lattice constant $a = 10.26 \text{ \AA}$.

1.1.2. Two-dimensional (2D) single-crystal system

A 2D structure with square-planar of Hofmann-type clathrate $\text{ML}_x\text{M}'(\text{CN})_4$ ($\text{L}=\text{H}_2\text{O}$, NH_3 , pyridine, *etc.*) are constructed by the CN bonding between the square-planar (also it is called as tetrahedral tetracyanometallate (II), $[\text{M}'(\text{CN})_4]^{2-}$ ($\text{M}'=\text{Ni}$, Pb , Pt and Au)) units and octahedral metal (M) units combined with auxiliary ligands (L_x) (**Figure 1.1b**).[35–36] In this section, I introduce the Hofmann-type structure as it belongs to transition metal cyanide compounds. There are a few 2D structures with water coordination, such as $\text{Ni}(\text{H}_2\text{O})_2\text{Ni}(\text{CN})_4$,[37] $\text{Cd}(\text{H}_2\text{O})_2\text{Ni}(\text{CN})_4 \cdot 4\text{H}_2\text{O}$,[38] $\text{Fe}(\text{H}_2\text{O})_2\text{Ni}(\text{CN})_4 \cdot 2\text{C}_4\text{H}_8\text{O}_2$,[39] and $\text{Co}(\text{H}_2\text{O})_2\text{Ni}(\text{CN})_4 \cdot 4\text{H}_2\text{O}$. [40] Recently, $\text{Mn}(\text{H}_2\text{O})_2[\text{Ni}(\text{CN})_4] \cdot 4\text{H}_2\text{O}$ and $\text{T}(\text{H}_2\text{O})_2[\text{Ni}(\text{CN})_4] \cdot x\text{H}_2\text{O}$ with $\text{T} = \text{Mn}$, Co , Ni were reported.[41–43] The $[\text{Ni}(\text{CN})_4]^{2-}$ units are critical for the formation of a 2D coordination network having a net topology, which connects to other metal nodes, extending the network. Murphy *et al.* reported a new porous coordination framework of $[\text{Zn}-\{\text{MnN}(\text{CN})_4(\text{H}_2\text{O})\}] \cdot 2\text{H}_2\text{O} \cdot \text{MeOH}$ using the functional $[\text{MnN}(\text{CN})_4]^{2-}$ subunits.[44] Recently, 2D cyanide bridges of $\{[\text{Cu}^{\text{I}}\text{Ni}^{\text{II}}(\text{CN})_4(\text{H}_2\text{O})_2] \cdot \text{H}_2\text{O}\}_n$ were also prepared using the solvothermal conditions method.[45]

In 1997, Holmes and Girolami[46] have initiated significant studies on some PBAs containing $\text{Cr}(\text{CN})_5(\text{NO})$ units to obtain new crystal structure. The powder XRD analysis results show that $\text{K}_{0.5}\text{Mn}[\text{Cr}(\text{CN})_5(\text{NO})]_{0.83} \cdot 4\text{H}_2\text{O} \cdot 1.5\text{MeOH}$ has a cubic structure. However,

Kou *et al.*[47] studied the reaction of $[\text{Ni}(\text{tn})_3]^{2+}$ ($\text{tn} = 1,3\text{-propanediamine}$) with $[\text{Cr}(\text{CN})_5(\text{NO})]^{3-}$ based on single-crystal X-ray diffraction analysis. It is found that the obtained crystal is 2D grid-like assembly of $[\text{Ni}(\text{tn})_2]_2[\text{Cr}(\text{CN})_5(\text{NO})]\text{OH}\cdot\text{H}_2\text{O}$ (space group $P\bar{1}$). For further investigation into the binding modes of $[\text{Cr}(\text{CN})_5(\text{NO})]^{3-}$ with transition metal complexes, they also studied the reaction of $[\text{Ni}(\text{tn})_3]^{2+}$ ($\text{tn} = 1,3\text{-propanediamine}$) with $[\text{Cr}(\text{CN})_5(\text{NO})]^{3-}$ and formed 2D of grid-like compound of $[\text{Ni}(\text{tn})_2]_2[\text{Co}(\text{CN})_6]\text{NO}_3\cdot 2\text{H}_2\text{O}$ with space group $P\bar{1}$.

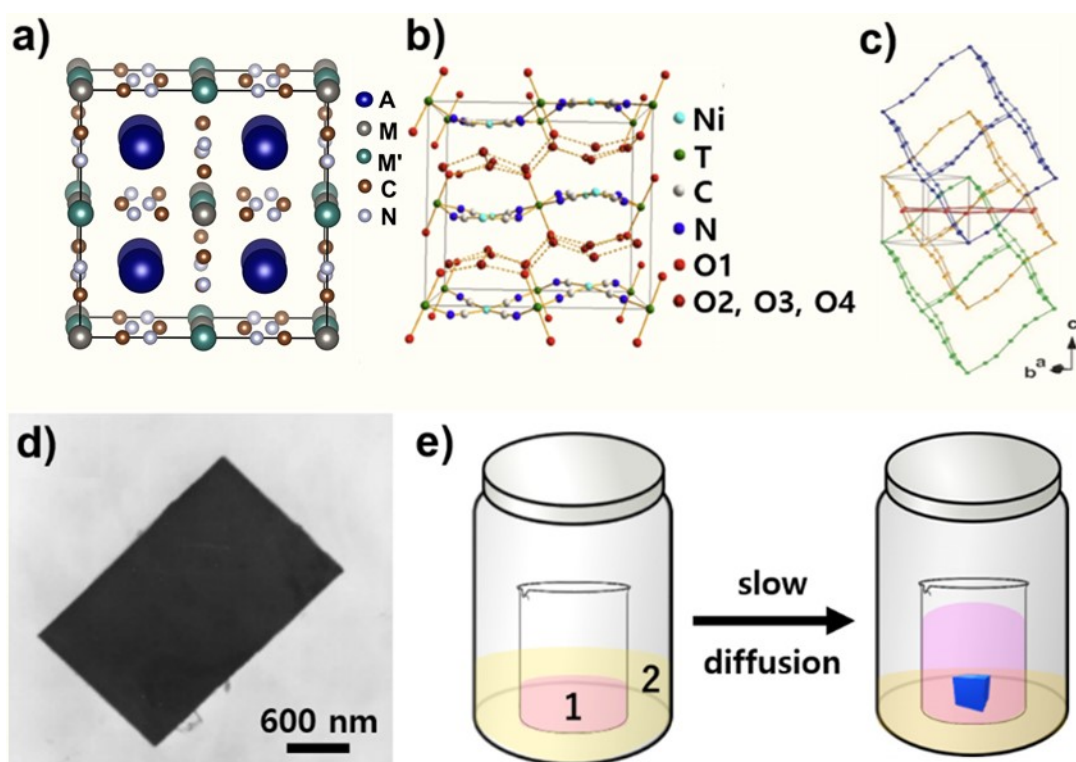


Figure 1.1 (a) Schematic of a single crystal of PBA $A_m M_x [M'(\text{CN})_6]_y \cdot n \text{H}_2\text{O}$, where M and M' = transition metal ions and A = an alkali-metal ion. (b) Hofmann-type $T(\text{H}_2\text{O})_2[\text{Ni}(\text{CN})_4] \cdot x \text{H}_2\text{O}$. (c) Three interpenetrating cubic nets of extended Co-CN-Ag-NC-Co linkages that form a 3D framework.[33] (d) SEM image of micron-size single-crystalline $\text{Fe}_4[\text{Fe}(\text{CN})_6]_3$ nanosheets.[34] (e) The slow diffusion method.

1.1.3. Crystal-growth approaches - Advantages of the vapor diffusion method (slow diffusion method)

Several methods have been reported for growing single crystals under different growth conditions and environments. The traditional hydrothermal method is carried out under harsh conditions, with high pressure as well as high temperatures.[45, 48-50] However, the most common method used to grow a crystal is vapor diffusion (slow diffusion) because of the simplicity of the experiments. Recently, many researchers reported growing a single crystal of PB and PBAs using the vapor diffusion method, also called the slow diffusion method.[11,19,23,24,44,51-53] Dong *et al.* successfully synthesized a single crystal of Na[MnCr(CN)₆] using this method, and it was the first strictly face-centered cubic lattice structure with PB family $A_mM_x[M'(CN)_6]_y \cdot nH_2O$ that has been characterized by single-crystal X-ray analysis.[23] The vapor diffusion method has been used to grow organic crystals that are highly soluble in a particular organic solvent but have poor solubility in other solvents (**Figure 1.1e**). Solvent 1 has a low vapor pressure (beaker 1). This beaker is then placed in a larger beaker (beaker 2) containing a volatile solvent that only slightly dissolves the crystal. After beaker 2 is sealed, the volatile solvent evaporates, and the gas diffuses into beaker 1 to form an oversaturated solution. Then nucleation and crystallization occur in the beaker 1.[54,55] In the vapor diffusion method, the crystallization can occur at a low temperature. For example, the RbMn[Fe(CN)₆]·H₂O single crystal[20] was formed even at 45°C, although one can expect that high temperature (higher than the melting points) is required to prepare a single crystal because these melting points of MnCl₂·4H₂O and K₃[Fe(CN)₆] are 56 and 200°C, respectively. Thus, the vapor diffusion method results in a crystal with high purity, good surface morphology, and uniform layer thickness.

1.1.4. Applications

Yuan *et al.* investigated the adsorption of a 3D single crystal of Mn₂X(CN)₈ (X = Mo (sample 1), W (sample 2)) with water, nitrogen, and hydrogen.[56] Samples 1 and 2 (**Figure 1.2a**) show three steps in the water adsorption isotherms. In the first step, three coordinated water molecules per formula unit were adsorbed at $P/P_0 = 0.01$. The second step was carried

out at $P/P_0 = 0.2$ to uptake one coordinated water molecule. The abrupt uptake behavior at low relative pressure is characteristic of strong $\text{H}_2\text{O}-\text{Mn}^{2+}$. The third step was at a range of $P/P_0 = 0.5-0.7$, corresponding to the adsorption of an additional three uncoordinated water molecules. The slow kinetics of adsorption in this range could be due to the narrow pores and/or slow changes in the crystal structure. The in-situ structural studies will be necessary to elucidate the nature of the crystal during this adsorption/desorption process. Ray and co-worker dried a single crystal of $[\text{Mn}[\text{Ni}(\text{CN})_4] \cdot 6\text{H}_2\text{O}]$ at 110°C under a nitrogen atmosphere, then kept it in open air for three days. The powder X-ray diffraction (PXRD) pattern shows that the dehydrated crystal was rehydrated (**Figure 1.2b**) and confirms the flexibility of the cyano-bridged coordination polymer.[41] Recently, the water vapor adsorption/desorption for a single crystal of $[\text{Mn}[\text{Ni}(\text{CN})_4] \cdot 6\text{H}_2\text{O}]$ after dehydration at 150°C was studied (**Figure 1.2c**).[57] The first stage showed a water vapor pressure (P/P_0) range of 0.4-0.5, in which the three water molecules adsorbed per unit could be the coordinated water. The second stage was at a range of $P/P_0 > 0.5$, which also showed that the three water molecules adsorbed per unit could be the interlayer water. These six water molecules are the fully hydrated form, suggesting a structural transformation to other crystal structures under different humidity ratios.

The nitrogen adsorption isotherm for $\text{Mn}_2\text{X}(\text{CN})_8$ ($\text{X}=\text{Mo}$ (sample 1), W (sample 2)) at 77 K showed that the adsorption is a type I isotherm (**Figure 1.2d**), and the surface area and pore volumes were $146 \text{ m}^2 \text{ g}^{-1}$ and $112 \text{ m}^2 \text{ g}^{-1}$ for sample 1 and $0.027 \text{ cm}^3 \text{ g}^{-1}$ and $0.020 \text{ cm}^3 \text{ g}^{-1}$ for sample 2, respectively. At high pressure, both samples adsorbed a small amount of nitrogen, presumably in multilayers on the external surface. Hydrogen adsorption at 1.1 bar and 77 K for both samples were 0.60 and 0.49 wt% (**Figure 1.2e**), respectively. The hydrogen adsorption increased with the increasing micropore volumes. The minimum volumetric H_2 storage densities for samples 1 and 2 were 11.36 and 10.98 g L^{-1} , respectively. **Figure 1.2e** shows that the adsorption of H_2 started in the initial stage, indicating a strong interaction between H_2 and the four coordinated Mn ions in both materials.

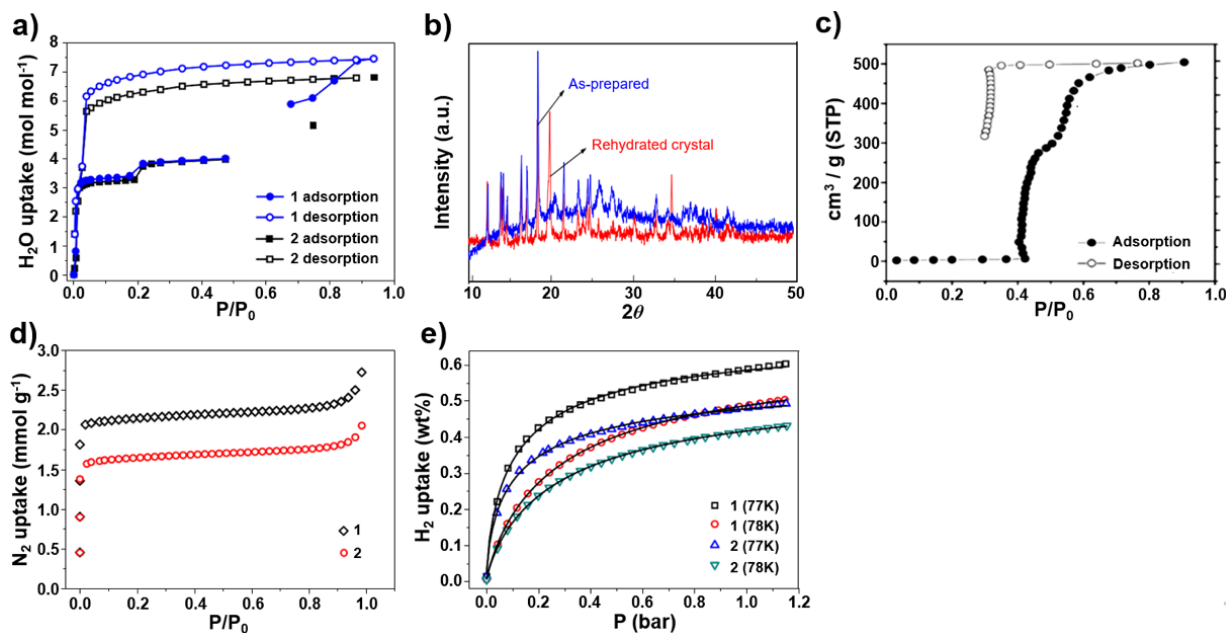


Figure 1.2 (a) Water adsorption/desorption isotherms for samples 1 and 2.[56] (b) PXRD patterns of $[\text{Mn}[\text{Ni}(\text{CN})_4]$ as a prepared and rehydrated complex after dehydration.[41] (c) Water adsorption/desorption isotherms for a single crystal of $\text{Mn}(\text{H}_2\text{O})_2[\text{Ni}(\text{CN})_4] \cdot 3(\text{H}_2\text{O})$ (d) N_2 adsorption isotherms for samples 1 and 2.[56] (e) Low-pressure H_2 adsorption isotherms for samples 1 and 2 at 77 and 87 K and the fit with the Langmuir Freundlich equation (solid lines).[56]

1.2. Nanostructured PB and PB analogues

1.2.1. 0D nanostructured PB and PB analogues (nanoparticles)

Since the discovery of size effects related to semiconductors and noble metals, such as quantum dots and catalytic gold nanoparticles, enormous efforts have been made to downsize solids. Owing to the significance of the size effect, 0D nanostructures have been generated as an independent factor that can affect the properties of solids. To explore 0D nanostructured PB and PB analogues, it is necessary to develop a controlled synthetic strategy. Because PB and PB analogues are usually prepared by crystallization, wet-chemical routes have been employed in most cases. The strategies developed previously can be mainly categorized as spatially controlled synthesis, kinetically controlled crystallization, and the post-fabrication method.

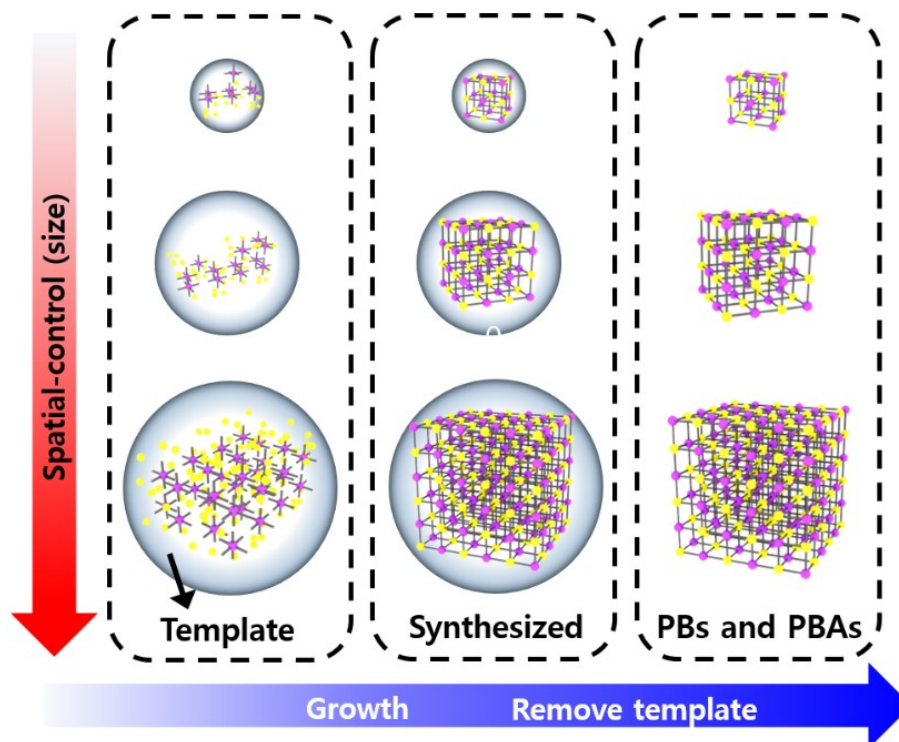


Figure 1.3 Scheme for spatially controlled synthesis of 0D PBAs in nanocavities.

Spatially controlled synthesis employs nanocavities as reactors for PBs and PBAs (**Figure 1.3**). The synthesized PB and PBAs gradually occupy the reactors. Once the cavities are fully filled, the walls hinder further growth, leading to 0D nanostructures. Depending on the stiffness of the walls, the molds can be categorized as hard or soft. For instance, by filling the pores in mesoporous silica with reactants, monodispersed PBA nanoparticles can be fabricated.[58] Since the pore sizes of mesoporous silica can be controlled well, the sizes of the generated PBA nanoparticles are adjustable, offering great feasibility to investigate the size-dependent properties. To remove the hard templates, a hydrofluoride or alkaline solution is used. To avoid using the harsh etchants, soft templates have been used because they can be removed by mild treatment. Polymers or surfactants can form nanodroplets or porous scaffolds through self-assembly or crystallization.[59–80] The nanodroplets or porous scaffolds can provide nanocavities for the crystallization of PB and PBAs. Moreover, the softness gives great flexibility to the cavities. Therefore, the size of the soft nanocavities can be adjusted easily, leading to nanoparticles with tunable sizes in a wide range.

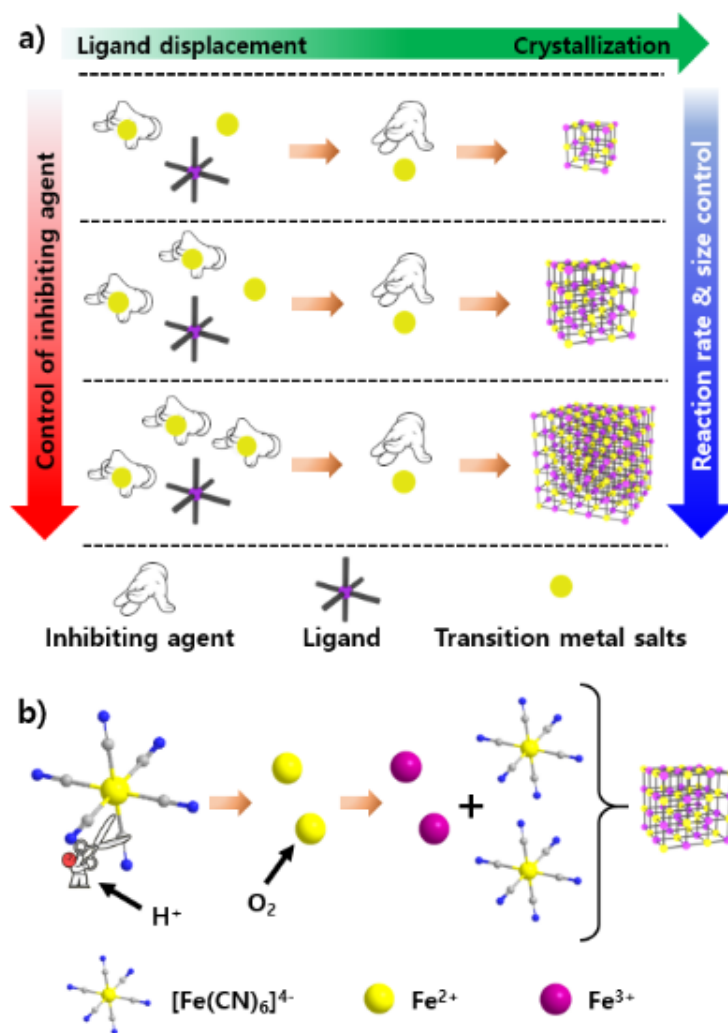


Figure 1.4 (a) Size-control synthesis of PBAs via inhibiting agent. (b) PBAs fabricated by decomposition of a single precursor.

Despite the advantages of spatially controlled synthesis, several steps involved in removal of the hard/soft templates lengthen the processing time and make the operation rather complicated. Kinetically controlled crystallization is another attractive strategy. The principle of this strategy is to control both crystal nucleation and growth by manipulating reaction rates[81–90] and/or inhibiting unnecessary crystal evolution with capping agents.[91–105] By regulating the reaction rates, ultra-small nanoparticles can be easily collected when the reaction rate is fast, whereas large nanoparticles are usually obtained by slowing down the reaction rate. The reaction rate can be controlled by the addition of an inhibiting agent (**Figure 1.4a**),[81–85] decomposition of single precursors (**Figure 1.4b**),[86–89] sequential growth,[90] or other

reaction parameters.[91–105] For instance, trisodium citrate can chelate with transition metal salts, then inhibit direct reaction between the transition metal salts and ligands.[81,83] Changing the amount of trisodium citrate makes the reaction rates tunable, permitting PB and PBA nanoparticle sizes to be controlled between 20 and 500 nm. The reaction rates can also be delayed by a single-precursor decomposition method when the common precipitation reaction is too fast. For example, dissociation of the $K_4[Fe(CN)_6]$ complex under the hydrothermal condition gradually produces Fe^{2+} ions, which can further react with the residual $[Fe(CN)_6]^{4-}$ anions to generate PB nanoparticles.[86–89] Because the dissociation rate of the $K_4[Fe(CN)_6]$ complex depends on the pH value, temperature, and concentration of the complex, the crystallization rate of PB and PBAs is controllable.

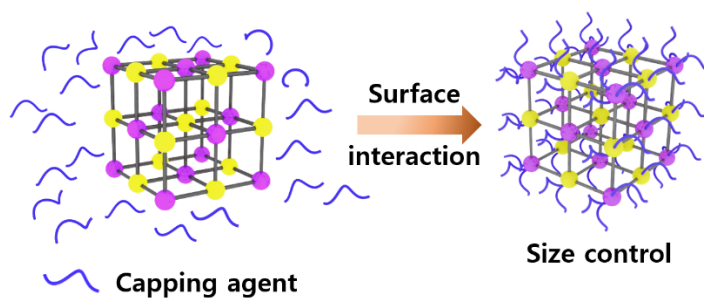


Figure 1.5 Control of PBA nanoparticles by a capping agent.

Rather than controlling the reaction rates, attaching capping agents to the crystal surface can significantly inhibit the growth of the nucleus (**Figure 1.5**).[91–105] By introducing a capping agent that has a strong surface interaction with the PB and PBAs nucleus, the extension/growth of the external crystal surface can be well controlled. Compared with the nanoparticles obtained by changing the reaction rates, the particles size-controlled by capping agents can be limited to a very small range, 2–10 nm. In particular, when the surfaces are anchored with the surfactants, monodispersed nanoparticles, which are soluble in organic solvents, can be obtained, making further processing easy.[105]

The above strategies allow the synthesis of monodispersed PBA nanoparticles. Further modifications of the nanostructures of PB and PBA nanoparticles are required to explore new

properties. For this purpose, chemical etching as a post-treatment is the most widely used [106–120] because the coordination bonds inside PB and PBAs can be broken either by protons or hydroxide ions (**Figure 1.6**). This strategy gives various dissociation rates at different crystal positions. When the facets dissolve faster than the corners and edges, nanoframes can be obtained by the direct etching of nanocubes.[108, 110] When the corners and edges dissolve more quickly, elongated particles can be obtained.[117] Moreover, the parts with more defects can be more easily etched than the perfect parts. On the basis of these facts, macro- or mesopores can be further introduced into the particles by controlled etching. Through intentional introduction of defects at the desired parts, hollow or porous materials can be fabricated.[115] Multiple cavities can even be made through controlled etching.[106] The properties of the 0D nanoparticles strongly correlate with their sizes and shapes. For instance, the magnetic property of PB nanoparticles depends on their sizes and shapes. A transition from ferromagnetism to superparamagnetism happens with the size reduction once the particle size is below the critical size.[66, 100] With the reduction in size, the surface anisotropy and interparticle dipolar interactions cannot be ignored, because the metal nodes exposed at the surface are in a different coordination environment than that inside the crystals. As a result, the magnetic anisotropy can be changed.[66] Creating hollow nanoparticles can also change the magnetic properties. Magnetizing hollow nanoparticles is easier than magnetizing solid particles.[115]

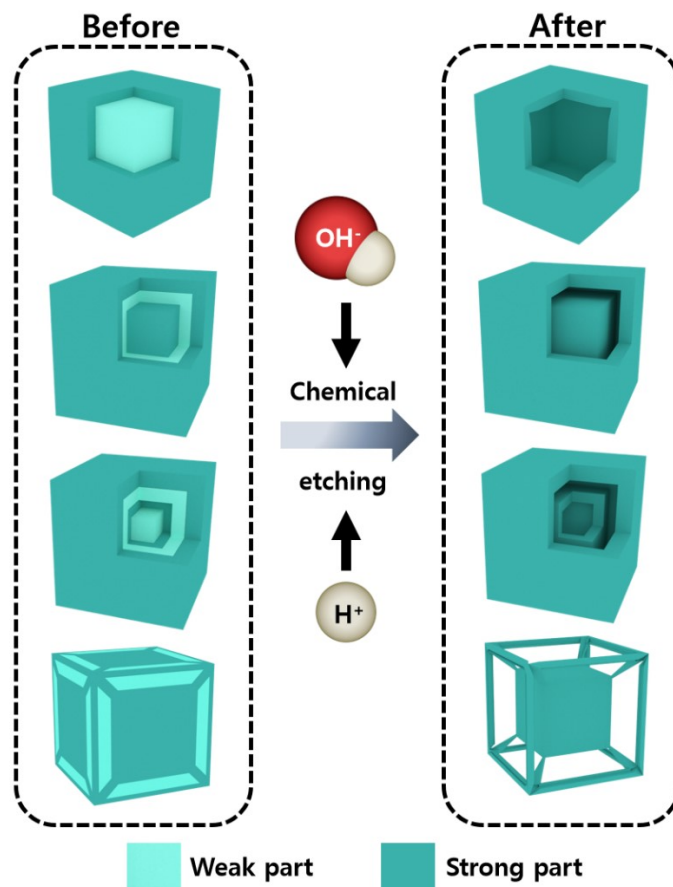


Figure 1.6 Post-fabrication of PBA nanoparticles by chemical etching.

The PBA solids are known to be good adsorbents for metal ions, particularly alkali ions. Because the size determines the length of the diffusion pathway, small particles are promising as adsorbents in water. One important example is Cs-ion removal. The small PB particles (20 nm) can adsorb Cs^+ ions much faster than the medium-sized PB particles (100 nm), which is important for fast removal of Cs^+ ions from contaminated water.[92] The performance of nanoparticles can be further enhanced by hierarchical porous structures. After etching by HCl, the hollow PB nanoparticles showed a 10-fold increase in Cs-ion uptake as compared with the commercial PB nanoparticles.[114, 119] The ability to store alkali ions eventually leads to the application of PB and PBAs as electrodes for alkali ion batteries. These nanoparticles have shown stable Na-ion/K-ion storage capability as electrodes for sodium-ion/potassium-ion batteries during a long-term cycling test while maintaining high current densities.[121–128] Owing to abundant cavities both on the outermost and inner parts, the loading or adsorption

capacity of drug molecules in PB and PBAs can be increased, making them useful as nanomedicine.[69, 120, 129–130] In addition, their replaceable Gd, Fe, or Mn nodes can boost MRI contrast.[69, 130]

1.2.2. 1D nanostructured PB and PB analogues (nanowires and nanorods)

Shape anisotropy plays a crucial role in the tuning properties of solids. The 1D structure usually shows a large shape anisotropy because of the high length-to-radius ratio. Therefore, the shape anisotropy brings interesting properties. The most significant examples have been found in carbon nanotubes and semiconductor nanowires. The unique nanostructures of these materials allow them to form strong bundles, penetrate cells, be assembled into high-performance devices, *etc.* Encouraged by the astonishing achievements in a related field, 1D nanostructured PB and PBAs have been investigated before. As with the above-mentioned 0D nanostructures, spatially controlled synthesis and kinetically controlled crystallization are two main methods (**Figure 1.7**).

The spatially controlled synthesis can be divided into half spatial control and full spatial control (**Figure 1.7a,b**).[131–140] For full spatial control, the crystal growth is fully confined inside a nanoreactor with a tube-like cavity. Adequate or continuous feeding of reactants ensures that the synthesized materials can fill the nanoreactor to replicate the shape of the cavity, leading to 1D nanostructures. For half spatial control, nucleation and the early growth stage of crystals are confined, forcing further growth in one direction. After growing outside the confined space, subsequent elongation follows the previous direction, increasing the length-to-radius ratio further. Compared to the full-spatial-control strategy, this method has no limitation on the final length of the nanowires. Kinetically controlled crystallization can also be realized by inducing the preferential growth of specific facets via a capping agent or self-assembly (**Figure 1.7c**).[141–145] For example, hexacyanometallates can be linked to surfactants. The synthesized molecules can align into worm-like structures in solution. When metal ion nodes are added to coordinate with the modified hexacyanometallates, the surfactant chains linked to the ligands automatically anchor on the surface of the generated PBAs, inhibiting isotropic growth. As a result, worm-like PBAs can be fabricated.[141]

The 1D structures show a significant influence on magnetic properties. Because the average number of magnetic interaction neighbors is small, the Curie temperature of the 1D solid becomes lower than the bulk one, because this temperature is known to be associated with the number of magnetic neighbors.[131–134] The alignment of nanocrystals along one direction also enhances the magnetic dipolar interaction. Therefore, the magnetic anisotropy can be significantly strengthened.[132]

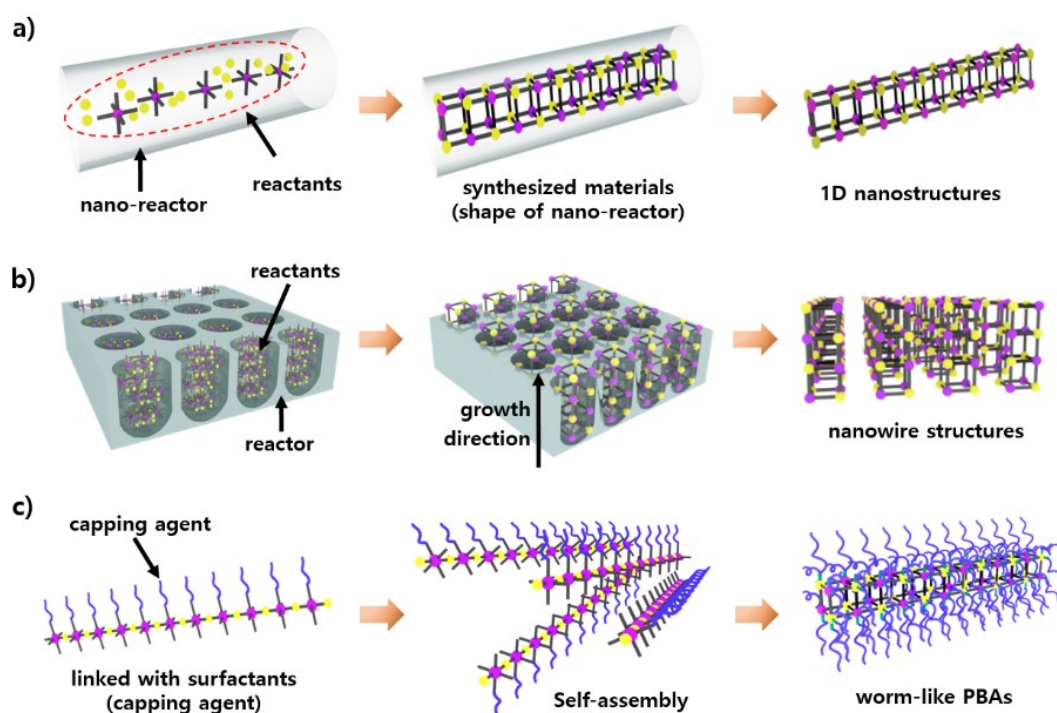


Figure 1.7 (a) Full spatial control of 1D PBA synthesis. (b) Half spatial control of 1D PBA synthesis. (c) Kinetically controlled synthesis of 1D PBAs.

1.2.3. 2D nanostructured PB and PB analogues

Compared to 0D and 1D nanostructures, the fabrication of a 2D structure is rather difficult, although it is very attractive. For the metal cyanides with a layer structure rather than the common cubic structure, the challenge is the precipitation rate, which is generally too fast, leading to poorly crystallized particles. With the addition of a reaction inhibitor in an appropriate amount, the kinetics of crystallization can be controlled (**Figure 1.8**). After slowing down the reaction rates, fewer nuclei can be generated, and slower growth occurs subsequently.

Therefore, the atoms/ions in the solution can assemble in a precise way, forming nanoflakes.[146]

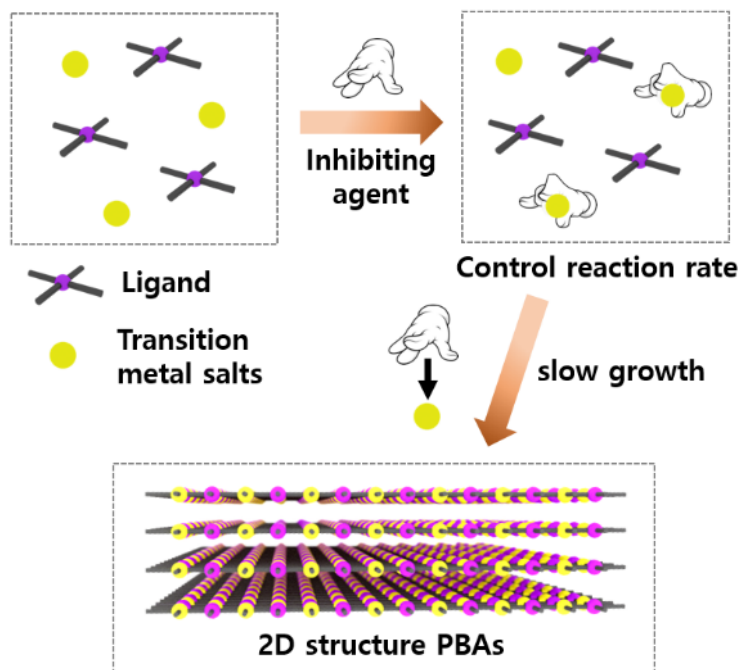


Figure 1.8 Scheme for the controlled synthesis of 2D PBAs using an inhibiting agent.

By introducing DMF into the reaction system, the surface of the PBAs can be preferentially capped by DMF molecules. The capping effect induces the anisotropic growth of the PBA nucleus, leading to PBA nanosheets. The crystallized polymers can also work as a template for the generation of 2D PBAs.[147] By linking PBAs and polymers, the PBAs can be fabricated between the planar spaces. As a result, the shape of the PBAs is confined to a 2D shape (**Figure 1.9**).[148,149] A more general way is to deposit PBAs on the surface of flat substrates. In these cases, the substrates can be wonderful supports for the formation of thin films. When the thickness of the deposited thin films is well-controlled, 2D PB and PBAs are synthesized naturally.[34,150–158] For instance, Mallah *et al.* employed the LB technique repeatedly in the fabrication of 2D PBAs. The PBA nanoparticles were carefully packed onto the surface of the substrates, thereby leading to dense 2D PBA structures.[153,155]

The 2D shape makes the crystal surface largely exposed, and stacking of the 2D nanostructure can happen easily. Evaporating a droplet of the nanoflake suspension enables the

nanoflakes to form an ordered stacking structure. This kind of stacking provided unexpected adhesive properties.[159] In addition, the 2D CPs showed superior catalytic activity toward the Fenton reaction as compared with the bulk ones.[147]

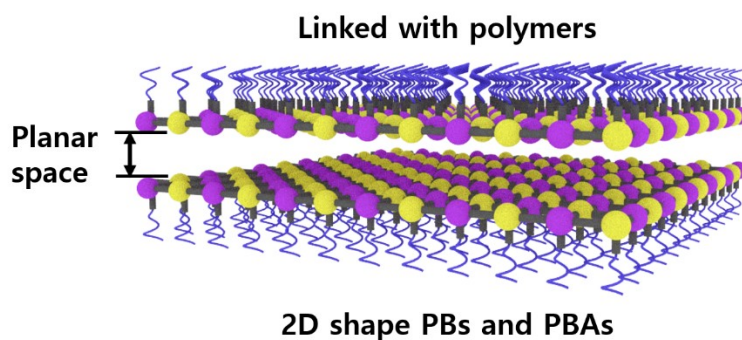


Figure 1.9 2D PBAs fabricated via surface capping.

1.2.4. Hybridized nanostructures

As the requirements for practical applications vary, it would be necessary to hybridize different PBAs together or with other solids. The hybridization of different PBAs is usually realized by epitaxy. Most of the PBAs have a close lattice structure, so the mismatch between them is small. A layer of PBA can easily grow on the top surface of another PBA's particles/films (**Figure 1.10**).[160–177] The challenge to perfect hybridization is the crystallization rate. Fortunately, this problem has been solved. There are several ways to control the crystallization rate. By using a peristaltic pump, feeding of the reactants can be kept very slow, and thus an outermost layer can grow on a nanoparticle to generate a core–shell structure.[173] The deposition speed can also be controlled by adding an inhibition agent.[106, 178] With the help of sodium citrate, a single-crystalline shell can be deposited on the surface of a single-crystalline core. Electrochemical deposition is another powerful strategy for controlling the deposition speed. Epitaxy on a PBA film has been achieved using this method.[174]

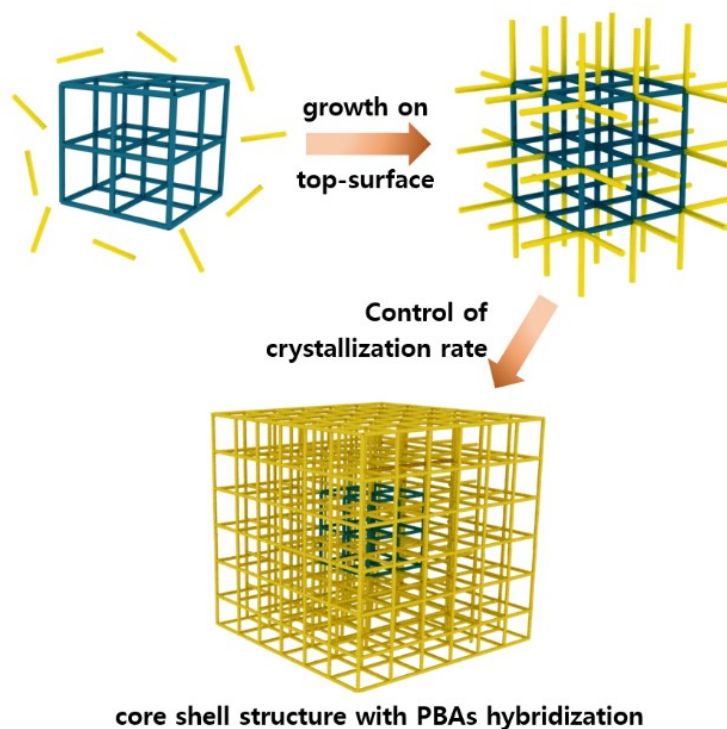


Figure 1.10 Epitaxy of PBAs on each other.

To hybridize PBAs with other solids such as metal or metal oxides, sequential growth or coordination replication has been carried out. Sequential growth generally relies on chemical modification of the substrates. The modified surface of the substrates can favor coordination with the metal nodes; therefore, the deposition of PBAs on the substrates is possible (**Figure 1.11**).[144] For instance, PBAs can be deposited on gold nanoparticles to generate core-shell particles.[179] Coordination replication has been used extensively in the deposition MOFs on metal oxides.[180,181] The key point is the simultaneous etching of metal oxides and the precipitation of MOFs. By using metal oxides as sacrificial substrates, the released metal ions in acid solution can be captured by the hexacyanometallates and form networks immediately. They grow on the surface of the sacrificial metal oxides, leading to a PBA/MO composite.

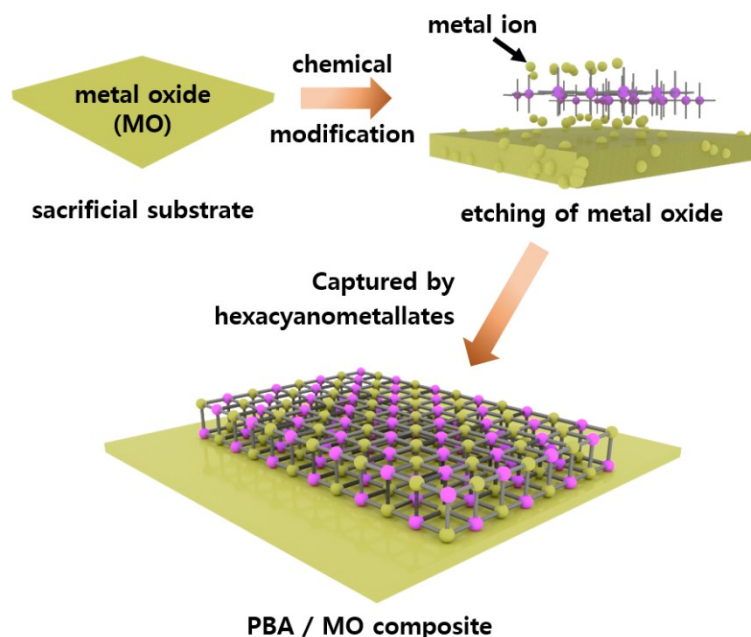


Figure 1.11 Sequential growth of PBAs on substrates.

The PBAs can be integrated with polymers (**Figure 1.12**). When polymeric hydrogel was used as the reactor, protons could be released at an elevated temperature in water. The released protons prompted the decomposition of hexacyanometallates, leading to the formation of PBAs inside the hydrogel.[182] The PBA-based hybrids not only exhibit functions from each component as a sum but also benefit from the synergistic effect of the combination. For instance, when a BiVO_4/PBA film was irradiated by an ultraviolet photon, the generated holes and electrons in BiVO_4 can be separated by PBAs and then boosted water splitting.[182] Even when two PBAs were carefully grown together, the hybrid solid showed a remarkable synergistic property. For a core-shell particle, the exchange anisotropy at the interface results in a large increase in the coercive field.[161] The T_c of the core-shell particle can be affected by the existence of an interface between the ferromagnetic and ferrimagnetic phases.[164] Enhancement of the T_c is caused by the proximity effect. When the core-shell particles were used for the electrochemical interaction of alkali ions, the imperfect arrangement of the metal nodes at the interface led to alternation of the coordination environment. This change alternates the redox potential of the nodes, making inert ions active during ion intercalation.

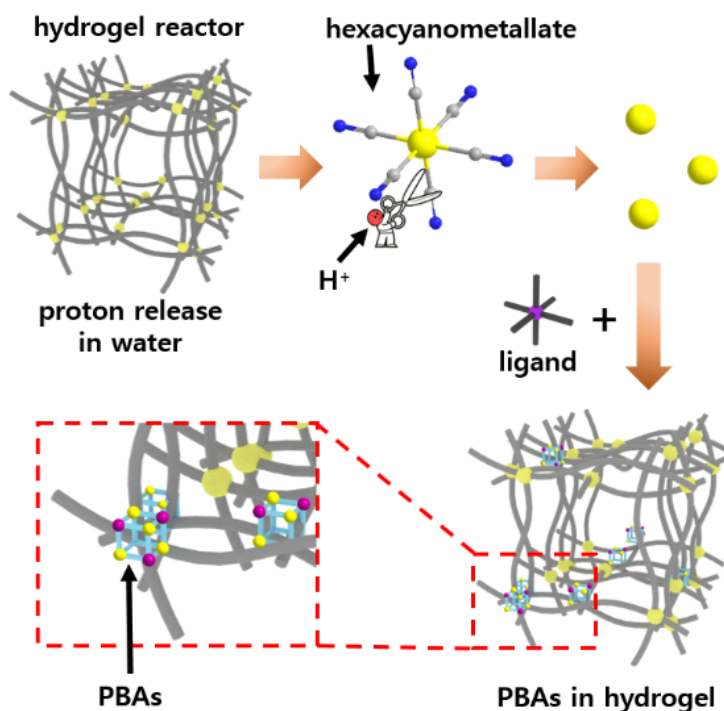


Figure 1.12 Hybridization of PBAs inside a hydrogel polymer.

1.3. Materials derived from PB and PBAs

PB and PBAs containing various kinds of metals (*e.g.*, Fe, Ni, Co, and Mn) can be effectively used as templates and precursors to synthesize porous or hollow nanomaterials with uniform sizes, varied compositions, and diverse morphologies and architectures. PB and PBAs offer a variety of derivatives, including metal oxides (MOs), metal sulfides (MSs), metal carbide, metal phosphide, alloy nanoparticles, and their composites with porous carbon or graphitic carbon nitride. These derivatives of PB and PBAs have been widely studied as electrode materials for batteries and supercapacitors, gas sensors, electrocatalysts, adsorbents, *etc.*

1.3.1. PB- and PBA-derived metal oxide nanostructures

The thermal treatment of PB and PBAs in air has been presented as an efficient and promising route for large-scale preparation of various highly porous transition metal oxides (TMOs), such as iron oxides (Fe_2O_3), [183-191] cobalt oxide (Co_3O_4), [192-196] nickel oxide, [197] spinel-type mixed oxides ($\text{A}_x\text{B}_{3-x}\text{O}_4$), [198-207] and perovskite (ABO_3) [208, 209] and composite oxides. [210-228] When PB or PBAs are treated in an air atmosphere, the

organic linkers are completely decomposed into gases, and the metal ions are oxidized to metal oxides. Although there are some templating approaches such as hard-templating and soft-templating methods,[229-232] PB- and/or PBA-derived materials always exhibit uniform particle sizes, a high surface area, interconnected pores, uniform element distribution from inside to outside, and diverse morphologies and architectures.

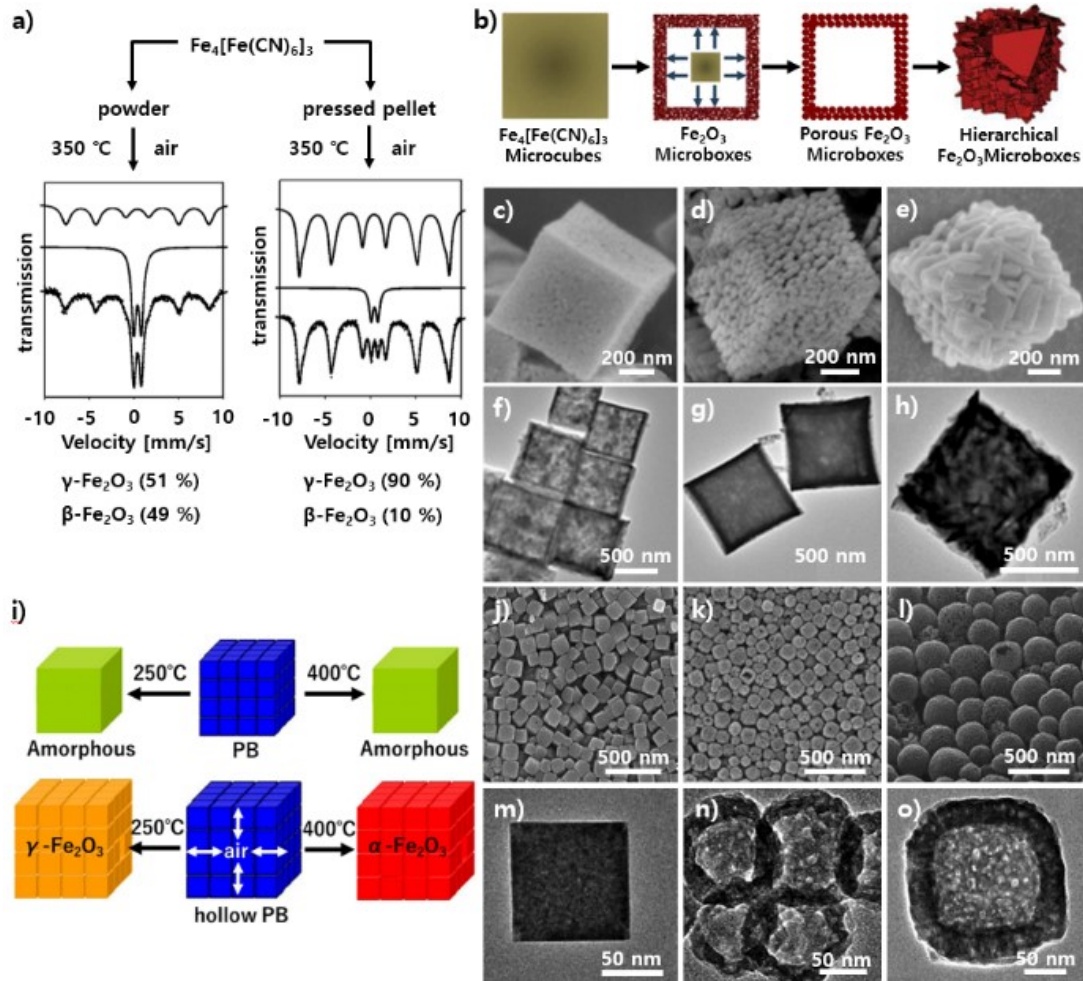


Figure 1.13 (a) The relationship between product contents and oxidation–diffusion conditions of PB annealed at 350°C . (b) Schematic illustration of the formation of hollow Fe_2O_3 microboxes and the evolution of the shell structure with the increasing calcination temperature. (c, e, g) FE-SEM and (d, f, h) TEM images of hollow Fe_2O_3 microboxes obtained at (c, d) 350°C , (e, f) 550°C , and (g, h) 650°C . (i) Schematic illustration of the relationship between product contents and PB particle size and calcination conditions. (j–l) SEM and (m–o) TEM

images of (j, m) PB, (k, n) hollow γ -Fe₂O₃, and (l, o) hollow α -Fe₂O₃ prepared by the calcination of different PB precursors at different temperatures.

Zboril *et al.* studied the effect of particle sizes and calcination temperatures on the decomposition behaviours of PB nanocubes.[183] It was found that amorphous Fe₂O₃ nanoparticles with ultra-small particles and a high specific surface area were prepared under a relatively low temperature (250°C). Then, an increase in PB particle size resulted in an increase in the particle size of amorphous Fe₂O₃ and a proportional reduction of the specific surface area of particles. When the calcination temperature was raised to 350°C, a mixture of cubic bixbyite β -Fe₂O₃ and cubic spinel γ -Fe₂O₃ was achieved. The molar ratio of β -Fe₂O₃ to γ -Fe₂O₃ decreased with an increase in the PB particle size. It is proposed that a larger particle size represents the system with less favorable conditions for the air–oxygen access and liberation of gaseous (CN)₂ (**Figure 1.13a**). In another example, Zhang *et al.* showed that the calcination temperature affects the morphological features of iron (III) oxide prepared by the calcination of PB (**Figure 1.13b–h**).[184] Hollow structured Fe₂O₃ were obtained via the Kirkendall effect, which is based on a nonequilibrium interdiffusion process. It was observed that a high calcination temperature resulted in a hierarchical shell structure with promising lithium storage properties, while at a low calcination temperature, iron (III) oxides with smooth shell structure were achieved. The heating rate was also reported to show the same effects on the morphological features of obtained Fe₂O₃ nanocubes.[185] Furthermore, Hu *et al.* reported the fabrication of iron oxide nanostructures with controlled crystalline phases from hollow Prussian blue (PB) derived from HCl etching in the presence of PVP (**Figure 1.13i–o**).[186] The cavity sizes in the starting PB nanocubes, as well as the calcination temperatures, were critical factors in achieving crystalline phase control of the obtained iron oxide. It was found that pure phase crystallized α -Fe₂O₃ and γ -Fe₂O₃ can be selectively formed by simply tuning the applied calcination temperatures and selecting the PB nanoparticles with different cavities. The well-crystallized hollow γ -Fe₂O₃ particles, derived from the thermal decomposition of large PB nanocubes at 250°C, possess a sufficient saturation magnetization (M_s) value.

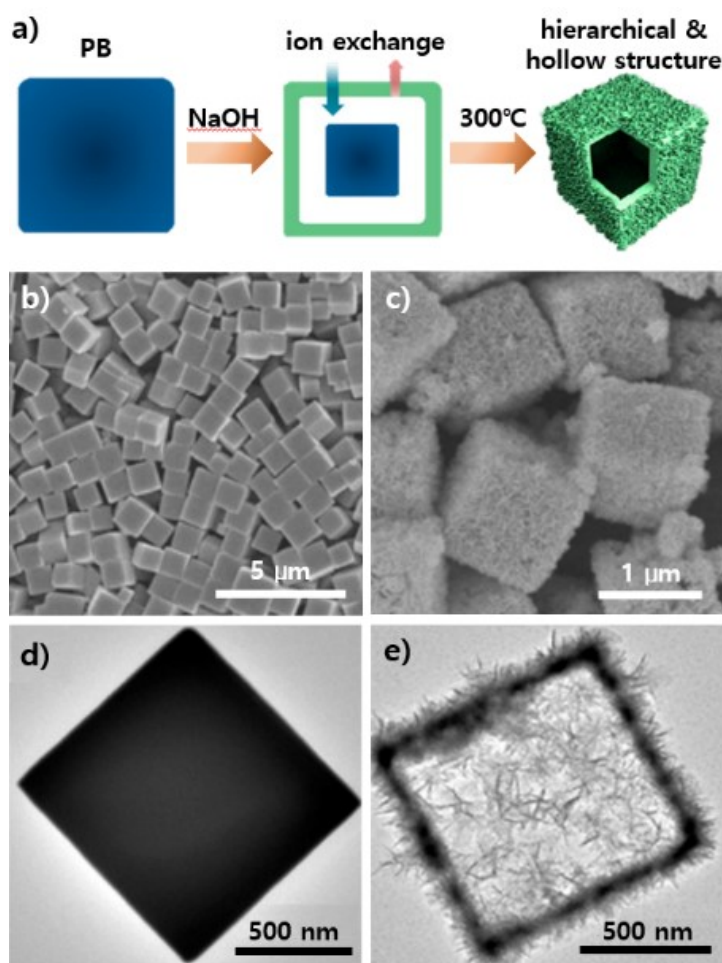


Figure 1.14 (a) Schematic illustration of the synthesis of hierarchical and hollow Fe_2O_3 microboxes from PB templates via a two-step strategy. (b, c) FE-SEM and (d, e) TEM images of (b, d) a PB cube before etching and (c, e) hierarchically single-shelled Fe_2O_3 microboxes obtained by the reaction of PB precursors with 0.2 M NaOH under hydrothermal conditions.

In addition to direct calcination, a two-step strategy has been developed for the synthesis of hierarchical and hollow porous Fe_2O_3 nanoboxes from PB, as shown in **Figure 1.14**.^[187,189] First, hierarchical $\text{Fe}(\text{OH})_3$ microboxes were prepared using the wet-chemical method, that is, an ion-exchange reaction between PB microcubes and NaOH solution. Second, a shape-retaining calcination process was used to obtain hierarchical and hollow structured Fe_2O_3 . The NaOH solution concentration and the reaction temperature are critical to the formation kinetics of hierarchical structured $\text{Fe}(\text{OH})_3$. Yolk–shelled or multishelled structures can also be achieved by control of the reaction kinetics using concentrated alkaline solution at

an elevated temperature. Hierarchical and hollow nanostructures possess various advantageous features, such as a high specific surface area and well-aligned porous morphology, that have received great attention for many applications. As an example, the as-prepared complex hollow Fe_2O_3 microboxes exhibit remarkable electrochemical performance as anode materials for lithium ion batteries.[189] When applied in H_2S sensors, they can provide effective gas-diffusion paths without sacrificing the high surface area as a result of their less agglomerated configurations.[187] Iron oxides have long been regarded as promising anode materials for LIBs because of their high theoretical capacity of about $1,000 \text{ mA h g}^{-1}$. The lithium storage mechanism of iron oxides is based on the redox conversion reaction, where the iron oxides are reduced to metallic Fe nanocrystals dispersed in a Li_2O matrix upon lithiation and then reversibly restored to their initial oxidation states upon delithiation.

Porous Co_3O_4 nanocages can be fabricated via the thermal decomposition of $\text{Co}_3[\text{Co}(\text{CN})_6]_2 \cdot n\text{H}_2\text{O}$ (Co-Co PBA) in air. The porous structure of the prepared Co_3O_4 nanocages was contributed by the removal of organic parts in the form of CO_2 and N_xO_y during the oxidative decomposition process. Yan *et al.* reported the synthesis of pure phase crystalline Co_3O_4 nanoparticles with a different morphology and structure by simple thermal decomposition of Co–Co PBA nanoparticles at different temperatures (**Figure 1.15a–d**).[195] Based on the TG curve, the thermal decomposition temperature of the PBA precursors should be performed at temperatures up to 350°C . When calcinated at relatively low temperatures, *e.g.*, 450 and 550°C , the Co–Co PBA could decompose to form porous hollow structured Co_3O_4 while retaining the original shape. With the calcination temperature raising, the crystallinity of Co_3O_4 gradually becomes better, while some of the porous hollow structured Co_3O_4 collapsed into solid dendritic grains due to the intense gas release. The proportion of the nanocage and nanoparticle depended on the annealing temperature. In another case, uniform polyhedron-like Co–Co PBA particles were prepared via an SDBS modified precipitation reaction (**Figure 1.15e–h**).[193] When used as precursors for the synthesis of Co_3O_4 , it was found that the as-prepared porous Co_3O_4 displays a concave structure on the surface, which is different from the porous structure obtained from other precursors. The Co–Co PBA microcubes can be etched

in ammonia solution at room temperature by a complex reaction between Co^{2+} and NH_4^+ without the addition of any surfactant (**Figure 1.15i–l**).^[194] It is worth noting that the etching behavior in Co–Co PBA is anisotropic, resulting in Co–Co PBA microframes with an open pore at each corner of the cube. After annealing under suitable temperature in air, the as-obtained Co–Co PBA microframes are then transformed to Co_3O_4 microframes with a porous shell. When evaluated as potential electrode materials, the Co_3O_4 microframes exhibit enhanced electrochemical performance, including a large specific capacity, long cycling stability, and excellent rate capability for LIBs and a small overpotential and good durability for the oxygen evolution reaction. Similarly, in case of the Co-M PBA (M = Co, Fe), an ion exchange reaction can occur with NaOH in solution, resulting in the formation of cobalt oxides (**Figure 1.15m–p**).^[196] Due to the $[\text{M}(\text{CN})_6]^{3-}$ being replaced and redissolved in solution, metal “M” will not be present in the final products, and pure cobalt oxides are obtained.

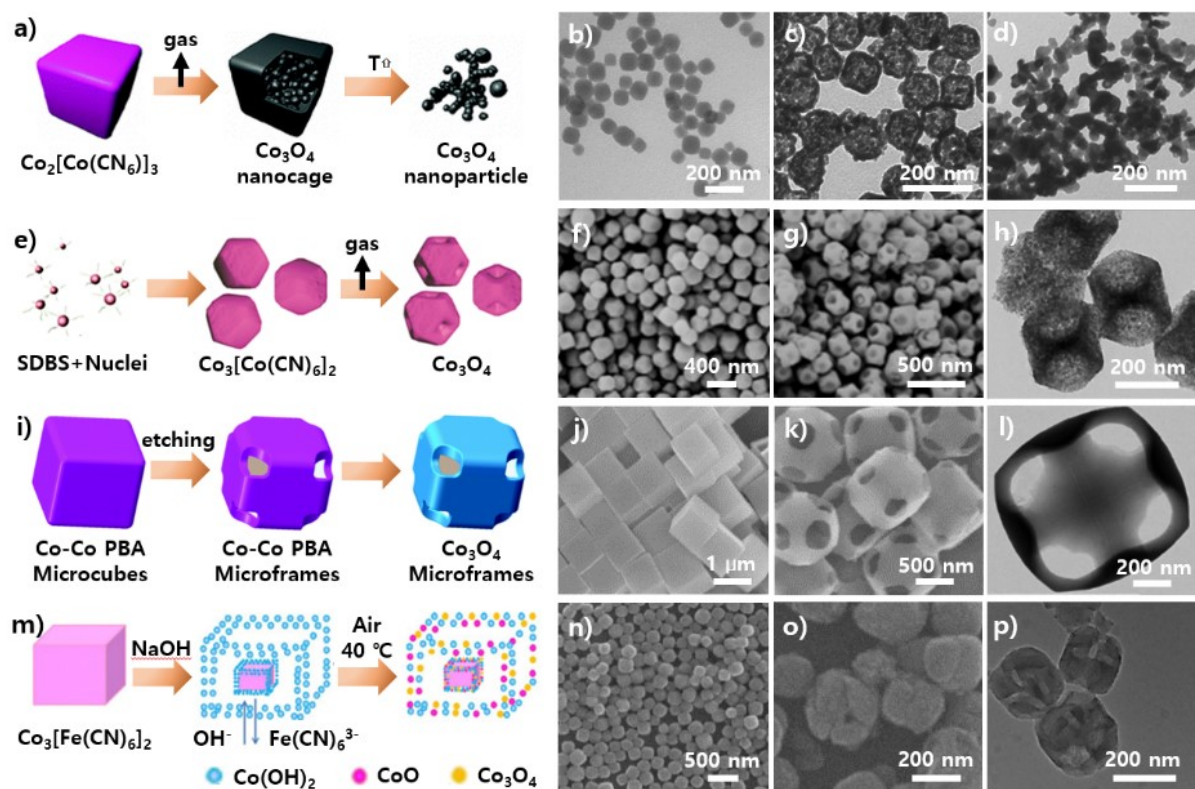


Figure 1.15 (a) Schematic illustration of the synthesis of Co_3O_4 nanocages and nanoparticles via thermal decomposition of $\text{Co}_2[\text{Co}(\text{CN})_6]_3$. TEM images of (b) the precursor $\text{Co}_3[\text{Co}(\text{CN})_6]_2$ and (c, d) the Co_3O_4 nanoparticles calcined at 450 and 850°C. (e) Schematic representation of the formation of Co_3O_4 porous polyhedrons. (f, g) SEM and (h) TEM images of (f) $\text{Co}_3[\text{Co}(\text{CN})_6]_2$ and (g, h) Co_3O_4 porous polyhedrons. (i) Schematic illustration of the formation process of Co_3O_4 microframes. SEM images of (j) Co–Co PBA microcubes, (k) Co–Co PBA microframes, and (l) Co_3O_4 microframes. (m) Schematic illustrating the preparation process of hollow CoO_x nanocubes with a porous shell. (n) SEM images of the PBA nanoparticles. (o) SEM and (p) TEM images of CoO_x nanocubes obtained by chemical etching in 0.02 M NaOH for 20 min.

Uniform and porous ZnO microspheres were obtained by annealing $\text{Zn}[\text{Zn}(\text{CN})_4] \cdot x\text{H}_2\text{O}$ (Zn-PBA) as templates and precursors.[238] It was found that the annealing condition has a significant impact on the composition and morphology of the products, as shown schematically in **Figure 1.16**. When calcined in air, the oxidative decomposition of the Zn-PBA microspheres was carried out uniformly within the sphere

because of the porous structure, resulting in polycrystalline ZnO microspheres. However, when Zn-PBA is first annealed in an Ar atmosphere and then in air, the ZnO of the yolk–shell structures is obtained with some amount of carbon residue. Under this calcination condition, the formation of the yolk–shell structure can be explained by its heterogeneous construction. In detail, the temperature gradient induces the surface nanoparticles first to decompose and form a dense ZnO shell. Then the decomposition of inner nanoparticles gradually leads to shrinkage of the microspheres and separation of the surface and the inner core. As a result, yolk–shell structures are generated. At the same time, decomposition of the organic linkers in the microspheres results in the porous structure. The as-prepared porous ZnO yolk–shell structures possess various advantageous features, including a large specific surface area, low density, a microreactor environment, and reduced transport lengths for both mass and charge transport. When applied as electrode materials of lithium ion batteries, these yolk–shell structured microspheres show excellent battery performance, such as high rate capacity and ultra-long cycle life.

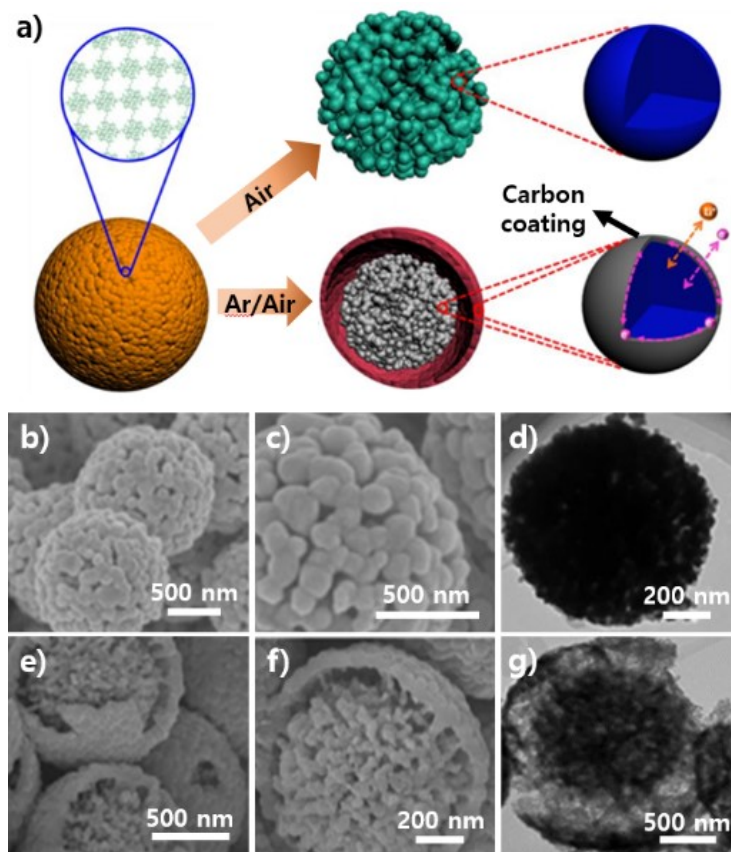


Figure 1.16 (a) Schematic illustrating the synthesis of porous ZnO or ZnO@C nanocrystals from $\text{Zn}[\text{Zn}(\text{CN})_4] \cdot x\text{H}_2\text{O}$ microspheres. (b, c) SEM and (d) TEM images of ZnO microspheres. (e, f) SEM and (g) TEM images of yolk–shell structured YC-ZnO.

In recent years, mixed transition metal oxides (with a formula of $\text{A}_x\text{B}_{3-x}\text{O}_4$, where A and B represent two different transition metals, such as Fe, Ni, Co, Mn, and Zn) have received increasing attention due to their excellent redox reactivity and electronic conductivity originating from the coupling of various metallic species and the valence variability of transition metals, which is beneficial in many energy-related applications. Additionally, the various combinations of the cations and the tunable stoichiometric/nonstoichiometric compositions in the MTMOs provide vast opportunities to manipulate the physical/chemical properties. Various spinel-type mixed oxides have been fabricated by annealing $\text{A}_3[\text{B}(\text{CN})_6]_2$ in air under controlled conditions. For example, Hu *et al.* reported a strategy for the synthesis of binary $\text{Fe}_{1.8}\text{Co}_{1.2}\text{O}_4$ porous nanostructures, involving conserved morphology and the thermal transformation of $\text{Fe}_3[\text{Co}(\text{CN})_6]_2 \cdot n\text{H}_2\text{O}$ nanoparticles (**Figure 1.17a**).^[206] The as-prepared

$\text{Fe}_{1.8}\text{Co}_{1.2}\text{O}_4$ product is comprised of many nanoparticles, without serious aggregation, and its morphology has undergone negligible change as compared with the precursor. Furthermore, the distribution of Fe, Co, and O in the porous nanocage is highly homogeneous at the atom scale. However, limited to the Fe/Co ratio in PBA, only the $\text{Fe}_{1.8}\text{Co}_{1.2}\text{O}_4$ spinel could be obtained from such a strategy. The constant ratio of transition metals in PBAs significantly limited the application of this method. Later, Li *et al.* improved this strategy using a cationic doping method, and $\text{Fe}_y\text{Co}_{1-y}[\text{Co}(\text{CN})_6]_{0.67} \cdot n\text{H}_2\text{O}$ was developed for the synthesis of $\text{Fe}_x\text{Co}_{3-x}\text{O}_4$ ($0 < x < 1$) (**Figure 1.17b**).^[199] Despite the change in the proportion of Fe, the resulting product still corresponded well with a spinel-type structure, and the distribution of elements was still uniform.

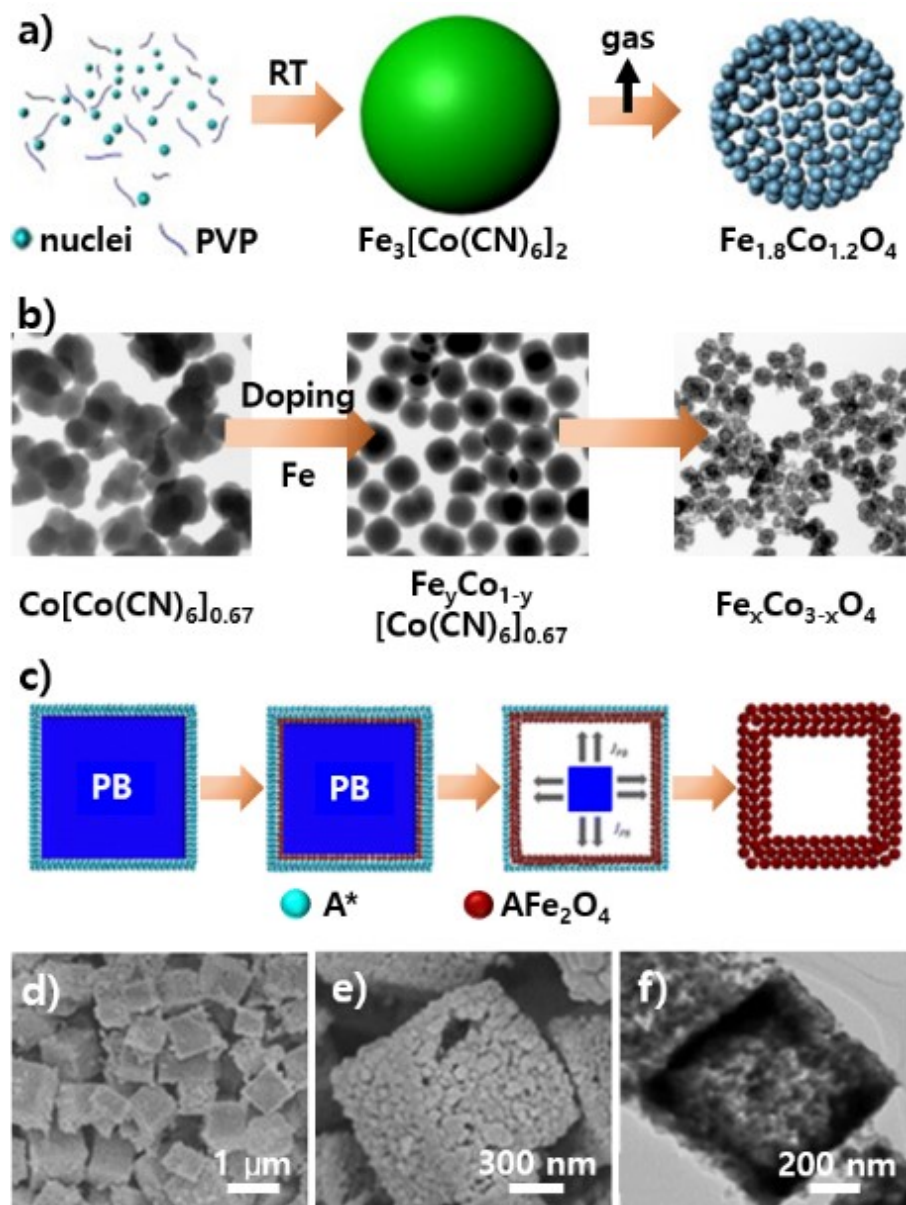


Figure 1.17 (a) Schematic illustration of the formation of $\text{Fe}_{1.8}\text{Co}_{1.2}\text{O}_4$ nanoporous particles. (b) Preparation procedure of $\text{Fe}_x\text{Co}_{3-x}\text{O}_4$ ($0 < x < 1$) nanocages. (c) Schematic illustration of the synthetic process of the Fe-based ternary metal oxide hollow structures. (d, e) FE-SEM images at different magnifications of the porous NiFe_2O_4 hollow cubes. (f) TEM images of the porous NiFe_2O_4 hollow cubes.

In another case, Yan *et al.* reported the synthesis of porous hollow spinel AFe_2O_4 ($\text{A} = \text{Ni}, \text{Co}, \text{Zn}$) nanoarchitectures via a co-calcining process of PB and the A element containing salts (**Figure 1.17c–f**).^[207] The PB precursor was first ground with the corresponding salt, and a layer of metal ion (A^+) was uniformly adsorbed on the surface of PB. During the heat

treatment, the outer surface of PB and A^+ reacted with oxygen to form the AFe_2O_4 shell, and simultaneously, a core-shell structured intermediate was formed. Then, through a classic unequal interdiffusion process (Kirkendall effect), the PB precursor and A containing salt are completely transformed into porous hollow AFe_2O_4 , which is hierarchically assembled and made up of numerous tiny nanoparticles. These distinguishing structural features make the ternary AFe_2O_4 viable in a wide range of applications. This versatile strategy successfully synthesized uniform $NiFe_2O_4$, $ZnFe_2O_4$, and $CoFe_2O_4$ hollow structures and is promising for the preparation of other hollow or unique structural materials to meet a wide range of applications.

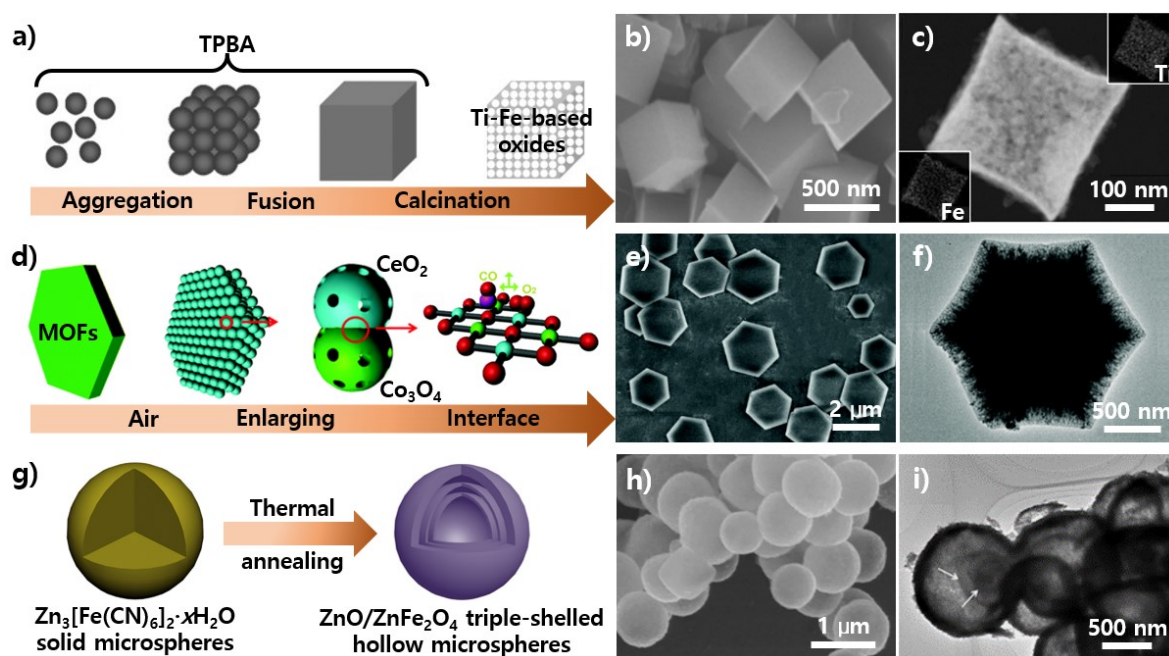


Figure 1.18 (a) Formation process of TPBA cubes and their thermal conversion to nanoporous Ti–Fe-based oxides. (b) SEM and (c) dark-field TEM images taken from one cube and the corresponding elemental mappings of both Ti and Fe. (d) Schematic illustration of the synthesis procedure for porous CeO_2/Co_3O_4 nanojunction. (e) SEM and (f) TEM images of the porous CeO_2/Co_3O_4 nanojunctions. (g) Schematic illustration of $ZnO/ZnFe_2O_4$ multishelled hollow spheres. (h) FE-SEM and (i) TEM images of as-prepared $ZnO/ZnFe_2O_4$ multishelled spheres.

Transition metal oxide nanocomposites, such as ZnO/Co₃O₄, NiO/Fe₃O₄, and NiO/Fe₃O₄/Co₃O₄, are another kind of attractive functional material that can be synthesized by calcining corresponding PBA precursors. For example, Hu *et al.* demonstrated the synthesis of titanium-containing PBA (TPBA) with well-defined cube structures with the assistance of a commercial Pluronic-F127 block copolymer (**Figure 1.18a–c**).[85] Then the as-prepared TPBA was successfully converted into nanoporous titanium–iron-based composite oxide cubes via thermal decomposition. Recently, Wang *et al.* developed a novel in situ synthetic strategy to fabricate porous CeO₂/Co₃O₄ nanojunctions via thermal decomposition of the as-synthesized Ce[Co(CN)₆] precursor in air (**Figure 1.18d–f**).[214] The unique nanojunctions possess numerous interfaces due to the CeO₂ and Co₃O₄ nanocrystals uniformly dispersed during the annealing process. In addition, the nanojunctions prepared using this strategy possess high specific surface areas (42.3 m² g⁻¹) and a large number of nanopores as gaseous molecules are released through MOF pyrolysis. In another case, hierarchical mesoporous bi-component-active ZnO/ZnFe₂O₄ submicrocubes have been fabricated by calcination of a single-resource PBA of Zn₃[Fe(CN)₆]₂ cubes in air at 500°C.[215] The hybrid ZnO/ZnFe₂O₄ is homogeneously constructed from well-dispersed nanocrystalline ZnO and ZnFe₂O₄ subunits at the nanoscale. Additionally, triple-shelled hollow binary ZnO/ZnFe₂O₄ metal oxide microspheres were synthesized through a morphology-inherited annealing treatment of Zn₃[Fe(CN)₆]₂·xH₂O solid microspheres (**Figure 1.18g–i**).[210] The formation of the triple-shelled hollow structure is mainly attributed to the nonequilibrium heat-treatment-induced heterogeneous contraction mechanism. The porous hybrid ZnO/ZnFe₂O₄ triple-shelled hollow microspheres are composed of crystalline ZnO and ZnFe₂O₄ nanodomains with homogeneous dispersion at the nanoscale and large void spaces between adjacent shells.

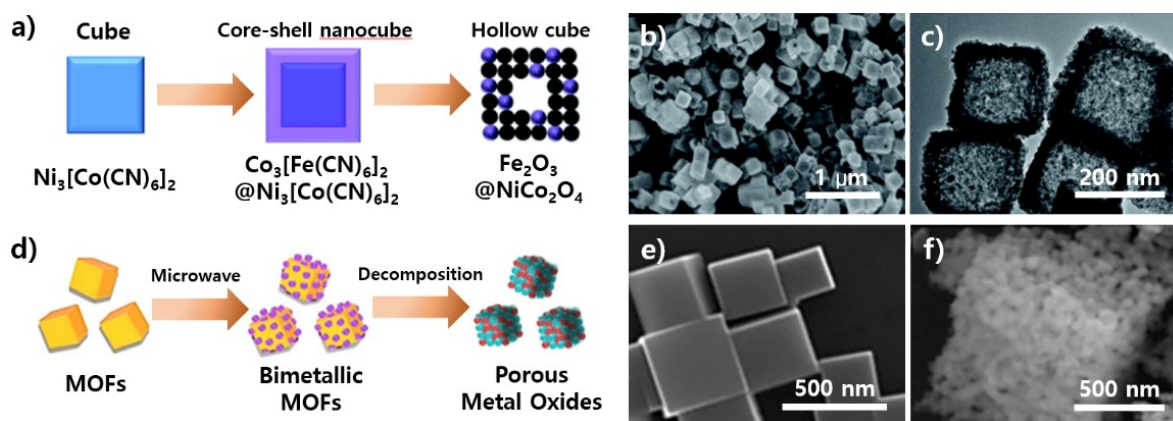


Figure 1.19 (a) Schematic of the procedure used to fabricate $\text{Fe}_2\text{O}_3@\text{NiCo}_2\text{O}_4$ porous nanocages. (b) SEM and (c) TEM images of $\text{Fe}_2\text{O}_3@\text{NiCo}_2\text{O}_4$ nanocages. (d) Schematic diagram of the synthesis process of porous composite metal oxides. SEM images of (e) MOFs and (f) porous metal oxides.

Aside from single PBA precursors, core-shell $\text{Co}_3[\text{Fe}(\text{CN})_6]_2@\text{Ni}_3[\text{Co}(\text{CN})_6]_2$ (CoFe@NiCo PBA) nanocubes have been reported as a source for the fabrication of core-shell $\text{Fe}_2\text{O}_3@\text{NiCo}_2\text{O}_4$ porous nanocages through the annealing process (**Figure 1.19a–c**).^[216] In the designed strategy, the core-shell structured CoFe@NiCo PBA precursors were prepared according to a step-by-step strategy, and $\text{Ni}_3[\text{Co}(\text{CN})_6]_2$ nanocubes were initially synthesized and applied as a core for epitaxial growth of a layer of $\text{Co}_3[\text{Fe}(\text{CN})_6]_2$ as a shell. The CoFe@NiCo precursor was then converted to a porous $\text{Fe}_2\text{O}_3@\text{NiCo}_2\text{O}_4$ hollow nanocage via heat treatment in air. The hollow interiors were contributed by volume loss and the release of the formed CO_2 and N_xO_y gases. The as-prepared $\text{Fe}_2\text{O}_3@\text{NiCo}_2\text{O}_4$ porous nanocages possess an average diameter of 213 nm and a shell thickness of 30 nm, with homogeneous distribution of NiCo_2O_4 and Fe_2O_3 crystallites in the shell. In another case, core-shell structured $\text{Fe}_4[\text{Fe}(\text{CN})_6]_3/\text{M}_x[\text{Fe}(\text{CN})_6]$ ($\text{M} = \text{Cu}, \text{Ni}, \text{Co}, \text{etc.}$) were synthesized using a cation-exchange strategy for the fabrication of porous composite metal oxides of $\text{Fe}_2\text{O}_3/\text{MO}_x$.^[217] It is proposed that the cation-exchange reaction is driven by differences in the solubility product constant (K_{sp}) of monometallic MOFs.

Furthermore, PB and PBAs can act as templates to form core-shell structured composites with various chemicals and then be applied as precursors for the preparation of

porous metal oxide composites. For example, the uniform $\text{Co}_3[\text{Co}(\text{CN})_6]_2$ nanocubes were coated with a layer of porous silica and then pyrolyzed to generate rattle-type $\text{Co}_3\text{O}_4@\text{SiO}_2$ nanoparticles.[223] Hierarchical double-shelled $\text{Fe}_2\text{O}_3/\text{Co}_3\text{O}_4$ microcubes were fabricated based on the annealing of double-shelled $\text{Fe}_4[\text{Fe}(\text{CN})_6]_3/\text{Co}(\text{OH})_2$ microcubes in air (**Figure 1.19d–f**).[219] Double-shelled $\text{Fe}_4[\text{Fe}(\text{CN})_6]_3/\text{Co}(\text{OH})_2$ microcubes were prepared by dispersing PB in a precipitation reaction system of cobalt hydroxide ($\text{Co}(\text{AC})_2$ and ammonium hydroxide). Recently, Yang *et al.* reported the use of PB to react with Zn acetate under microwave irradiation, forming hydroxides and carbonate nanosheets on the surface of PB.[211] Then porous $\text{ZnO}/\text{ZnFe}_2\text{O}_3$ composite nanoparticles were obtained through a calcination process.

Table 1.1 Summaries of PB/PBA-derived porous metal oxides with compositions and applications.

Compositions	Precursors	Thermal conditions	Applications	Ref.
Fe ₂ O ₃ microcubes	Fe ₄ [Fe(CN) ₆] ₃ ·xH ₂ O	350°C for 6 h in air; heating rate: 2°C·min ⁻¹	Adsorbent for inorganic and organic pollution	[184]
Fe ₂ O ₃ nanoboxes	Fe ₄ [Fe(CN) ₆] ₃	NaOH etching	H ₂ S	[189]
Fe ₂ O ₃ microboxes	Fe ₄ [Fe(CN) ₆] ₃	350, 550, and 650°C for 6 h in air; heating rate: 2°C·min ⁻¹	LIBs	[188]
α-Fe ₂ O ₃ , γ-Fe ₂ O ₃	Etched Fe ₄ [Fe(CN) ₆] ₃	250 or 400°C for 4 h in air; heating rate: 1°C·min ⁻¹	Magnetic materials	[186]
Amorphous Fe ₂ O ₃ , α-Fe ₂ O ₃ , γ-Fe ₂ O ₃	Fe ₄ [Fe(CN) ₆] ₃	250 or 350°C in air	/	[193]
α-Fe ₂ O ₃ nanocubes	Fe ₄ [Fe(CN) ₆] ₃	350°C for 6 h in air; heating rate: 1°C·min ⁻¹	LIBs	[191]
Fe ₂ O ₃	(Fe ₄ [Fe(CN) ₆] ₃ ·xH ₂ O)	250 or 400°C for 1 h in air; heating rate: 1°C·min ⁻¹	Catalysts: drug delivery	[190]
Co ₃ O ₄	Co ₃ [Co(CN) ₆] ₂ ·xH ₂ O	NH ₃ -H ₂ O etching, 600°C for 1 h in air	LIBs	[194]
Co ₃ O ₄ nanocages	Co ₃ [Co(CN) ₆] ₂	400°C for 1 h in air	LIBs	[192]
Co ₃ O ₄	Co ₃ [Co(CN) ₆] ₂	430°C for 1 h in air	LIBs	[193]
Co ₃ O ₄ nanocages	Co ₃ [Co(CN) ₆] ₂	450, 550, 650, 750, 850°C for 1 h in air; heating rate: 10°C·min ⁻¹	LIBs	[195]
CoO _x	Co ₃ [Fe(CN) ₆] ₂	NaOH etching	Glucose sensors	[196]
NiO nanosheets	Ni[Ni(CN) ₄]	300, 400, 500°C for 1 h in air; heating rate: 5°C·min ⁻¹	Supercapacitors	[197]
Fe _x Co _{3-x} O ₄	Fe _y Co _{1-y} [Co(CN) ₆] ₂ ·2H ₂ O	500°C for 1 h in air	Catalyst: peroxydisulfate	[199]
Mn _{1.8} Fe _{1.2} O ₄	Mn ₃ [Fe(CN) ₆] ₂ ·nH ₂ O	600°C for 2 h in air; heating rate: 10°C·min ⁻¹	LIBs	[200]
Mn _x Co _{3-x} O ₄ nanocages	Mn ₃ [Co(CN) ₆] ₂ ·nH ₂ O	450°C for 2 h in air; heating rate: 1°C·min ⁻¹	Catalyst: eliminate NO _x	[201]

NiFe ₂ O ₄ nanocubes	Ni ₃ [Fe(CN) ₆] ₂ ·xH ₂ O	350°C for 2 h in air; heating rate: 3°C·min ⁻¹	Acetone sensor	[203]
Spinel Mn _x Co _{3-x} O ₄	Mn ₃ [Co(CN) ₆] ₂ ·nH ₂ O	400°C for 1 h in air	LIBs	[202]
NiFe ₂ O ₄ nanocages	Ni ₂ Fe(CN) ₆	350°C for 2 h in air; heating rate: 1°C·min ⁻¹	LIBs	[204]
Co _x Mn _{3-x} O ₄	Mn ₃ [Co(CN) ₆] ₂ ·nH ₂ O	430°C for 2 h in air; heating rate: 2°C·min ⁻¹	Na–Air/seawater batteries	[223]
Mn _x Co _{3-x} O ₄ nanocages	Mn _y Co _{1-y} [Co(CN) ₆] _{0.67} ·xH ₂ O	400°C for 2 h in air	Catalyst: peroxy monosulfate	[205]
SmFe ₂ O ₃	Sm[Fe(CN) ₆] ₂ ·xH ₂ O	400°C for 2 h in air; heating rate: 2°C·min ⁻¹	NO ₂ sensor	[209]
BiFeO ₃	Bi[Fe(CN) ₆] ₂ ·4H ₂ O	400°C for 1 h in air; heating rate: 3°C·min ⁻¹	/	[208]
ZnO/ZnFe ₂ O ₄ microspheres	Zn ₃ [Fe(CN) ₆] ₂ ·xH ₂ O	550°C for 2 h in air; heating rate: 1°C·min ⁻¹	Acetone sensor	[210]
ZnO/ZnFe ₂ O ₄	PB@Zn(OH) ₂	600°C for 2 h in air	LIBs	[211]
MnO _x -FeO _y nanocages	Mn ₃ [Fe(CN) ₆] ₂ ·nH ₂ O	500°C for 5 h in air; heating rate: 2°C·min ⁻¹	Catalysts for deNO _x	[212]
ZnO/ZnFe ₂ O ₄	Zn ₃ [Fe(CN) ₆] ₂ ·xH ₂ O	500°C for 1 h in air; heating rate: 1°C·min ⁻¹	Gas sensors	[213]
CeO ₂ /Co ₃ O ₄ nanojunctions	Ce[Co(CN) ₆] ₂	600°C for 3 h in air; heating rate: 5°C·min ⁻¹	Catalyst: CO oxidation	[214]
Fe ₂ O ₃ @NiCo ₂ O ₄	Co ₃ [Fe(CN) ₆] ₂ @Ni ₃ [Co(CN) ₆] ₂	450°C for 6 h in air; heating rate: 2°C·min ⁻¹	LIBs	[216]
Fe ₂ O ₃ /MO _x , M=Cu, Ni, Co, etc.	Fe ₄ [Fe(CN) ₆] ₃ /M _x [Fe(CN) ₆] ₃	600°C for 2 h in air; heating rate: 2°C·min ⁻¹	LIBs	[217]
Co ₃ O ₄ @SiO ₂	Co ₃ [Co(CN) ₆] ₂ @SiO ₂	550°C for 1 h in air; heating rate: 10°C·min ⁻¹	Catalyst: CO oxidation	[218]
Fe ₂ O ₃ /Co ₃ O ₄ hollow microcubes	Fe ₄ [Fe(CN) ₆] ₃ /Co(OH) ₂	650°C for 6 h in air; heating rate: 2°C·min ⁻¹	LIBs	[219]
Iron–manganese oxide	Mn ₃ [Co(CN) ₆] ₂ ·nH ₂ O	450°C for 2 h in air; heating rate: 2°C·min ⁻¹	Electrocatalyst: HER, ORR	[220]
Mn–Ru oxide	Mn ₂ [Ru(CN) ₆] ₃ ·xH ₂ O	400°C for 2 h in air; heating rate: 1°C·min ⁻¹	Electrocatalyst: ORR	[221]
K _{0.8} Ti _{4.3} Fe _{3.7} O ₁₆	K _{0.25} Ti[Fe _{0.875} (CN) ₆] ₃ ·6H ₂ O	600°C for 2 h in air; heating rate: 10°C·min ⁻¹	Magnetic materials	[222]

Mn ₃ O ₄ -Co ₃ O ₄	Mn ₃ [Co(CN) ₆] ₂ ·nH ₂ O	450°C for 0.5h, 1 h, 3 h in air; heating rate: 1°C·min ⁻¹	Supercapacitors	[225]
Ag/Co ₃ O ₄	Ag ₃ [Co(CN) ₆]	150°C for 240 h, 200°C for 48 h, 250°C for 8 h, 300°C for 2 h, 400°C for 1 h in air	Catalyst: CO oxidation	[224]
ZnO/Co ₃ O ₄	Zn ₃ [Co(CN) ₆] ₂	500°C for 2 h in air; heating rate: 10°C·min ⁻¹	LIBs	[226]
CoNiFe mixed oxides	K _r Co _s Ni _t [Fe(CN) ₆] ₂ ·xH ₂ O	250, 350, 450°C for 1 h in air; heating rate: 10°C·min ⁻¹	Ferromagnet	[227]
Ag/ZnFe ₂ O ₄	Ag-loaded Zn ₃ [Fe(CN) ₆] ₂ ·xH ₂ O	500°C for 4 h in air; heating rate: 2°C·min ⁻¹ to 200°C, then 1°C·min ⁻¹ to 500°C	Photocatalyst	[228]

1.3.2. PB-derived metal carbides and alloys

PB and PBAs, with both designable metal ion centers and organic ligands, are promising precursors for the one-step synthesis of metal carbides/alloy@carbon composites.[234-264] PB and PBAs are coordination polymers, which are rich in carbon, nitrogen, and transition metals and can be used as ideal precursors for the fabrication of nitrogen-doped carbon/graphene with metal carbides/alloys. Transition metal carbides/alloys generally can be synthesized by the thermal decomposition of PB and PBAs in an inert atmosphere. For example, Aparicio *et al.* studied the thermal decomposition behaviors of PB in an argon atmosphere with a wide temperature range, from room temperature to 1000°C.[234] At a relatively low temperature (<400°C), the decomposition reaction is based on the successive loss of water molecules, the change in the crystal structure of Prussian blue, and the evolution of cyanogen (CN₂). A continuously rising temperature (400–700°C) will induce the formation of various polymorphs of iron carbides (*e.g.*, Fe₂C, Fe₇C₃, and Fe₃C). When the temperature was higher than 700°C, the iron carbide started to decompose and finally caused the formation of metallic iron and carbon. Zakaria *et al.* demonstrated the synthesis of hollow iron carbide (Fe₂C) spheres by thermal treatment of the triple-shelled PB hollow spheres under different temperatures in nitrogen.[235] When the triple-shelled PB hollow spheres were annealed at 450°C, the morphology was well inherited, and the as-obtained Fe₂C phase was mixed with graphite, free carbon, and metallic iron. After annealing at high temperature (550 and 700°C), the morphology of the product was completely collapsed, and contamination was reduced. Such hollow spheres and their derivatives provide a great opportunity for a new solid-state inorganic chemistry and could be applicable in the future for the synthesis of different hybrid metal carbides/alloys with fine structures through thermal treatment of PB analogues under nitrogen.

The combination of metal carbides with other nanomaterials for the fabrication of metal carbide-based hybrids is an effective and practical strategy to improve and extend their applications. Barman *et al.* reported an environmentally friendly and simple strategy for the synthesis of an Fe/Fe₃C nanoparticle encapsulated by N-doped graphene layers by pyrolyzing

PB.[263] In this case, PB is used as a single precursor with a cyanide group as the source of carbon and nitrogen and Fe^{2+} and Fe^{3+} as the sources of Fe/Fe₃C nanoparticles. When calcined at a high temperature, polymeric carbon nitride generated from the addition/condensation reaction of a cyanimide group and then decomposed to generate a large number of cyano fragments (*e.g.*, C_2N^{2+} , C_3N^{2+} , and C_3N^{3+})[238] at above 700°C. Simultaneously, $\text{Fe}^{2+/3+}$ ions are reduced to form nanosized Fe crystallites in the reducing environment. Then, the as-formed nanosized Fe crystallites can act as catalysts leading to the conversion of cyano fragments into N-doped graphene layers. The yield of the resulting encapsulated nanostructured product for PB was ~50%. Carbon nitride fragmentation is mainly responsible for doping and for the growth of these nanostructures. It is worth noting that carbon nitride decomposes into N₂ gas at a high temperature (850°C), which will lead to a decrease in N-doping. More recently, Song *et al.* reported the synthesis of Fe/Fe₃C@N-doped-carbon porous hierarchical polyhedrons by simple thermal decomposition of $\text{Zn}_3[\text{Fe}(\text{CN})_6]_2 \cdot x\text{H}_2\text{O}$ in a nitrogen atmosphere (**Figure 20a–d**). The as-prepared Fe/Fe₃C@N-C polyhedrons inherited well the shape of the precursor and are constructed by numerous Fe/Fe₃C@N-doped-carbon core–shell structured nanoparticles and carbon nanotubes on the surface of the polyhedrons. Additionally, this material exhibits a large specific surface area of 182.5 m² g⁻¹ and an excellent ferromagnetic property.

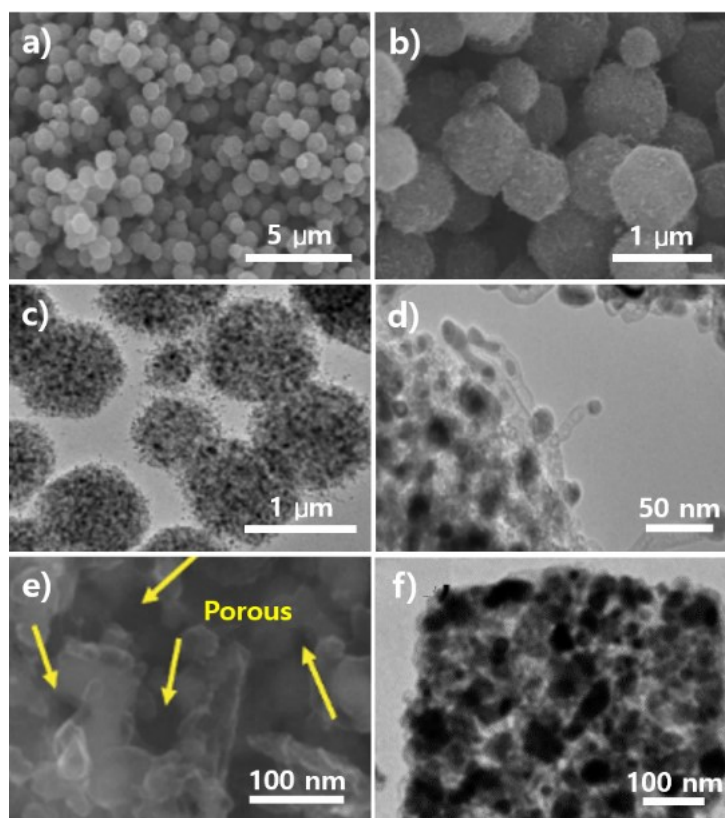


Figure 1.20 (a, b) SEM, (c) TEM, and (d) HR-TEM images of the as-prepared Fe/Fe₃C@N-doped carbon. The (e) SEM and (f) TEM images of N-doped Fe/Fe₃C@C/RGO.

Wen *et al.* demonstrated the fabrication of a novel core-shell structured hybrid of nitrogen-doped porous Fe/Fe₃C@C nanoboxes supported on graphene sheets (denoted as N-doped Fe/Fe₃C@C/RGO) through the direct pyrolysis of GO-based PB nanocubes (**Figure 1.20e, f**).^[260] The resulting PB/GO precursors were prepared by dispersing highly uniform PB nanocubes in the GO solution under stirring. In the pyrolysis process, the as-prepared PB nanocubes were converted to porous N-doped Fe/Fe₃C@C nanoboxes with a well-inherited morphology except for a small amount of shrinkage. The PB nanocubes also provided the N source for the conversion of GO into nitrogen-doped reduced graphene oxide (NRGO) sheets. The as-prepared NRGO acts not only as a support for N-doped Fe/Fe₃C@C hybrids but also as a bridge to connect the neighboring nanoboxes, thereby enhancing the overall electron-transfer capability.

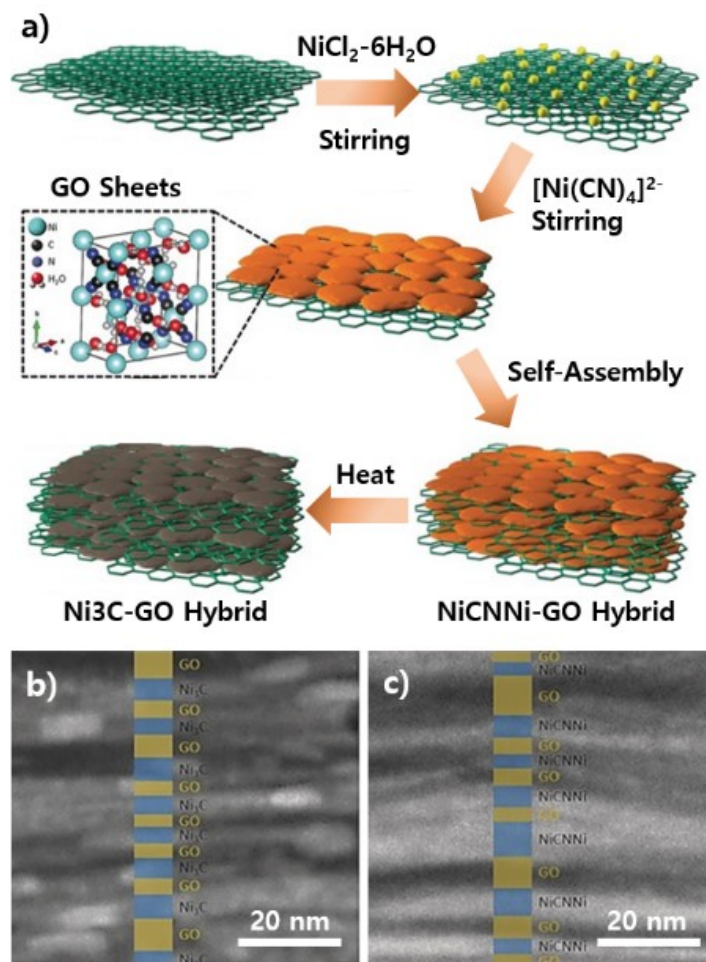


Figure 1.21 (a) Formation process of NiCNi–GO hybrids (composites) through layer-by-layer assembly of graphene oxide sheets held together by coordination polymers, and thermal conversion to the Ni₃C–GO hybrid (composite). (b) Cross-sectional TEM images of a Ni-PBA-GO hybrid and (c) a Ni₃C–GO hybrid.

In addition to iron carbide, other metal carbide composites and their composites have been synthesized. For example, Zakaria *et al.* reported the synthesis of flake-like nickel carbide (Ni₃C) through the thermal decomposition of Ni(H₂O)₂[Ni(CN)₄]·4H₂O (Ni PBA) nanoflakes (**Figure 1.21a–c**).^[261] The Ni PBA nanoflake precursors were first fabricated via a trisodium citrate dihydrate–modified reaction between Ni²⁺ and [Ni(CN)₄]²⁻ ions. When calcined at 450°C, well-crystallized Ni₃C nanoparticles were generated. Upon further heating at 550°C, Ni₃C decomposed and converted into the cubic nickel metal and porous carbon. Although well-crystallized Ni₃C is obtained at 450°C, the original 2D morphology was completely collapsed

and destroyed because of crystallization and fusion of the metal framework. Furthermore, the same group demonstrated the synthesis of a layer-by-layer structure of a Ni₃C-GO composite via thermal treatment of Ni PBA-coated GO sheets.[261] The Ni PBA-coated GO sheets assembled with ordered lamellar nanomaterials were prepared by in situ crystallization of Ni PBA nanoflakes on the surface of GO sheets. The regulated thermal treatment process in nitrogen results in a Ni₃C-GO composite with a morphology similar to that of the Ni PBA-GO layer-by-layer starting precursor. The stability of the Ni PBA-GO layer-by-layer structure at high temperature prevented the collapse and destruction of frameworks during the crystallization and fusion process.

As mentioned above, the PB and PBA powders were directly carbonized into metal/alloy carbon composites in an inert atmosphere at high temperature. For example, Sivanantham *et al.* Reported the fabrication of metal-rich, core-shell Co@NC covered with thin carbon layer via the thermal decomposition of a Co-Co PBA at 600–900°C in a N₂ atmosphere (**Figure 1.22a–c**).[244] During the annealing process, Co²⁺ ions from the precursor will be converted to Co nanoparticles by reducing gases under high temperatures, while the remaining CN⁻ groups are carbonized and catalyzed into N-rich graphene layers outside the metallic particles. The cobalt nanoparticles with average diameter of 25 nm were covered by the thin carbon layer with well disperse and uniform. Also, the core-shell nanoparticle was interrelated via the carbon shell with nanometer-sized voids. These voids can optimize the interface between the active site and the electrolyte. Additionally, transition metal alloy nanoparticles, such as FeCo, NiFe, and NiCo, encapsulated in highly nitrogen-doped graphene layers can be synthesized by the direct annealing of corresponding PBA nanoparticles at high temperature in inert atmospheres. Zheng *et al.* demonstrated the preparation of podlike N-doped CNTs with encapsulated FeNi alloy NPs by the direct annealing of [Ni₂Fe(CN)₆] precursors at 600°C in an Ar flow (**Figure 1.22d–g**).[264] In this case, it is proposed that Ni²⁺ and Fe²⁺ ions from the precursor were first reduced to NiFe alloys under high temperatures. Due to their high catalytic activity, CN⁻ group linkers were subsequently catalyzed into

nitrogen-doped nanotubes. The as-prepared composites showed a well-defined podlike structure with large metal NiFe alloy particles located at the ends of the nanotubes.

In another case, polydopamine (PDA) was introduced to form $\text{Fe}_3[\text{Co}(\text{CN})_6]_2@\text{PDA}$ nanocubes (NCs). After thermal treatment under a nitrogen flow at 700°C , the precursors could be transferred into a new type of core-shell structured $\text{FeCo}@\text{nitrogen-doped graphitic carbon NC}$. [262] PDA was reported to be an ideal precursor for modifying the surface of all types of solid materials, regardless of their chemical nature, and which can be pyrolyzed into highly conductive nitrogen-doped porous carbon. When the $\text{Fe}_3[\text{Co}(\text{CN})_6]_2$ NCs were immersed in a buffer solution of dopamine, dopamine was self-polymerized at the surface of $\text{Fe}_3[\text{Co}(\text{CN})_6]_2$ NCs to form $\text{Fe}_3[\text{Co}(\text{CN})_6]_2@\text{PDA}$ NCs. It was found that both the cyanide ligand and PDA acted as carbon and nitrogen sources and were successfully catalyzed into the N-doped graphitic carbon instead of amorphous carbon by FeCo nanoparticles. Further, Su *et al.* reported the introduction of ruthenium (Ru) into $\text{Co}_3[\text{Co}(\text{CN})_6]_2$ via an ion-exchange reaction between Ru^{3+} and Co^{3+} for the preparation of RuCo nanoalloys wrapped in N-doped graphene layers ($\text{RuCo}@\text{NC}$). More recently, a similar strategy was adopted by the same group for using Ir-doped $\text{Co}_3[\text{Co}(\text{CN})_6]_2$ to synthesize IrCo nanoalloys encapsulated in N-doped graphene layers.

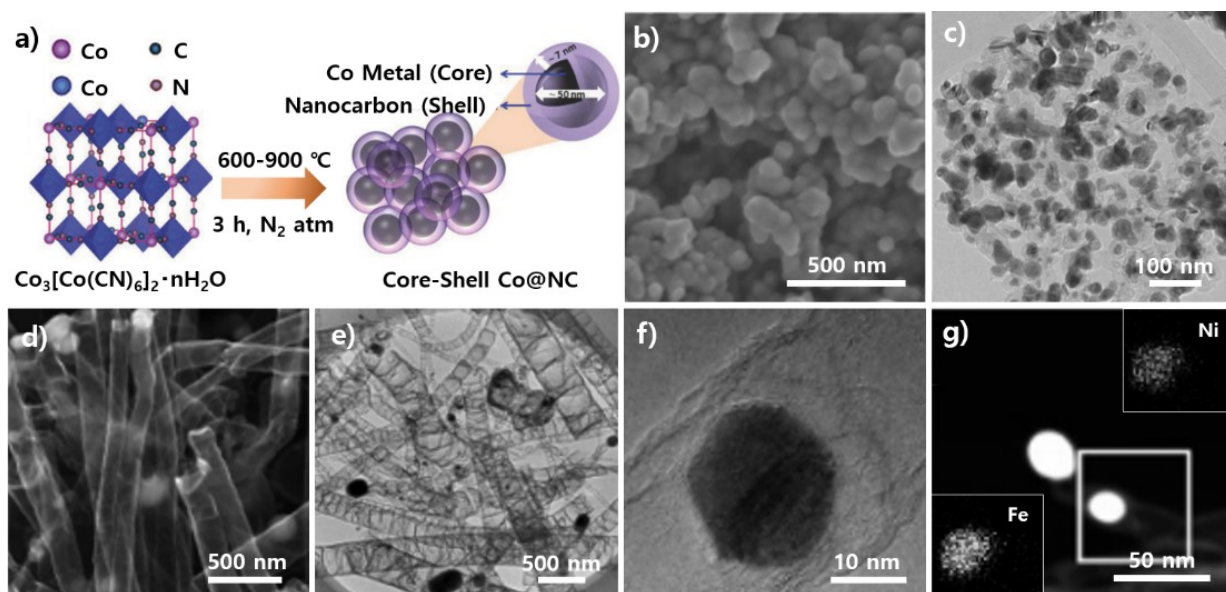


Figure 1.22 (a) Formation of the core–shell Co@N-doped carbon from $\text{Co}_3[\text{Co}(\text{CN})_6]_2 \cdot n\text{H}_2\text{O}$. Precursor pyrolysis at different temperatures between 600 and 900 °C for 3 h in an N_2 atmosphere. Morphology and structural characterization of the core–shell Co@N-doped carbon catalyst: (b) FE-SEM and (c) HR-TEM images. (d) SEM, (e) TEM, (f) HR-TEM images and (g) elemental mapping of pod (N)-FeNi (FeNi alloy nanoparticle) reveal the homogeneous distribution of Ni and Fe elements in the metal nanoparticles.

Table 1.2 Summaries of PB/PBA-derived porous metal carbides/nanoparticles and applications.

Compositions	Precursors	Preparation	Applications	Performance	Rref.
FeCo alloy/carbon composites	CoFe-PBA	750°C for 5 h in Ar	Electrocatalysts for solar cell	Power conversion efficiency: 9.20% under AM 1.5 G irradiation	[236]
Fe/C@mSiO ₂	PB@SiO ₂	400–600°C for 3 h in H ₂ atmosphere	Adsorbent for removal and recovery of heavy metals	$K_{\text{obs}} \approx 0.04$	[237]
Fe/Fe ₃ C@N-doped porous carbon hybrid	Zn ₃ [Fe(CN) ₆] ₂ ·xH ₂ O	800°C for 1 h in N ₂	HER	$E_{10\text{mA/cm}^2} = 236$ mV; Tafel slope = 59.6 mV dec ⁻¹	[238]
CoFe nanoalloy/N-doped carbon	Fe ₃ [Co(CN) ₆] ₂	600°C for 1 h in N ₂	ORR, OER	ORR: $E_{3\text{mA/cm}^2} = 0.68$ V vs. RHE; OER: $E_{10\text{mA/cm}^2} = 1.55$ V vs. RHE; over potential: 0.38 V at 10 mA/cm ²	[239]
FeCo alloy/carbon composites	Fe ₃ [Co(CN) ₆] ₂ /Co ₃ [Fe(CN) ₆] ₂	700°C for 6 h in N ₂	Microwave absorption	Absorption frequency range: over -10 dB in 3.2–18.0 GHz	[240]
Ir-Co alloy/N-doped carbon cages	Ir-Co ₃ [Co(CN) ₆] ₂	500–800°C for 4 h in N ₂	HER	$E_{10\text{mA/cm}^2} = 23$ mV; Tafel slope = 23 mV dec ⁻¹	[241]
Core-shell NiFe alloy/N-doped graphitic carbon	NiFe-PBA, urea	350°C for 2 h in air, 80°C for 4 h with urea in solution, 800°C for 2 h in Ar	OER	Onset potential: 1.48 V vs. RHE; $E_{10\text{mA/cm}^2} = 320$ mV; Tafel slope = 41 mV dec ⁻¹	[242]
NiCo alloy/graphitic carbon	Ni ₃ [Co(CN) ₆] ₂ ·12H ₂ O	600–900°C for 3 h in N ₂	ORR	Half-wave potential: 0.81 V vs. RHE; Tafel slope = 52.1 mV dec ⁻¹	[243]
Co/N-doped carbon	Co ₃ [Co(CN) ₆] ₂ ·nH ₂ O	600–900°C for 3 h in N ₂	OER	$E_{10\text{mA/cm}^2} = 330$ mV; Tafel slope = 41 mV dec ⁻¹ ; long durability of over 400 h	[244]
PdMnCo alloy/N-doped carbon	Mn ₃ [Co(CN) ₆] ₂ , PdCl ₂	750°C for 4 h in Ar,	HER	Tafel slope = 31 mV dec ⁻¹	[245]

		ultrasonication for 90 s in PdCl ₂ methanol solution			
Ni ₃ C carbon, Ni nanoparticles	Ni-(H ₂ O) ₂ [Ni(CN) ₄]·xH ₂ O	420°C (Ni ₃ C), 550°C (Ni) for 1 h in N ₂	ORR	Ni ₃ C: E _{10 mA/cm²} = -240 mV vs. Ag/AgCl; Ni: E _{10 mA/cm²} = -129 mV vs. Ag/AgCl	[246]
FeCoNi alloy@N-doped graphitic carbon	Fe ₃ [Co(CN) ₆] ₂ @Ni ₃ [Co(CN) ₆] ₂	600°C for 4 h in N ₂	OER	E _{10 mA/cm²} = 288 mV vs. RHE	[247]
FeCo alloy@N-doped graphitic carbon	FeCo-PBA/carbon nanotubes	600°C for 2 h in N ₂	ORR, OER	ORR: half-wave potential 0.79 V vs. RHE; OER: onset potential 1.52 V vs. RHE; E _{10 mA/cm²} = 1.61 V vs. RHE	[248]
Ru-Co nanoalloys/N-doped graphene	Ru-doped Co ₃ [Co(CN) ₆] ₂	600°C for 4 h in N ₂	HER	E _{10 mA/cm²} = 28 mV vs. RHE; Tafel slope = 31 mV dec ⁻¹ ; stability: over 10,000 cycles	[255]
Fe ₂ C@amorphous carbon	PB	600°C for 2 h in N ₂	LIBs	Rate capacity: 509.1 mA h g ⁻¹ at 6 A g ⁻¹ ; stability: 100% capacity retained after 150 cycles at 1 A g ⁻¹	[250]
NiFe@N-doped graphene	Fe[Ni(CN) ₄], Ni ₃ [Fe(CN) ₆] ₂ , Ni ₂ [Fe(CN) ₆]	900°C for 2 h in N ₂ , leached with 0.5 M H ₂ SO ₄ at 80°C for 3 h	OER	E _{10 mA cm⁻²} = 360 mV, highly durable: no degradation after 20,000 cycles	[249]
Co encapsulated in nitrogen-doped bamboo-like carbon nanotubes	Co ₃ [Co(CN) ₆] ₂	700°C for 1 h in N ₂	Catalyst: degradation of organic pollutants	RhB (10 mg L ⁻¹) completely removed in 7 min using 0.1 g L ⁻¹ Co/N-CNTs and 0.2 g L ⁻¹ PMS	[251]
Pt-CoFe@N-doped carbon	4.60% Pt-doped Co ₃ [Fe(CN) ₆] ₂	800°C for 4 h in N ₂	HER	E _{10 mA cm⁻²} = 45 mV vs. RHE; Tafel slope: 32 mV dec ⁻¹	[252]

CoFe/carbon	$\text{Co}_3[\text{Fe}(\text{CN})_6]_2$	550, 650, 750°C for 2 h in N_2	Microwave absorption	Minimum reflection loss value of -43.5 dB at 9.92 GHz, effective absorption bandwidth of 4.3 GHz (below -10 dB)	[253]
Fe/Fe ₂ C graphene	PB	450, 550, 700°C for 1 h in N_2	ORR	Onset potential: -200 mV vs. Ag/AgCl	[235]
Fe-C/nitrogen-doped 3D porous carbons	PB/GO 10%	700°C for 1 h in Ar	ORR	(In 0.1 M KOH) onset potential: 0.940 V vs. RHE, half-wave potential: 0.793 V vs. RHE; (in 0.5 M H ₂ SO ₄) onset potential: 0.828 V vs. RHE, half-wave potential: 0.597 V vs. RHE	[254]
Fe/Fe ₃ C@C matrix	PB@PDA	800°C for 2 h in N_2	Absorption of uranium (VI)	Maximum sorption capacity of 203 mg g ⁻¹	[256]
Co ₃ ZnC/Co nanojunctions/N-doped graphene	$\text{Zn}_3[\text{Co}(\text{CN})_6]_2$	600–900°C for 4 h in N_2	OER	$E_{10 \text{ mA cm}^{-2}} = 366 \text{ mV vs. RHE}$; Tafel slope = 81 mV dec ⁻¹	[257]
Co@N-doped graphene, Co@NG acid	$\text{Co}_3[\text{Co}(\text{CN})_6]_2$	400–900°C for 1 h in Ar	Zinc-air batteries	HER: half-wave potential: 0.83 V vs. RHE in 1M KOH; onset potential/half wave potential: 0.77/0.58 V vs. RHE in 0.5 M H ₂ SO ₄ ORR: onset overpotential: ≈70 mV, $E_{10 \text{ mA/cm}^2} = 220 \text{ mV}$ 1 M KOH; onset overpotential: 50 mV, $E_{10 \text{ mA/cm}^2} = 183 \text{ mV}$ in 0.5 M H ₂ SO ₄	[258]
Co ₃ ZnC@carbon	$\text{Zn}_3[\text{Co}(\text{CN})_6]_2 \cdot n\text{H}_2\text{O}$ / PVP	300°C for 1 h, then 600°C for 2 h in N_2	LIBs	Capacity: 608 mA h g ⁻¹ after 300 cycles at 100 mA g ⁻¹ ; stability: 423 mA h g ⁻¹ after 1,150 consecutive cycles at 1 A g ⁻¹	[259]

Fe/Fe ₃ C@N-doped graphene	Fe ₄ [Fe(CN) ₆] ₃	750–1050°C for 2 h	OER	OER: onset potential: 0.6 V vs. AgCl/Ag, E _{10 mA/cm²} = 0.77 V vs. AgCl/Ag; ORR	[263]
FeNi alloy encapsulated in podlike N-doped carbon nanotubes	Ni ₂ Fe(CN) ₆	600°C for 2 h in Ar	Counter electrode materials for solar cells	Power conversion efficiency of 8.82%	[264]

1.3.3. PB-derived metal sulfides and selenides

Generally, PB and PBAs can be converted into metal sulfides/selenides through calcination in sulfur/selenium vapor or chemical reaction with sulfur/selenium compounds (*e.g.*, sodium sulfide (Na_2S), ammonium thiomolybdate ($(\text{NH}_4)_2\text{MoS}_4$), and sodium selenite (Na_2SeO_3)) in solution.[265-277] For example, Cao *et al.* reported an easy and efficient one-step simultaneous decomposition and sulfidation approach to the synthesis of $\text{Co}_{0.37}\text{Fe}_{0.26}\text{S}$ nanocubes by annealing $\text{Co}_3[\text{Fe}(\text{CN})_6]_2$ precursors in a sulfur vapor.[266] The experiment was conducted by calcinating CoFe-PBA and S powders in a tube furnace at a high temperature under an argon gas flow. The sulfur powder was placed on the upstream side of an alumina boat, while the as-prepared $\text{Co}_3[\text{Fe}(\text{CN})_6]_2$ nanocubes were placed on the downstream side. The S powders will vaporize into sulfur vapor and surround the CoFe-PBA at high temperatures. The metal ions liberated from the CoFe-PBA upon decomposition will react with sulfur steam and lead to the formation of $\text{Co}_{0.37}\text{Fe}_{0.26}\text{S}$ nanoparticles embedded in a carbon shell. Lin *et al.* reported the synthesis of bi-active $\text{NiS}_2@\text{CoS}_2/\text{N}$ -doped porous carbon composites by annealing the mixture of $\text{Ni}_3[\text{Co}(\text{CN})_6]_2@\text{PDA}$ core-shell nanocubes and sulfur.[267] The as-prepared yolk-shell $\text{NiS}_2@\text{CoS}_2/\text{N}$ -doped porous carbon nanocubes exhibit a mesoporous structure with plenty of $\text{NiS}_2@\text{CoS}_2$ heteronanocrystals uniformly anchored on a porous carbon matrix. The mesoporous nanocubes provided a large specific surface area of $286 \text{ m}^2\text{g}^{-1}$ with a narrow pore-size distribution.

In another case, $\text{Ni}[\text{Ni}(\text{CN})_4] \cdot x\text{H}_2\text{O}$ nanoplates were transformed into NiS or NiSe_2 through a thermally induced sulfurization or selenization process, respectively (**Figure 1.23**).[268] The as-obtained NiS and NiSe_2 nanoplates retained well the morphology of the precursors with a porous carbon matrix derived from carbonization of the cyano group. More recently, Huang *et al.* demonstrated a CVD strategy for the synthesis of $\text{CoS}_2\text{-CoSe}_2@\text{NC}$ composite nanocubes via simultaneous sulfidation and selenization of a $\text{Co}_3[\text{Co}(\text{CN})_6]_2@\text{PDA}$. The as-prepared $\text{CoS}_2\text{-CoSe}_2@\text{NC}$ composites preserve the uniform cube-like shape of the precursors after the conversion process, with plenty of CoS_2 and CoSe_2 nanocrystals uniformly dispersed in the porous carbon matrix.

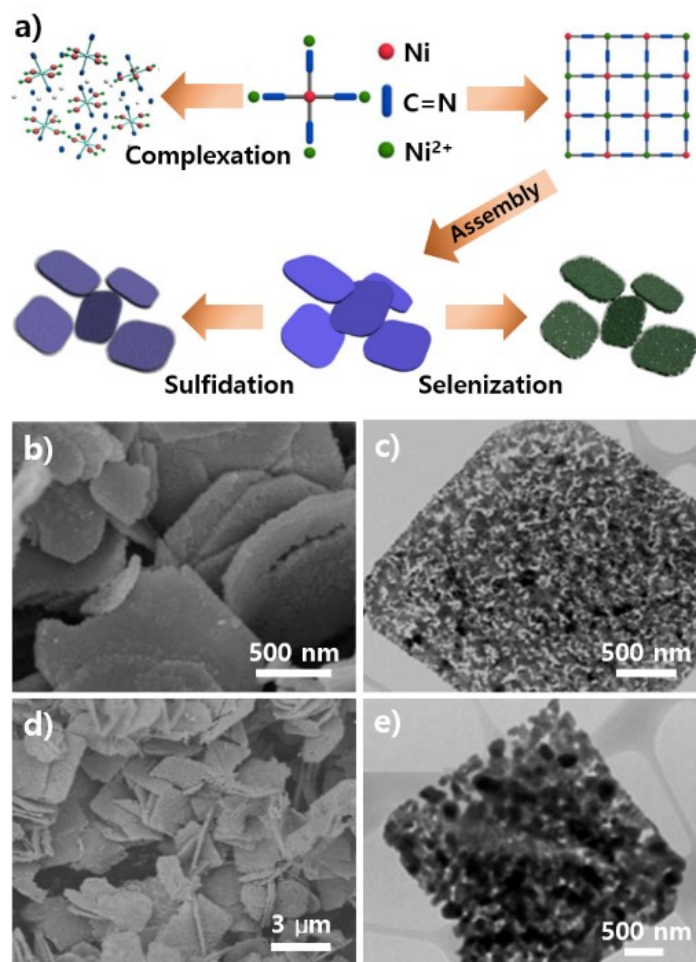


Figure 1.23 (a) Schematic illustration of the preparation of a Ni-based MOF and the derived NiS and NiSe₂ nanoplates. (b) SEM and (c) TEM images of as-prepared NiS nanoplates. (d) SEM and (e) TEM images of the as-obtained NiSe₂ nanoplates.

Yu *et al.* developed a novel strategy for the synthesis of NiS nanoframes from Ni-Co PBA nanocubes via solution-based chemical reaction (**Figure 1.24a–e**).^[276] The as-prepared NiS nanoframes were highly uniform and retained the original cubic shape well, with only 12 edges left. The formation of such unique frame-like topologies was attributed to the Kirkendall effect and the chemical-etching/anion-exchange reaction between $[\text{Co}(\text{CN})_6]^{3-}$ and S^{2-} moieties. In detail, the high curvature of the edge areas of the Ni-Co PBA nanocubes lead to its being more defective as compared with the smooth plane surface. In the presence of S^{2-} , the edges are etched and then subjected to the exchange reaction with S^{2-} to form a NiS thin shell in the edge areas. As the reaction proceeds, the chemical-etch/anion-exchange reaction will

occur both along the exposed sides of the less-etched middle plane and in the inward parts of the porous NiS shell via the interdiffusion of Ni^{2+} and S^{2-} ions. The newly formed NiS nuclei supply the growth of the preformed NiS skeleton on the edges. Due to their smaller size, the outward diffusion of Ni^{2+} ions is faster than the inward diffusion of S^{2-} ions. According to the Kirkendall effect, the unequal diffusion of reacting species (Ni^{2+} and S^{2-} ions) results in the formation of frame-like structures. The size of the NiS nanoframes was also readily adjustable by controlling the size of the PBA precursors. In another case, uniform 3D hierarchical NiS_2 microspheres were synthesized via a chemical-etching/ion-exchange reaction between the Ni-Co-PBA and $(\text{NH}_4)_2\text{S}$. [269] Uniform γ -NiOOH/ NiS_x hierarchical microspheres were initially formed and were then transformed into NiS_2 via a controlled annealing treatment. It was found that in the alkaline $(\text{NH}_4)_2\text{S}$ solution, the Ni-Co-PBA first reacts with the ionized OH^- to form flake-like γ -NiOOH. As the reaction proceeded, the anion-exchange reaction occurred between OH^- and S^{2-} on the surface of γ -NiOOH due to the different solubilities of hydroxides and sulfides. It is worth noting that the concentration of the reactants and the reaction time have a great influence on the morphology of the products.

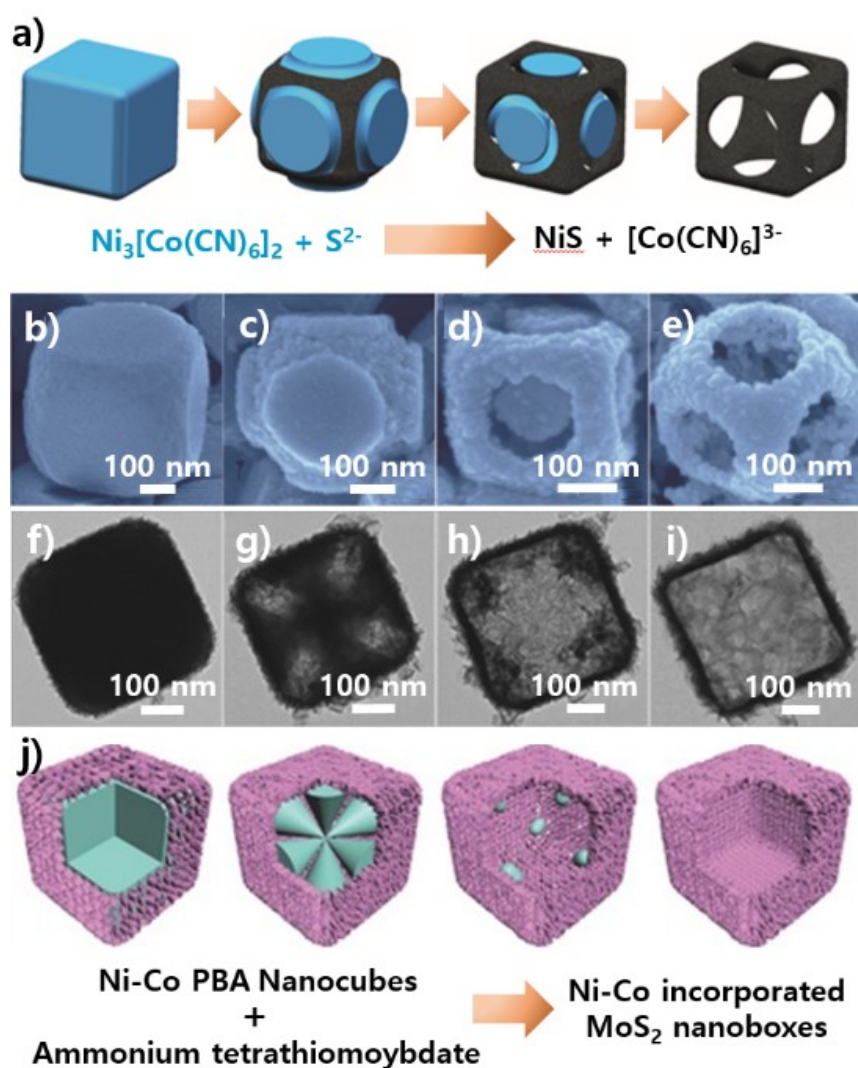


Figure 1.24 (a) Schematic illustration of the formation process of NiS nanoframes. (b–e) FE-SEM images of the products obtained after reaction for (b) 0 h, (c) 0.5 h, (d) 2 h, and (e) 6 h. TEM images of the as-synthesized products obtained at different time intervals: (f) 1 h, (g) 6 h, (h) 12 h, and (i) 20 h. (j) Schematic illustration of the formation process of Ni–Co–MoS₂ nanoboxes.

A synergistic strategy has been developed for the synthesis of hollow structured MoS₂ nanoboxes with incorporated nickel and cobalt (Ni–Co–MoS₂) (**Figure 1.24f–j**).^[270] In this case, uniform Ni₃[Co(CN)₆]₂ nanocubes are applied as the sacrificial template and precursor to react with (NH₄)₂MoS₄ under a solvothermal condition. In detail, NH₃ decomposed from ammonium tetrathiomolybdate will dissolve a Ni–Co PBA by complexing with Ni(II). Co(III) cations are reduced to the Co(II) species and dissolved into the solution. It is worth mentioning

that the dissolution process is anisotropic due to the uneven distribution of defects. At the same time, MoS₂ nanosheets produced from ammonium tetrathiomolybdate start to grow on the surface of Ni–Co PBA nanocubes under solvothermal conditions. What is more, some free nickel and cobalt ions can be embedded into MoS₂ nanosheets. In another case, Guo *et al.* developed a two-step temperature-raising hydrothermal-reaction strategy for the preparation of a core–shell structured Co₃S₄@MoS₂ heterostructure.[276] Uniform Co₃[Fe(CN)₆]₂ nanocubes were employed as both morphological templates and precursors to react with Na₂S and Na₂MoO₄ under a hydrothermal condition. At a relatively low temperature of 120°C, Co₃S₄ nanoboxes were formed first, based on the ionic exchange reaction between Fe(CN)₆³⁻ and S²⁻, and subsequently, an elevated temperature of 200°C induced the in situ growth of MoS₂ nanosheets on the surface of Co₃S₄ nanoboxes.

More recently, the solution-based ion-exchange reaction was successfully applied in the transformation of PBAs into metal selenides.[275] For example, Feng *et al.* demonstrated the synthesis of ultrathin nanosheet–assembled hierarchical CoSe₂ microboxes through an anion-exchange reaction between Co₃[Co(CN)₆]₂ and Na₂SeO₃ at an elevated temperature (**Figure 1.25**). The as-obtained product inherited the cubic shape and dimension of the PBA precursor well except for the rough surface. The formation of the hollow structure can be explained by the Kirkendall effect. Specifically, under the thermal condition, the released Se²⁻ ions replace [Co(CN)₆]³⁻ and combine with Co²⁺ ions to form a thin shell made of CoSe₂ nanosheets; this acts as a physical barrier to hinder the chemical reaction between outer Se²⁻ ions and inner Co²⁺ ions. Because of the larger size of Se²⁻ ions, their inward diffusion is slower than the outward diffusion of Co²⁺ ions. As a result, a cavity formed in the CoSe₂ shell after the selenization reactions.

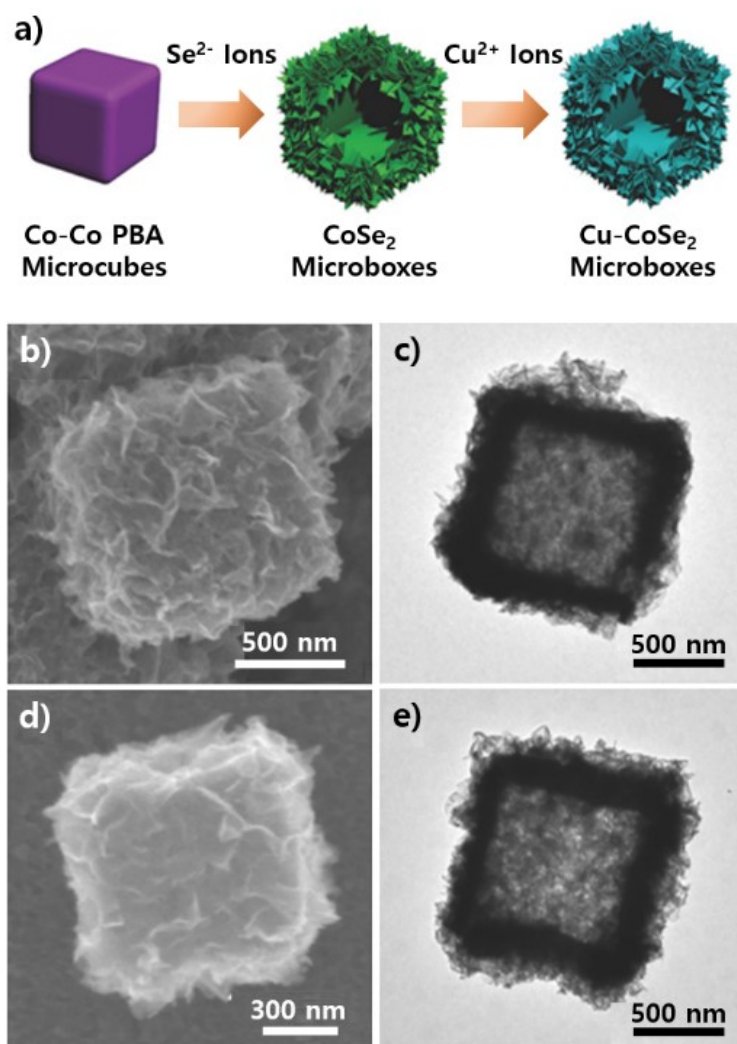


Figure 1.25 (a) Schematic illustration of the two-step ion-exchange reactions for the synthesis of Cu-CoSe₂ microboxes. (b) SEM and (c) TEM images of CoSe₂ microboxes. (d) SEM and (e) TEM images of Cu-CoSe₂ microboxes.

Table 1.3 Summaries of PB/PBA-derived porous metal sulfides/selenide, their complexes with carbon, and their applications.

Compositions	Precursors	Preparation	Applications	Performance	Rref.
Co-Fe-MoS _x hollow nanoboxes	Co-Fe PBA, (NH ₄) ₂ MoS ₄	Solvothermal, 200°C for 20 h; 350°C for 2 h in Ar	Electrode catalysts for solar cells	Power-conversion efficiency: 9.63% under AM 1.5 G irradiation	[265]
NiS ₂ @CoS ₂ / N- doped carbon nanocubes	Ni-Co PBA@PDA	Pyrolysis at 400°C for 3 h in Ar	LIBs/NaIBs	LIBs: reversible capacity 600 mA h g ⁻¹ after 100 cycles at 1.0 A g ⁻¹ NaIBs: reversible capacity 600 mA h g ⁻¹ after 250 cycles at 1.0 A g ⁻¹	[267]
NiS ₂ hierarchical microspheres	NiCo-PBA, (NH ₄) ₂ S	Hydrothermal, 100°C for 10 h; 350°C for 2 h in N ₂	Electrocatalysts for solar cells	Power-conversion efficiency: 8.46% under AM 1.5 G irradiation	[269]
Co ₃ S ₄ @MoS ₂ heterostructure	CoFe-PBA, thioacetamide, Na ₂ MoO ₄ ·2H ₂ O	Solvothermal, 120°C for 10 h and 200°C for 6 h; 350°C for 12 h in N ₂	HER, OER	HER: E _{10mAcm⁻²} = 136 mV, Tafel slope = 74 mV decade ⁻¹ OER: E _{10mAcm⁻²} = 280 mV, Tafel slope = 43 mV decade ⁻¹	[271]
MoS-Co nanoboxes	Co ₃ [Co(CN) ₆] ₂ , (NH ₄) ₂ MoS ₄	Solvothermal, 210°C for 12 h	HER	Onset potential: 53 mV vs. RHE, E _{10mAcm⁻²} = 155 mV, Tafel slope = 55 mV decade ⁻¹	[272]
Co _{0.37} Fe _{0.26} S	CoFe-PBA, S powder	350°C for 12 h in Ar	OER	E _{10mAcm⁻²} = 1.5 V vs. RHE, Tafel slope = 37.2 mV decade ⁻¹	[266]

Carbon-coated (Fe, Co) bimetallic sulfide	CoFe-PBA, thiourea	500°C for 3 h in Ar flow	NaIBs	Rate capacity: 122.3 mA h g ⁻¹ at 5 A g ⁻¹ ; reversible capacity: 87 mA h g ⁻¹ after 150 times at 500 mA g ⁻¹	[273]
Co-Fe-Se, Co-Fe-S	CoFe-PBA	Co-Fe-Se: solvothermal 160°C for 3 h with Se powder; Co-Fe-S: Na ₂ S ethanol ultrasonication	Electrocatalysts for solar cells	Power-conversion efficiency: 9.58 and 9.06% for Co-Fe-Se and Co-Fe-O, respectively	[275]
Ni-Co-MoS ₂ nanoboxes	NiCo-PBA, (NH ₄) ₂ MoS ₄	Solvothermal, 210°C for 20 h	HER	E _{10 mA/cm²} = 155 mV vs. RHE, Tafel slope = 51 mV decade ⁻¹	[270]
NiS and NiSe ₂ nanoplates	Ni[Ni(CN) ₄]·xH ₂ O, S/Se powder	400°C for 3 h in Ar	LIBs/NaIBs	LIBs: (NiS) initial discharge/charge capacities: 1311/972 mA h g ⁻¹ , reversible capacity: 468 mA h g ⁻¹ after 100 cycles at 1 A g ⁻¹ ; (NiSe ₂) discharge/charge capacities: 992 mA h g ⁻¹ / 758 mA h g ⁻¹ , reversible capacity: 286 mA h g ⁻¹ after 100 cycles at 1 A g ⁻¹ NaIBs: (NiS) initial discharge/charge capacities: 763/381 mA h g ⁻¹ , reversible capacity: 166 mA h g ⁻¹ after 100 cycles at 1 A g ⁻¹ ; (NiSe ₂) discharge/charge capacities: 1008 mA h g ⁻¹ / 517 mA h g ⁻¹ , reversible capacity: 311 mA h g ⁻¹ after 100 cycles at 1 A g ⁻¹	[268]

NiS nanoframe (300 nm)	NiCo-PBA, Na ₂ S		Pseudocapacitor, HER	Specific capacitance: 2,112 F g ⁻¹ at 1 A g ⁻¹ , stability: 91.8% after 4,000 cycles at 4 A g ⁻¹ HER: E _{10mA/cm²} = 115 mV	[276]
Cu-doped CoSe ₂ microboxes	Co ₃ [Co(CN) ₆] ₂ , Na ₂ SeO ₃ , N ₂ H ₄ ·2H ₂ O, Cu(NO ₃) ₂	Hydrothermal, 160°C for 8 h; 160°C for 4 h	NaIBs	Reversible charge capacity: 492 mA h g ⁻¹ at 0.05 A g ⁻¹ ; rate capability: 185 mA h g ⁻¹ at 3 A g ⁻¹ ; capacity retention 94% after 500 cycles at 1 A g ⁻¹	[277]
CoS ₂ -CoSe ₂ / N-doped carbon nanocubes	CoCo PBA@PDA, S powder, Se powder	350°C for 2 h in N ₂	Electrodes for dye-sensitized solar cells	Power conversion efficiency: 8.45% under AM 1.5 G irradiation	[274]

1.3.4. PB-derived metal phosphides

In recent years, PB and PBAs have been shown to be excellent precursors for the synthesis of porous or hollow transition metal phosphide (TMP) nanoarchitectures.[278-288] For example, $\text{Ni}(\text{H}_2\text{O})_2[\text{Ni}(\text{CN})_4]$ (Ni-Ni PBA) nanoplates are employed as precursors to obtain nickel phosphides with similar porous plate-like nanostructures.[278] In a typical procedure, the Ni-Ni PBA nanoplates were transferred into porous nickel phosphides by annealing at the downstream side of NaH_2PO_2 powder at 300°C under an Ar flow. When the temperature rises to $\geq 250^\circ\text{C}$, NaH_2PO_2 powder decomposes to release PH_3 , which could be diffused with the airflow to $\text{Ni}(\text{H}_2\text{O})_2[\text{Ni}(\text{CN})_4]$ and directly react with $\text{Ni}(\text{H}_2\text{O})_2[\text{Ni}(\text{CN})_4]$ to form nickel phosphides. The as-obtained product is characterized as a mixture of Ni_5P_4 and Ni_2P incorporated into a porous amorphous carbon layer, with Ni_2P as the major component. During the phosphidation reaction, the 2D morphology is well maintained, while the surface of the nanoplates becomes rough and porous. Similarly, mesoporous FeP/C composite nanocubes have been designed and fabricated through low-temperature phosphorization of the PB precursors.[279] In another case, Tian *et al.* developed a novel two-step strategy for the synthesis of cobalt phosphide double-shelled nanocages (CoP-NCs) (**Figure 1.26a-c**).[280] In the first step, porous spinel Co_3O_4 hollow nanocages were obtained via thermal decomposition of Co-PBA NCs at 450°C in air. In the second step, phosphidation of Co_3O_4 -NCs was conducted by annealing at 320°C under an Ar flow with NaH_2PO_2 as the phosphorus source. The formation of double-shell CoP nanocages from Co_3O_4 -NCs can be explained by the Kirkendall effect. In detail, PH_3 released from NaH_2PO_2 can penetrate the nanoporous Co_3O_4 -NCs, leading to the simultaneous formation of CoP layers from both exterior and interior sides. However, the outward diffusion of cobalt ions is faster than the inward diffusion of phosphorus ions. Consequently, the original Co_3O_4 shell is separated into two thinner CoP shells.

Apart from single TMP, Hao *et al.* demonstrated the fabrication of binary transition metal phosphide ($\text{Co}_x\text{Fe}_{1-x}\text{P}$) nanocubes with different Co and Fe ratios by phosphating a Co-Fe PBA. Three different Co-Fe PBA precursors were initially fabricated through the coprecipitation of CoCl_2 and $\text{K}_3[\text{Fe}(\text{CN})_6]$ at different ratios. After a general low-temperature

phosphidation reaction under a N_2 flow, the as-prepared Co-Fe PBA precursors were converted into $Co_{0.71}Fe_{0.29}P$, $Co_{0.59}Fe_{0.41}P$, and $Co_{0.38}Fe_{0.62}P$ in the case of the $CoCl_2:K_3[Fe(CN)_6]$ ratio being 3:1, 3:2, and 3:4, respectively. During the phosphidation process, all three products of $Co_xFe_{1-x}P$ inherit the cubic structure well except when converting to a porous structure. Additionally, the difference in Co and Fe ratios has an obvious influence on the pore volume and specific surface area of the products.

Recently, carbon-based materials (*e.g.*, graphene) were introduced to modify PB- and PBA-derived TMP nanomaterials for the purpose of improving their electrical conductivity. For instance, Venugopal *et al.* reported the synthesis of iron phosphide (FeP) particles incorporated into a 3D porous graphene aerogel via the phosphating of PB-loaded graphene aerogel (PB/GA).[286] For the formation of PB/GA, Fe^{3+} cation first adsorbed on the surface of GO by interacting with anionic GO functional groups in a solution. After the addition of $K_3[Fe(CN)_6]$ and L-cysteine to the solution, small PB particles were formed on the surface of graphene layers. Finally, PB-loaded graphene hydrogels were obtained due to the cross-linking of GO by heating at a moderate temperature using ethylene diamine and L-cysteine. The phosphidation reaction was conducted by heating PB/GA with NaH_2PO_2 as a phosphorus source at $400^\circ C$ in a N_2 flow. In another case, a unique architecture of core-shell porous $FeP@CoP$ phosphide nanocubes interconnected by reduced graphene oxide (RGO) nanosheets was designed and synthesized (**Figure 1.26d–g**).[282] This strategy involves the synthesis of core-shell $Co(OH)_2@PB$, coating with graphene oxide, and a subsequent simple phosphorization treatment. In detail, core-shell structured $Co(OH)_2@PB$ nanocubes are first fabricated by depositing a layer of $Co(OH)_2$ nanocrystals on the surface of PB microcubes through the reaction between Co^{2+} ions and ammonia in solution. Then the $Co(OH)_2@PB$ microcubes are modified with PDDA (a cationic polyelectrolyte) to carry positive charges. The negatively charged GO nanosheets can tightly coat the surface of the $Co(OH)_2@PB$ microcubes via electrostatic interaction to form a uniform hybrid $GO@Co(OH)_2@PB$. After subsequent phosphorization at $300^\circ C$ in an Ar atmosphere, the as-prepared $GO@Co(OH)_2@PB$ was converted into porous core-shell structured RGO nanosheets-coated $CoP@FeP$ microcubes.

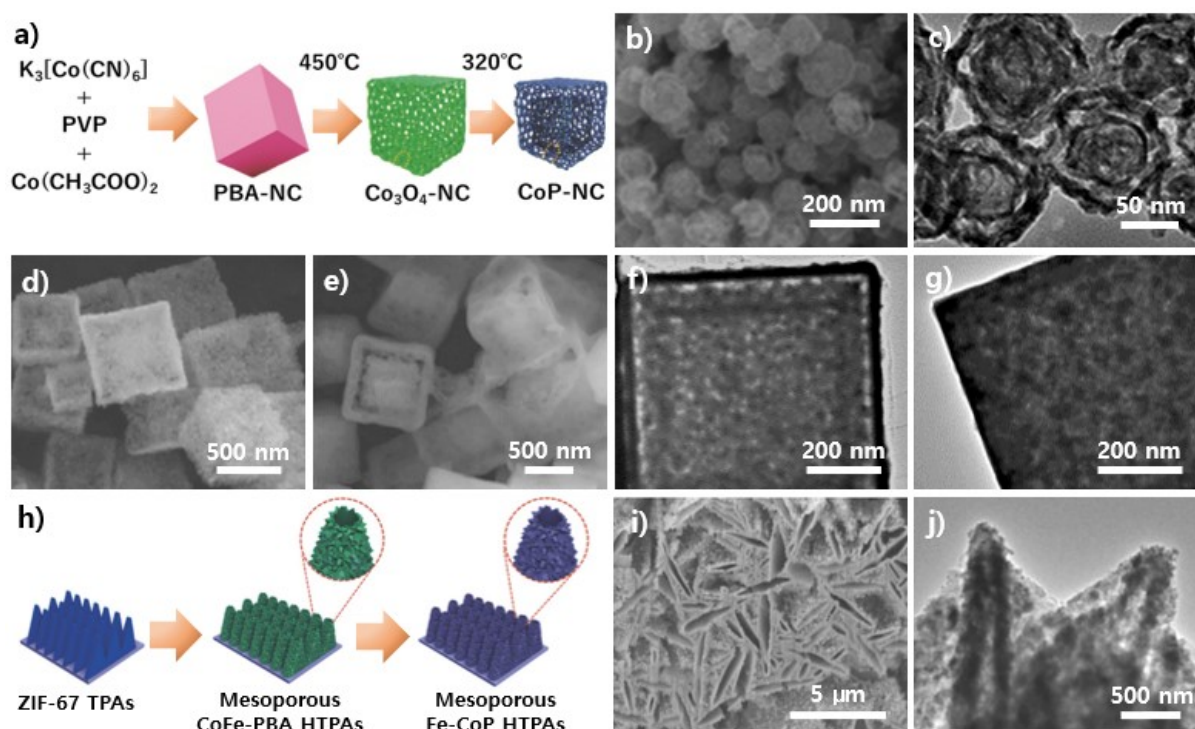


Figure 1.26 (a) Schematic of the synthesis route of double-shelled CoP nanocages. (b) SEM and (c) TEM images of CoP nanocages. SEM images of (d) C-FeP microcubes and (e) CoP@C-FeP phosphide microcube composites. TEM images of (f) a core-shell structured CoP@FeP microcube and (g) porous C-FeP microcube. (h) Schematic illustration of the preparation of mesoporous Fe-CoP HTPAs. (i) SEM and (j) TEM images of the mesoporous Fe-CoP HTPAs.

In addition to carbon-based supports, PB and PBAs can be grown on various other support materials and subsequently converted into various metal phosphide architectures. For example, a Ni₂P/Fe₂P nanoflake array on titanium foil was synthesized from a Ni-Fe PBA precursor through a low-temperature phosphidation reaction.^[283] Specifically, a layer of nickel hydroxide nanoflakes was first grown on the Ti foil as a template and then transformed into 3D Ni-Fe PBA arrays by reacting with K₃[Fe(CN)₆]. Then the as-prepared 3D Ni-Fe PBA arrays were phosphidated with NaH₂PO₂ at 350°C under a N₂ flow. In another case, a novel architecture of Fe-doped CoP hollow triangle plate arrays with distinct hierarchical porous shells was designed and fabricated by Hu and associates (**Figure 1.26h–j**).^[284] In detail, ZIF-67 triangle plate arrays were first deposited on the surface of nickel foam via a simple reaction of Co(NO₃)₂ with 2-methylimidazole (MIM) in an aqueous solution at room temperature. Then

the as-synthesized ZIF-67 triangle plate arrays were converted into hierarchical hollow array structured $\text{Co}_2[\text{Fe}(\text{CN})_6]$ through a critical post-synthetic ligand exchange reaction between MIM and $\text{K}_4[\text{Fe}(\text{CN})_6]$, which was subsequently phosphated at 300°C under a N_2 gas flow to produce Fe-doped CoP that retained the hollow array structure. The as-prepared mesoporous Fe-doped CoP hollow triangle plate arrays possess a variety of advantageous features as electrocatalysts, such as a synergetic bimetal composition, abundant active sites, short electron and ion transport pathways, and high structural strength.

Table 1.4 Summaries of PB/PBA-derived porous metal phosphides, their complexes with carbon, and their applications.

Compositions	Precursors	Thermal conditions	Applications	Performance	Ref.
Ni ₅ P ₄ -Ni ₂ P@C nanoplates	Ni(H ₂ O) ₂ [Ni(CN) ₄]	300°C for 2 h in Ar with NaH ₂ PO ₂	OER	$E_{10 \text{ mA/cm}^{-2}} = 1.53 \text{ V vs. RHE}$; Tafel plots = 64 mV decade ⁻¹	[278]
FeP/carbon nanocubes	PB	450°C for 1 h in Ar, 320°C for 1 h in Ar with NaH ₂ PO ₂	NaIBs, HER	NaIBs: Initial discharge/capacity: 740/506 mA h g ⁻¹ HER: $E_{\text{onset}} = 80 \text{ mV vs. RHE}$; Tafel slope = 40 mV dec ⁻¹	[279]
CoP double-shelled nanocages	Co ₃ [Co(CN) ₆] ₂ ·nH ₂ O	450°C in air; 320°C in Ar with NaH ₂ PO ₂			[280]
FeP/3D graphene aerogel	PB, graphene oxide	400°C in N ₂ with NaH ₂ PO ₂	HER	$E_{10 \text{ mAcm}^{-2}} = 150 \text{ mV vs. RHE}$ in 0.5 M H ₂ SO ₄ ; Tafel slope = 65 mV dec ⁻¹	[281]
C-FeP@CoP@RGO	PB@Co(OH) ₂ @graphene oxide	300°C for 2 h in Ar with NaH ₂ PO ₂	NaIBs	Initial discharge/charge capacity: 968.0/551.4 mA h g ⁻¹ ; coulombic efficiency: 56.9%; reversible capacity: 456.2 mA h g ⁻¹ after 200 cycles at 0.1 mA g ⁻¹	[282]
Ni ₂ P/Fe ₂ P nanoflake array on titanium foil	Ni ₃ [Fe(CN) ₆] ₂	350°C in N ₂ with NaH ₂ PO ₂ ·H ₂ O	HER	$E_{10 \text{ mA cm}^{-2}} = 70 \text{ mV vs. RHE}$ in 0.5 M H ₂ SO ₄ ; Tafel slope = 52 mV dec ⁻¹	[283]

Fe-doped CoP hollow triangle plate arrays on nickel foam	$\text{Co}_2[\text{Fe}(\text{CN})_6]$ array	300°C for 2 h in N_2 with $\text{NaH}_2\text{PO}_2 \cdot \text{H}_2\text{O}$	HER; OER	HER: $E_{10 \text{ mA cm}^{-2}} = 98 \text{ mV vs. RHE}$ in 1 M KOH; Tafel plots = 69 mV dec^{-1} OER: $E_{10 \text{ mA cm}^{-2}} = 230 \text{ mV vs. RHE}$ in 1 M KOH; Tafel plots = 43 mV dec^{-1}	[284]
$\text{Co}_{0.71}\text{Fe}_{0.29}\text{P}$, $\text{Co}_{0.59}\text{Fe}_{0.41}\text{P}$, $\text{Co}_{0.38}\text{Fe}_{0.62}\text{P}$ nanocubes	$\text{CoCl}_2:\text{K}_3[\text{Fe}(\text{CN})_6]$ with different ratio	350, 450, 550°C for 2 h under N_2 flow with NaH_2PO_2	HER	Onset potentials: 54, 31, 57 mV; Tafel slope: 53, 52, 60 mV decade^{-1} (Ar-saturated 0.5 M H_2SO_4) Onset potentials: 58, 39, 69 mV; Tafel slope: 77, 72, 78 mV decade^{-1} (1.0 M KOH)	[285]
FeP nanocubes	PB	450°C for 2 h under N_2 flow with NaH_2PO_2	Peroxidase	H_2O_2 detection limitation: 0.62 μM	[286]
Ni-Co-P ($\text{Co}_2\text{P}/\text{CoP}/\text{Ni}_2\text{P}$)	$\text{Ni}_3[\text{Co}(\text{CN})_6]_2 \cdot 12\text{H}_2\text{O}$	300°C for 2 h under N_2 flow with NaH_2PO_2	HER	$E_{10 \text{ mA cm}^{-2}} = 150 \text{ mV vs. RHE}$; Tafel slope: 60.1 mV dec^{-1}	[287]
Ni-Fe-P/nickel foam	$\text{Ni}_3[\text{Fe}(\text{CN})_6]_2$	350°C for 2 h under N_2 flow with NaH_2PO_2	HER; OER	HER: $E_{10 \text{ mA cm}^{-2}} = 98 \text{ mV vs. RHE}$ OER: $E_{10 \text{ mA cm}^{-2}} = 150 \text{ mV vs. RHE}$ (1 M KOH)	[288]

1.4. Perspective

As a witness to the rapid development in nanoarchitectonics with regard to PB and PBAs, this chapter introduces versatile paths toward the nanostructures and demonstrates strong relationship between nanoarchitectonics and properties. Nanoarchitectonics not only produce high-quality images but also bring great opportunities for tailoring/adding properties/functions of PBAs. Further, nanoarchitectonics are a bridge between PBAs and other functional materials. Various high-performance materials could be derived from nanostructured PB and PBAs.

References

- [1] J. C. Brice, *Crystal growth processes*, Blackie Halsted Press, **1986**.
- [2] H. S. Nalwa and S. Miyata, *Nonlinear optics of organic molecules and polymers*, CRC press, New York, **1997**.
- [3] R. A. Laudise, *The growth of single crystals*, Prentice Hall Inc., New Jersey, **1970**.
- [4] E. L. Thomas, J. N. Millican, E. K. Okudzeto and J. Y. Chan, *Comments Inorg. Chem.* **2006**, 27, 1-39.
- [5] *Frontiers in crystalline matter: from discovery to technology*, The National Academies Press: Washington, D.C, **2009**.
- [6] W. A. Phelan, M. C. Menard, M. J. Kangas, G. T. McCandless, B. L. Drake and J. Y. Chan, *Chem. Mater.* **2012**, 24, 409-420.
- [7] A. Ludi and H. U. Güdel, *Structural chemistry of polynuclear transition metal cyanides*. In *Inorganic Chemistry* spring: Berlin/Heidelberg, **1973**, pp. 1-21.
- [8] J. Keggin and F. Miles, *Nature* **1936**, 137, 577-578.
- [9] S. F. Kettle, E. Diana, E. M. C. Marchese, E. Boccaleri and P. L. Stanghellini, *J. Raman Spectroscopy* **2011**, 42, 2006-2014.
- [10] E. Bustos and L. A. Godínez, *Int J Electrochem Sci* **2011**, 6, 1-36.
- [11] H. J. Buser, D. Schwarzenbach, W. Petter and A. Ludi, *Inorg. Chem.* **1977**, 16, 2704-2710.

- [12] P. Franz, C. Ambrus, A. Hauser, D. Chernyshov, M. Hostettler, J. Hauser, L. Keller, K. Krämer, H. Stoeckli-Evans, P. Pattison, H.B.Bürgi, and S.Decurtins, *J. Am. Chem. Soc.* **2004**, *126*, 16472-16477.
- [13] F. Herren, P. Fischer, A. Ludi and W. Hälg, *Inorg. Chem.* **1980**, *19*, 956-959.
- [14] A. Widmann, H. Kahlert, I. Petrovic-Prelevic, H. Wulff, J.V. Yakhmi, N. Bagkar and F. Scholz, *Inorg. Chem.* **2002**, *41*, 5706-5715.
- [15] S.-i. Ohkoshi, H. Tokoro, M. Utsunomiya, M. Mizuno, M. Abe and K. Hashimoto, *J. Phys. Chem. B* **2002**, *106*, 2423-2425.
- [16] S.-i. Ohkoshi, T. Matsuda, H. Tokoro and K. Hashimoto, *Chem. Mater.* **2005**, *17*, 81-84.
- [17] L. Egan, K. Kamenev, D. Papanikolaou, Y. Takabayashi and S. Margadonna, *J. Am. Chem. Soc.* **2006**, *128*, 6034-6035.
- [18] H. Tokoro, S.-i. Ohkoshi and K. Hashimoto, *Appl. Phys. Lett.* **2003**, *82*, 1245-1247.
- [19] H. Tokoro, M. Shiro, K. Hashimoto and S. i. Ohkoshi, *Z. Anorg. Allg. Chem.* **2007**, *633*, 1134-1136.
- [20] E. J. M. Vertelman, T. T. A. Lummen, A. Meetsma, M. W. Bouwkamp, G. Molnar, P. H. M. van Loosdrecht and P. J. van Koningsbruggen, *Chem. Mater.* **2008**, *20*, 1236-1238.
- [21] K. W. Chapman, P. J. Chupas and C. J. Kepert, *J. Am. Chem. Soc.* **2006**, *128*, 7009-7014.
- [22] E. J. M. Vertelman, E. Maccallini, D. Gournis, P. Rudolf, T. Bakas, J. Luzon, R. Broer, A. Pugzlys, T. T. A. Lummen, P. H. M. Van Loosdrecht and P.J. Van Koningsbruggen, *Chem. Mater.* **2006**, *18*, 1951-1963.
- [23] W. Dong, L.-N. Zhu, H.-B. Song, D.-Z. Liao, Z.-H. Jiang, S.-P. Yan, P. Cheng and S. Gao, *Inorg. Chem.* **2004**, *43*, 2465-2467.
- [24] J. L. Heinrich, J. J. Sokol, A. G. Hee and J. R. Long, *J. Solid State Chem.* **2001**, *159*, 293-301.
- [25] L. G. Beauvais, M. P. Shores and J. R. Long, *Chem. Mater.* **1998**, *10*, 3783-3786.
- [26] M. V. Bennett, L. G. Beauvais, M. P. Shores and J. R. Long, *J. Am. Chem. Soc.* **2001**, *123*, 8022-8032.
- [27] A. L. Goodwin, K. W. Chapman and C. J. Kepert, *J. Am. Chem. Soc.* **2005**, *127*, 17980-17981.

- [28] S. Margadonna, K. Prassides and A. N. Fitch, *J. Am. Chem. Soc.* **2004**, *126*, 15390-15391.
- [29] A. Ludi, H. U. Güdel and V. Dvořák, *Helv. Chim. Acta* **1967**, *50*, 2035-2039.
- [30] L. Pauling and P. Pauling, *Proc. Natl. Acad. Sci. U. S. A.* **1968**, *60*, 362-367.
- [31] A. Ludi and H. U. Güdel, *Helv. Chim. Acta* **1968**, *51*, 2006-2016.
- [32] A. L. Goodwin, M. Calleja, M. J. Conterio, M. T. Dove, J. S. O. Evans, D. A. Keen, L. Peters and M. G. Tucker, *Science* **2008**, *319*, 794-797.
- [33] M. C. Conterio, A. L. Goodwin, M. G. Tucker, D. A. Keen, M. T. Dove, L. Lars and J. S. O. Evans, *J. Phys.: Condens. Matter* **2008**, *20*, 255225-255238.
- [34] Q. Pan, K. Huang, S. Ni, F. Yang and D. He, *Mater. Res. Bull.* **2009**, *44*, 388-392.
- [35] K. A. Hofmann and F. Küspert, *Zeitschrift für anorganische Chemie* **1897**, *15*, 204-207.
- [36] T. Iwamoto, T. Nakano, M. Morita, T. Miyoshi, T. Miyamoto and Y. Sasaki, *Inorg. Chim. Acta* **1968**, *2*, 313-316.
- [37] Y. Mathey and C. Mazieres, *Can. J. Chem.* **1974**, *52*, 3637-3644.
- [38] W. K. Ham, T. J. R. Weakley and C. J. Page, *J. Solid State Chem.* **1993**, *107*, 101-107.
- [39] T. Kitazawa, M. Fukunaga, M. Takahashi and M. Takeda, *Mol. Cryst. Liq. Cryst.*, **1994**, *244*, 331-336.
- [40] T. Niu, G. Crisci, J. Lu and A. J. Jacobson, *Acta Crystallogr. Sect. C: Cryst. Struct. Commun.* **1998**, *54*, 565-567.
- [41] A. Ray, I. Bhowmick, W. S. Sheldrick, A. D. Jana and M. Ali, *J. Solid State Chem.* **2009**, *182*, 2608-2612.
- [42] J. Rodríguez-Hernández, A. A. Lemus-Santana, C. N. Vargas and E. Reguera, *C. R. Chimie* **2012**, *15*, 350-355.
- [43] O. Reyes-Martinez, E. Torres-García, G. Rodríguez-Gattorno and E. Reguera, *Materials* **2013**, *6*, 1452-1466.
- [44] M. J. Murphy, D. M. D'Alessandro and C. J. Kepert, *Dalton Transactions* **2013**, *42*, 13308-13310.
- [45] Y.-L. Qin, B.-W. Yang, G.-F. Wang and H. Sun, *Acta Crystallographica Section C: Structural Chemistry* **2016**, *72*, 555-560.
- [46] S. M. Holmes and G. S. Girolami, *Mol. Cryst. Liq. Cryst.*, **1997**, *305*, 279-290.

- [47] H.-Z. Kou, J.-K. Tang, D.-Z. Liao, S. Gao, P. Cheng, Z.-H. Jiang, S.-P. Yan, G.-L. Wang, B. Chansou and J.-P. Tuchagues, *Inorg. Chem.* **2001**, *40*, 4839-4844.
- [48] K. Takeshi, S. Hiroe, N. Masashi, N. Hiroyasu, N. Katsutoshi and T. Yusaku, *Chem. Lett.* **2007**, *36*, 756-757.
- [49] C.-Y. Li, C.-Y. Hsieh, H.-M. Lin, H.-M. Kao and K.-H. Lii, *Inorg. Chem.* **2002**, *41*, 4206-4210.
- [50] B. Mu, Q. Li, L. Lv, D.-D. Yang, Q. Wang and R.-D. Huang, *J. Solid State Chem.* **2015**, *226*, 1-10.
- [51] T. Pretsch, K. W. Chapman, G. J. Halder and C. J. Kepert, *Chem. Commun.* **2006**, 1857-1859.
- [52] T. Matsuda, H. Tokoro, M. Shiro, K. Hashimoto and S.-i. Ohkoshi, *Acta Crystallogr. Sect. E: Struct. Rep. Online* **2008**, *64*, i11-i12.
- [53] B. Tao, H. Xia, X. Jiang and Y. F. Zhu, *Russian Journal of Coordination Chemistry* **2011**, *37*, 367-370.
- [54] H. Jiang and C. Kloc, *MRS Bull.* **2013**, *38*, 28-33.
- [55] J. R. S. Waring, *Acta Crystallographica Section A*, **1970**, *26*, 1-18.
- [56] A. Yuan, H. Zhou, G. Diao, P. D. Southon, C. J. Kepert and L. Liu, *Int. J. Hydrogen Energy* **2014**, *39*, 884-889.
- [57] A. Alowasheir, S. Tominaka, Y. Ide, Y. Yamauchi and Y. Matsushita, *CrystEngComm* **2018**, *20*, 6713-6720.
- [58] G. Fornasieri, M. Aouadi, P. Durand, P. Beaunier, E. Rivière and A. Bleuzen, *Chem. Commun.* **2010**, *46*, 8061-8063.
- [59] S. Vaucher, J. Fielden, M. Li, E. Dujardin and S. Mann, *Nano Lett.* **2002**, *2*, 225-229.
- [60] S. Vaucher, M. Li and S. Mann, *Angew. Chem. Int. Ed.* **2000**, *39*, 1793-1796.
- [61] M. F. Dumont, O. N. Risset, E. S. Knowles, T. Yamamoto, D. M. Pajerowski, M. W. Meisel and D. R. Talham, *Inorg. Chem.* **2013**, *52*, 4494-4501.
- [62] F.-X. Bu, C.-J. Du, Q.-H. Zhang and J.-S. Jiang, *CrystEngComm* **2014**, *16*, 3113-3120.
- [63] M. Cao, X. Wu, X. He and C. Hu, *Chem. Commun.* **2005**, *17*, 2241-2243.

- [64] N. Kondo, A. Yokoyama, M. Kurihara, M. Sakamoto, M. Yamada, M. Miyake, T. Ohsuna, H. Aono and Y. Sadaoka, *Chem. Lett.* **2004**, *33*, 1182-1183.
- [65] F. Volatron, L. Catala, E. Rivière, A. Gloter, O. Stéphan and T. Mallah, *Inorg. Chem.* **2008**, *47*, 6584-6586.
- [66] L. Catala, T. Gacoin, J. P. Boilot, É. Rivière, C. Paulsen, E. Lhotel and T. Mallah, *Adv. Mater.* **2003**, *15*, 826-829.
- [67] E. Dujardin and S. Mann, *Adv. Mater.* **2004**, *16*, 1125-1129.
- [68] D. H. Buchold and C. Feldmann, *Chem. Mater.* **2007**, *19*, 3376-3380.
- [69] Y. Guari, J. Larionova, M. Corti, A. Lascialfari, M. Marinone, G. Poletti, K. Molvinger and C. Guérin, *Dalton Trans.* **2008**, *28*, 3658-3660.
- [70] A. de la Escosura, M. Verwegen, F. D. Sikkema, M. Comellas-Aragones, A. Kirilyuk, T. Rasing, R. J. Nolte and J. J. Cornelissen, *Chem. Commun.* **2008**, *13*, 1542-1544.
- [71] A. M. Collins, S. Mann and S. R. Hall, *Nanoscale* **2010**, *2*, 2370-2372.
- [72] A. Tokarev, P. Agulhon, J. Long, F. Quignard, M. Robitzer, R. A. Ferreira, L. D. Carlos, J. Larionova, C. Guérin and Y. Guari, *J. Mater. Chem.* **2012**, *22*, 20232-20242.
- [73] J. Larionova, L. Salmon, Y. Guari, A. Tokarev, K. Molvinger, G. Molnár and A. Bousseksou, *Angew. Chem.* **2008**, *120*, 8360-8364.
- [74] I. Boldog, A. B. Gaspar, V. Martínez, P. Pardo - Ibañez, V. Ksenofontov, A. Bhattacharjee, P. Gütllich and J. A. Real, *Angew. Chem. Int. Ed.* **2008**, *47*, 6433-6437.
- [75] J. Larionova, Y. Guari, C. Sangregorio and C. Guérin, *New J. Chem.* **2009**, *33*, 1177-1190.
- [76] J. Larionova, Y. Guari, C. Blanc, P. Dieudonné, A. Tokarev and C. Guérin, *Langmuir* **2008**, *25*, 1138-1147.
- [77] Q. Sheng, R. Liu and J. Zheng, *Nanoscale* **2012**, *4*, 6880-6886.
- [78] R. McHale, N. Ghasdian, Y. Liu, H. Wang, Y. Miao and X. Wang, *Macromol. Rapid Commun.* **2010**, *31*, 856-860.
- [79] B. Michael, *Chem. Commun.* **2010**, *46*, 4574-4576.
- [80] X. Roy, J. K.-H. Hui, M. Rabnawaz, G. Liu and M. J. MacLachlan, *J. Am. Chem. Soc.* **2011**, *133*, 8420-8423.

- [81] M. Hu, S. Ishihara, K. Ariga, M. Imura and Y. Yamauchi, *Chem. Eur. J.* **2013**, *19*, 1882-1885.
- [82] F. Shiba, M. Nito, K. Kawakita and Y. Okawa, *Particul. Sci. Technol.* **2015**, *33*, 671-676.
- [83] Y. D. Chiang, M. Hu, Y. Kamachi, S. Ishihara, K. Takai, Y. Tsujimoto, K. Ariga, K. C. W. Wu and Y. Yamauchi, *Eur. J. Inorg. Chem.* **2013**, *18*, 3141-3145.
- [84] G. Fu, W. Liu, S. Feng and X. Yue, *Chem. Commun.* **2012**, *48*, 11567-11569.
- [85] M. Hu and Y. Yamauchi, *Chem. Asian J.* **2011**, *6*, 2282-2286.
- [86] M. Hu and J. Jiang, *Mater. Res. Bull.* **2011**, *46*, 702-707.
- [87] M. Hu, J.-S. Jiang, R.-P. Ji and Y. Zeng, *CrystEngComm* **2009**, *11*, 2257-2259.
- [88] X.-J. Zheng, Q. Kuang, T. Xu, Z.-Y. Jiang, S.-H. Zhang, Z.-X. Xie, R.-B. Huang and L.-S. Zheng, *J. Phys. Chem. C* **2007**, *111*, 4499-4502.
- [89] X. Wu, M. Cao, C. Hu and X. He, *Cryst. Growth Des.* **2006**, *6*, 26-28.
- [90] S. Tricard, F. Charra and T. Mallah, *Dalton Trans.* **2013**, *42*, 15835-15845.
- [91] J. Gu, S. Fu, C. Jin, X. Liu, Y. Gao, J. Wu, Z. Bian, H. Tian, L. Wang and F. Gao, *J. Solid State Chem.* **2016**, *239*, 64-68.
- [92] H. Ming, N. L. Torad, Y.-D. Chiang, K. C.-W. Wu and Y. Yamauchi, *CrystEngComm* **2012**, *14*, 3387-3396.
- [93] M. Hu, J.-S. Jiang, C.-C. Lin and Y. Zeng, *CrystEngComm* **2010**, *12*, 2679-2683.
- [94] X. Shen, S. Wu, Y. Liu, K. Wang, Z. Xu and W. Liu, *J. Colloid Interface Sci.* **2009**, *329*, 188-195.
- [95] Q. Meng, W. Zhang, M. Hu and J.-S. Jiang, *Chem. Commun.* **2016**, *52*, 1957-1960.
- [96] D. M. Pajerowski, F. A. Frye, D. R. Talham and M. W. Meisel, *New J. Physics* **2007**, *9*, 222.
- [97] D. Brinzei, L. Catala, C. Mathonière, W. Wernsdorfer, A. Gloter, O. Stephan and T. Mallah, *J. Am. Chem. Soc.* **2007**, *129*, 3778-3779.
- [98] L. Catala, A. Gloter, O. Stephan, G. Rogez and T. Mallah, *Chem. Commun.* **2006**, *9*, 1018-1020.
- [99] N. Kondo, M. Kurihara, M. Yamada, M. Miyake, M. Nishijima, T. Ohsuna, F. Mizukami and M. Sakamoto, *Chem. Lett.* **2005**, *34*, 590-591.

- [100] T. Uemura, M. Ohba and S. Kitagawa, *Inorg. Chem.* **2004**, *43*, 7339-7345.
- [101] T. Uemura and S. Kitagawa, *J. Am. Chem. Soc.* **2003**, *125*, 7814-7815.
- [102] S. Yamada, K. Kuwabara and K. Koumoto, *Mater. Sci. Eng. B* **1997**, *49*, 89-94.
- [103] M. Yamada and S.-y. Yonekura, *J. Phys. Chem. C* **2009**, *113*, 21531-21537.
- [104] L. Hu, P. Zhang, Q. Chen, H. Zhong, X. Hu, X. Zheng, Y. Wang and N. Yan, *Cryst. Growth Des.* **2012**, *12*, 2257-2264.
- [105] M. Yamada, M. Arai, M. Kurihara, M. Sakamoto and M. Miyake, *J. Am. Chem. Soc.* **2004**, *126*, 9482-9483.
- [106] M. Hu, A. A. Belik, M. Imura and Y. Yamauchi, *J. Am. Chem. Soc.* **2013**, *135*, 384-391.
- [107] M. Hu, Y. Ju, K. Liang, T. Suma, J. Cui and F. Caruso, *Adv. Funct. Mater.* **2016**, *26*, 5827-5834.
- [108] W. Zhang, Y. Zhao, V. Malgras, Q. Ji, D. Jiang, R. Qi, K. Ariga, Y. Yamauchi, J. Liu and J. S. Jiang, *Angew. Chem. Int. Ed.* **2016**, *55*, 8228-8234.
- [109] R. Chen, Y. Huang, M. Xie, Q. Zhang, X. Zhang, L. Li and F. Wu, *ACS Appl. Mater. Interfaces* **2016**, *8*, 16078-16086.
- [110] L. Han, X. Y. Yu and X. W. Lou, *Adv. Mater.* **2016**, *28*, 4601-4605.
- [111] J. Nai, B. Y. Guan, L. Yu and X. W. D. Lou, *Sci. Adv.* **2017**, *3*, e1700732.
- [112] Y. Yue, Z. Zhang, A. J. Binder, J. Chen, X. Jin, S. H. Overbury and S. Dai, *ChemSusChem* **2015**, *8*, 177-183.
- [113] O. N. Risset, E. S. Knowles, S. Ma, M. W. Meisel and D. R. Talham, *Chem. Mater.* **2012**, *25*, 42-47.
- [114] M. Hu, N. L. Torad and Y. Yamauchi, *Eur. J. Inorg. Chem.* **2012**, *30*, 4795-4799.
- [115] M. Hu, S. Furukawa, R. Ohtani, H. Sukegawa, Y. Nemoto, J. Reboul, S. Kitagawa and Y. Yamauchi, *Angew. Chem. Int. Ed.* **2012**, *51*, 984-988.
- [116] C. Zhai, N. Du, H. Zhang and D. Yang, *J. Alloys Compd.* **2011**, *509*, 8382-8386.
- [117] M. Hu, J.-S. Jiang and Y. Zeng, *Chem. Commun.* **2010**, *46*, 1133-1135.
- [118] Y. Yue, A. J. Binder, B. Guo, Z. Zhang, Z. A. Qiao, C. Tian and S. Dai, *Angew. Chem. Int. Ed.* **2014**, *53*, 3134-3137.

- [119] N. L. Torad, M. Hu, M. Imura, M. Naito and Y. Yamauchi, *J. Mater. Chem.* **2012**, *22*, 18261-18267.
- [120] H.-Y. Lian, M. Hu, C.-H. Liu, Y. Yamauchi and K. C.-W. Wu, *Chem. Commun.* **2012**, *48*, 5151-5153.
- [121] C. D. Wessells, S. V. Peddada, R. A. Huggins and Y. Cui, *Nano Lett.* **2011**, *11*, 5421-5425.
- [122] C. D. Wessells, R. A. Huggins and Y. Cui, *Nat. Commun.* **2011**, *2*, 550.
- [123] J. Qian, C. Wu, Y. Cao, Z. Ma, Y. Huang, X. Ai and H. Yang, *Adv. Energy Mater.* **2018**, *8*, 1702619.
- [124] Y. You, X.-L. Wu, Y.-X. Yin and Y.-G. Guo, *Energy Environ. Sci.* **2014**, *7*, 1643-1647.
- [125] X. Wu, W. Deng, J. Qian, Y. Cao, X. Ai and H. Yang, *J. Mater. Chem. A* **2013**, *1*, 10130-10134.
- [126] C. Fang, Y. Huang, W. Zhang, J. Han, Z. Deng, Y. Cao and H. Yang, *Adv. Energy Mater.* **2016**, *6*, 1501727.
- [127] D. Su, A. McDonagh, S. Z. Qiao and G. Wang, *Adv. Mater.* **2017**, *29*, 1604007.
- [128] H. Sun, W. Zhang and M. Hu, *Crystals* **2018**, *8*, 23.
- [129] J. Xu, F.-X. Bu, Y.-F. Guo, W. Zhang, M. Hu and J.-S. Jiang, *J. Nanosci. Nanotechnol.* **2018**, *18*, 3230-3238.
- [130] X. Cai, W. Gao, M. Ma, M. Wu, L. Zhang, Y. Zheng, H. Chen and J. Shi, *Adv. Mater.* **2015**, *27*, 6382-6389.
- [131] P. Zhou, D. Xue, H. Luo and X. Chen, *Nano Lett.* **2002**, *2*, 845-847.
- [132] P. Zhou, D. Xue, H. Luo, J. Yao and H. Shi, *Nanotechnology* **2003**, *15*, 27.
- [133] H. Luo, X. Chen, P. Zhou, H. Shi and D. Xue, *J. Electrochem. Soc.* **2004**, *151*, C567-C570.
- [134] P. Zhou and D. Xue, *J. Appl. Phys.* **2004**, *96*, 610-614.
- [135] B. Gao, J. Yao and D. Xue, *J. Magn. Magn. Mater.* **2010**, *322*, 2505-2508.
- [136] Y. Ding, G. Gu, H.-L. Yang and X.-H. Xia, *J. Nanosci. Nanotechnol.* **2009**, *9*, 2381-2386.
- [137] Y. Xian, Y. Hu, F. Liu, Y. Xian, L. Feng and L. Jin, *Biosens. Bioelectron.* **2007**, *22*, 2827-2833.
- [138] L. Qian and X. Yang, *Talanta* **2006**, *69*, 957-962.

- [139] J. Yao, D. Xue and P. Zhou, *J. Electrochem. Soc.* **2006**, *153*, C608-C611.
- [140] A. Johansson, E. Widenkvist, J. Lu, M. Boman and U. Jansson, *Nano Lett.* **2005**, *5*, 1603-1606.
- [141] L. Catala, C. Mathonière, A. Gloter, O. Stephan, T. Gacoin, J.-P. Boilot and T. Mallah, *Chem. Commun.* **2005**, 746-748.
- [142] X. Roy, J. K. H. Hui, M. Rabnawaz, G. Liu and M. J. MacLachlan, *Angew. Chem. Int. Ed.* **2011**, *50*, 1597-1602.
- [143] H.-L. Sun, H. Shi, F. Zhao, L. Qi and S. Gao, *Chem. Commun.* **2005**, 4339-4341.
- [144] S. Sunkari, S. Nagashima, M. Murata, H. Nishihara, Y. Matsui, K. Nishio and H. Masuda, *Chem. Lett.* **2006**, *35*, 406-407.
- [145] P. Liu, C. Liang, J. Xu, J. Fang, J. Zhao and W. Shen, *Bull. Korean Chem. Soc.* **2010**, *31*, 1336-1338.
- [146] M. Hu, S. Ishihara and Y. Yamauchi, *Angew. Chem. Int. Ed.* **2013**, *52*, 1235-1239.
- [147] F.-X. Bu, M. Hu, W. Zhang, Q. Meng, L. Xu, D.-M. Jiang and J.-S. Jiang, *Chem. Commun.* **2015**, *51*, 17568-17571.
- [148] G. Liang, J. Xu and X. Wang, *J. Am. Chem. Soc.* **2009**, *131*, 5378-5379.
- [149] S. Bao, T. Liu, G. Liang, H. Gao, F. Zhu and Q. Wu, *Chem. Eur. J.* **2012**, *18*, 15272-15276.
- [150] V. Vo, H.-J. Kim, H.-Y. Kim, J.-E. Park, Y. Kim, S. Huh and S.-J. Kim, *Microporous Mesoporous Mater.* **2012**, *163*, 211-214.
- [151] E. Coronado, A. Forment - Aliaga, E. Pinilla - Cienfuegos, S. Tatay, L. Catala and J. A. Plaza, *Adv. Funct. Mater.* **2012**, *22*, 3625-3633.
- [152] M. Clemente-León, E. Coronado, A. n. López-Muñoz, D. Repetto, L. Catala and T. Mallah, *Langmuir* **2012**, *28*, 4525-4533.
- [153] S. Tricard, C. Costa-Coquelard, S. Mazerat, E. Rivière, V. Huc, C. David, F. Miserque, P. Jegou, S. Palacin and T. Mallah, *Dalton Trans.* **2012**, *41*, 4445-4450.
- [154] A. K. Rossos, R. g. Y. Gengler, D. S. Badali and R. D. Miller, *Langmuir* **2016**, *32*, 9706-9713.

- [155] M. Clemente-León, E. Coronado, A. n. López-Muñoz, D. Repetto, C. Mingotaud, D. Brinzei, L. Catala and T. Mallah, *Chem. Mater.* **2008**, *20*, 4642-4652.
- [156] L.-D. Feng, J.-M. Shen, X.-H. Li and J.-J. Zhu, *J. Phys. Chem. C* **2008**, *112*, 7617-7623.
- [157] Y.-Y. Song, W. Z. Jia, Y. Li, X. H. Xia, Q. J. Wang, J. W. Zhao and Y. D. Yan, *Adv. Funct. Mater.* **2007**, *17*, 2808-2814.
- [158] W. Jin, A. Toutianoush, M. Pyrasch, J. Schnepf, H. Gottschalk, W. Rammensee and B. Tieke, *J. Phys. Chem. B* **2003**, *107*, 12062-12070.
- [159] Y. Zhao, W. Li, X. Jiang, F. Li, X. Li, W. Zhang, J.-S. Jiang, J. Liu, K. Ariga and M. Hu, *ACS nano* **2017**, *11*, 3662-3670.
- [160] L. Catala, D. Brinzei, Y. Prado, A. Gloter, O. Stéphan, G. Rogez and T. Mallah, *Angew. Chem. Int. Ed.* **2009**, *48*, 183-187.
- [161] Y. Prado, M. A. Arrio, F. Volatron, E. Otero, C. Cartier dit Moulin, P. Sainctavit, L. Catala and T. Mallah, *Chem. Eur. J.* **2013**, *19*, 6685-6694.
- [162] M. K. Peprah, D. VanGennep, P. A. Quintero, O. N. Risset, T. V. Brinzari, C. H. Li, M. F. Dumont, J.-s. Xia, J. J. Hamlin and D. R. Talham, *Polyhedron* **2017**, *123*, 323-327.
- [163] M. Wan, Y. Tang, L. Wang, X. Xiang, X. Li, K. Chen, L. Xue, W. Zhang and Y. Huang, *J. Power Sources* **2016**, *329*, 290-296.
- [164] P. Bhatt, A. Kumar, S. Meena, M. Mukadam and S. Yusuf, *Chem. Phys. Lett.* **2016**, *651*, 155-160.
- [165] A. C. Felts, M. J. Andrus, E. S. Knowles, P. A. Quintero, A. R. Ahir, O. N. Risset, C. H. Li, I. Maurin, G. J. Halder and K. A. Abboud, *The Journal of Physical Chemistry C* **2016**, *120*, 5420-5429.
- [166] C.-H. Lee, C.-M. Wu, E. Batsaikhan, H.-C. Li, C. H. Li, M. K. Peprah, D. R. Talham, M. W. Meisel and W.-H. Li, *J. Phys. Chem. B* **2015**, *119*, 29138-29147.
- [167] O. N. Risset and D. R. Talham, *Chem. Mater.* **2015**, *27*, 3838-3843.
- [168] C. H. Li, M. K. Peprah, D. Asakura, M. W. Meisel, M. Okubo and D. R. Talham, *Chem. Mater.* **2015**, *27*, 1524-1530.
- [169] B. Kong, C. Selomulya, G. Zheng and D. Zhao, *Chem. Soc. Rev.* **2015**, *44*, 7997-8018.
- [170] M. Okubo, C. H. Li and D. R. Talham, *Chem. Commun.* **2014**, *50*, 1353-1355.

- [171] H. Oubouchou, A. Slimani and K. Boukheddaden, *Phys. Rev. B* **2013**, *87*, 104104.
- [172] D. Asakura, C. H. Li, Y. Mizuno, M. Okubo, H. Zhou and D. R. Talham, *J. Am. Chem. Soc.* **2013**, *135*, 2793-2799.
- [173] D. M. Pajerowski, J. E. Gardner, F. A. Frye, M. J. Andrus, M. F. Dumont, E. S. Knowles, M. W. Meisel and D. R. Talham, *Chem. Mater.* **2011**, *23*, 3045-3053.
- [174] Y. Kurihara and Y. Moritomo, *Jpn. J. Appl. Phys.* **2011**, *50*, 060210.
- [175] M. F. Dumont, E. S. Knowles, A. Guet, D. M. Pajerowski, A. Gomez, S. W. Kycia, M. W. Meisel and D. R. Talham, *Inorg. Chem.* **2011**, *50*, 4295-4300.
- [176] M. Presle, J. Lemainque, J.-M. Guigner, E. Larquet, I. Maurin, J.-P. Boilot and T. Gacoin, *New J. Chem.* **2011**, *35*, 1296-1301.
- [177] M. Ishizaki, Y. Sajima, S. Tsuruta, A. Gotoh, M. Sakamoto, T. Kawamoto, H. Tanaka and M. Kurihara, *Chem. Lett.* **2009**, *38*, 1058-1059.
- [178] F. Li, W. Zhang, A. Carné-Sánchez, Y. Tsujimoto, S. Kitagawa, S. Furukawa and M. Hu, *Inorg. Chem.* **2018**, *57*, 8701-8704.
- [179] G. Maurin - Pasturel, J. Long, Y. Guari, F. Godiard, M. G. Willinger, C. Guerin and J. Larionova, *Angew. Chem.* **2014**, *126*, 3953-3957.
- [180] L. Han, P. Tang, A. I. Reyes-Carmona, B. R. Rodríguez-García, M. Torrén, J. R. Morante, J. Arbiol and J. R. Galan-Mascaros, *J. Am. Chem. Soc.* **2016**, *138*, 16037-16045.
- [181] Y.-F. Guo, Q.-C. Fang, J. Xu, F.-X. Bu, W. Zhang, M. Hu and J.-S. Jiang, *J. Nanosci. Nanotechnol.* **2018**, *18*, 3059-3066.
- [182] F. S. Hegner, I. Herraiz-Cardona, D. Cardenas-Morcoso, N. R. López, J.-R. Galán-Mascarós and S. Gimenez, *ACS Appl. Mater. Interfaces* **2017**, *9*, 37671-37681.
- [183] R. Zboril, L. Machala, M. Mashlan, V. Sharma, *Cryst. Growth & Des.* **2004**, *4*, 1317-1325.
- [184] X. Li, Y. Liu, C. L. Zhang, T. Wen, L. Zhuang, X. X. Wang, G. Song, D. Y. Chen, Y. J. Ai, T. Hayat, X. K. Wang, *Chem. Eng. J.* **2018**, *336*, 241-252.
- [185] M. Hu, J. S. Jiang, F. X. Bu, X. L. Cheng, C. C. Lin, Y. Zeng, *RSC Adv.* **2012**, *2*, 4782-4786.

- [186] M. Hu, A. A. Belik, M. Imura, K. Mibu, Y. Tsujimoto, Y. Yamauchi, *Chem. Mater.* **2012**, *24*, 2698-2707.
- [187] K. Tian, X.-X. Wang, Z.-Y. Yu, H.-Y. Li, X. Guo, *ACS Appl. Mater. Interfaces* **2017**, *9*, 29669-29676.
- [188] L. Zhang, H. B. Wu, S. Madhavi, H. H. Hng, X. W. Lou, *J. Am. Chem. Soc.* **2012**, *134*, 17388-17391.
- [189] L. Zhang, H. B. Wu, X. W. Lou, *J. Am. Chem. Soc.* **2013**, *135*, 10664-10672.
- [190] Z. M. B., B. A. A., L. Chia-Hung, H. Han-Yun, L. Yu-Te, M. Victor, Y. Yusuke, W. K. C.-W., *Chem. Asian J.* **2015**, *10*, 1457-1462.
- [191] L. Zhang, H. B. Wu, R. Xu, X. W. Lou, *CrystEngComm* **2013**, *15*, 9332-9335.
- [192] L. Hu, N. Yan, Q. W. Chen, P. Zhang, H. Zhong, X. R. Zheng, Y. Li, X. Y. Hu, *Chem. Eur. J.* **2012**, *18*, 8971-8977.
- [193] Y. Chen, L. Hu, *J. Solid State Chem.* **2016**, *239*, 23-29.
- [194] Y. Feng, X.-Y. Yu, U. Paik, *Chem. Commun.* **2016**, *52*, 6269-6272.
- [195] N. Yan, L. Hu, Y. Li, Y. Wang, H. Zhong, X. Hu, X. Kong, Q. Chen, *J. Phys. Chem. C* **2012**, *116*, 7227-7235.
- [196] Y. Song, J. He, H. Wu, X. Li, J. Yu, Y. Zhang, L. Wang, *Electrochim. Acta* **2015**, *182*, 165-172.
- [197] M. B. Zakaria, H. Ming, S. R. Rahul, P. Malay, T. Kimiko, M. Victor, C. Seyong, D. S. Xue, K. J. Ho, I. Masataka, I. Shinsuke, Y. Yusuke, *Chem. Eur. J.* **2015**, *21*, 3605-3612.
- [198] X. Zhao, F. Li, B. Li, T. Zhang, Q. Teng, L. Wang, H. Wang, Y. Zhang, *J. Phys. Chem. Solids* **2018**, *113*, 134-141.
- [199] X. Li, Z. Wang, B. Zhang, A. I. Rykov, M. A. Ahmed, J. Wang, *Appl. Catal. B: Environ.* **2016**, *181*, 788-799.
- [200] F. Zheng, D. Zhu, X. Shi, Q. Chen, *J. Mater. Chem. A* **2015**, *3*, 2815-2824.
- [201] L. Zhang, L. Shi, L. Huang, J. Zhang, R. Gao, D. Zhang, *ACS Catal.* **2014**, *4*, 1753-1763.
- [202] L. Hu, P. Zhang, H. Zhong, X. R. Zheng, N. Yan, Q. W. Chen, *Chem. Eur. J.* **2012**, *18*, 15049-15056.

- [203] X.-F. Wang, W. Ma, F. Jiang, E.-S. Cao, K.-M. Sun, L. Cheng, X.-Z. Song, *Chem. Eng. J.* **2018**, 338, 504-512.
- [204] H. Guo, T. Li, W. Chen, L. Liu, J. Qiao, J. Zhang, *Sci. Rep.* **2015**, 5, 13310.
- [205] J. Deng, Y.-q. Cheng, Y.-a. Lu, J. C. Crittenden, S.-q. Zhou, N.-y. Gao, J. Li, *Chem. Eng. J.* **2017**, 330, 505-517.
- [206] L. Hu, Y. Huang, Q. Chen, *J. Alloys Compd.* **2013**, 559, 57-63.
- [207] H. Yu, H. Fan, B. Yadian, H. Tan, W. Liu, H. H. Hng, Y. Huang, Q. Yan, *ACS Appl. Mater. Interfaces* **2015**, 7, 2675126757.
- [208] L. Xu, F. X. Bu, M. Hu, C. Y. Jin, D. M. Jiang, Z. J. Zhao, Q. H. Zhang, J. S. Jiang, *Chem. Commun.* **2014**, 50, 13849-13852.
- [209] H.-T. Huang, W.-L. Zhang, X.-D. Zhang, X. Guo, *Sens. Actuator B* **2018**, 265, 443-451.
- [210] X.-Z. Song, L. Qiao, K.-M. Sun, Z. Tan, W. Ma, X.-L. Kang, F.-F. Sun, T. Huang, X.-F. Wang, *Sens. Actuators B* **2018**, 256, 374-382.
- [211] X. Yang, H. Xue, Q. Yang, R. Yuan, W. Kang, C.-S. Lee, *Chem. Eng. J.* **2017**, 308, 340-346.
- [212] L. Yan, Y. Liu, K. Zha, H. Li, L. Shi, D. Zhang, *ACS Appl. Mater. Interfaces* **2017**, 9, 2581-2593.
- [213] W. Li, X. Wu, J. Chen, Y. Gong, N. Han, Y. Chen, *Sens. Actuators B* **2017**, 253, 144-155.
- [214] C. L. Wang, D. D. Wang, Y. Yang, R. Li, C. L. Chen, Q. W. Chen, *Nanoscale* **2016**, 8, 19761-19768.
- [215] H. Linrui, L. Lin, Z. Longhai, P. Gang, Y. Changzhou, Z. Xiaogang, *Adv. Funct. Mater.* **2015**, 25, 238-246.
- [216] G. Huang, L. Zhang, F. Zhang, L. Wang, *Nanoscale* **2014**, 6, 5509-5515.
- [217] X. Yang, Y.-B. Tang, X. Huang, H. T. Xue, W. P. Kang, W. Y. Li, T.-W. Ng, C.-S. Lee, *J. Power Sources* **2015**, 284, 109-114.
- [218] N. Yan, Q. W. Chen, F. Wang, Y. Wang, H. Zhong, L. Hua, *J. Mater. Chem. A* **2013**, 1, 637-643.
- [219] Z. Li, B. Li, L. Yin, Y. Qi, *ACS Appl. Mater. Interfaces* **2014**, 6, 8098-8107.

- [220] B. Rezaei, A. R. Taghipour Jahromi, A. A. Ensafi, *Electrochim. Acta* **2018**, *283*, 1359-1365.
- [221] M. B. Zakaria, T. Chikyow, *New J. Chem.* **2017**, *41*, 8196-8202.
- [222] H. Ming, B. A. Alexei, S. Hiroaki, N. Yoshihiro, I. Masataka, Y. Yusuke, *Chem. Asian J.* **2011**, *6*, 3195-3199.
- [223] M. Abirami, S. M. Hwang, J. Yang, S. T. Senthilkumar, J. Kim, W.-S. Go, B. Senthilkumar, H.-K. Song, Y. Kim, *ACS Appl. Mater. Interfaces* **2016**, *8*, 32778-32787.
- [224] S. X. Bao, N. Yan, X. H. Shi, R. Li, Q. W. Chen, *Appl. Catal. a-Gen.* **2014**, *487*, 189-194.
- [225] H. Pang, J. Deng, J. Du, S. Li, J. Li, Y. Ma, J. Zhang, J. Chen, *Dalton Trans.* **2012**, *41*, 10175-10181.
- [226] D. Q. Zhu, F. C. Zheng, S. H. Xu, Y. G. Zhang, Q. W. Chen, *Dalton Trans.* **2015**, *44*, 16946-16952.
- [227] M. B. Zakaria, M. S. A. Hossain, M. J. A. Shiddiky, S. Mohammed, Y. Ekrem, K. J. Ho, B. A. Alexei, I. Yusuke, H. Ming, T. Satoshi, Y. Yusuke, *Chem. Eur. J.* **2016**, *22*, 15042-15048.
- [228] S. Wu, X. Shen, G. Zhu, H. Zhou, Z. Ji, K. Chen, A. Yuan, *Appl. Catal. B: Environ.* **2016**, *184*, 328-336.
- [229] S. Tanaka, Y. V. Kaneti, R. Bhattacharjee, M. N. Islam, R. Nakahata, N. Abdullah, S.-i. Yusa, N.-T. Nguyen, M. J. A. Shiddiky, Y. Yamauchi, M. S. A. Hossain, *ACS Appl. Mater. Interfaces* **2018**, *10*, 1039-1049.
- [230] Y. Lü, W. Zhan, Y. He, Y. Wang, X. Kong, Q. Kuang, Z. Xie, L. Zheng, *ACS Appl. Mater. Interfaces* **2014**, *6*, 4186-4195.
- [231] X. Yin, H. Li, H. Wang, Z. Zhang, R. Yuan, J. Lu, Q. Song, J.-G. Wang, L. Zhang, Q. Fu, *ACS Appl. Mater. Interfaces* **2018**, *10*, 29496-29504.
- [232] Y. V. Kaneti, J. Tang, R. R. Salunkhe, X. Jiang, A. Yu, K. C. Wu, Y. Yamauchi, *Adv. Mater.* **2017**, *29*, 1604898.
- [233] H. Fan, H. Yu, Y. Zhang, J. Guo, Z. Wang, H. Wang, X. Hao, N. Zhao, H. Geng, Z. Dai, Q. Yan, J. Xu, *Nano Energy* **2017**, *33*, 168-176.
- [234] C. Aparicio, L. Machala, Z. Marusak, *J. Therm. Anal. Calorim.* **2012**, *110*, 661-669.

- [235] M. B. Zakaria, *RSC Adv.* **2016**, *6*, 10341-10351.
- [236] M.-S. Wu, H.-C. Shih, J.-C. Lin, *Electrochim. Acta* **2018**, *279*, 231-240.
- [237] Q. Wang, Y. Zhao, W. Luo, W. Jiang, J. Fan, L. Wang, W. Jiang, W.-x. Zhang, J. Yang, *Chem. Commun.* **2018**, *54*, 5887-5890.
- [238] C. S. Song, S. K. Wu, X. P. Shen, X. L. Miao, Z. Y. Ji, A. H. Yuan, K. Q. Xu, M. M. Liu, X. L. Xie, L. R. Kong, G. X. Zhu, S. A. Shah, *J. Colloid Interface Sci.* **2018**, *524*, 93-101.
- [239] Z. Shang, Z. Chen, Z. Zhang, J. Yu, S. Tan, F. Ciucci, Z. Shao, H. Lei, D. Chen, *J. Alloys Compd.* **2018**, *740*, 743-753.
- [240] D. W. Liu, R. Qiang, Y. C. Du, Y. Wang, C. H. Tian, X. J. Han, *J. Colloid Interface Sci.* **2018**, *514*, 10-20.
- [241] P. Jiang, J. T. Chen, C. L. Wang, K. Yang, S. P. Gong, S. Liu, Z. Y. Lin, M. S. Li, G. L. Xia, Y. Yang, J. W. Su, Q. W. Chen, *Adv. Mater.* **2018**, *30*, 1705324.
- [242] D. Chen, W. Kuang-Hsu, S. Jason, Z. Shenmin, A. Rose, W. Da-Wei, *ChemElectroChem* **2018**, *5*, 732-736.
- [243] S. Arumugam, S. Sangaraju, *ChemElectroChem* **2018**, *5*, 1937-1943.
- [244] S. Arumugam, G. Pandian, E. Luis, M. B. Peter, M. R. Kishan, S. Sangaraju, *Adv. Energy Mater.* **2018**, *8*, 1702838.
- [245] R. R. Zhang, Z. T. Sun, R. L. Feng, Z. Y. Lin, H. Z. Liu, M. S. Li, Y. Yang, R. H. Shi, W. H. Zhang, Q. W. Chen, *ACS Appl. Mater. Interfaces* **2017**, *9*, 38419-38427.
- [246] M. B. Zakaria, E. Z. M. Ebeid, M. M. Abdel-Galeil, T. Chikyow, *New J. Chem.* **2017**, *41*, 14890-14897.
- [247] Y. Yang, Z. Y. Lin, S. Q. Gao, J. W. Su, Z. Y. Lun, G. L. Xia, J. T. Chen, R. R. Zhang, Q. W. Chen, *ACS Catal.* **2017**, *7*, 469-479.
- [248] H. Wang, F. Yin, P. Lv, T. Fan, X. He, B. Chen, *Int. J. Hydrogen Energy* **2017**, *42*, 2127-2133.
- [249] L. Du, L. Luo, Z. Feng, M. Engelhard, X. Xie, B. Han, J. Sun, J. Zhang, G. Yin, C. Wang, Y. Wang, Y. Shao, *Nano Energy* **2017**, *39*, 245-252.
- [250] H. Che, Y.-S. He, X.-Z. Liao, H.-J. Zhang, W. Zhang, Z.-F. Ma, *ChemistrySelect* **2017**, *2*, 1854-1859.

- [251] M. Chen, L. Zhu, Y. Zhang, J. Zou, H. Tang, *J. Environ. Chem. Eng.* **2017**, *5*, 5322-5330.
- [252] J. T. Chen, Y. Yang, J. W. Su, P. Jiang, G. L. Xia, Q. W. Chen, *ACS Appl. Mater. Interfaces* **2017**, *9*, 3596-3601.
- [253] X. Zeng, B. Yang, L. Zhu, H. Yang, R. Yu, *RSC Adv.* **2016**, *6*, 105644-105652.
- [254] J. H. Xue, L. Zhao, Z. Y. Dou, Y. Yang, Y. Guan, Z. Zhu, L. L. Cui, *RSC Adv.* **2016**, *6*, 110820-110830.
- [255] J. Su, Y. Yang, G. Xia, J. Chen, P. Jiang, Q. Chen, *Nat. comm.* **2017**, *8*, 14969.
- [256] T. Wen, X. X. Wang, J. Wang, Z. S. Chen, J. X. Li, J. Hu, T. Hayat, A. Alsaedi, B. Grambow, X. K. Wang, *Inorg. Chem. Front.* **2016**, *3*, 1227-1235.
- [257] J. W. Su, G. L. Xia, R. Li, Y. Yang, J. T. Chen, R. H. Shi, P. Jiang, Q. W. Chen, *J. Mater. Chem. A* **2016**, *4*, 9204-9212.
- [258] M. Zeng, Y. Liu, F. Zhao, K. Nie, N. Han, X. Wang, W. Huang, X. Song, J. Zhong, Y. Li, *Adv. Funct. Mater.* **2016**, *26*, 4397-4404.
- [259] L. B. Ma, T. Chen, G. Y. Zhu, Y. Hu, H. L. Lu, R. P. Chen, J. Liang, Z. X. Tie, Z. Jin, J. Liu, *J. Mater. Chem. A* **2016**, *4*, 15041-15048.
- [260] Y. Hou, T. Huang, Z. Wen, S. Mao, S. Cui, J. Chen, *Advanced Energy Materials* **2014**, *4*, 1400337.
- [261] M. B. Zakaria, C. L. Li, Q. M. Ji, B. Jiang, S. Tominaka, Y. Ide, J. P. Hill, K. Ariga, Y. Yamauchi, *Angew. Chem. Int. Ed.* **2016**, *55*, 8426-8430.
- [262] J. Xi, Y. Xia, Y. Xu, J. Xiao, S. Wang, *Chem. Commun.* **2015**, *51*, 10479-10482.
- [263] B. K. Barman, K. K. Nanda, *Green Chem.* **2016**, *18*, 427-432.
- [264] X. Zheng, J. Deng, N. Wang, D. Deng, W.-H. Zhang, X. Bao, C. Li, *Angew. Chem. Int. Ed.* **2014**, *53*, 7023-7027.
- [265] C. Xu, Y. Jiang, J. Yang, W. Wu, X. Qian, L. Hou, *Chem. Eng. J.* **2018**, *343*, 86-94.
- [266] Z. Cao, T. Zhou, W. Xi, Y. Zhao, *Electrochim. Acta* **2018**, *263*, 576-584.
- [267] Y. Lin, Z. Qiu, D. Li, S. Ullah, Y. Hai, H. Xin, W. Liao, B. Yang, H. Fan, J. Xu, C. Zhu, *Energy Storage Mater.* **2018**, *11*, 67-74.

- [268] H. Fan, H. Yu, X. Wu, Y. Zhang, Z. Luo, H. Wang, Y. Guo, S. Madhavi, Q. Yan, *ACS Appl. Mater. Interfaces* **2016**, *8*, 25261-25267.
- [269] S. Huang, H. Wang, Y. Zhang, S. Wang, Z. Chen, Z. Hu, X. Qian, *RSC Adv.* **2018**, *8*, 5992-6000.
- [270] X.-Y. Yu, Y. Feng, Y. Jeon, B. Guan, X. W. Lou, U. Paik, *Adv. Mater.* **2016**, *28*, 9006-9011.
- [271] Y. Guo, J. Tang, Z. Wang, Y.-M. Kang, Y. Bando, Y. Yamauchi, *Nano Energy* **2018**, *47*, 494-502.
- [272] G. Chen, W. F. Dong, B. L. Li, Y. H. Deng, X. H. Wang, X. F. Zhang, H. Q. Luo, N. B. Li, *Electrochim. Acta* **2018**, *276*, 81-91.
- [273] J. Chen, S. Li, V. Kumar, P. S. Lee, *Adv. Energy Mater.* **2017**, *7*, 1700180.
- [274] S. Huang, H. Wang, S. Wang, Z. Hu, L. Zhou, Z. Chen, Y. Jiang, X. Qian, *Dalton Trans.* **2018**, *47*, 5236-5244.
- [275] Y. Jiang, X. Qian, Y. Niu, L. Shao, C. Zhu, L. Hou, *J. Power Sources* **2017**, *369*, 35-41.
- [276] X.-Y. Yu, L. Yu, H. B. Wu, X. W. Lou, *Angew. Chem.* **2015**, *127*, 5421.
- [277] Y. Fang, X.-Y. Yu, X. W. Lou, *Adv. Mater.* **2018**, *30*, 1706668.
- [278] X.-Y. Yu, Y. Feng, B. Guan, X. W. Lou, U. Paik, *Energy Environ. Sci.* **2016**, *9*, 1246-1250.
- [279] Y. V. Lim, S. Huang, Y. Zhang, D. Kong, Y. Wang, L. Guo, J. Zhang, Y. Shi, T. P. Chen, L. K. Ang, H. Y. Yang, *Energy Storage Mater.* **2018**, *15*, 98-107.
- [280] J. Tian, H. Zhu, J. Chen, X. Zheng, H. Duan, K. Pu, P. Chen, *Small* **2017**, *13*, 1700798.
- [281] N. K. A. Venugopal, S. L. Yin, Y. H. Li, H. R. Xue, Y. Xu, X. N. Li, H. J. Wang, L. Wang, *Chem. Asian J.* **2018**, *13*, 679-685.
- [282] Z. Li, L. Zhang, X. Ge, C. Li, S. Dong, C. Wang, L. Yin, *Nano Energy* **2017**, *32*, 494-502.
- [283] Y. Ge, P. Dong, S. R. Craig, P. M. Ajayan, M. Ye, J. Shen, *Adv. Energy Mater.* **2018**, *8*, 1800484.
- [284] E. Hu, J. Ning, D. Zhao, C. Xu, Y. Lin, Y. Zhong, Z. Zhang, Y. Wang, Y. Hu, *Small* **2018**, *14*, 1704233.

- [285] J. Hao, W. Yang, Z. Zhang, J. Tang, *Nanoscale* **2015**, 7, 11055-11062.
- [286] W. Yang, J. Hao, Z. Zhang, B. Zhang, *J. Colloid Interface Sci.* **2015**, 460, 55-60.
- [287] Y. Feng, X.-Y. Yu, U. Paik, *Chem. Commun.* **2016**, 52, 1633-1636.
- [288] C. Xuan, Z. Peng, K. Xia, J. Wang, W. Xiao, W. Lei, M. Gong, T. Huang, D. Wang, *Electrochim. Acta* **2017**, 258, 423-432.

Chapter 2

Two-dimensional cyano-bridged coordination polymer of $\text{Mn}(\text{H}_2\text{O})_2\text{Ni}(\text{CN})_4$]: structural analysis and proton conductivity measurements upon dehydration and rehydration

2.1. Introduction

Coordination polymers (CPs) including porous coordination polymers (PCPs) have attracted great attention because of their potentiality in advanced applications including adsorption,[1–3] separation,[4] proton conduction[5,6] and water delivery in remote areas.[7] Compared with classical solid-state materials such as oxides, the crystal structures of CPs are transformed by a weak stimulus such as a humidity difference,[8,9] adsorption of guest molecules[10,11] and pressure,[12] because of their structural flexibility. The structural flexibility originates from the flexibility of linker molecules and the existence of voids, though the coordination spheres are like those in classical solid-state materials. In addition to the two examples found in dense CPs, the structures of PCPs are widely investigated and known to respond to other stimuli, such as adsorption/desorption of molecules.[13] Upon water adsorption/ desorption, CPs tend to become amorphous, because water molecules can strongly coordinate to metal cations and then break the original coordination networks. Such changes sometimes lead to the formation of another crystal structure,[8] and the crystal structure transformation proceeds with coordination network retention but may proceed with cleavage and formation of coordination bonds.[14]

Two-dimensional (2D) materials including layered metal oxides and their nanosheets,[15] and other 2D materials such as graphene and borophane,[16–18] are widely investigated because of their unique electronic and catalytic properties.[19,20] The former materials are mostly composed of coordination spheres of transition metals and oxygen ions and their bonding is considered to be ionic, while the latter materials are composed of main group elements and their bonding is covalent. In addition to the properties associated with the atomic arrangements in the layers, these 2D materials are used as adsorbents for accommodating guest molecules in the interlayer spaces.[21–23] 2D CPs are between those categories: they contain coordination spheres of transition metals, which are linked with molecules consisting of main group elements. In hydrated 2D CPs, some of the interlayer water molecules coordinate to metal ions and others are non-coordinated ones stabilized by hydrogen bonds, and thus dehydration/rehydration may induce crystal structure transformations.[24,25]

Such properties associated with the interlayer space have been investigated well,[26–28] but the structural details of the layers of 2D CPs upon intercalation/deintercalation were less investigated.[29,30] Cyano-bridged 2D CPs are known as Hofmann-type polymers, $M^{II}X_2M^{II}(CN)_4$ [4,31] where M is a divalent transition metal (M = Mn, Fe, Co, Ni, Cu, Zn and Cd) and forms an octahedral coordination with four N atoms of the cyanide-groups and two other ligands of X (X = H₂O, NH₃ *etc.*), and M' is another divalent transition metal (M' = Ni, Pd and Pt) forming a square planar coordination with cyanide molecules.[24,32-43] Coordination bonds of cyano-groups and transition metals are generally strong like covalent bonds due to the high Lewis basicity of cyanometallates, which enables the molecule to coordinate to other metals.[44] Thus, cyano-bridged 2D CPs are expected to exhibit structural transformations upon dehydration/ rehydration without breakage of coordination networks. This feature is useful for acquiring a better understanding of the structure transformation of flexible CPs. Here I report detailed structural analysis of a 2D cyano-bridged CP, which is composed of Mn and Ni ions, by X-ray diffraction and discuss the capability for proton conduction through the water networks formed in the interlayer space on the basis of the results obtained by humidity-controlled, single-crystal proton conductivity measurements. The crystal structure of the cyano-bridged MNi system itself ($[MNi(CN)_4(H_2O)_2] \cdot 3H_2O$) (M = Mn, Co, Ni), and its transformations upon dehydration/rehydration were reported previously.[24,38,45,46] Though their phase transformations are known to occur between the L₀ phase (fully hydrated) and L₁ phase (partially dehydrated), there is still no detailed structural information on the dehydrated sample prepared from the L₀ phase. This lack of detailed information after structure transformation often happens due to the low crystallinity of the transformed structures (due to stacking faults and turbostratic stacking disorder).[47] Because the material consists of interlayer water molecules, and its networks change upon dehydration and hydration, the proton conductivity of these structures is worth measuring.

2.2. Experimental Sections

2.2.1. Synthesis

All chemicals were obtained from commercial sources and were used without further purification. Crystals of cyano-bridged CPs with Ni and Mn ions were prepared by a slow diffusion method:[48] a 20 mL small vial was placed within a 100 mL large vial. The vials were filled with an aqueous solution of 0.5 M RbCl at room temperature. 5 mL of cooled 1 M MnCl₂ (kept in an ice bath) was injected into the bottom of the small vial and 5 ml of cooled 1 M K₂ [Ni(CN)₄] was injected into the bottom of the large vial. The vials were kept at 45°C in a water bath for one week. Then, yellow crystals, which were formed on the bottom of the small vial, were recovered by filtration and washed several times with water. The chemical composition was determined by elemental analysis at the National Institute for Materials Science (NIMS) Materials Analysis Station: (found, calc'd in wt%), Mn (19.7, 17.8), Ni (21.1, 19.0) and Rb (0.00, 0.00). The Mn/Ni molar ratios are 1.00 (found) and 1.00 (calc'd), suggesting that the errors originated from the water content. The water content was determined from thermogravimetric analysis (TG-DTA) (**Figure 2-11a**). The phase purity of the sample was confirmed by powder X-ray diffraction (PXRD) using a Rigaku Ultima-III Rin 2000 diffractometer with monochromated Cu K α radiation ($\lambda = 1.5418 \text{ \AA}$) operated at 40 kV and 40 mA.

2.2.2. X-ray diffraction

The crystal structures of the as-synthesized material were determined by single-crystal X-ray diffraction (SC-XRD) using a RIGAKU Saturn CCD diffractometer equipped with a VariMax confocal optics for MoK α radiation at 293 K and 100 K. Unit cell refinements and data reduction were carried out by using the d*trek package in the CrystalClear software suite.[49] All structures were solved using a novel dual-space algorithm method (SHELXT)[50] and subsequently refined against F^2 using SHELXL[51] via the WinGX interface.[52] The structure was visualized using the VESTA program.[53] The CIF files of the structure described herein are available for the structure at 100 K (CCDC no. 1836007) and at 293 K

(CCDC no. 1855079). The structure is identical to the one reported previously (CCDC no. 278583). The hydrogen atoms in all the structures have been removed for the sake of clarity.

The crystal structures of the humidity-controlled samples were analysed using the synchrotron high-resolution powder X-ray diffraction (HR-PXRD) data collected on a two-dimensional semiconductor detector (PILATUS 100 K) ($\lambda = 0.999634 \text{ \AA}$). These synchrotron radiation experiments were performed at the BL5S2 of Aichi Synchrotron Radiation Center (AichiSR), Japan (Proposal No. 201706084 under a support of Dr. Satoshi Tominaka (NIMS, Japan)). The samples were dried overnight under vacuum at room temperature, and then exposed to nitrogen gas containing different amounts of moisture at a controlled relative humidity (RH) of 0, 40, 80 and 100% at 25°C for more than half a day. Then, the samples were sealed in Lindemann glass capillaries. The structure of the as-synthesized sample (RH=100%) and that of the fully rehydrated sample (RH=100%) were refined by the Rietveld method using the GSAS-II software [54] and the crystal structure information was obtained by SC-XRD. The structure of the sample at RH = 100 and 0% was determined by the real-space method by modifying the structure model for the single crystal of the 100% RH sample. The information is summarised in **Table 2.1**.

Table 2.1 Lattice constants obtained by the SC-XRD and PXRD data

Compound	Phase I (293 K)	Phase I (113 K)	Phase I (298 K)	Phase II (298 K)	Phase I (298 K) Rehydrated phase
Formula	MnNiC ₄ N ₄ O ₆	MnNiC ₄ N ₄ O ₆	MnNiC ₄ N ₄ O _{9.259}	MnNiC ₄ N ₄ O _{4.604}	Mn _{0.93} NiC ₄ N ₄ O _{9.373}
Space group	<i>Pnma</i>	<i>Pnma</i>	<i>Pnma</i>	<i>Imma</i>	<i>Pnma</i>
<i>a</i> (Å)	12.3058(3)	12.0750(3)	12.30625(17)	14.5229(15)	12.3066(9)
<i>b</i> (Å)	14.1261(3)	14.0779(3)	14.12662(2)	7.2962(8)	14.1272(12)
<i>c</i> (Å)	7.3105(2)	7.3144(2)	7.31004(11)	9.0371(10)	7.3101(6)
α (°)	90	90	90	90	90
β (°)	90	90	90	90	90
γ (°)	90	90	90	90	90
V (Å ³)	1270.81(5)	1243.38(5)	1270.82(4)	957.59(2)	1270.91(2)
<i>R</i> 1 (%) / <i>R</i> _{wp} (%)*	3.93	2.73	7.74	11.39	6.78

Method	SC-XRD	SC-XRD	Synchrotron HR-PXRD	Synchrotron HR-PXRD	Synchrotron HR-PXRD
--------	--------	--------	---------------------	---------------------	---------------------

2.2.3. Water adsorption/desorption isotherms

Water adsorption-desorption isotherms were collected by using a BELSORP-max-11-N-SPBI at 25°C. 5 mg of the as-synthesized compound was degassed at 150°C for 16 h before adsorption measurements. This condition can remove all the water molecules from the structure. The sample after this measurement (\sim RH = 30%, retained for a day) and the one dried at 150°C for 12 h under vacuum were analysed by PXRD using a Rigaku RINT 2500X diffractometer with Cu K α radiation. These samples were sealed by Kapton tape to avoid rehydration by air.

2.2.4. Proton conductivity measurements of single-crystal

Single-crystal proton conductivities were measured by the AC impedance method using a BioLogic MTZ-35 impedance analyser with an AC amplitude of 100 mV from 1 kHz to 1 Hz at 21°C.[8,55] The single crystal samples were mounted in a metallic cell, where Au microelectrodes[56] were placed. The contact between the crystals and Au electrodes was improved by the physical pressure induced by a spring of the metallic cell through the silicone layer of Kapton tape as reported previously.[56] The humidity in the cell was controlled by gas flow prepared by mixing humid nitrogen and dry nitrogen. The humidity of the gas was monitored using a Graphtec B-530 humidity sensor before adding the cell. The samples were kept in relative humidity (80%) at 21°C overnight for the measurement of the L₀ phase. Then, these samples were dried at 21°C, with a relative humidity of \sim 0%, overnight to measure the conductivity of phase L₁.

2.2.4. Other measurements

Fourier-transform infrared spectroscopy (FTIR) was used to investigate the chemical groups, especially the condition of CN bonds. The samples were pelletized with KBr windows, and then the spectra were collected in the range from 500 to 4000 cm⁻¹ at RT by using a Thermo Scientific Nicolet 4700. The spectrum of the as-synthesized sample has a broad absorption feature at 2125 cm⁻¹ corresponding to the C \equiv N stretching. The bands located at 3625–3250 cm⁻¹ and 1658 cm⁻¹ correspond to the presence of water molecules. Thermogravimetric

analysis/differential thermal analysis (TG-DTA) were performed simultaneously from room temperature to 600°C, using a Hitachi HT-Seiko Instrument Exter 6300 TG/DTA in air at a heating rate of 5°C min⁻¹.

2.3. Results and Discussion

View Article Online Paper The prepared samples are clear pale-yellow crystals in the size range of submillimeters to millimeters (**Figure 2-1**). The crystal structure of the as-synthesized sample, [MnNi(CN)₄(H₂O)₂] · 3H₂O, was solved and refined by SC-XRD as an orthorhombic unit cell in the *Pnma* space group with lattice constants of $a = 12.3058(3)$ Å, $b = 14.1261(3)$ Å and $c = 7.3105(2)$ Å at 293 K (this crystal structure matches the one measured at low temperature (100 K), **Table 2.1**). This structure, phase I, is similar to the one reported previously (L₀ phase),[24] though my crystal has one less water molecules probably due to partial dehydration. The structure is composed of cyano-bridged, layered CPs having alternating Mn and Ni sites (**Figure 2-2**). The Mn ions are coordinated by four N atoms of cyano groups and two water molecules to form octahedral coordination spheres. The Ni ions are coordinated by only four C atoms to form a square planar coordination environment. The cyano-groups and metal cations are in the same plane, forming the cyano-bridged layered structure, which is a typical Hofmann-type cyano-bridged coordination polymer.[57,58] The selected bond lengths and angles are summarized in **Table 2.1** These bond distances are almost consistent with those in the reported structure containing more water molecules,[24] meaning that the partial dehydration does not affect the atomic structures largely. The number of water molecules was determined by TGA (found 29.6 wt%, calc'd 32.7 wt%) and these water molecules are classified into three types: (i) two non-coordinated molecules exist in the interlayer spaces. These water molecules are stabilized in the interlayer spaces through hydrogen bonding as suggested by the broad O–H band in the FTIR spectrum (**Figure 2-3b**). This corresponds to the first weight loss in the TGA data (RT to 60°C, **Figure 2-4** found 12.0 wt%, calc'd 11.7%). (ii) Two water molecules are coordinated to Mn ions. Some of their hydrogen atoms do not form hydrogen bonding, namely are isolated, as found by the presence of sharp O–H stretching peak at 3626 cm⁻¹ in the FTIR spectrum.[59] This corresponds to the

third weight loss in the TGA data (up to 150°C; found 10.6 wt%, calc'd 14.3 wt%). (iii) One molecule might form very weak coordination or interaction to the Ni ion as Ni–O, with a distance of 2.78(9) Å (though it should be negligibly weak). This corresponds to the second weight loss in the TGA data (found 7.0 wt%, calc'd 6.7 wt%). This three-step dehydration was also reported in more hydrated crystals.[24]



Figure 2-1 Photograph of the $[\text{Mn}(\text{H}_2\text{O})_2\text{Ni}(\text{CN})_4]\cdot 3\text{H}_2\text{O}$ single crystal as-synthesis

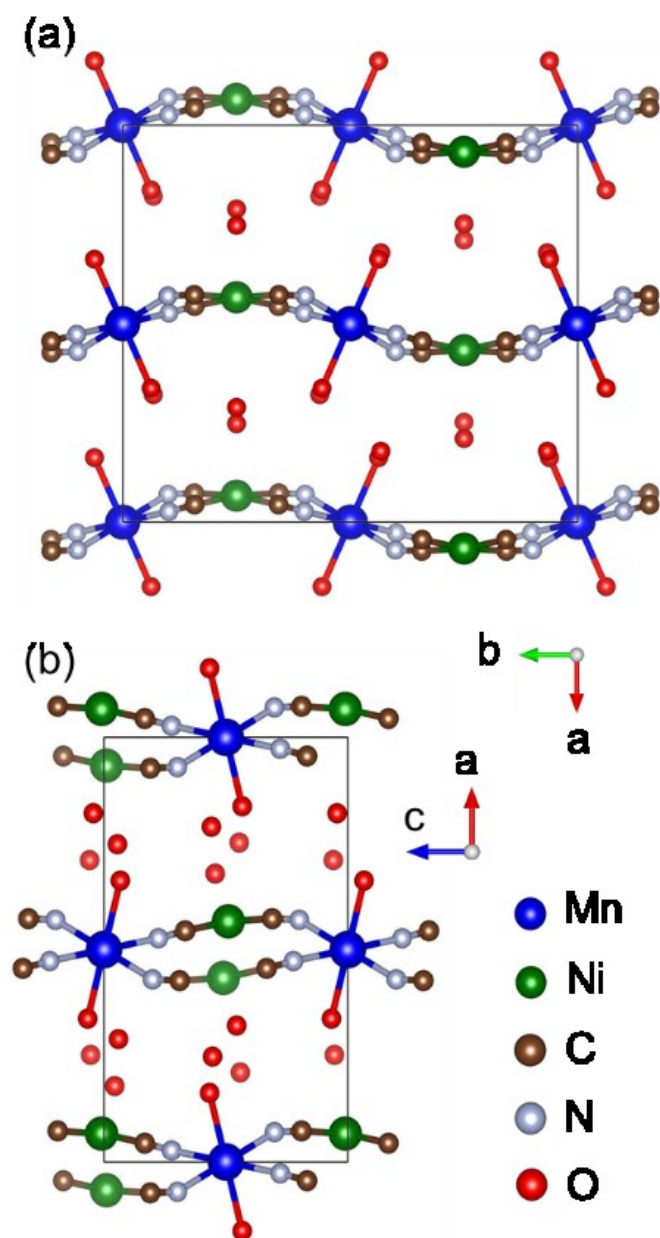


Figure 2-2 Crystal structure of the as-synthesized sample (phase I) obtained by SXRD. (a) The cyano-bridged layers seem to stack parallel to the *bc* plane from the structure model shown along the *c* axis. (b) The tilts of coordinated water molecules are opposite between adjacent layers.

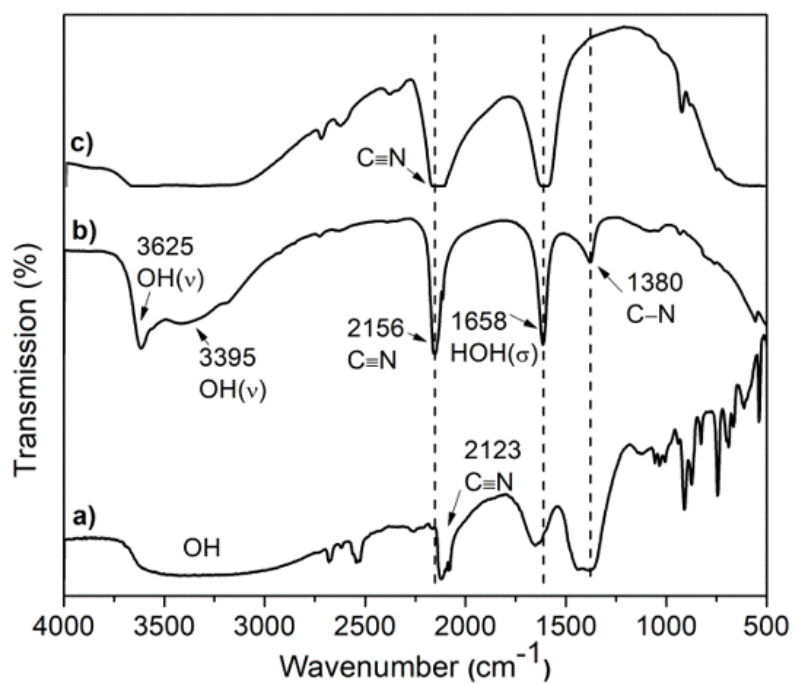


Figure 2-3 FTIR spectra of (a) $\text{K}_2(\text{Ni}(\text{CN})_4) \cdot x\text{H}_2\text{O}$, (b) $[\text{MnNi}(\text{CN})_4(\text{H}_2\text{O})_2] \cdot 3\text{H}_2\text{O}$ and (c) the dehydrated sample, RH = 0% (phase II).

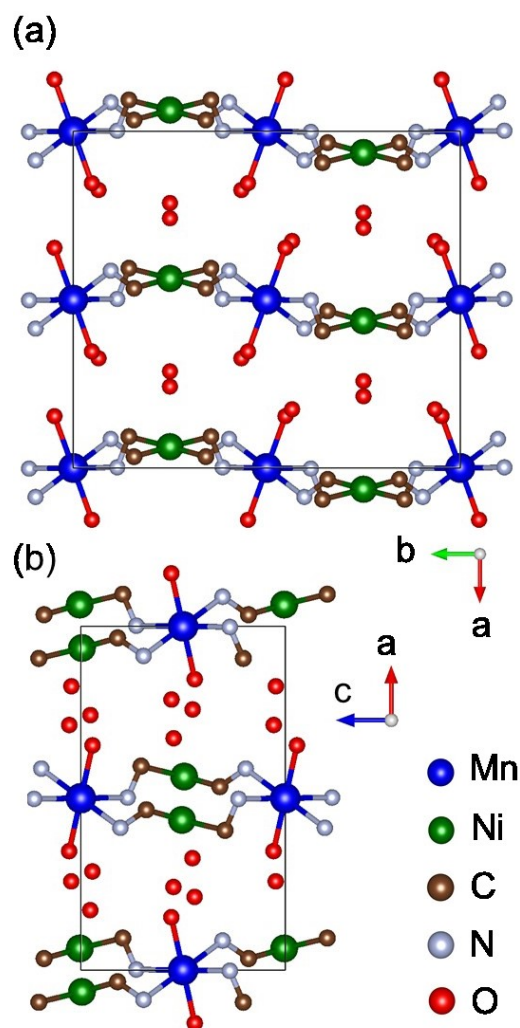


Figure 2-4 Crystal structure of phase I (HR=100%) obtained by PXRD.

From the SC-XRD result at 293 K of the as-synthesized sample, the Mn–O bonds form O–Mn–O linear coordination with a Mn–O distance of 2.2357(8) Å and an O–Mn–O angle of 180.0°. The averaged distances of Ni–C bonds and C–N bonds in the Ni(CN)₄²⁻ complex are 1.856 Å and 1.153 Å, respectively, which are in good agreement with similar complexes.[43] The C≡N–Mn angles are 176.06(6)° and 158.59(9)°, and the N≡C–Ni angles are 175.74(9)° and 177.66(10)° as shown in **Table 2.2**. The frequencies of the C–N stretching vibration in the IR spectra are known to imply the states of co-ordination environments such as the electronegativity and oxidation states of metal ions as well as coordination numbers.[58,60] As shown in **Figure 2-3b**, the ratio of C≡N to C–N stretching vibration bands in [MnNi(CN)₄(H₂O)₂]₃·3H₂O is larger than that in K₂[Ni(CN)₄] (**Figure 2-3a**), suggesting that

more electrons exist in the π -orbitals of CN molecules in the former and the Ni–N bonds are considered ionic. The sample dehydrated at room temperature does not show C–N stretching vibration bands and shows only the C \equiv N stretching, indicating the localization of electrons in CN molecules, making it more ionic than the hydrated sample.

Table 2.2 Selected bond lengths (Å) and angles (°) in phase I (determined by SC–XRD) at 293 K.

Ni–C1	1.8566(8)	Mn–N2	2.1950(8)
Ni–C2	1.8572(8)	N–C	1.1541(11)
Mn–O	2.2357(8)	N–C	1.1529(11)
Mn–N1	2.1979(8)	Ni–O	2.7823(18)
O4–Mn–O4	180.0	C2–N2–Mn	176.06(6)
N1–Mn–N2	90.87(4)	C1–Ni–C2	173.94(4)
N2–Mn–N1	89.13(4)	C2–Ni–C2	89.04(5)
O4–Mn–N2	87.78(4)	C1–Ni–C1	89.83(5)
O4–Mn–N1	87.38(3)	C1–Ni–C2	90.25(4)
O4–Mn–N1	92.62(3)	N1–C1–Ni	175.74(9)
C1–N1–Mn	158.59(9)	N2–C2–Ni	177.66(10)
C1–Ni–O	94.96(4)		

The sample can be fully dehydrated above 150°C as mentioned above, and thus the sample was dried at 150°C for 12 h. The water vapor adsorption isotherm (**Figure 2-5a**) indicates that the fully dehydrated sample adsorbs six water molecules per [MnNi(CN)₄] unit via two steps: first, an abrupt absorption of three water molecules per unit was observed in the water vapor pressure (P/P_0) range of 0.4–0.5. These water molecules are the coordinated ones and the moderately stable molecules found from the TGA data. Second, a further increase of humidity shows another adsorption of water molecules (three per unit) in the range of $P/P_0 > 0.5$, which are probably the interlayer water molecules. The number of water molecules in the fully hydrated sample is in good agreement with the previous report.[24] The desorption isotherm exhibits dehydration around $P/P_0 = 0.3$. This hysteresis suggests a structural

transformation upon humidity change. I tried to measure the desorption isotherm down to the further lower humidity range, but the measurements took a very long time probably due to the gradual release of water vapour.

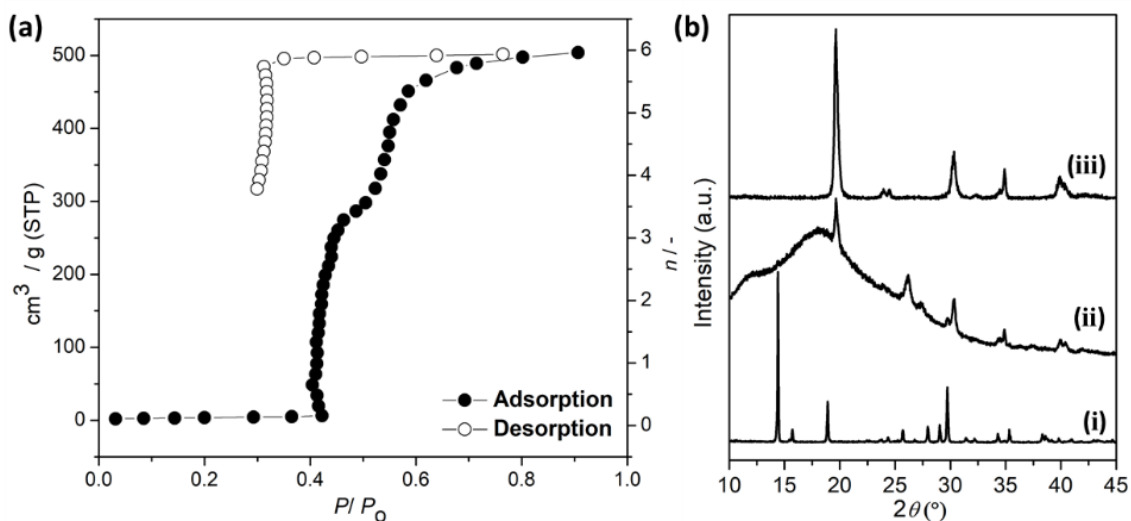


Figure 2-5 Analyses of the fully dehydrated sample. (a) Water vapour adsorption/desorption isotherm measurements at 25 °C. The vertical axis shows the number of adsorbed water molecules per formula of $\text{MnNi}(\text{CN})_4$, n . (b) PXRD patterns of (i) the as-synthesized sample, (ii) the fully dehydrated one (150 °C), and (iii) the rehydrated one (*i.e.*, the sample after the water-vapor adsorption/desorption isotherm measurement shown in panel ‘b’).

The initial full dehydration amorphized the crystalline sample as found from the diffuse scattering intensity with tiny and broad Bragg peaks in the PXRD pattern (**Figure 2-5b**). After the water vapour desorption measurement, I recovered the partially rehydrated sample, and then measured its PXRD pattern. The diffuse scattering intensity disappeared, and thus I consider that the fully-dehydrated structure is amorphous. Note that the PXRD measurements shown in **Figure 2-5a** were not humidity-controlled and thus the Bragg peaks found for the dehydrated sample are attributed to partial rehydration. Because the Bragg peaks for the rehydrated sample are not assignable to the as-synthesized phase, the structure is considered to transform into another crystal structure. For better understanding this structural transformation, I performed synchrotron HR-PXRD experiments for the samples prepared at controlled

humidity (**Figure 2-6**). The HR-PXRD patterns are constant up to RH = 80%, then the pattern for the sample rehydrated at 100% RH was consistent with that for the as-synthesized sample. The crystal structure at RH = 100% (phase I) was refined by the Rietveld method in the orthorhombic cell unit ($a = 12.30625(17)$, $b = 14.12662(2)$, and $c = 7.31004(11)$ Å, $Pnma$; $R_{wp} = 7.74\%$, goodness-of-fit (GOF) = 1.61; **Figure 2-7a** and **2-4**, **Tables 2.1** and **2.2**) with a chemical formula of $[\text{Mn}(\text{H}_2\text{O})_2\text{Ni}(\text{CN})_4] \cdot 3\text{H}_2\text{O}$. This agrees well with the one obtained by SC-XRD (as-synthesized sample), which indicates that the crystal structure of phase I did not change with grinding or milling of the crystal when the sample was prepared. One of the non-coordinated water molecules may have some interaction with Ni ions, because it forms a relatively short Ni–O distance of 2.792(11) Å around the tip position of the square pyramid coordination (C–Ni–O angle = 107.6(5)°). Because this distance is far longer than the typical distance for the coordination to Mn and Ni (*cf.* Mn–O bond = 2.2357(9) and Ni–C bond = 1.8 Å, **Table 2.3**), it may not be coordination bonding.

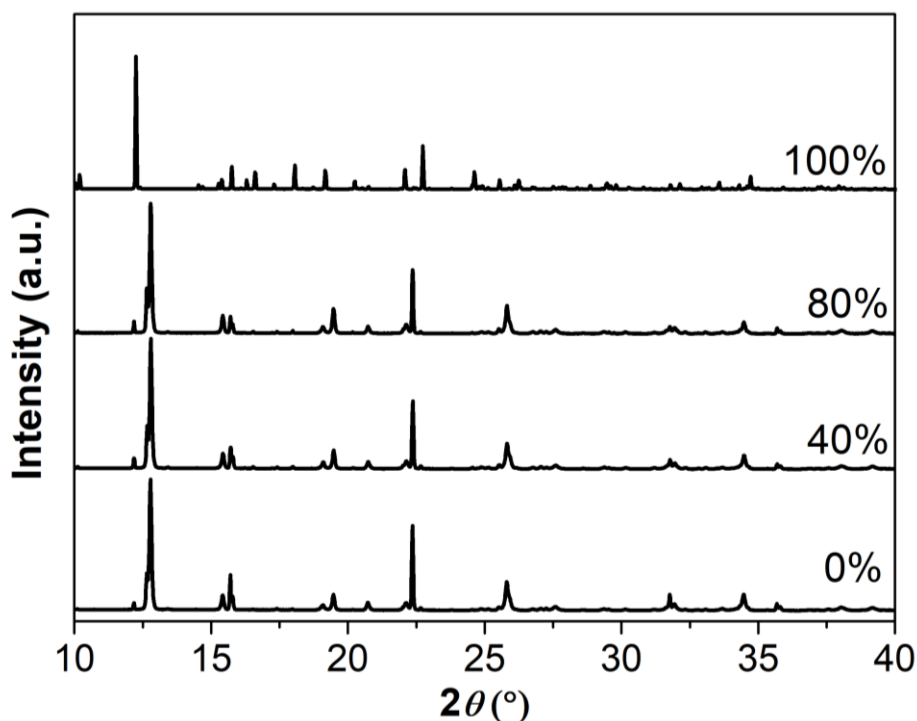


Figure 2-6 Humidity dependence of synchrotron HR-PXRD patterns ($\lambda = 0.999634$ Å).

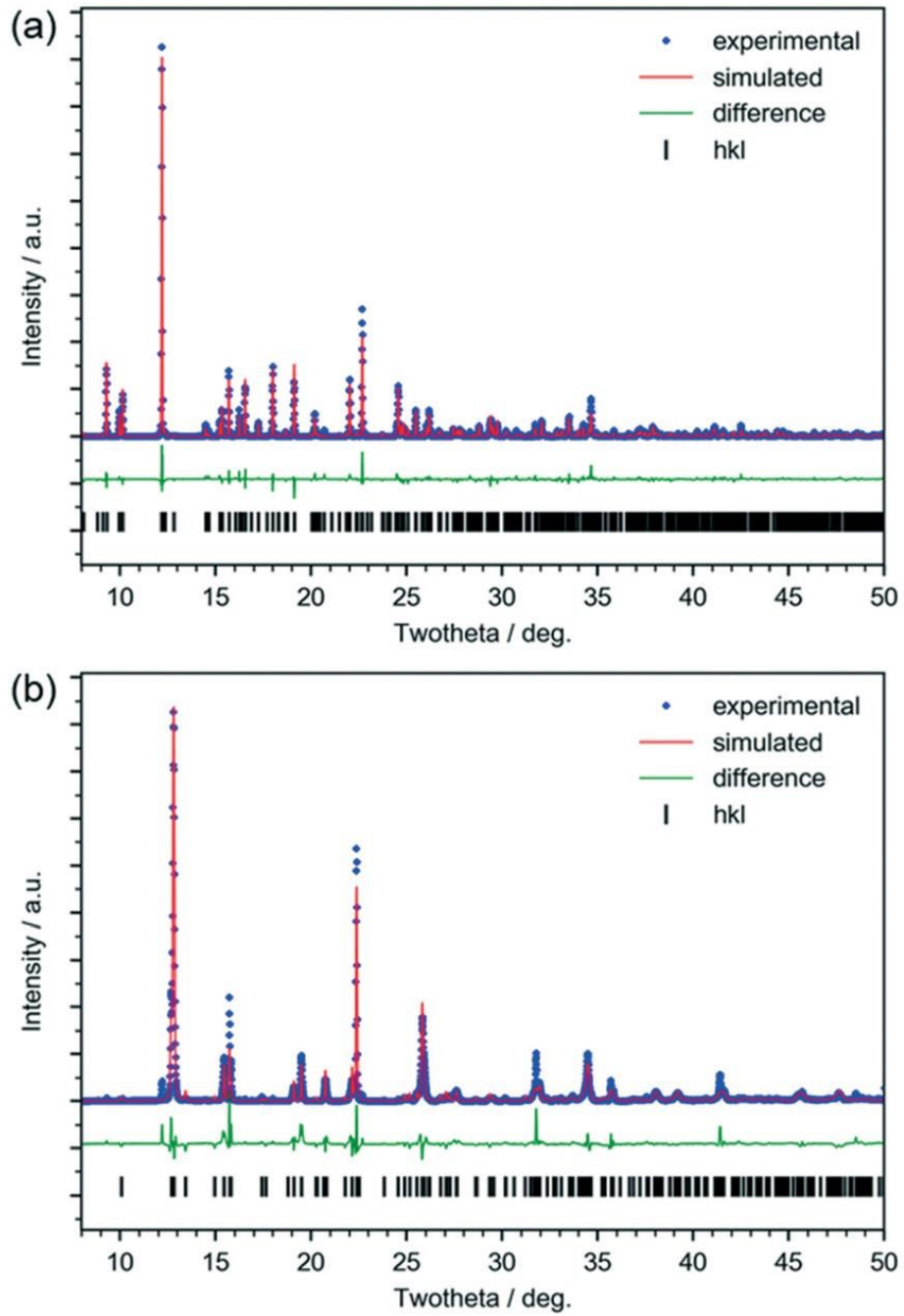


Figure 2-7 Rietveld analysis results of the synchrotron HR-PXRD patterns ($\lambda = 0.999634 \text{ \AA}$).
(a) As-synthesized sample, RH = 100% (phase I). (b) Dehydrated sample, RH = 0% (phase II).

Table 2.3 Selected bond lengths (Å) and angles (°) in phase I (determined by HR-PXRD).

Ni–C1	1.8565(9)	Mn–N2	2.1950(10)
Ni–C2	1.8573 (9)	N–C	1.307(15)
Mn–O	2.2357(9)	N–C	1.394(14)
Mn–N1	2.1980(10)	Ni–O	2.792(11)
O4–Mn–O4	180.0	C2–N2–Mn	124.5(8)
N1–Mn–N2	91.4(5)	C1–Ni–C2	177.9(6)
N1–Mn–N2	88.5(4)	C2–Ni–C2	89.1(9)
O4–Mn–N2	96.0(4)	C1–Ni–C1	86.8(7)
O4–Mn–N1	94.2(4)	C2–Ni–C1	91.9(5)
O4–Mn–N2	84.0(4)	N1–C1–Ni	109.9(9)
O4–Mn–N1	85.8(4)	N2–C2–Ni	141.5(10)
C1–N1–Mn	120.3(8)	C2–Ni–O	107.6(5)

Upon dehydration at room temperature, this structure transforms into phase II (discussed in the following paragraphs), which returns to phase I upon rehydration at ~100% humidity, that is, the transformation is reversible ($a = 12.3066(9)$ Å, $b = 14.1272(12)$ Å and $c = 7.3101(6)$ Å, **Table 2.1**, **Figure 2-8** and **2-9**). The structure of phase II (**Figure 2-10**), which was formed by keeping the as-synthesized sample under vacuum at RT (RH = 0%), was determined and refined by the Rietveld method in an orthorhombic unit cell ($a = 9.0371(10)$, $b = 14.5229(15)$, and $c = 7.2962(8)$ Å, $Pmma$; $R_{wp} = 11.39\%$, GOF = 2.30; **Figure 2-7b**) with a chemical formula of $[\text{Mn}(\text{H}_2\text{O})_2\text{Ni}(\text{CN})_4] \cdot \text{H}_2\text{O}$. The number of water molecules is consistent with the TGA result (**Figure 2-11b**). The FTIR spectrum (**Figure 2-3c**) shows the presence of hydrogen bond networks (broad O–H stretching, >2800 cm^{-1}). This composition and the diffraction pattern are consistent with those obtained for the sample obtained by rehydrating the fully dehydrated sample shown in **Figure 2-5**. The modest quality of fitting is probably due to the presence of the remaining phase I as suggested by the peak around 12° , assigned to the 002 diffractions.

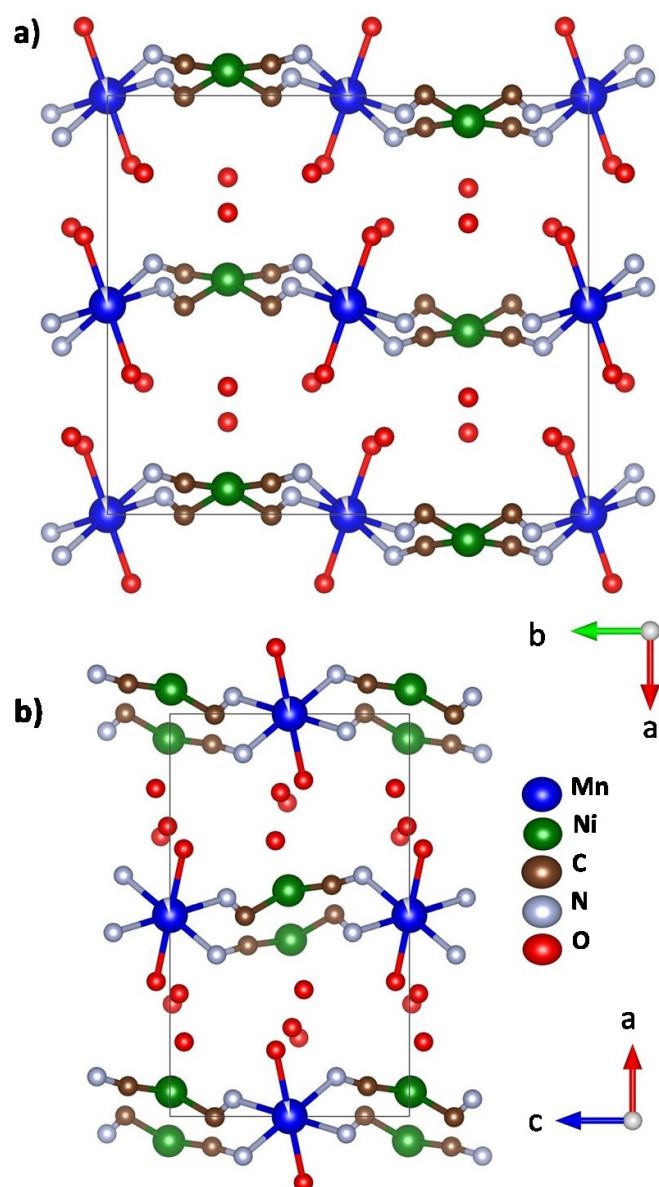


Figure 2-8 Crystal structure of re-hydrated sample (phase I) obtained by PXRD.

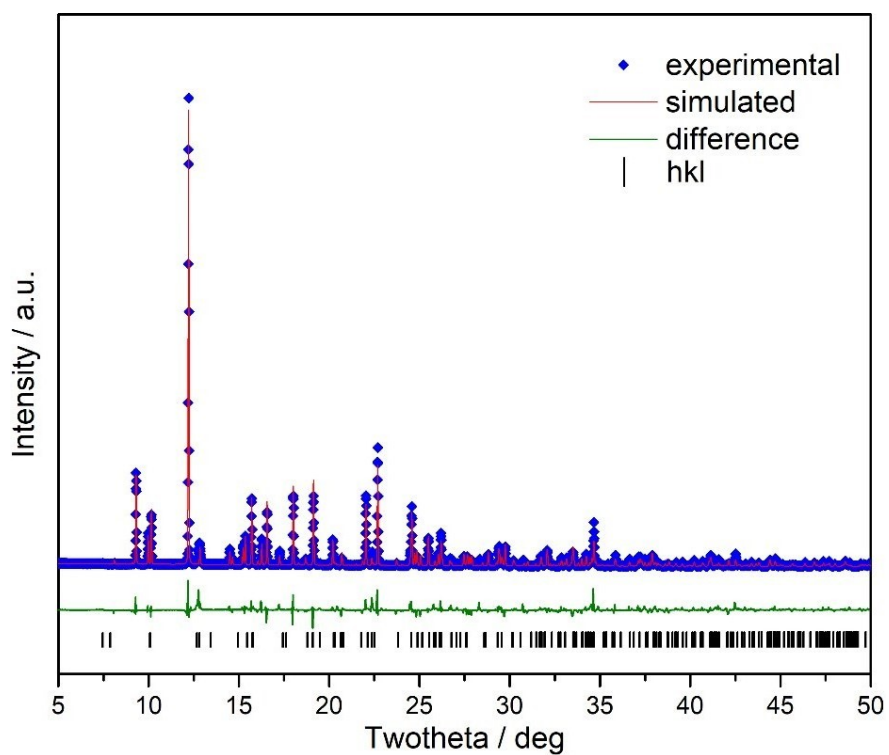


Figure 2-9 Rietveld analysis result of the PXRD patterns for rehydrated sample (RH = 100%)

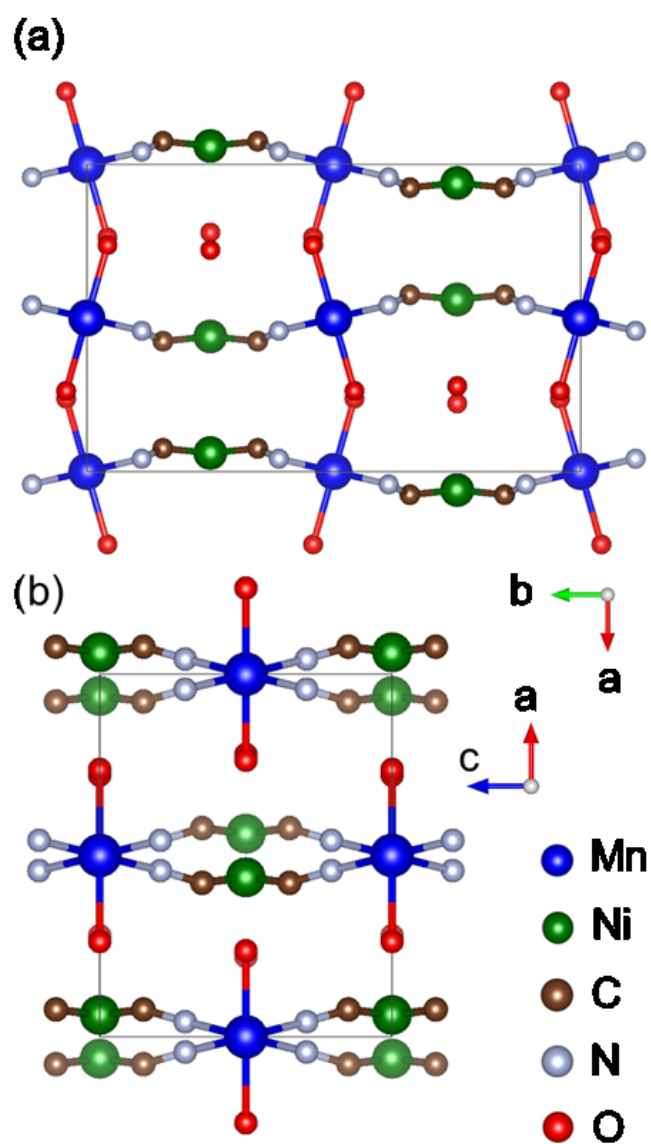


Figure 2-10 Crystal structure of the sample dehydrated at room temperature under vacuum (phase II) solved by powder diffraction data. (a) The layers do not seem to stack parallel. (b) The tilts of coordinated water molecules are apparently different from those in phase I.

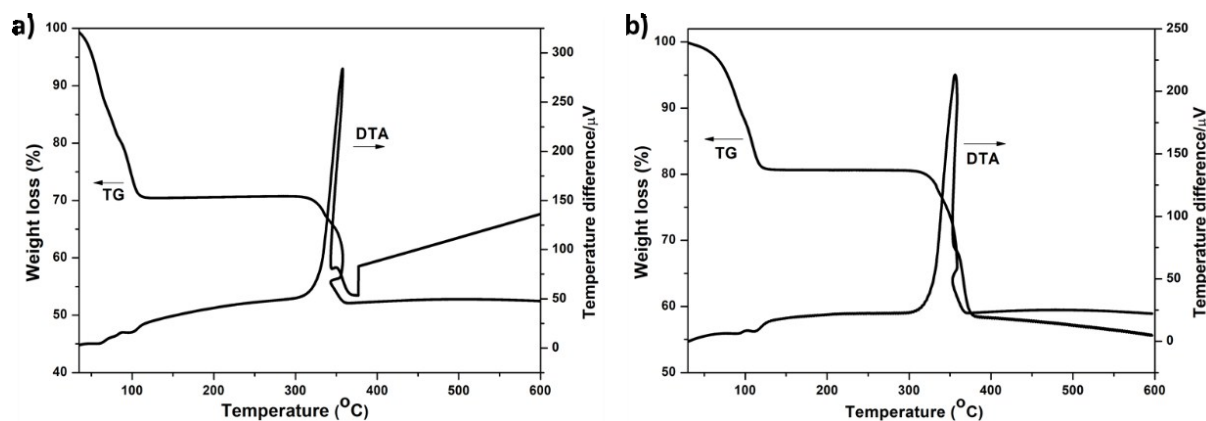


Figure 2-11 Thermogravimetric–differential thermal analysis (TG-DTA) for (a) crystal phase I and (b) crystal phase II. The data were collected in air with a scan rate of $5^{\circ}\text{C min}^{-1}$. The gradual water molecules weight losses observed below the 150°C for both phases.

The obtained structure model for phase II (**Figure 2-10**) shows that the coordination networks are retained, but their curvatures are different (*cf.* **Figure 2-12**). The coordination environments are constant (*cf.* bond length and angles in **Table 2.4**) and the coordination networks become slightly more isotropic (Mn \cdots Mn distances in phase I = 7.06331 \AA and 7.31003 \AA ; those in phase II = 7.26145 \AA and 7.29619 \AA). However, the tilts of MnO_6 octahedra are different between these phases. This is probably due to the formation of water channels in phase II, where hydrogen bonds between O atoms are formed by the presence of water molecules as $\text{Mn-O}\cdots\text{H}_2\text{O}\cdots\text{O-Mn}$ as shown in **Figure 2-12**. In phase I, the H_2O molecules form hydrogen bonding networks (**Figure 2-12a**). The Ni–O distance between the non-coordinated water molecules and the Ni ions increased up to $3.06(2)\text{ \AA}$, indicating that there is no interaction between these atoms. Thus, the non-coordinated water molecules are stabilized only by the hydrogen bonds (O \cdots O distance of $3.027(19)\text{ \AA}$). Note that the O \cdots O distances between H_2O and MnO or H_2O in phase I are shorter ($<2.9\text{ \AA}$, **Figure 2-13a**), thus hydrogen bonding in phase I is stronger than that in phase II. I conclude that the reformation of the hydrogen bonds plays a key role in the phase transition even if it is a weak interaction. This phase II is consistent with the L_1 phase, which was directly prepared and analysed

previously,[45] thus I confirmed that dehydration of the L_0 phase can form the L_1 phase though the treatment causes stacking disorder and cracks.

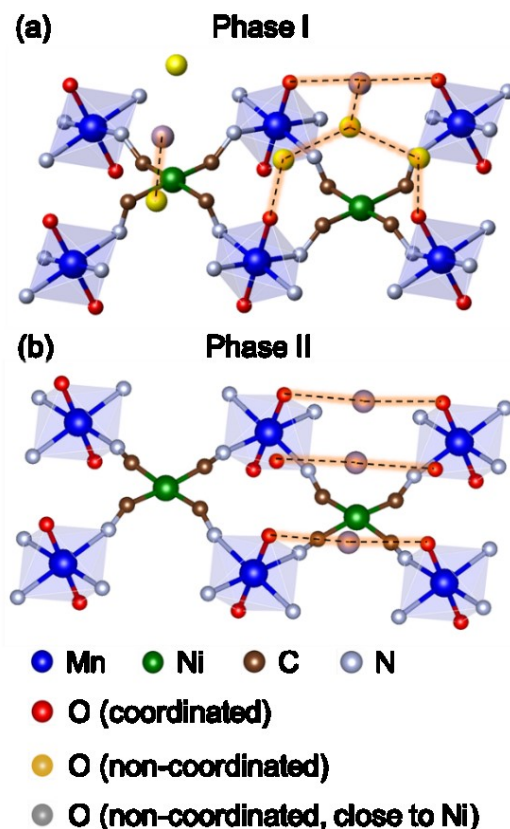


Figure 2-12 Comparison of hydrogen bonds and structures of phase I (a) and phase II (b) solved using PXRD data. The orange dotted lines illustrate hydrogen bonds of O–O distances within 3.1 Å.

Table 2.4 Selected bond lengths (Å) and angles (°) in phase II (determined by HR-PXRD).

Ni–C	1.774(18)	Mn–N	2.246(15)
Mn–O	2.229(14)	C–N	1.25(3)
Ni–O	3.06(2)	O–Mn–N	91.9(6)
O–Mn–O	180.0	C–N–Mn	163.9(14)
N–Mn–N	180.0	C–Ni–C	171.1(14)
N1–Mn–N2	84.9(8)	C1–Ni–C2	103.4(12)
N2–Mn–N2	95.1(8)	C2–Ni–C1	75.9(12)
O–Mn–N	88.1(6)	N–C–Ni	152.1(16)

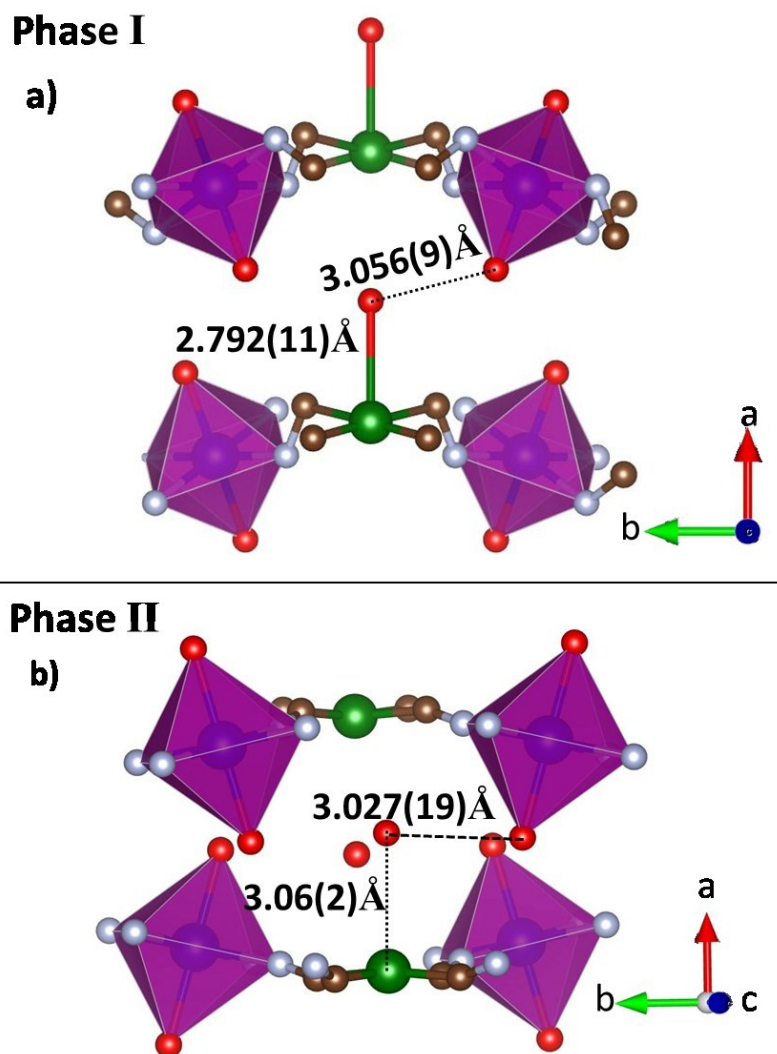


Figure 2-13 Distance between oxygen bond and Ni–O coordination bond on a) phase I and b) phase II.

As discussed above, the interlayer space contains water molecules, which form hydrogen bonding networks in particular in the L_0 phase (phase I, **Figure 2-2**). In general, hydrogen bonding networks composed of O–O distances in the range of 2.70–2.95 Å are favorable for proton conduction.[61,62] Because the L_0 phase has such paths of O–O distances of 2.8–2.86 Å along both the b axis (e.g., O1–O4–O3–O2–O1) and the c axis (e.g., O1–O2–O3–O4–O1) (**Figure 2-14**), I investigated the capability for proton conduction through the 2D networks. Note that the hydrogen bonds in the L_1 phase are segregated, and thus no proton conduction is expected. A yellow crystal with a 1 mm width, a 2.5 mm length and a 0.5 mm thickness was mounted on two Au microelectrodes having an 80 μm gap (**Figure 2-15**). The

impedance data (**Figure 2-16**) show phase shifts of ca. -90° in the frequency range from 100 kHz to 1 Hz at both relative humidities of 80% and 1.4%, meaning that both L_0 and L_1 phases are insulating. In particular, the spectra are consistent with that for the microelectrode cell without samples, and thus I consider that their dielectric constants are too small to be measured by the system. Thus, the water molecules in the interlayer spaces, even though some of them coordinate to the Mn ions, do not dissociate into protons. This fact in turn suggests that the interlayer spaces of 2D cyano-bridged coordination polymers are non-ionic.

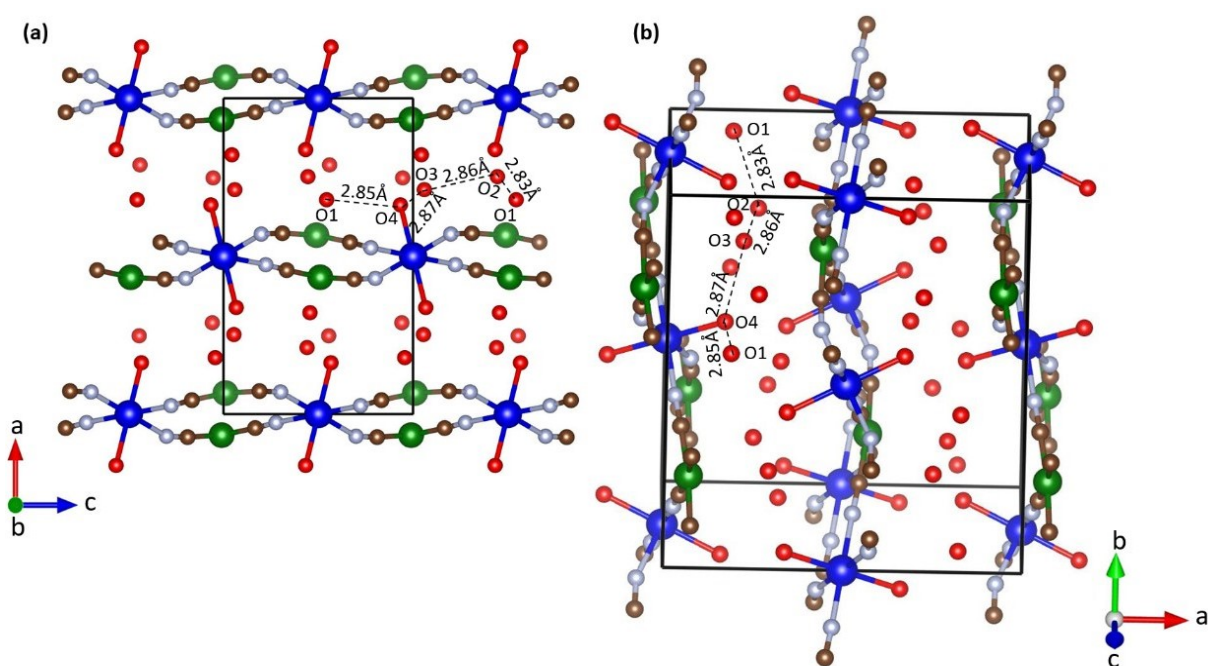


Figure 2-14 Hydrogen bonding network and O–O distances in phase I.

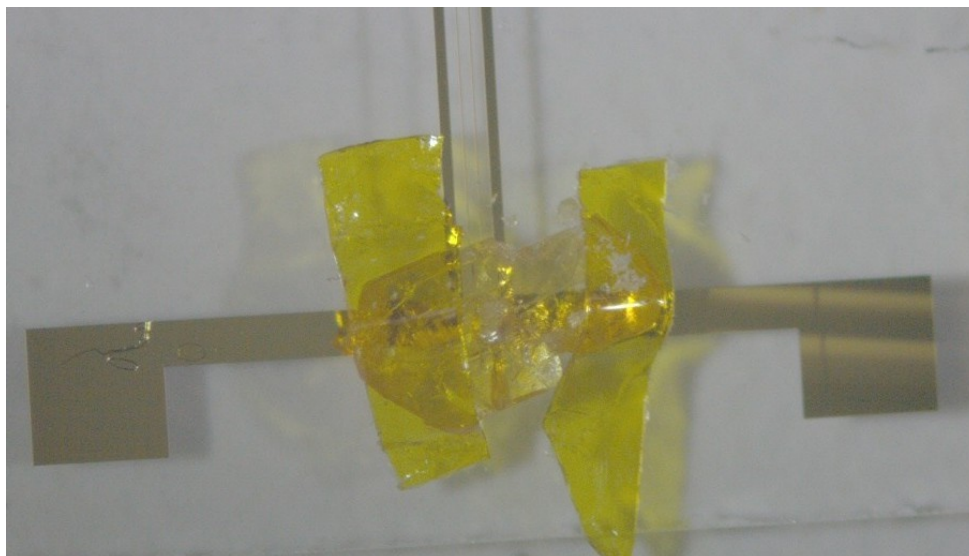


Figure 2-15 Photograph of the microelectrodes for the single-crystal impedance measurement. A crystal (1 mm wide x 0.5 mm thick) was contacted with microelectrodes having a 80 mm gap using a Kapton tape.

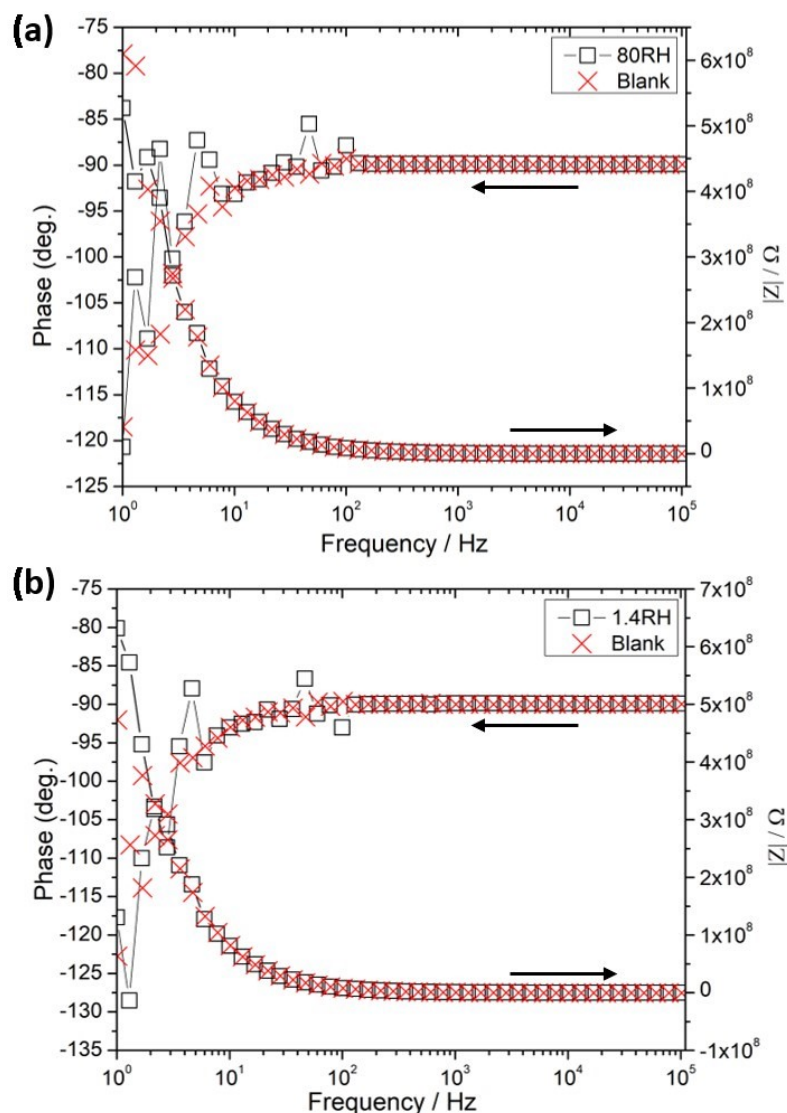


Figure 2-16 Bode plots of impedance data for a $\text{Mn}(\text{H}_2\text{O})_2[\text{Ni}(\text{CN})_4]$ single crystal measured at (a) RH= 80% and (b) 1.4%.

2.4. Conclusion

Through detailed structural analysis, I found that the as-synthesized crystals of $[\text{Mn}(\text{H}_2\text{O})_2\text{Ni}(\text{CN})_4] \cdot 3\text{H}_2\text{O}$ transformed into another crystalline phase $[\text{Mn}(\text{H}_2\text{O})_2\text{Ni}(\text{CN})_4] \cdot \text{H}_2\text{O}$ upon dehydration via a topotactic route. The structure of the framework itself changes as the tilt of MnO_6 octahedra changes in response to the change in hydrogen bonds between these water molecules though the two-dimensional cyano-bridged networks are retained. The water molecules, in particular the hydrogen bonds, play a key role in the structure transformation upon dehydration/hydration in the 2D cyano-bridged CPs, that

is, such frameworks are flexible enough to respond to humidity. I investigated the capability for proton conduction through the hydrogen bonding networks using single crystals, but they were found to be insulating. This information may be useful for the applications of these cyano-bridged CPs in adsorption and solid- state ionics.

References

- [1] M. Eddaoudi, J. Kim, N. Rosi, D. Vodak, J. Wachter, M. O. Keefte, O. M. Yaghi, M. Eddaoudi, J. Kimrn, N. Rosi, O. M. Yaghi, *Science* **2002**, *295*, 469-472.
- [2] J. Gao, X. Zhang, S. Xu, F. Tan, X. Li, Y. Zhang, Z. Qu, X. Quan, J. Liu, *Chemistry - A European Journal* **2014**, *20*, 1957-1963.
- [3] O. M. Yaghi, G. Li, H. Li, *Nature* **1995**, *378*, 703-706.
- [4] L. Boudjema, E. Mamontova, J. Long, J. Larionova, Y. Guari, P. Trens, *Inorganic Chemistry* **2017**, *56*, 7598-7601.
- [5] H. T. Shin-ichi Ohkoshi, Kosuke Nakagawa, Keisuke Tomono, Kenta Imoto, Yoshihide Tsunobuchi, *ournal of the American Chemical Society* **2010**, *132*, 6620-6621.
- [6] K. Imoto, K. Nakagawa, H. Miyahara, S. I. Ohkoshi, *Super-ionic conductive magnet based on a cyano-bridged Mn-Nb bimetal assembly*, **2013**,*13*, 4673-4677.
- [7] H. Furukawa, F. Gándara, Y.-B. Zhang, J. Jiang, W. L. Queen, M. R. Hudson, O. M. Yaghi, *Journal of the American Chemical Society* **2014**, *136*, 4369-4381.
- [8] T. D. Dao, T. Nagao, A. K. Cheetham, *Journal of the American Chemical Society* **2014**, *137*, 3-6.
- [9] M. Ohtani, K. Takase, P. Wang, K. Higashi, K. Ueno, N. Yasuda, K. Sugimoto, M. Furuta, K. Kobiro, *CrystEngComm* **2016**, *18*, 1866-1870.
- [10] Y. Yue, J. A. Rabone, H. Liu, S. M. Mahurin, M. R. Li, H. Wang, Z. Lu, B. Chen, J. Wang, Y. Fang, S. Dai, *Journal of Physical Chemistry C* **2015**, *119*, 9442-9449.
- [11] M. J. Kalmutzki, C. S. Diercks, O. M. Yaghi, *Advanced Materials* **2018**, *30*, 1704304
- [12] E. C. Spencer, M. S. R. N. Kiran, W. Li, U. Ramamurty, N. L. Ross, A. K. Cheetham, *Angewandte Chemie - International Edition* **2014**, *53*, 5583-5586.

- [13] C. Serre, C. Mellot-Draznieks, S. Surblé, N. Audebrand, Y. Filinchuk, G. Férey, *Science* **2007**, *315*, 1828-1831.
- [14] J. Ariñez-Soriano, J. Albalad, C. Vila-Parrondo, J. Pérez-Carvajal, S. Rodríguez-Hermida, A. Cabeza, J. Juanhuix, I. Imaz, D. MasPOCH, *Chemical Communications* **2016**, *52*, 7229-7232.
- [15] M. Osada, T. Sasaki, *Journal of Materials Chemistry* **2009**, *19*, 2503-2511.
- [16] J. C. Meyer, A. K. Geim, M. I. Katsnelson, K. S. Novoselov, T. J. Booth, S. Roth, *Nature* **2007**, *446*, 60-63.
- [17] H. Nishino, T. Fujita, N. T. Cuong, S. Tominaka, M. Miyauchi, S. Iimura, A. Hirata, N. Umezawa, S. Okada, E. Nishibori, A. Fujino, T. Fujimori, S. Ito, J. Nakamura, H. Hosono, T. Kondo, *Journal of the American Chemical Society* **2017**, *139*, 13761-13769.
- [18] K. Sakaushi, A. Lyalin, S. Tominaka, T. Taketsugu, K. Uosaki, *ACS Nano* **2017**, *11*, 1770-1779.
- [19] X. Huang, Z. Yin, S. Wu, X. Qi, Q. He, Q. Zhang, Q. Yan, F. Boey, H. Zhang, *Small* **2011**, *7*, 1876-1902
- [20] X. Huang, X. Qi, F. Boey, H. Zhang, *Chem. Soc. Rev.* **2012**, *41*, 666-686.
- [21] G. Massasso, J. Long, C. Guerin, A. Grandjean, B. Onida, Y. Guari, J. Larionova, G. Maurin, S. Devautour-Vinot, *Journal of Physical Chemistry C* **2015**, *119*, 9395-9401.
- [22] D. Sangian, Y. Ide, Y. Bando, A. E. Rowan, Y. Yamauchi, *Small* **2018**, *14*, 1800551-1800564.
- [23] N. Takahashi, K. Kuroda, *Journal of Materials Chemistry* **2011**, *21*, 14336-14353.
- [24] A. Ray, I. Bhowmick, W. S. Sheldrick, A. D. Jana, M. Ali, *Journal of Solid State Chemistry* **2009**, *182*, 2608-2612.
- [25] M. Sadakiyo, T. Yamada, K. Honda, H. Matsui, H. Kitagawa, *Journal of the American Chemical Society* **2014**, *136*, 7701-7707.
- [26] S. Y. Ke, C. C. Wang, *CrystEngComm* **2015**, *17*, 8776-8785.
- [27] W. W. He, S. L. Li, Y. Q. Lan, *Inorganic Chemistry Frontiers* **2018**, *5*, 279-300.
- [28] J. H. Lee, S. Park, S. Jeoung, H. R. Moon, *CrystEngComm* **2017**, *19*, 3719-3722.
- [29] I. Kalf, P. Mathieu, U. Englert, *New Journal of Chemistry* **2010**, *34*, 2491-2495.

- [30] J. Canivet, A. Fateeva, Y. Guo, B. Coasne, D. Farrusseng, *Chem. Soc. Rev.* **2014**, *43*, 5594-5617.
- [31] F. L. Liu, J. Tao, *Chemistry - A European Journal* **2017**, *23*, 18252-18257.
- [32] T. Iwamoto, T. Nakano, M. Morita, T. Miyoshi, T. Miyamoto, Y. Sasaki, *Inorganica Chimica Acta* **1968**, *2*, 313-316.
- [33] W. Lin, W. J. Rieter, K. M. L. Taylor, *Angewandte Chemie International Edition* **2009**, *48*, 650-658.
- [34] M. B. Zakaria, M. Hu, R. R. Salunkhe, M. Pramanik, K. Takai, V. Malgras, S. Choi, S. X. Dou, J. H. Kim, M. Imura, S. Ishihara, Y. Yamauchi, *Chemistry - A European Journal* **2015**, *21*, 3605-3612.
- [35] S. Akyüz, A. B. Dempster, R. L. Morehouse, *Spectrochimica Acta* **1989**, *120*, 1989-2004.
- [36] W. K. Ham, T. J. R. Weakley, C. J. Page, *Journal of Solid State Chemistry* **1993**, *107*, 101-107.
- [37] Y. L. Qin, B. W. Yang, G. F. Wang, H. Sun, *Acta Crystallographica Section C: Structural Chemistry* **2016**, *72*, 555-560.
- [38] J. Rodríguez-Hernández, A. A. Lemus-Santana, C. N. Vargas, E. Reguera, *Comptes Rendus Chimie* **2012**, *15*, 350-355.
- [39] N. J. Robertson, Z. Qin, G. C. Dallinger, E. B. Lobkovsky, S. Lee, G. W. Coates, *Dalton Transactions* **2006**, 5390-5395.
- [40] E. Kasap, S. Özcelik, *Journal of Inclusion Phenomena and Molecular Recognition in Chemistry* **1997**, *28*, 259-267.
- [41] T. Niu, G. Crisci, J. Lu, A. J. Jacobson, *Acta Crystallographica Section C: Crystal Structure Communications* **1998**, *54*, 565-567.
- [42] S. Akyüz, A. B. Dempster, R. L. Morehouse, *Spectrochimica Acta Part A: Molecular Spectroscopy* **1974**, *30*, 1989-2004.
- [43] R. Vafazadeh, A. Dehghani-Firouzabadi, A. C. Willis, *Acta Chimica Slovenica* **2017**, 686-691.
- [44] A. G. Sharpe, *The Chemistry of Cyano Complexes of the Transition Metals*, **1976**.

- [45] O. Reyes-Martinez, E. Torres-García, G. Rodríguez-Gattorno, E. Reguera, *Materials* **2013**, *6*, 1452-1466.
- [46] Y. Mathey, C. Mazieres, *Canadian Journal of Chemistry* **1974**, *52*, 3637-3644.
- [47] A. J. Fletcher, K. M. Thomas, M. J. Rosseinsky, *Journal of Solid State Chemistry* **2005**, *178*, 2491-2510.
- [48] W. Dong, L.-N. Zhu, H.-B. Song, D.-Z. Liao, Z.-H. Jiang, S.-P. Yan, P. Cheng, S. Gao, *Inorganic Chemistry* **2004**, *43*, 2465-2467.
- [49] Rigaku Corporation, *CrystalClear*, Tokyo, Japan, **2005**.
- [50] G. M. Sheldrick, *Acta Crystallographica Section A Foundations and Advances* **2015**, *71*, 3-8.
- [51] G. M. Sheldrick, *Acta Crystallographica Section C: Structural Chemistry* **2015**, *71*, 3-8.
- [52] L. J. Farrugia, *J. Appl. Cryst.* **2012**, *45*, 849.
- [53] K. Momma, F. Izumi, *Journal of Applied Crystallography* **2011**, *44*, 1272-1276.
- [54] B. H. Toby, R. B. Von Dreele, *Journal of Applied Crystallography* **2013**, *46*, 544-549.
- [55] S. Tominaka, A. K. Cheetham, *RSC Advances* **2014**, *4*, 54382-54387.
- [56] S. Tominaka, S. Henke, A. K. Cheetham, *Crystengcomm* **2013**, *15*, 9400-9407.
- [57] Z. Kartal, A. Ölmez, *Zeitschrift fur Naturforschung - Section A Journal of Physical Sciences* **2005**, *60*, 537-540.
- [58] D. Türköz, Z. Kartal, S. Bahçeli, *Zeitschrift fur Naturforschung - Section A Journal of Physical Sciences* **2004**, *59*, 523-526.
- [59] A. Novak, in *Large Molecules*, Springer, **1974**, pp. 177-216.
- [60] Z. Kartal, D. Türközy, S. Bahçeli, *Acta Physica Slovaca* **2004**, *54*, 97-103.
- [61] P. Colomban, *Proton conductors: Solids, membranes, and gels-materials and devices.*, **1992**.
- [62] S. Tominaka, T. Cheetham, A. K. Cheetham, *RSC Adv.* **2014**, *4*, 54382-54387.

2.5. Appendix

The proton conductivity of single crystal $[\text{Mn}(\text{H}_2\text{O})_2\text{Ni}(\text{CN})_4]\cdot 4\text{H}_2\text{O}$ was measured by two ways. The first method was by keeping the single crystal phase I at the desired relative humidity (RH) (80 and 1.4%) for overnight at 21°C before measurement. The results of the impedance data showed that the resistance values of both samples were almost the same as the blank cell value. The proton conductivity values at RH 80% and RH 1.4% were $1.89 \times 10^{-11} \text{ S}\cdot\text{cm}^{-1}$ and $1.58 \times 10^{-11} \text{ S}\cdot\text{cm}^{-1}$, respectively, which indicated that the samples are insulators.[1] The other method was by measuring the crystal under different humidity ratio starting from phase I (RH 100 to 40%). **Figure 2-17** shows that the conductivity value was $2.08 \times 10^{-7} \text{ S}\cdot\text{cm}^{-1}$ at RH 95%, and this value started to decrease with decreasing the humidity ($1.28 \times 10^{-13} \text{ S}\cdot\text{cm}^{-1}$ for RH 40%), which was typical of dehydrated samples,[2,3] indicating the humidity played key roles in the proton transport.[4] Compared to other cyano-bridged coordination polymers (CPs) (**Table 2.5**), my sample showed lower conductivity, but comparable conductivity to classic solid-state conductors (10^{-3} to $10^{-8} \text{ S}\cdot\text{cm}^{-1}$).[5] It is very interesting to note that the conductivity at RH 80% in both ways was judged to be insulator. This indicates that the structure at RH 80% was not fully dehydrated. As the humidity ratio is increased, water started to be expelled from the structure and the conductivity rapidly decreased due to the decrease in the water hydrogen-bonding network. The high-resolution powder X-ray diffraction (HR-PXRD) (**Figure 2-18**) of the sample obtained at RH 80% showed a different phase to that obtained at RH 100%, but almost similar to that achieved at low RH (*e.g.*, 0%), in which the phase transformation could be clearly identified.

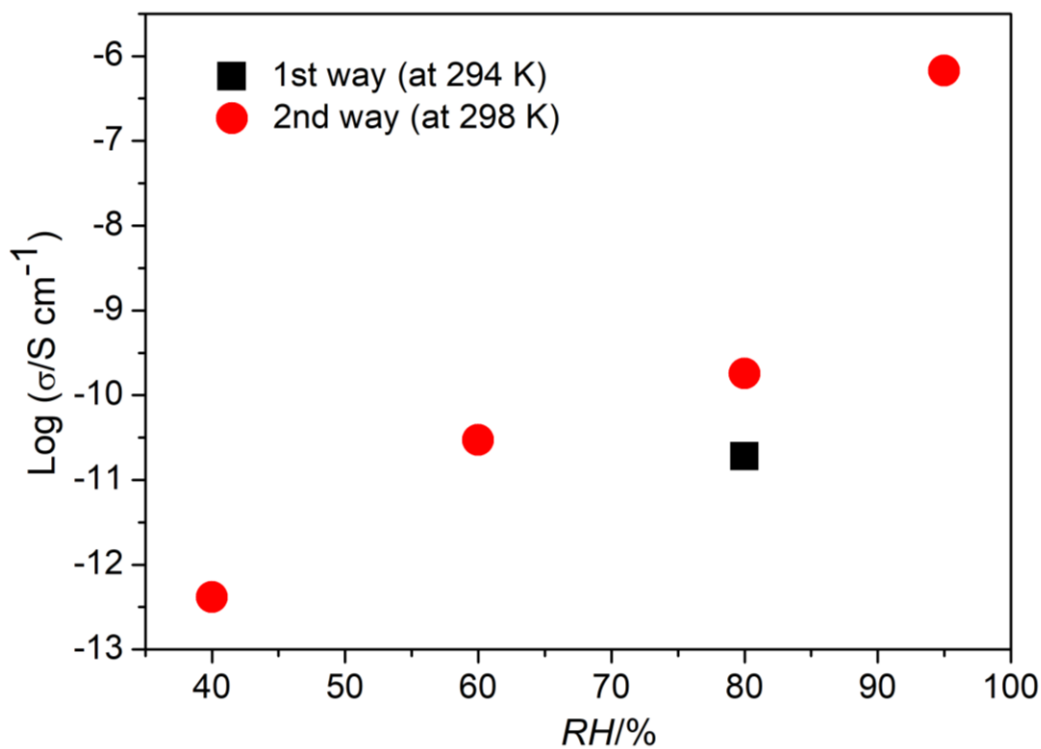


Figure 2-17 Plot of σ vs relative humidity for single crystal $[\text{Mn}(\text{H}_2\text{O})_2\text{Ni}(\text{CN})_4] \cdot x\text{H}_2\text{O}$

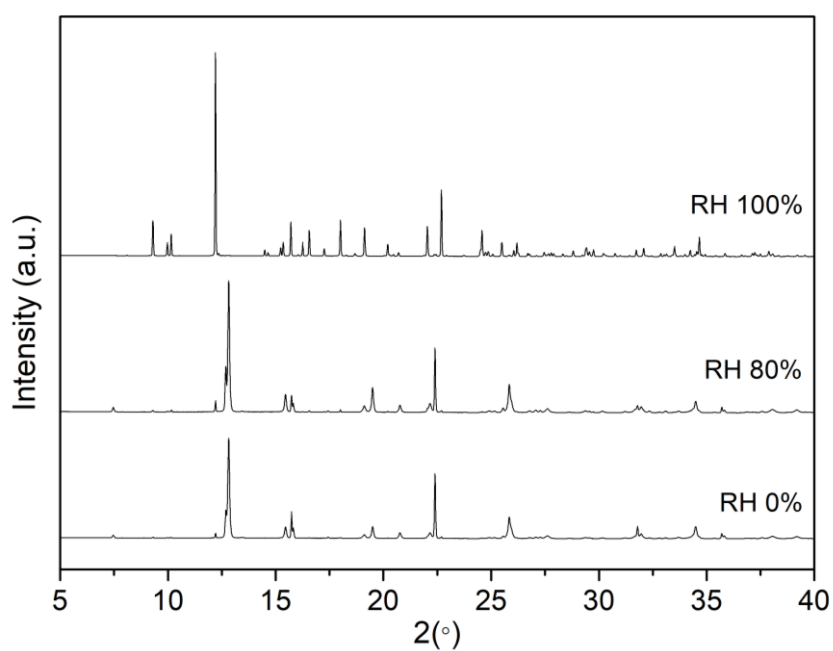


Figure 2-18 HR-XRD patterns of single crystal $[\text{Mn}(\text{H}_2\text{O})_2\text{Ni}(\text{CN})_4] \cdot x\text{H}_2\text{O}$ at different humidity ratio

Table 2.5 The comparing to other cyano-bridged coordination polymer materials.

Sample	Method	Condition	Proton conductive (S.cm ⁻¹)	Reference
[Mn(H ₂ O) ₂ Ni(CN) ₄].3H ₂ O	Changing in humidity ratio	RH 95%	2.1x10 ⁻⁷	Present work
		RH 80%	1.9x10 ⁻¹¹ 5.6x10 ⁻¹¹	
Li ₃ Fe(CN) ₆	-	Anhydrous	<10 ⁻¹¹	[3]
Li ₃ Fe(CN) ₆	High pressure	~5 GPa	Above 10 ⁻³	[6]
Mn ^{II} ₃ [Nb ^{IV} (CN) ₈] ₂ (4-NH ₂ py) ₁₀ (4-NH ₂ pyH ⁺) ₂ .12H ₂ O	Changing in temperature and humidity ratio	At 295 K RH 100%	1.0x10 ⁻⁴	[4]
		At 322 K RH 100%	4.6x10 ⁻⁴	
		At 300 K RH 45%	3.2x10 ⁻⁸	
Co[Cr(CN) ₆] _{2/3} .zH ₂ O	Changing in temperature and humidity ratio	At 293 K RH 100%	1.2x10 ⁻³	[7]
		At 308 K RH 100%	1.7x10 ⁻³	
At 293 K RH 8%		3.2x10 ⁻⁸		
V ^{II} [Cr ^{III} (CN) ₆] _{2/3} .zH ₂ O		At 293 K RH 100%	1.6x10 ⁻³	
		At 323 K RH 100%	2.6x10 ⁻³	
Fe ₄ [Fe(CN) ₆] ₃ .14H ₂ O	-	At 300 K	5.57x10 ⁻⁵	[8]
Fe ₄ [Ru(CN) ₆] ₃ .18H ₂ O			5.05x10 ⁻⁶	
K _{1.2} Ru _{3.6} [Ru(CN) ₆] ₃ .16H ₂ O			5.69x10 ⁻³	

References

- [1] S. Tominaka, T. Cheetham, A. K. Cheetham, *RSC Adv.* **2014**, *4*, 54382-54387.
- [2] S. Pili, S. P. Argent, C. G. Morris, P. Rought, V. Garcia-Sakai, Ian P. Silverwood, Timothy L. Easun, M. Li, Mark R. Warren, Claire A. Murray, Chiu C. Tang, S. Yang, M. Schroder, *J. Am. Chem.* **2016**, *138*, 6352-6355.
- [3] K. Tennakone, P. de, *physica status solidi (a)* **1984**.
- [4] K. Imoto, K. Nakagawa, H. Miyahara, S. Ohkoshi, *Crystal Growth & Design* **2013**, *13*, 4673-4677.
- [5] S. Tominaka, S. Henke, A. K. Cheetham, *CrystEngComm* **2013**, *15*, 9400-9407.

- [6] K. Li, H. Zheng, T. Hattori, A. Sano-Furukawa, C. A. Tulk, J. Molaison, M. Feygenson, I. N. Ivanov, W. Yang, H. K. Mao, *Inorganic Chemistry* **2015**, *54*, 11276-11282.
- [7] H. T. Shin-ichi Ohkoshi, Kosuke Nakagawa, Keisuke Tomono, Kenta Imoto, Yoshihide Tsunobuchi, *ournal of the American Chemical Society* **2010**, *132*, 6620-6621.
- [8] J. N. Behera, D. M. D. Alessandro, N. Soheilnia, J. R. Long, V. Di, L. Berkeley, B. California, *Chem. Mater* **2009**, *21*, 1922-1926.

Chapter 3

Single Crystal Growth of Two-Dimensional Cyano-Bridged Coordination Polymer of $[\text{Co}(\text{H}_2\text{O})_2\text{Ni}(\text{CN})_4] \cdot 4\text{H}_2\text{O}$ Using Trisodium Citrate Dihydrate

3.1. Introduction

Recently, coordination polymers (CPs) including porous coordination polymers (PCPs), metal-organic frameworks (MOFs) and Prussian blue (PB) have received much attention due to their high adsorption capacities and molecular recognition abilities by tuning the pore size and structure.[1,2] Furthermore, these materials have found applications in gas storage and separation, adsorption, sensors, catalysis, magnetism, proton conduction, drug delivery systems, have been extensively studied.[1,2] Two-dimensional (2D) structures are very interesting because they exhibit many unique physical and chemical properties that are not observable in bulk materials.[3-5] The interlayer spaces of 2D structures permit guest molecules to effectively enter the micropores in the CPs. It is known that 2D cyano-bridged CPs have a Hoffman type complexes with general formula $[M'L_2M(CN)_4]$, where M^{II} and M^{II} are transition metals. This structure is made up of square planar transition metal centers surrounded by C-bound cyanide ligands, which are assembled by M^{II} atoms linked at the N end of the CN ligands.[6]

Since single crystals of CPs are necessary to carefully study their inherent chemical and physical properties, many researchers have studied the single crystal structure of 2D CPs of the tetra-cyanometallates (II) anions, $[\text{Ni}(\text{CN})_4]^{2-}$, $[\text{Pd}(\text{CN})_4]^{2-}$ and $[\text{Pt}(\text{CN})_4]^{2-}$ with Mn, Fe, Ni, Co, Cd, Zn, Cu, and most of these CPs have been obtained by the slow diffusion method.[6-11] On the other hand, the solid crystals were obtained by vigorous mixing solution method[12], but some impurities are sometimes included due to the rapid precipitation process. To the best of my knowledge, the slow diffusion method is a very powerful tool for growing single crystals of cyano-bridged CPs, but it is not for all the cases.

In this chapter, I report the first preparation of single crystal of $\text{Co}(\text{H}_2\text{O})_2\text{Ni}(\text{CN})_4 \cdot 4\text{H}_2\text{O}$ via a sophisticated combination method of the above traditional slow diffusion method with use of trisodium citrate dihydrate (TSCD). The TSCD can serve as a chelating agent to control the nucleation rate and the crystal growth.

3.2. Experimental Sections

3.2.1. Single-crystal X-ray diffraction (SC-XRD)

Crystal structures of the obtained single crystals were determined by single-crystal X-ray diffractometry (SC-XRD) using a RIGAKU Saturn CCD diffractometer equipped with a VariMax confocal optical for MoK α radiation at 113 K. Unit cell refinements and data reduction were carried out by using the d* trek package in CrystalClear software suite.[13] The structures were solved using a novel dual-space algorithm method (SHELXT)[14] and subsequently refined against F² using SHELXL[15] via the WinGX interface.[16] The structure were visualized using the VESTA program.[17] This measurement was conducted at National Institute for Materials Science (NIMS) Materials Analysis Station. The CIF files of the structure described herein are available for the crystal structure with TSCD at 113 K (CCDC no. 1853369) and without TSCD at 113 K (CCDC no.1856704).

3.2.2. Characterization and other measurements.

The phase purity and composition of the sample were checked using powder X-ray diffraction (PXRD) using a Rigaku Ultima-III Rin 2000 diffractometer with monochromated CuK α radiation ($\lambda = 1.5418 \text{ \AA}$) operated at 40 kV and 40 mA. Scanning electron microscopy (SEM) images were taken by Hitachi SU8000 scanning microscope at an accelerating voltage of 10 kV. The transmission electron microscopy (TEM) observation was performed using a JEM-2100F TEM system operated at 200 kV and equipped with energy-dispersive spectrometer. The UV-vis spectra were collected using a JASCO V-570 UV/Vis/NIR spectrophotometer. Fourier-transform infrared spectroscopy (FTIR) was used to investigate the chemical composition, especially the condition of CN bonds. The samples were palletized with KBr windows, and then, the spectra were collected in the range of 500 to 4000 cm⁻¹ at room temperature by using Thermoscientific Nicolet 4700. The spectrum has a sharp band at 2160 cm⁻¹ corresponding to the C \equiv N stretching. The bands located 3753–2748 cm⁻¹ and 1631 cm⁻¹ correspond to the presence of water molecules. Thermogravimetric analysis/differential thermal analysis (TG–DTA) was performed simultaneously from room temperature to 400°C,

using a Hitachi HT-Seiko Instrument Exter 6300 TG/DTA in air with a heating rate of $5^{\circ}\text{C min}^{-1}$.

3.2.3. Water adsorption/desorption isotherms.

Water adsorption/desorption isotherms were collected by using BELSORP-max-11-N-SPBI at 25°C . In a typical procedure, 5 mg of the single crystal was degassed at 150°C for overnight before adsorption measurements. During TG-DTA, all water molecules were removed from the structure upon heat treatment at 150°C . The sample obtained after this measurement and the crystal dried at 150°C for 1 h in an electric furnace at a rate of $1^{\circ}\text{C min}^{-1}$ were analyzed by PXRD using Rigaku RINT 2500X diffractometer with $\text{CuK}\alpha$ radiation.

3.3. Results and Discussion

For the preparation of the single crystal, I utilized the traditional slow diffusion method using RbCl solution.[18] First, a small 20 mL vial was placed within a large 100 mL vial. The vials were filled with an aqueous solution of 0.5 M RbCl at room temperature. 1 M CoCl_2 and 300 g trisodium citrate dihydrate (TSCD) were dissolved in 5 mL of water to form a clear solution under magnetic stirring, which was then cooled for several hours (kept in an ice bath). This solution was injected into the bottom of the small vial and 5 mL of cooled 1 M $\text{K}_2[\text{Ni}(\text{CN})_4]$ solution was injected into the bottom of the large vial. The vials were kept at 45°C in a water bath for several weeks. Pink crystals (**Figure 3-1**) were formed at the bottom of the small vial and recovered by filtration and washed several times with water. For comparison, the same experiment was carried out without TSCD.

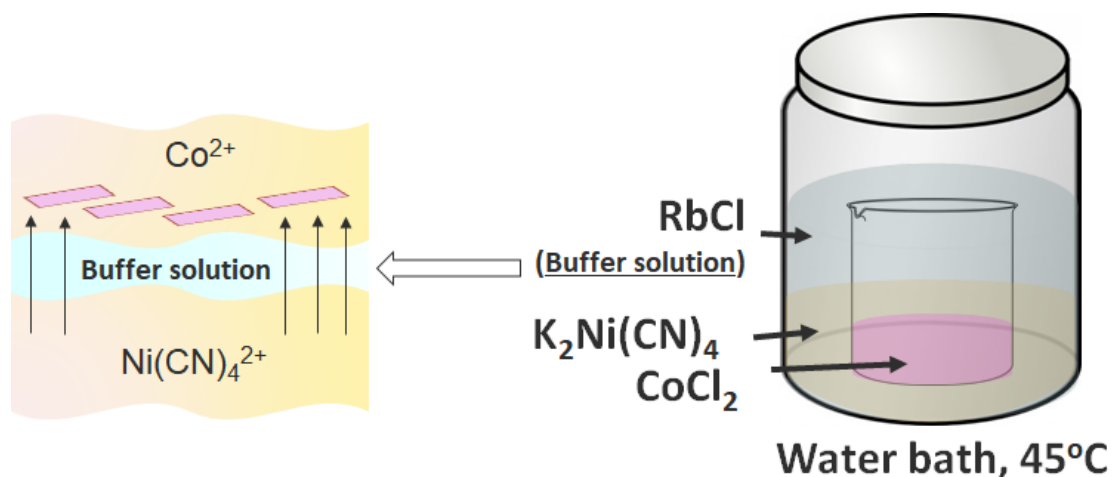


Figure 3-1 Preparation method of the single crystal $\text{Co}(\text{H}_2\text{O})_2\text{Ni}(\text{CN})_4 \cdot 4\text{H}_2\text{O}$ by the slow deposition method.

The morphology and surface of the obtained crystals were investigated by SEM and TEM, as shown in **Figure 3-2**. It is clear that the obtained single crystal exhibits a 2D shape. The surface of the sample prepared without TSCD is composed of several aggregated crystals (**Figure 3-2d**). On the other hand, the surface becomes extremely smooth with the use of TSCD (**Figure 3-2b-c**). Powder XRD patterns of the two samples (obtained with and without TSCD) show similar diffraction peaks, indicating both crystal structures are the same (**Figure 3-3**). The chemical composition of the obtained crystal was determined by the inductively coupled plasma mass spectrometry (ICP-MS) analysis. The Co/Ni molar ratio is 1.00, and no presence of potassium (K) is detected.

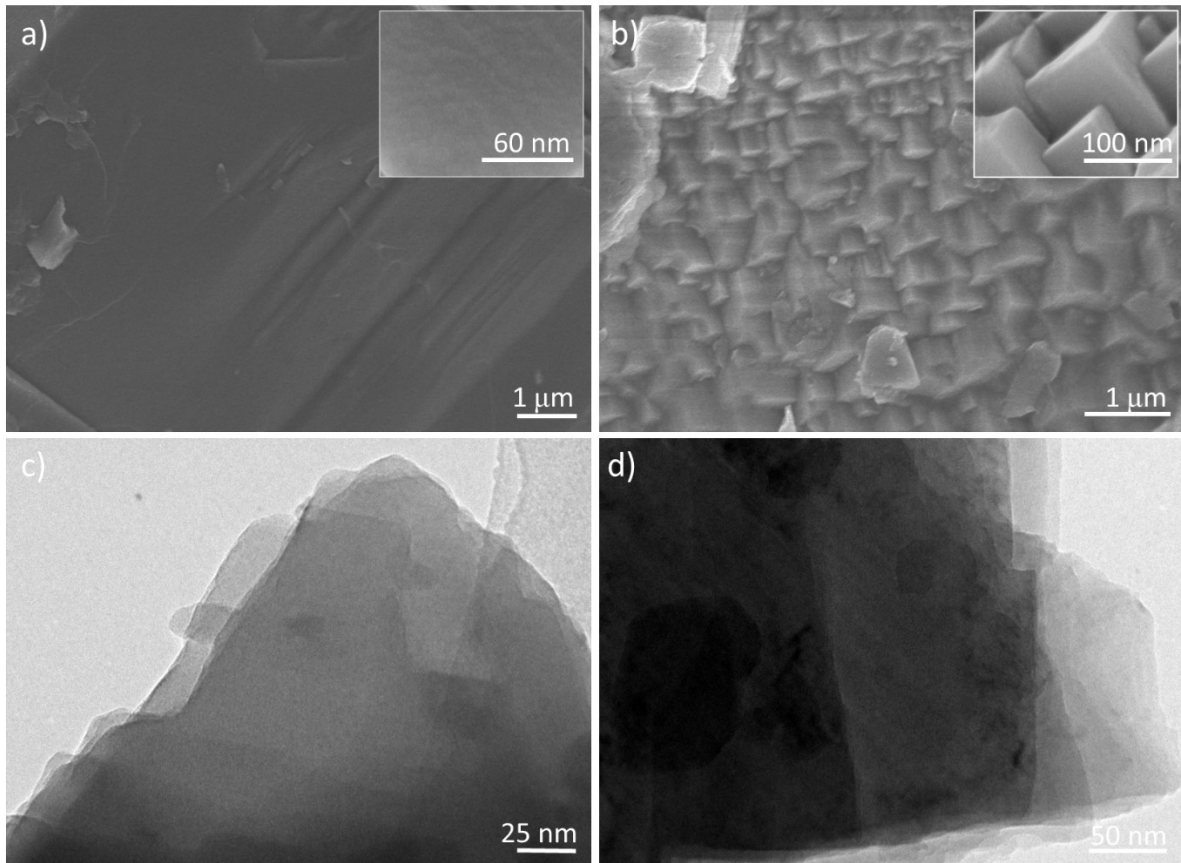


Figure 3-2 (a) Low-magnified SEM image, (b) SEM image of the surface morphology, (c) TEM image of the single crystal obtained with TSCD, and (d) SEM image of the surface morphology of the single crystal obtained without TSCD.

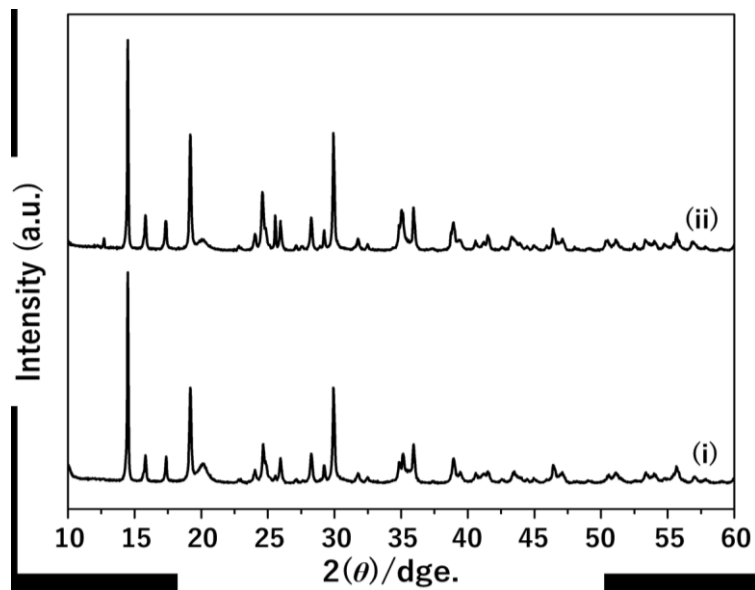


Figure 3-3 PXRD patterns of the obtained crystals (i) with TSCD and (ii) without TSCD, respectively.

It is well known that the balance between nucleation and crystal growth determines the final products. Actually, the reaction with TSCD was quite slow. It took more than 3 weeks until the precipitation of crystals was visually confirmed. To understand the interaction between citrate ions and Co ions, UV-Vis analysis was performed (**Figure 3-4**). The pure CoCl_2 solution without TSCD shows a broad peak from 400 to 550 nm. After the addition of TSCD to CoCl_2 solution, the absorption drastically increases indicating a significant coordination effect of citrate ions with Co^{2+} ions.[19] As the citrate ions can easily combine with dissolved metal ions, the coordination reaction rate between Co^{2+} and $[\text{Ni}(\text{CN})_4]^{2-}$ becomes very slow. This is the best condition for achieving the formation of a perfect single crystal with a very smooth crystal surface (**Figure 3-2b-c**).

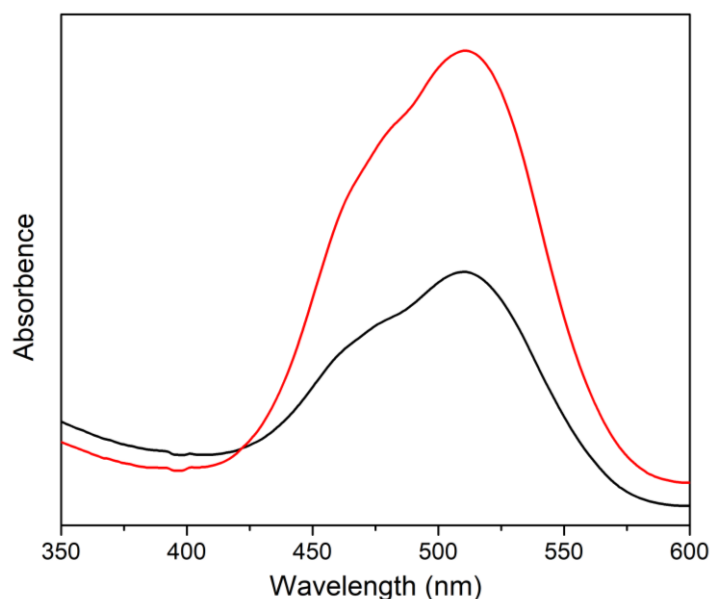


Figure 3-4 UV/Vis data of CoCl_2 solution (i) without TSCD and (ii) with TSCD, respectively.

The unit cell for the single crystal of $\text{Co}(\text{H}_2\text{O})_2\text{Ni}(\text{CN})_4 \cdot 4\text{H}_2\text{O}$ (prepared with TSCD) was obtained from single crystal XRD at 113 K, as shown in **Figure 3-5**. The structure is composed of metal cyanide sheets determined as an orthorhombic unit cell in the $Pnma$ space group with lattice constants of $a=11.9855(5)$ Å, $b=13.8820(6)$ Å and $c=7.1557(3)$ Å; $V=1190.58(9)$ Å³, $Z=4$ (**Table 3.1**). The obtained structure matches well with a previous report,[7] which is similar to the Hofmann type with formula of $(\text{Co}(\text{H}_2\text{O})_2[\text{Ni}(\text{CN})_4]) \cdot 4\text{H}_2\text{O}$.

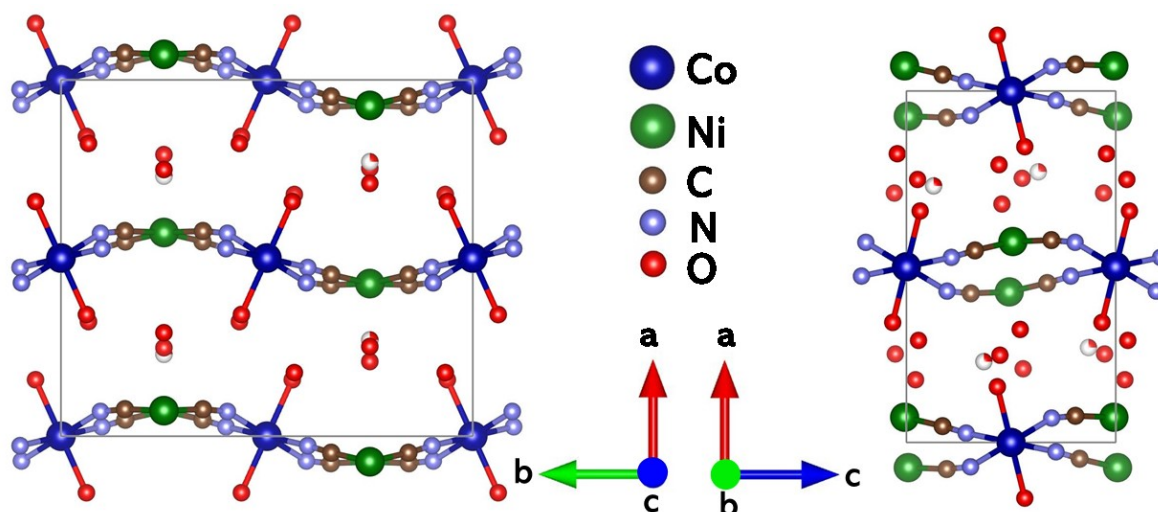


Figure 3-5 The obtained single crystal prepared with TSCD, as characterized by SC-XRD at 113 K.

Table 3.1 Crystal structure data measured at 113 K.

Space group	<i>Pnma</i>
<i>a</i> (Å)	11.9855(5)
<i>b</i> (Å)	13.8820(6)
<i>c</i> (Å)	7.1557(3)
α (°)	90
β (°)	90
γ (°)	90
$V(\text{Å}^3)$	1190.58(9)
R_1	3.64

The FTIR spectrum shows a sharp and intense peak at 2160 cm^{-1} which can be assigned to the cyanide groups in Ni-CN-Co (**Figure 3-6**).[20] This band is shifted to a higher wavenumber compared to $\nu(\text{CN})$ in $\text{K}_2[\text{Ni}(\text{CN})_4]\cdot\text{H}_2\text{O}$ (2122 cm^{-1}), suggesting a lowered symmetry of the $[\text{Ni}(\text{CN})_4]^{2-}$ entity. This result therefore indicates the existence of bridging cyanide groups.[21] The OH stretching vibration and the bending vibration of water molecules

are evidenced by the broad peaks in the range of 3753-2860 cm^{-1} and the peak at 1631 cm^{-1} , respectively.[9] In general, the strong and broad peak observed around 3600-3200 cm^{-1} corresponds to the O-H stretching vibration of surface and interlayer water molecules.[22]

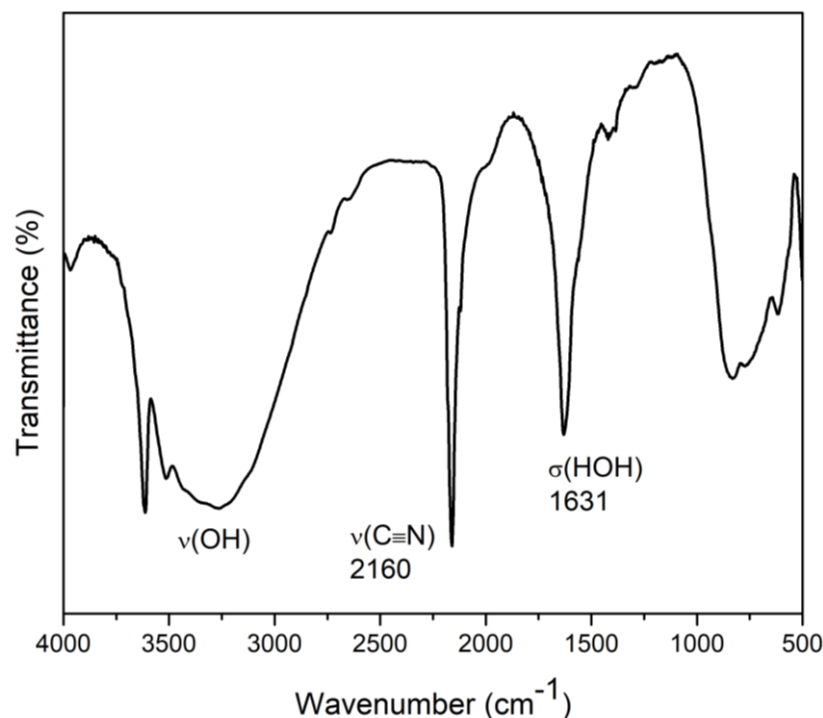


Figure 3-6 FT-IR data of the obtained single crystal prepared with TSCD.

Figure 3-7 shows the thermogravimetry (TG) and differential thermal analysis (DTA) of the single crystal of $\text{Co}(\text{H}_2\text{O})_2\text{Ni}(\text{CN})_4 \cdot 4\text{H}_2\text{O}$ (prepared with TSCD). The TG-DTA curve shows three stages of removal of water molecules (29.5 % from the total compound weight) from room temperature to 150°C. This is in good agreement with previous 2D Hoffman type CPs.[10] The first stage of weight loss (12.0 %) from room temperature to 70°C corresponds to the removal of two water molecules which exist as non-coordinated water molecules between the interlayer space connected by hydrogen bonding. The second stage shows a weight loss of about 6.0 % at 90°C, corresponding to the loss of one water molecule (calculated 6.6%). This water molecule could weakly interact with Ni ion (O–Ni 2.6638(14) Å, **Figure 3-5**). The third stage of weight loss at 108°C (11.5%) is due to the loss of two water molecules, most likely the water coordinated to Co ion (Mn–O 2.1370(8) Å, **Figure 3-5**). These results suggest

the possible interaction between crystal metal and water molecules, as indicated by the presence of coordinated water and non-coordinated water.[9] The above results further imply that there are five water molecules in the crystal, which do not match with the single crystal XRD result.

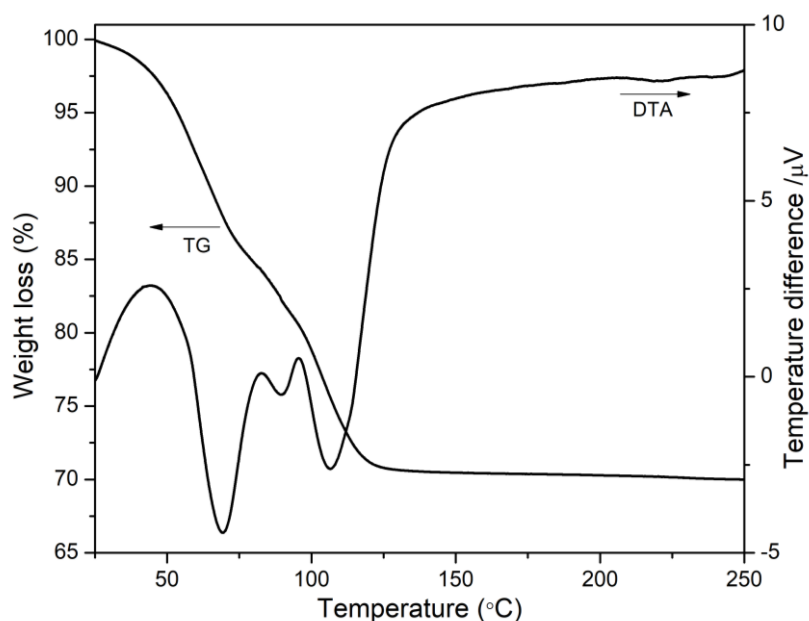


Figure 3-7 TG-DTA curve of the single crystal of $\text{Co}(\text{H}_2\text{O})_2\text{Ni}(\text{CN})_4 \cdot 4\text{H}_2\text{O}$ prepared with TSCD.

A similar situation has been observed in a previous literature. Ray *et al.* reported a single crystal of $\text{Mn}(\text{H}_2\text{O})_2\text{Ni}(\text{CN})_4 \cdot 4\text{H}_2\text{O}$ which was confirmed by single crystal XRD analysis. Based on this chemical formula, this crystal should have 6 water molecules, but the obtained TG curve showed only 5 water molecules containing 3 lattice and 2 coordination water molecules.[10] I suppose that one water molecule can be lost when I prepared the sample for the TG-DTA. This one water molecule which can be easily evaporated is thought to be the non-coordinated water, because it can evaporate even at room temperature. In order to investigate the hydrophilicity, vapor adsorption property and flexibility of the single crystal 2D $\text{Co}(\text{H}_2\text{O})_2\text{Ni}(\text{CN})_4 \cdot 4\text{H}_2\text{O}$, water vapor adsorption experiment was performed at room temperature (**Figure 3-8a**). The sample was fully dehydrated under vacuum to remove all water

molecules. The PXRD pattern of the sample shows that the fully dehydrated sample displays a new crystal structure (**Figure 3-8b**). The majority of CPs has the ability to transform into other crystal structure after dehydration, as transformation.[23] The crystal color also changes from pink to violet after the dehydration, which can be attributed to the water molecules play an important role in the phase change in the degree of aquation of interstitial Co(II) (**Figure 3-10**).[24]

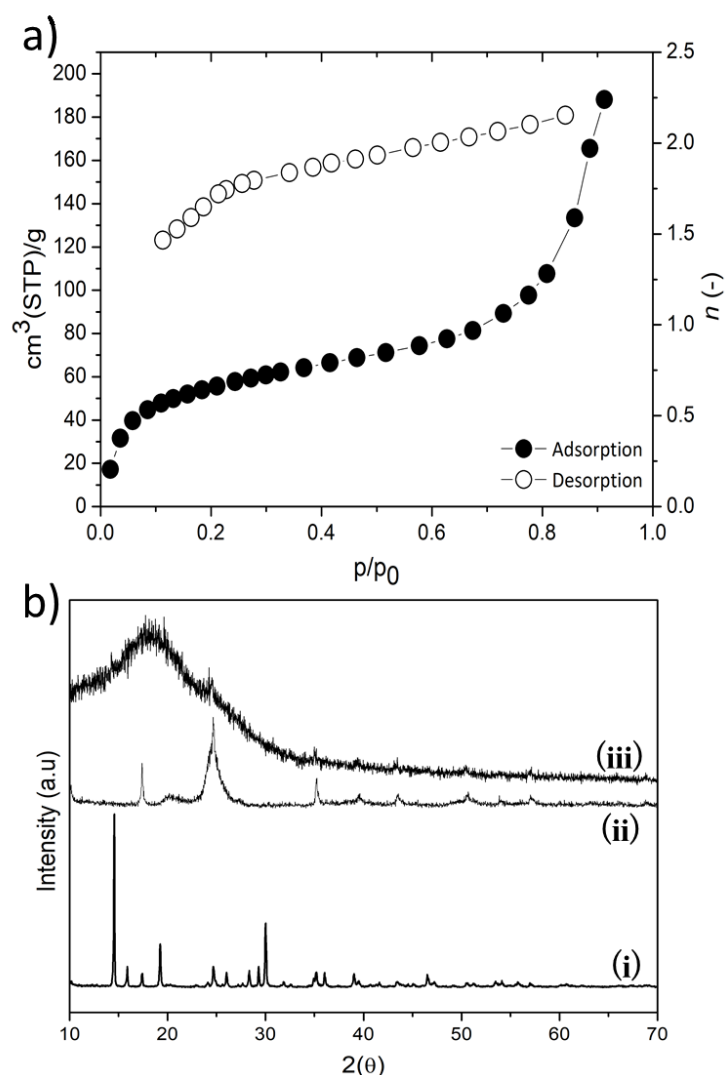


Figure 3-8 (a) Water adsorption/desorption isotherms at 25°C for fully dehydrated sample (heat-treated at 150°C for 1 hours). The vertical axis (right side) shows the number of adsorbed water molecules per the formula of $\text{CoNi}(\text{CN})_4$. (b) PXRD patterns of (i) as-synthesized single crystal sample, (ii) fully dehydrated sample (This sample was sealed by Kapton tape to avoid the adsorption of water from air.), and (iii) rehydrated sample after immersion in water.

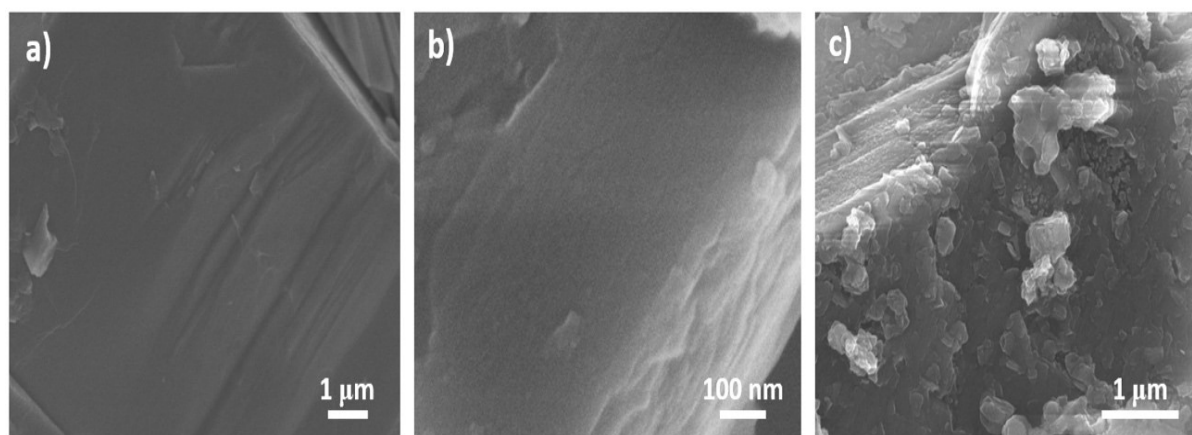


Figure 3-9 SEM images of (a) the original single crystal of $\text{Co}(\text{H}_2\text{O})_2\text{Ni}(\text{CN})_4 \cdot 4\text{H}_2\text{O}$ prepared with TSCD, (b) the fully dehydrated sample, and (c) the fully rehydrated sample after immersion in water.

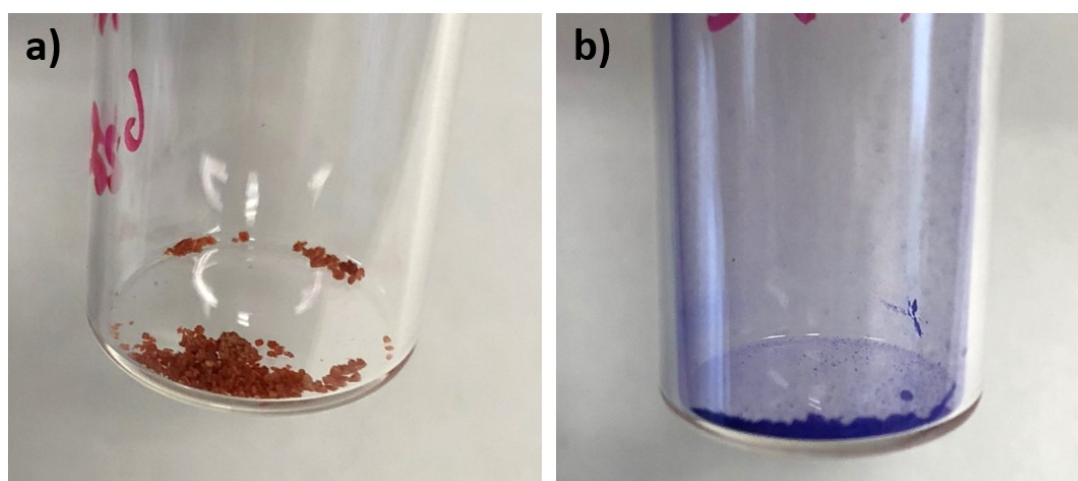


Figure 3-10 Colors of (a) the original single crystal of $\text{Co}(\text{H}_2\text{O})_2\text{Ni}(\text{CN})_4 \cdot 4\text{H}_2\text{O}$ prepared with TSCD and (b) the fully dehydrated sample.

In the water adsorption/desorption isotherm, the maximum water adsorption value is about $188 \text{ cm}^3 \text{ g}^{-1}$ at $P/P_0 = 0.91$ (**Figure 3-8a**), indicating that the sample absorbs about two water molecules per $[\text{CoNi}(\text{CN})_4]$ unit. The PXRD pattern of the sample after water vapor adsorption/desorption shows the existence of an amorphous phase without any clear diffraction peaks. Even after immersion in water, the sample does not show any obvious peaks (**Figure 3-8b**). The obtained crystal transforms to another crystal phase by dehydration (at 150°C for 1

hour) which cannot be fully hydrated anymore (*i.e.*, the crystal structure is not flexible enough to absorb six water molecules).

3.4. Conclusion

In conclusion, I have successfully prepared single crystal of $\text{Co}(\text{H}_2\text{O})_2\text{Ni}(\text{CN})_4 \cdot 4\text{H}_2\text{O}$ with a very smooth surface through a controlled crystallization process with the assistance of TSCD. I strongly believe that my approach will be useful for preparation of other types of single crystals with new chemical and physical properties.

References

- [1] R. Kitaura, G. Onoyama, H. Sakamoto, R. Matsuda, S. Noro, S. Kitagawa, *Angewandte Chemie International Edition* **2004**, *43*, 2684-2687.
- [2] L. Boudjema, E. Mamontova, J. Long, J. Larionova, Y. Guari, P. Trens, *Inorganic Chemistry* **2017**, *56*, 7598-7601.
- [3] K. S. Novoselov, A. K. Geim, S. V. Morozov, D. Jiang, Y. Zhang, S. V. Dubonos, I. V. Grigorieva, A. A. Firsov, *Science* **2004**, *306*, 666-669.
- [4] Y. Zhang, Y.-W. Tan, H. L. Stormer, P. Kim, *Nature* **2005**, *438*, 201-204.
- [5] H. Yang, N. Coombs, Ö. Dag, I. Sokolov, G. A. Ozin, *Journal of Materials Chemistry* **1997**, *7*, 1755-1761.
- [6] Y. L. Qin, B. W. Yang, G. F. Wang, H. Sun, *Acta Crystallographica Section C: Structural Chemistry* **2016**, *72*, 555-560.
- [7] O. Reyes-Martinez, E. Torres-García, G. Rodríguez-Gattorno, E. Reguera, *Materials* **2013**, *6*, 1452-1466.
- [8] N. J. Robertson, Z. Qin, G. C. Dallinger, E. B. Lobkovsky, S. Lee, G. W. Coates, *Dalton Transactions* **2006**, 5390-5395.
- [9] J. Rodríguez-Hernández, A. A. Lemus-Santana, C. N. Vargas, E. Reguera, *Comptes Rendus Chimie* **2012**, *15*, 350-355.
- [10] A. Ray, I. Bhowmick, W. S. Sheldrick, A. D. Jana, M. Ali, *Journal of Solid State Chemistry* **2009**, *182*, 2608-2612.

- [11] W. K. Ham, T. J. R. Weakley, C. J. Page, *Journal of Solid State Chemistry* **1993**, *107*, 101-107.
- [12] KENNETH D. KARLIN, *Progress in Inorganic Chemistry Advisory Board*, JOHN WILEY & SONS, INC., New York, **1997**
- [13] Rigaku Corporation, *CrystalClear*, Tokyo, Japan, **2005**.
- [14] G. M. Sheldrick, *Acta Crystallographica Section A Foundations and Advances* **2015**, *71*, 3-8.
- [15] G. M. Sheldrick, *Acta Crystallographica Section C: Structural Chemistry* **2015**, *71*, 3-8.
- [16] L. J. Farrugia, *J. Appl. Cryst.* **2012**, *45*, 849.
- [17] K. Momma, F. Izumi, *Journal of Applied Crystallography* **2011**, *44*, 1272-1276.
- [18] E. J. M. Vertelman, T. T. A. Lummen, A. Meetsma, M. W. Bouwkamp, G. Molnar, P. H. M. Van Loosdrecht, P. J. Van Koningsbruggen, *Chemistry of Materials* **2008**, *20*, 1236-1238.
- [19] M. B. Zakaria, M. Hu, R. R. Salunkhe, M. Pramanik, K. Takai, V. Malgras, S. Choi, S. X. Dou, J. H. Kim, M. Imura, S. Ishihara, Y. Yamauchi, *Chemistry - A European Journal* **2015**, *21*, 3605-3612.
- [20] Z. Kartal, A. Ölmez, *Zeitschrift für Naturforschung - Section A Journal of Physical Sciences* **2005**, *60*, 537-540.
- [21] S. Kürçüoğlu, T. Hökelek, M. Aksel, O. Z. Yeşilel, H. Dal, *Journal of Inorganic and Organometallic Polymers and Materials* **2011**, *21*, 602-610.
- [22] L. Zhang, J. Zhu, X. Jiang, D. G. Evans, F. Li, *Journal of Physics and Chemistry of Solids* **2006**, *67*, 1678-1686.
- [23] A. Alowasheir, S. Tominaka, Y. Ide, Y. Yamauchi, Y. Matsushita, *CrystEngComm* **2018**, *20*, 6713-6720.
- [24] D. F. Shriver, D. B. Brown, *Inorganic Chemistry* **1969**, *8*, 42-46

Chapter 4

Graphene-Wrapped Nanoporous Nickel-Cobalt Oxide Flakes for Electrochemical Supercapacitors

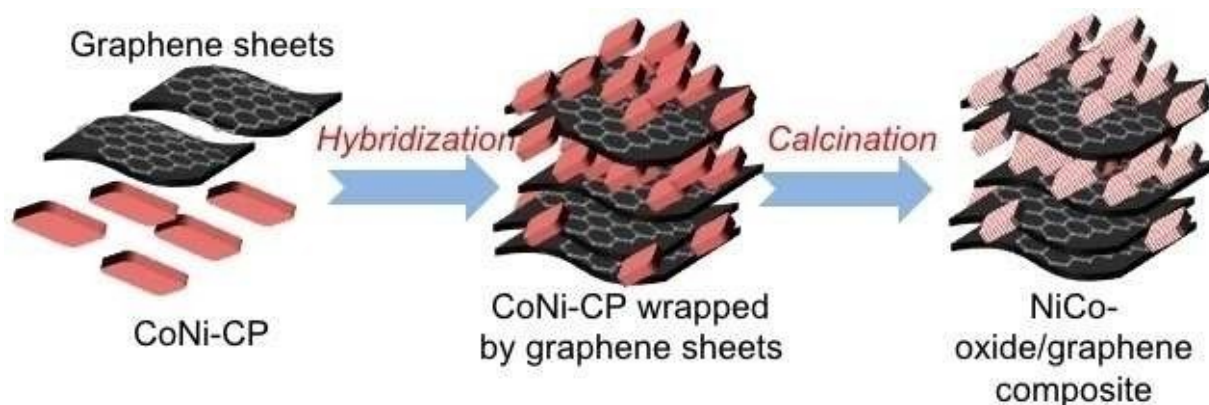
4.1. Introduction

Although carbon materials have been widely utilized for a myriad of applications, their use as electrode materials for supercapacitor applications is of particular interest due to the looming energy concerns. A variety of carbon materials, including, activated carbon, mesoporous carbon, carbon nanotubes, and graphene sheets have been proved to be of tremendous use in electrochemical energy storage, particularly supercapacitors.[1] Among the various nanocarbons, two-dimensional (2D) graphene based structures have garnered much attention and shows better performance toward supercapacitors applications because they possess highly active surface sites for the electrochemical reaction pathway.[2,3] However, due to the limitations of single materials, researchers are focusing on design and use of composite hybrid materials with dual functional properties to improve the energy and power density of the electrochemical device. The hybridization of graphene and other components have been widely studied for the preparation of highly efficient nanoarchitectures. Especially, graphene-based hybrid materials including doped graphene sheets,[4,5] graphene-CNTs,[6,7] graphene-conducting polymers [8–10] have been extensively investigated in the recent past.

Transition metal oxides are one of the promising class of electrode materials for supercapacitors because of their high pseudocapacitive property.[11–13] However, their poor electronic conductivity limits their electrochemical performance, usually leading to rapid decay in capacity. Methods to enhance electrical conductivity are required for future high-performance supercapacitors and to improve their electrochemical storage capability. One effective strategy is to prepare three dimensional (3D) architectures consisting of different 2D materials, particularly, graphene (G).[14] Such a structure can provide high interfacial surface area and many active centers.

In this chapter, I report a novel approach for hybridizing NiCo oxide flakes with graphene sheets (G) (**Scheme 4-1**). Positively charged cyano-bridged CoNi CP flakes (CoNi-CP) were mixed with negatively charged G surface containing suspension. Due to effective electrostatic force, both the materials are hybridized to form CoNi-CP/G composite. The as-prepared CoNi-CP/G composite was thermally treated in air to remove organic components

without affecting the integrity of the parent G sheets. During the thermal treatment, the CoNi-CP flakes wrapped into G sheets were concomitantly converted to NiCo oxide, resulting in a new composite consisting of NiCo oxide flakes and G sheets (NiCo-oxide/G). The as-prepared NiCo-oxide/G composite shows high specific capacitance ($\sim 199 \text{ F g}^{-1}$) at a scan rate of 5 mV s^{-1} and features the good capacitance retention.



Scheme 4-1. Schematic illustration of the synthetic pathway of CoNi-CP/G composite and its thermal decomposition to NiCo-oxide/G composite.

4.2. Experimental Sections

4.2.1. Chemicals

Natural graphite flakes (10 mesh) was purchased from Alfa Aesar, USA. Anhydrous N-methyl-2-pyrrolidinone (NMP) and potassium tetracyanonickelate (II) hydrate were purchased from Sigma-Aldrich. Trisodium citrate dihydrate and cobalt (II) chloride anhydrous were purchased Nacalai Tesque, Inc., Japan. All reagents were used without further purifications.

4.2.2. Preparation of cyano-bridged CoNi-CP flakes.

Following to Zakaria *et al.* work,[15] 59.6 mg of cobalt chloride anhydrous and 100 mg of trisodium citrate dihydrate were mixed together in 20 mL water to form a clear solution. Meanwhile, 130 mg of $\text{K}_2[\text{Ni}(\text{CN})_4]$ was prepared in 20 mL water to form another clear solution.

Then, the two solutions were mixed together under magnetic stirring until the mixture became clear. The obtained solution was aged for 24 hours, followed by the formation of a green precipitate which was collected by centrifugation. After washing with water and ethanol extensively, the precipitate (CoNi-CP) was well-dispersed in water again to form a colloidal solution of CoNi-CP flakes.

4.2.3. Preparation of graphene sheets.

The graphite was dispersed in NMP by sonicating in a low power sonic bath (UT-606H) for 1 hour. The resulting dispersion was aged for approximately 24 hours to allow any unstable aggregates to form. Again, the dispersions were undergone sonication for 1 hour more and aged for 24 hours. The resultant dispersion was then centrifuged using a Sigma 3-30K centrifuge for 90 minutes at 500 rpm. After centrifugation, decantation was carried out by pipetting off the top half of the dispersion. The exfoliated graphene dispersion in NMP was obtained.

4.2.4. Preparation of NiCo-oxide/G composite.

To prepare the hybrid structure, the graphene nanosheets suspension was mixed with CoNi CP flakes colloidal solution under mild stirring overnight. The precipitate was obtained by centrifugation and the sample was dried under vacuum at 80°C to get the CoNi-CP/G composite. The powders (50 mg) were placed in a melting pot. The melting pot was then heated inside a furnace from room temperature to 350 °C at a heating rate of 5°C min⁻¹. Subsequently, the sample was annealed for 1 hour and allowed to cool inside the furnace naturally. Finally, the obtained powder (NiCo-oxide/G composite) was collected for characterization. All calcination process was carried out in the air.

4.2.5. Characterization.

Wide-angle XRD patterns of the samples were collected using a Rigaku RINT 2500X diffractometer with monochromated Cu-K α radiation (40 kV, 40 mA) and the data was collected in the 2θ range of 10-70°. The lattice parameters were refined by the Pawley method using the GSAS-II software [16] and the zero shifts of the patterns were corrected and background subtraction. Fourier-transform infrared spectroscopy (FT-IR) was used to

investigate the chemical groups, especially condition of CN bonds. The samples were pelletized with KBr, and then the spectra were collected in the range from 500 to 4000 cm^{-1} at room temperature using Thermoscientific Nicolet 4700. The morphological characterization of the samples was performed using a Hitachi SU8000 scanning electron microscope (SEM). Transmission electron microscopy (TEM) observation was performed using a JEM-2100F TEM system that was operated at 200 kV and equipped with energy-dispersive spectrometer (EDS). Atomic force microscope (AFM) images were obtained using multi-mode scanning probe microscope (SPM), Bruker MM- SPM. The Raman spectra were Implemented by Horiba-Jovin Yvon T64000 with the excitation Laser 364 nm. Thermogravimetric analysis (TGA) was measured by using Hitachi HT-Seiko instrument Exter 6300 TG/DTA, RT-1100 $^{\circ}\text{C}$ in the air.

4.2.6. Electrode preparation and electrochemical measurements.

Graphite substrates coated with the active materials were used as working electrodes. Firstly, graphite substrates were polished using a fine polisher and rinsed with deionized water. Subsequently, the substrates were etched in a 0.1 M HCl solution at room temperature for 10 min, rinsed with deionized water in an ultrasonic bath for 30 minutes and dried. The working electrodes were manufactured by mixing the active material (NiCo oxide and NiCo-oxide/G composites) with polyvinylidene fluoride (PVDF, 20%) binder in a small amount of N-Methyl-2- pyrrolidone (NMP) solvent. The as-prepared slurry was coated on the graphite substrate and dried at 80 $^{\circ}\text{C}$ in a vacuum oven for 2 hours. The masses of the electrodes were measured using an ultra-microbalance (Mettler-Toledo).

The electrochemical measurements were performed using a CHI660E electrochemical workstation (CH Instruments Inc., USA). A conventional three-electrode cell consisted a Pt-wire as a counter electrode, Ag/AgCl as the reference electrode and the modified graphite electrode as the working electrode. A 3 M aqueous KOH solution was used as the electrolyte. Cyclic voltammetry (CV) measurements were conducted at various scan rates. The average specific capacitance (C_{sp}) values were calculated from the CV curves using the equation;

$$C_{\text{sp}} = \frac{1}{ms(V_f - V_i)} \int_{V_i}^{V_f} I(V) dV$$

where C_{sp} is the capacitance ($F\ g^{-1}$), m is the mass of the active electrode material (g), s is the potential scan rate ($mV\ s^{-1}$), V_f and V_i are the integration limits of the voltammetric curve (V), and $I(V)$ denotes the response current density ($A\ cm^{-2}$). For every experiment, the typical area under consideration was $1\ cm^2$.

4.3. Results and Discussion

Cyano-bridged CoNi-CP flakes were prepared according to previous report.[17] Briefly, cobalt chloride solution and trisodium citrate dihydrate solution were mixed together to form a clear solution. Meanwhile, $K_2[Ni(CN)_4]$ solution was prepared in water to form another clear solution. Then, the two solutions were mixed together under magnetic stirring until the mixture becomes clear. The obtained solution was aged for 24 hours, followed by the formation of a green precipitate which was collected by centrifugation. After washing with water and ethanol extensively, the precipitate was dispersed in water again. The detailed experimental procedure is given in the experimental section (in the supporting information). The obtained CoNi CP flakes were well dispersed in water to form a homogeneous colloidal (**Figure 4-1 a-1**). The zeta potential of the obtained CoNi- CP flakes dispersed in water was positive (+5.31 mV).[18] In general, the surface charge of cyano-bridged CPs is controlled under synthetic conditions using polymer or capping agents. For example, poly (allylamine hydrochloride) was used to coat bare Prussian blue-based cubes, switching the surface charges of nanoparticles from negative to positive zeta potential (from -23.5 mV to +17.9 mV).[19]

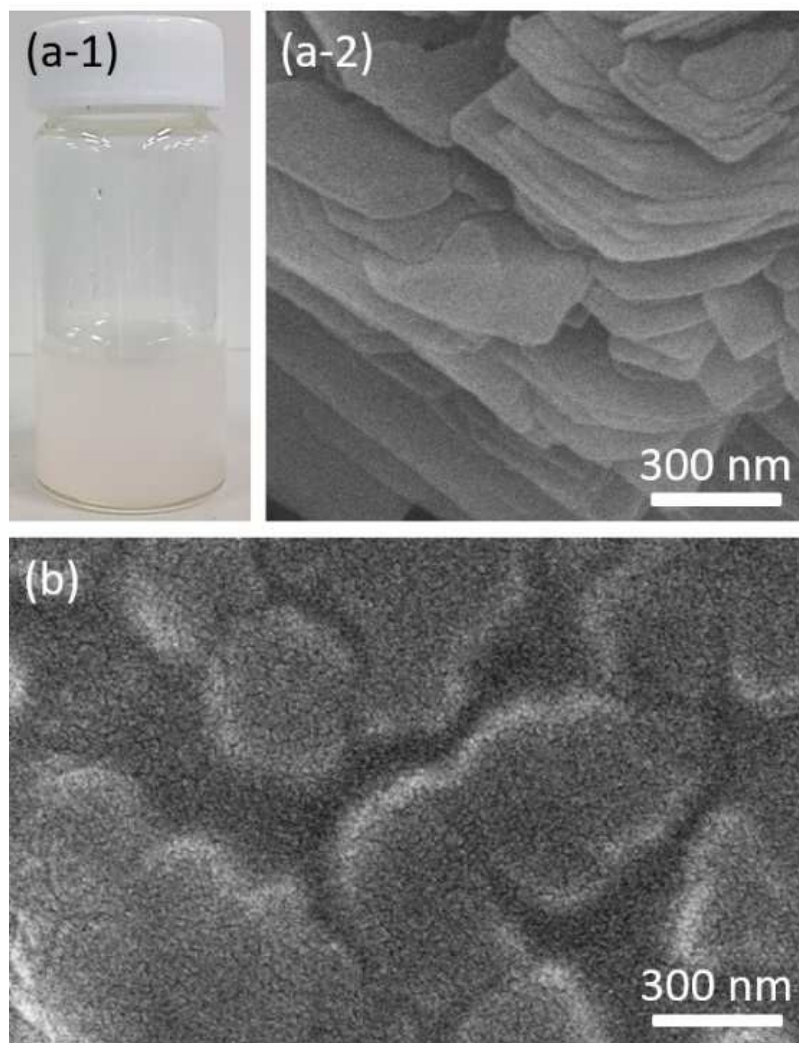


Figure 4-1 (a-1) Photograph of suspension and (a-2) SEM image of CoNi-CP flakes. (b) SEM image of CoNi-CP/G composite.

SEM image of the typical CoNi-CP flakes with an average lateral size of around 300 nm is shown in **Figure 4-1 a-2**. The thickness of the obtained CoNi CP flakes was determined to be around 20–30 nm by AFM (**Figure 4-2a**). The powder X-ray diffraction (XRD) patterns of the obtained CoNi-CP is shown in **Figure 4-3**. The Pawley fitting of this XRD pattern results reveal that the structure is orthorhombic in the *Pnma* space group. The structure is identical to the crystal structure of $[(\text{Co}(\text{H}_2\text{O})_2)(\text{Ni}(\text{CN})_4)] \cdot 4\text{H}_2\text{O}$ (CCDC 59366). The result of the structure determination and crystallographic details are presented in **Table 4.1**. The FT-IR spectra is depicted in **Figure 4-4**. The typical sharp and strong peak at 2160 cm^{-1} corresponding to the $\text{C}\equiv\text{N}$ stretching vibration and weak C-N is observed at 1378 cm^{-1} . The $\text{C}\equiv\text{N}$ signal is

shifted to high frequency in comparison to $\text{K}_2\text{Ni}(\text{CN})_4$ due to its connection to metal atoms and removal of electrons from weak orbital.[20,21] Several peaks at 3600, 3500– 3000 and 1630 cm^{-1} indicate that water molecules exist in the compound. Especially, the stretching frequency at 3600 cm^{-1} corresponds to the free -OH bond. This free water molecule could be in the interlayer space.

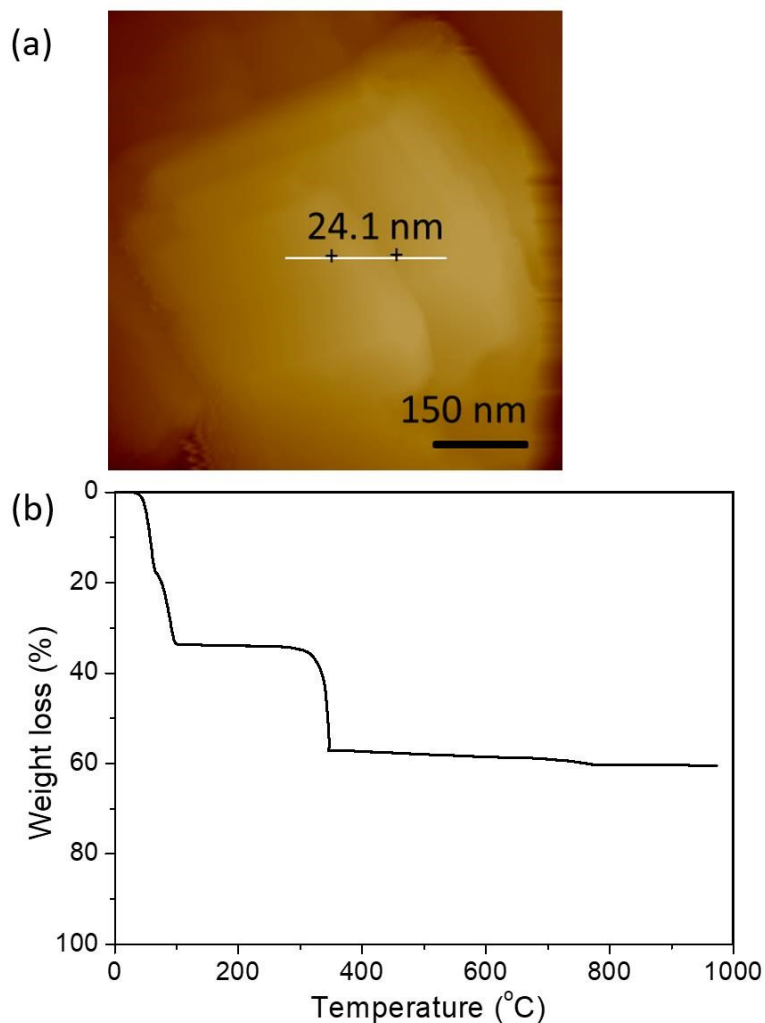


Figure 4-2 (a) AFM image and (b) thermogravimetric (TG) curve of CoNi-CP flakes in air. Note: In the first stage, adsorbed solvents such as water molecules are removed from room temperature until around 150°C. From this stage, the number of water molecules was calculated to be about six water molecules (per one unit) including the coordinate and non-coordinated water molecules. The same water number was also reported in other Hofmann-type 2D CPs.[22,23]

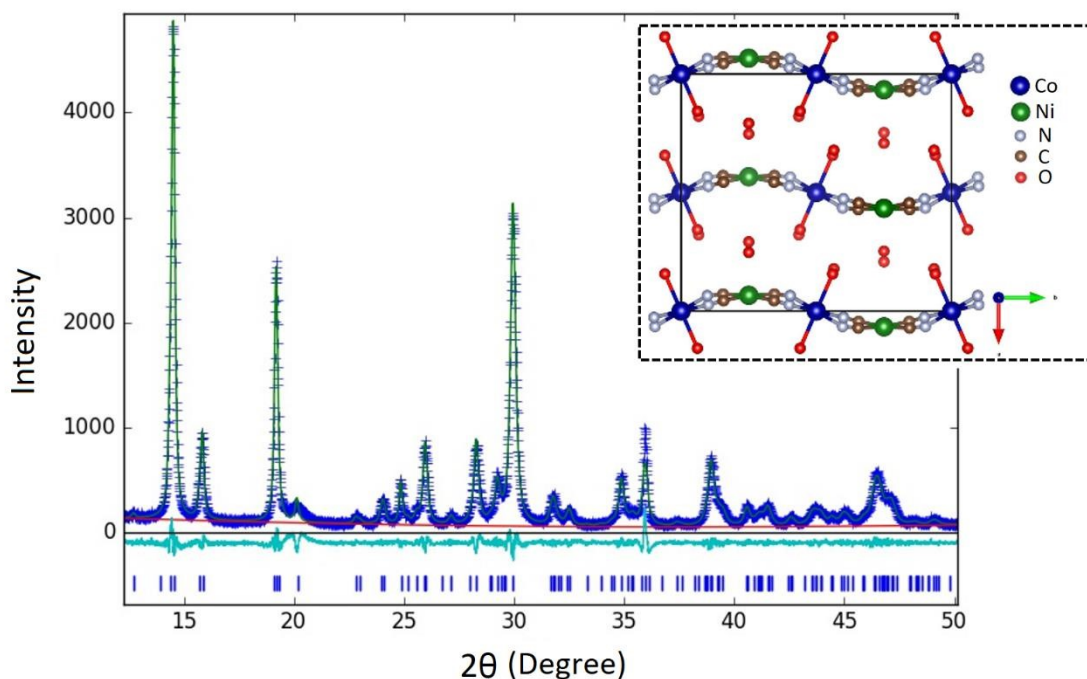


Figure 4-3 Analysis of the obtained PXRD patterns of CoNi-CP using the Pawley fitting method (Inset: $[\text{Co}(\text{H}_2\text{O})_2\text{Ni}(\text{CN})_4]\cdot 4\text{H}_2\text{O}$ crystal structure.)

Table 4.1 Lattice constants refined by the Pawley fitting method.

Formula	$[\text{Co}(\text{H}_2\text{O})_2\text{Ni}(\text{CN})_4]\cdot 4\text{H}_2\text{O}$
Space group	<i>Pnma</i>
<i>a</i> (Å)	12.2278(8)
<i>b</i> (Å)	13.9497(16)
<i>c</i> (Å)	7.1725(7)
α (°)	90
β (°)	90
γ (°)	90
<i>V</i> (Å ³)	1223.45(2)
w <i>R</i> (%)	9.444
GOF	1.53

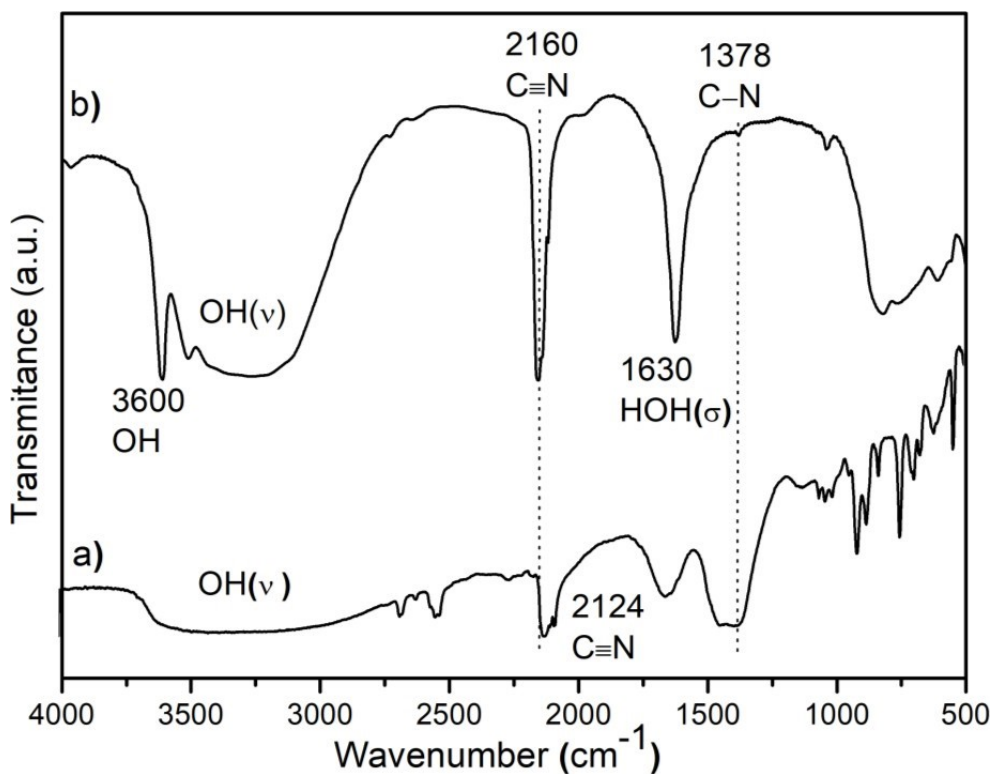


Figure 4-4 FT-IR spectra of (a) K₂ [Ni(CN)₄] salt and (b) CoNi-CP flakes.

Graphene suspension was prepared by a sonication of graphite flakes in N-methyl-2-pyrrolidinone (NMP) solvent for few hours followed by ageing overnight.[24] The zeta potential of the exfoliated graphene suspension was measured thrice and the calculated average value was found to be -8.02 mV. Thin graphene sheets with large lateral size around 2 μm were obtained as shown in the scanning electron microscope (SEM) and transmission electron microscope (TEM) images (**Figure 4-5**). The selected area electron diffraction (SAED) patterns depict a hexagonal arrangement which is characteristic of graphene sheets. In most parts, the thickness of the obtained graphene nanosheets is around 1 nm, as determined by AFM (**Figure 4-5e**). Bilayers and multilayers nanosheets are also observed (**Figure 4-5f**). The obtained graphene sheets were further characterized by Raman spectroscopy (**Figure 4-6**). In addition to the typical D and G bands at around 1350 cm⁻¹ and 1579.4 cm⁻¹ respectively a broad 2D band at 2710 cm⁻¹ is also observed, indicating the two-dimensional morphology of graphene sheets. The G band is usually assigned to the E_{2g} phonon of C sp² atoms, while the D band is due to the conversion of sp² hybridized carbon to sp³ hybridized carbon atoms which relates to

the amount of disorder.[24] In previous study, the graphene oxide (GO) nanosheets was used for preparation of NiO/GO composite.[18] The Raman spectrum of the GO nanosheets shows similar peak intensities of the G and D bands. However, in the present study, it is revealed that the intensity of G band is obviously higher compared to that of the D band, indicating the large lateral size of the in-plane sp^2 domains and fewer defects.

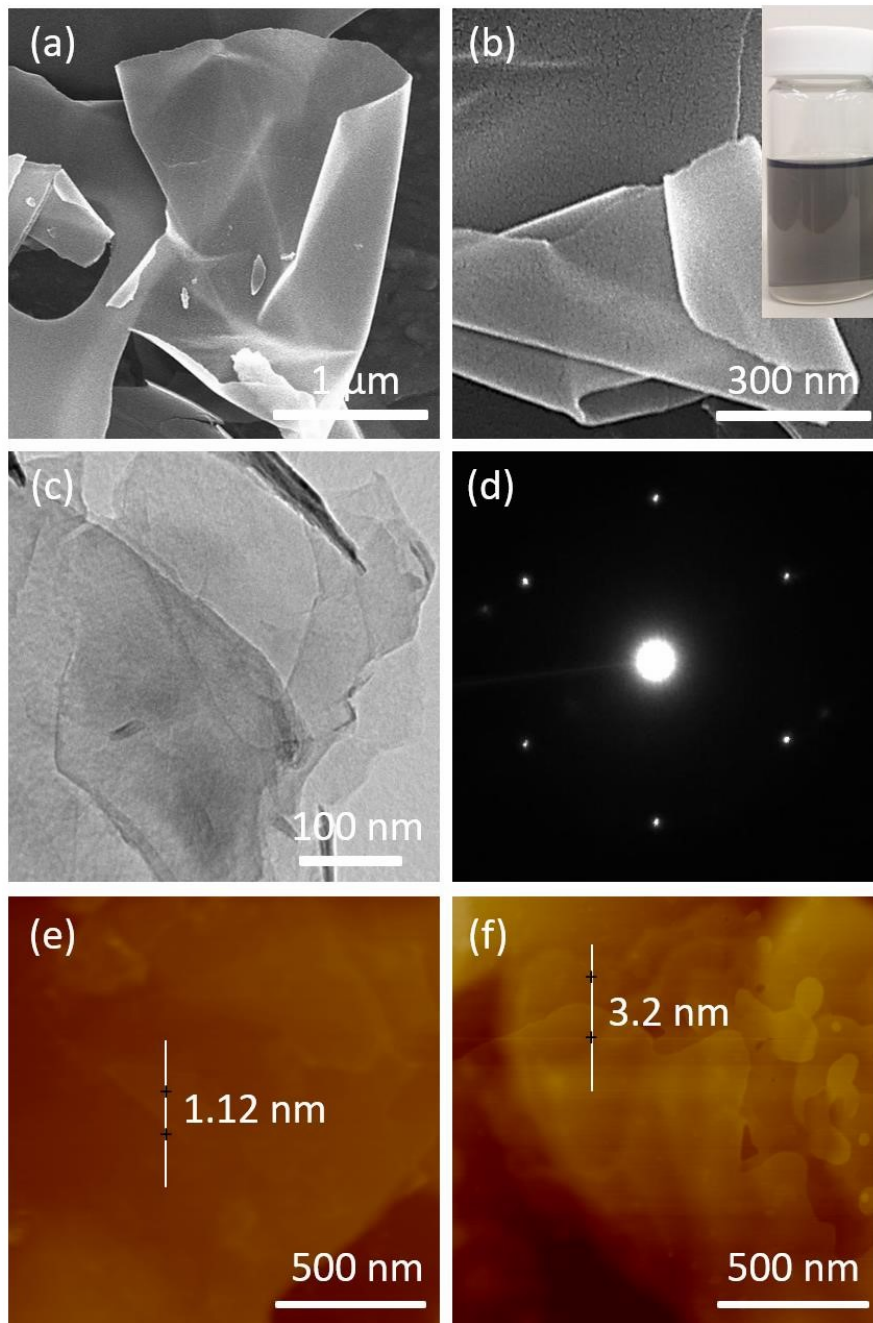


Figure 4-5 (a, b) SEM images (inset: photograph of graphene suspension), (c) TEM image, (d) ED patterns, and (e, f) AFM images of graphene sheets.

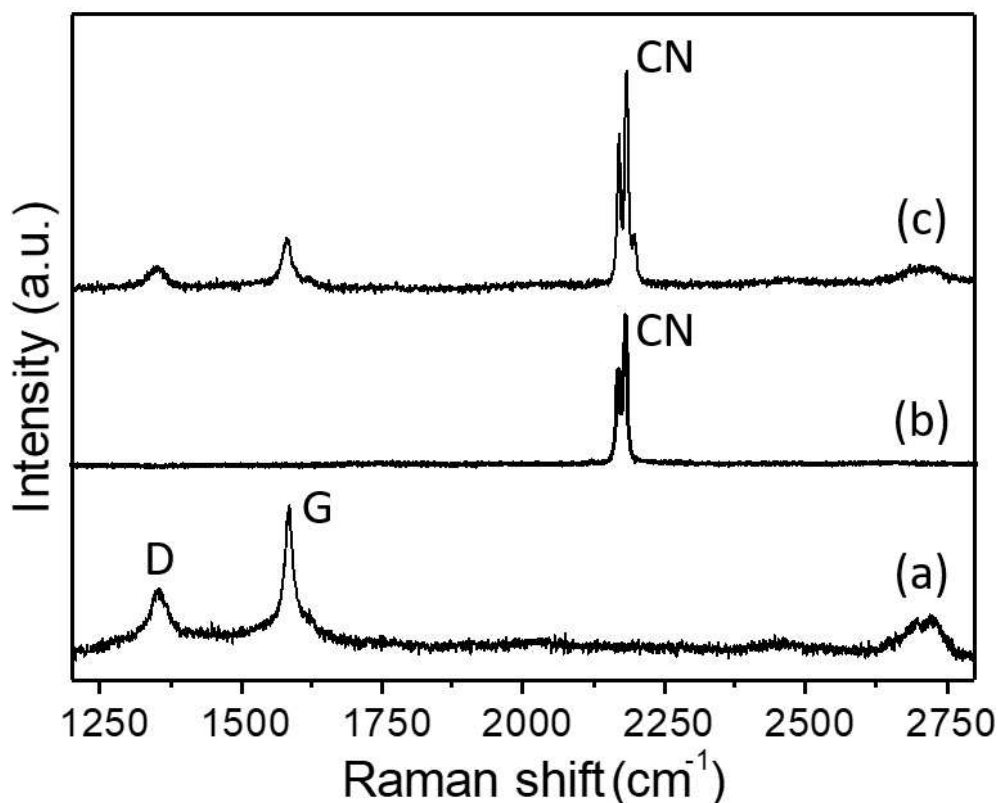


Figure 4-6 Raman spectra for (a) graphene, (b) CoNi-CP and (c) CoNi-CP/G composite.

To prepare the hybrid structure, the graphene nanosheets suspension was mixed with CoNi CP flakes colloidal solution under mild stirring overnight (**Figure 4-1 b**). To remove the solvents, the samples were dried under vacuum at 80°C to get the CoNi-CP/G composite (**Scheme 4-1**). The powders were heated inside a furnace from room temperature to the designed temperature (350°C) in air. Finally, the obtained powder (NiCo-oxide/G composite) was collected for characterization. The detailed experimental procedure is given in the experimental section.

SEM images of the typical CoNi-CP/G samples before thermal treatment are shown in **Figure 4-1 b**. The CoNi CP flakes can be observed with the large-sized graphene nanosheets. Raman spectra for the CoNi-CP/G sample shows a peak at 2184 cm⁻¹ that is characteristic of CN-stretching (**Figure 4-6**), which remains even after hybridization with graphene nanosheets. The CoNi-CP/G composite also shows similar wide-angle XRD patterns as CoNi-CP, indicating that the original crystal structure does not collapse.

The thermal degradation of CoNi-CP was analyzed using thermogravimetric (TG) analysis in air (**Figure 4-2b**). Similar to the thermal degradation of cyano-bridged coordination polymers in air, two major weight losses are noticed. In the first stage, adsorbed solvents such as water molecules are removed from room temperature until around 150°C. No further weight loss is observed until around 260°C. After this, the second weight loss is observed and continued until ~ 350°C. This weight loss corresponds to the loss of CN groups, resulting in NiCo oxide. The crystal structure of the finally obtained NiCo oxide and NiCo-oxide/G composite was investigated using wide-angle XRD (**Figure 4-7**). From the inductively coupled plasma (ICP) analysis, the compositional ratio of Co:Ni in the NiCo-oxide/G composite after the calcination was measured to be around 1:1. Compared to the standard PDF No. 20-0781, the major peaks are ascribed to spinel $\text{Ni}_x\text{Co}_{3-x}\text{O}_4$. Two additional peaks corresponding to NiO as well as one weak peak corresponding to Ni are also observed. Even though the sample was calcined in air, un-oxidized Ni phase was formed. Similar phenomenon has been observed in previous study.[25] This is probably because of different diffusion rate of Ni species during thermal treatment. Thus, some Ni species are out of the major spinel $\text{Ni}_x\text{Co}_{3-x}\text{O}_4$ crystal structure.

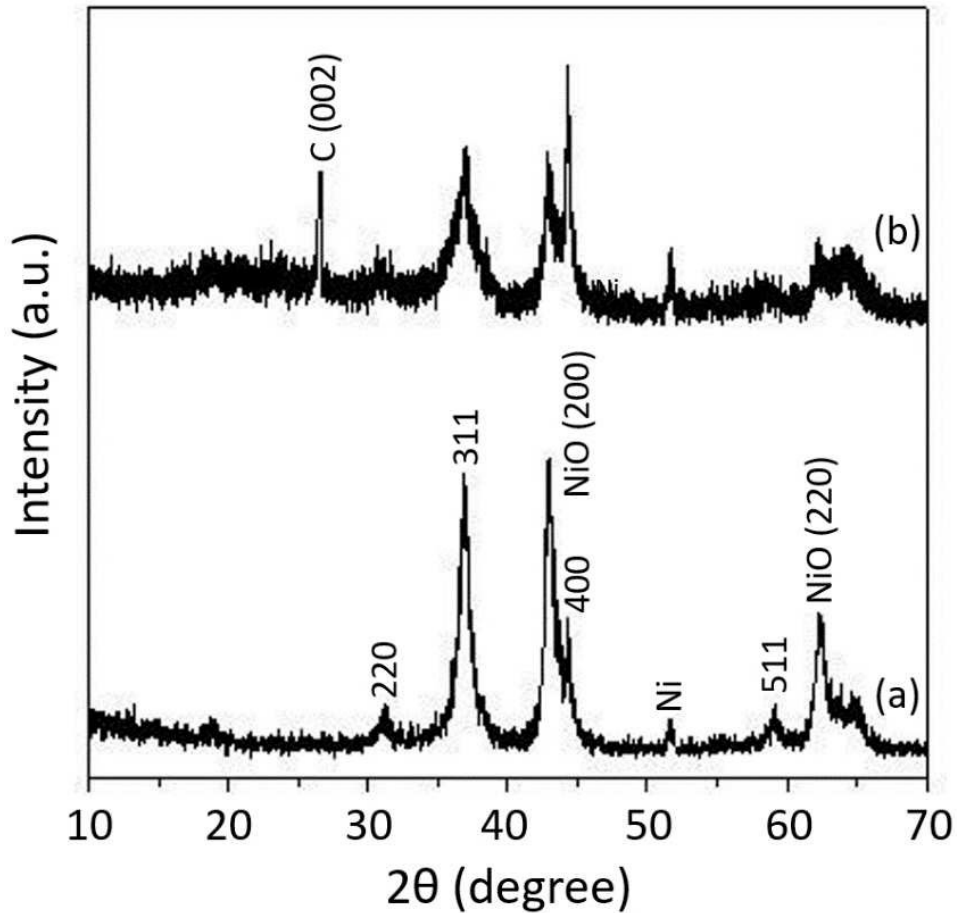


Figure 4-7 Wide-angle XRD patterns for (a) NiCo oxide, (b) NiCo-oxide/G composite.

Figure 4-8 shows the SEM and TEM images of NiCo oxide and NiCo-oxide/G composite obtained after thermal treatment. SEM images show that the obtained NiCo oxide retains the original sheet like morphology, and it features porous structure because the removal of CN-groups by heating. From the TEM image of NiCo-oxide/G composite, it is observed that the nanoporous flakes are wrapped between the graphene sheets. The ED patterns show ring-like patterns which can be assigned to the spinel crystal phase.

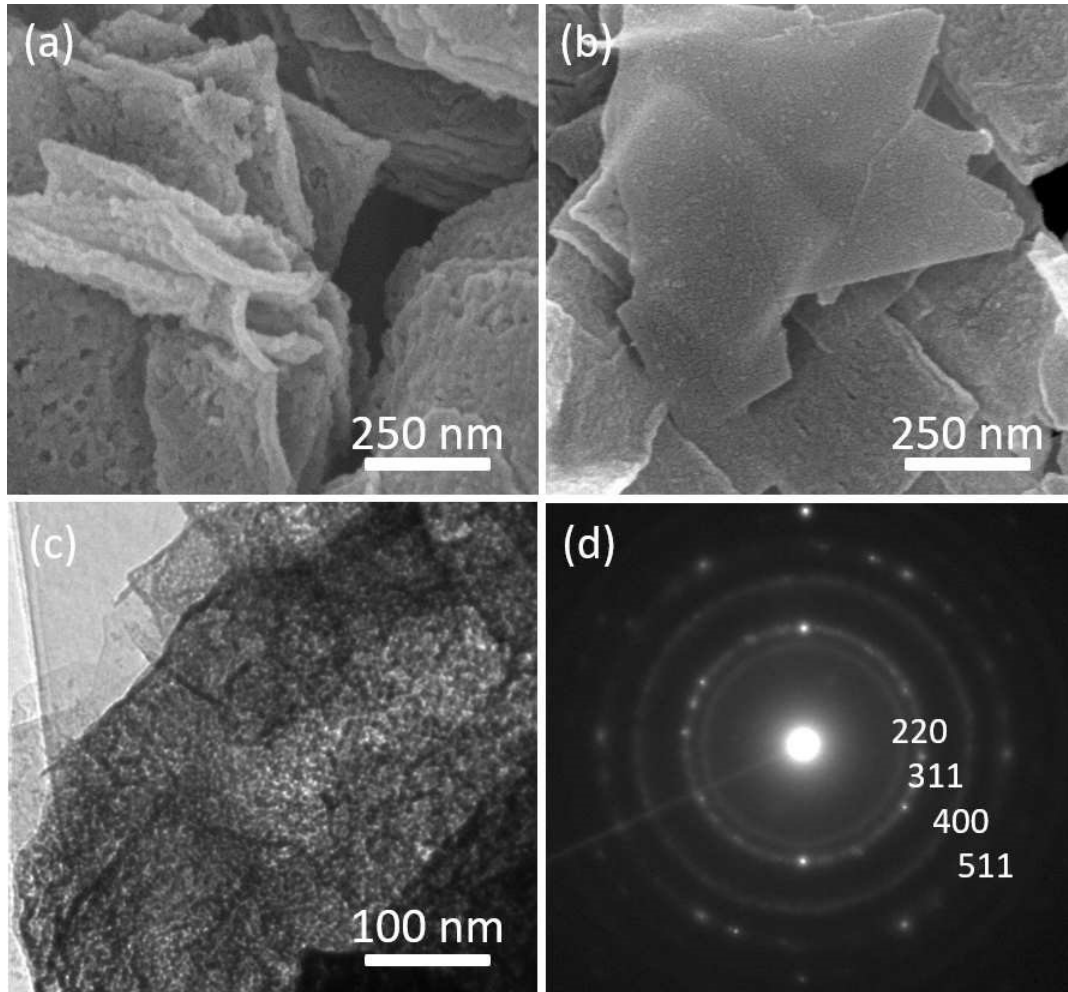


Figure 4-8 (a) SEM image of NiCo-oxide and (b) SEM image, (c) TEM image and (d) ED patterns for NiCo-oxide/G composite.

The NiCo-oxide/G hybrid composites find a number of applications. In particular, these composites can offer richer charge storage contributions from the electrochemically active nickel and cobalt ions. In order to probe the capacitive behaviour of these hybrid composites, the NiCo-oxide/G electrodes along with the control electrodes; NiCo oxide and graphene sheets were investigated by cyclic voltammetry (CV) in an aqueous electrolyte of 3 M KOH at various scan rates as shown in **Figure 4-9**. To study the contribution of the current obtained from commercial graphite, a bare graphite was run as a standard electrode as shown in **Figure 4-9a**. In the case of NiCo oxide (**Figure 4-9b**) and NiCo-oxide/G composite (**Figure 4-9d**), the CV curves exhibit broad and pronounced oxidation and reduction peaks clearly, indicating the capacitive behaviour of these composite electrodes. Typically, the redox peaks indicate that the

capacitive response originates from the faradaic redox reactions.[26] The presence of broad peaks could possibly be due to the contribution of various NiCo oxides.[27] Similar redox peaks were observed for NiCo-oxides as well as for nickel cobaltite-based materials.[28,29] Notably, the NiCo-oxide/G electrode presents a considerably larger current density than the counterpart, the NiCo oxide electrode. Thus, an enhancement of electrochemical activity by hybridization of two components can be easily recognized from the representative CV curves.

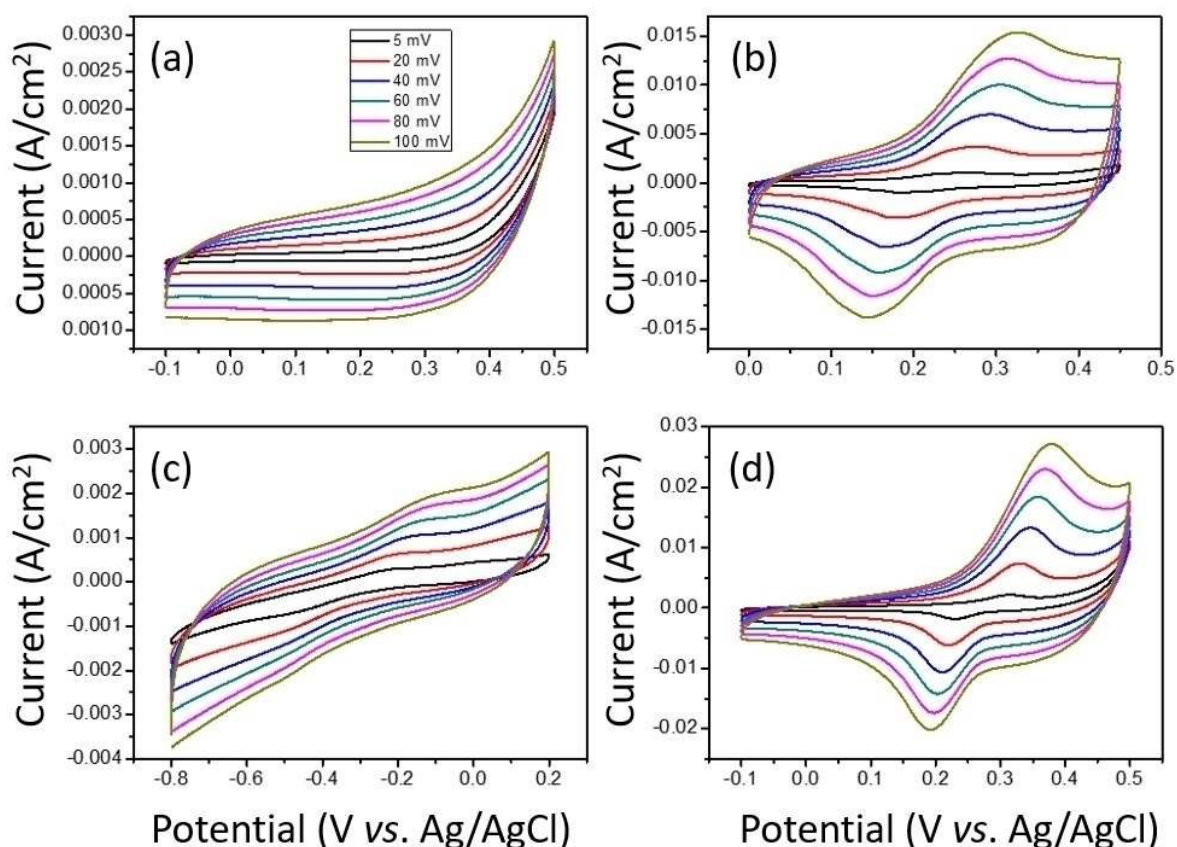


Figure 4-9 Cyclic voltammograms (CVs) of (a) commercial graphite, (b) NiCo-oxide, (c) graphene sheets, (d) NiCo-oxide/G composite, at different scan rates.

Further, the CV curves of these electrodes were recorded at different scan rates ranging from 5 to 100 mV s^{-1} to evaluate the high-rate discharge performance. As the scan rate increases, the anodic peak shifts to a higher potential whereas, the cathodic peak shifts to a lower potential. In both the electrodes (NiCo oxide and NiCo-oxide/G), the CV loops show typical redox couples, illustrating the high redox reversibility and typical pseudocapacitive behavior of the

electrodes compared with that of bare graphite or even graphene, electrodes (**Figure 4-9**). Even at a higher scan rate of 100 mV s^{-1} the CV curves of the hybrid electrode shows a pair of redox peaks, indicating fast redox reactions. The specific capacitance was determined from the CV curves by integrating over the full CV curve are given in **Table 4.2**. The calculated specific capacitance was found to be 199 F g^{-1} for the NiCo-oxide/G composites at a scan rate of 5 mV s^{-1} .

Table 4.2 The calculated specific capacitance values of different samples at different scan rates.

Scan rate (mV)	Graphite (F/g)	Graphene nanosheets (F/g)	NiCo oxide (F/g)	NiCo-oxide/G composite (F/g)
5	13.8	126	148	199
20	9.98	70.5	135	172
40	8.67	54.2	126	158
60	7.99	47.2	119	149
80	7.48	43.9	113	142
100	7.08	41.1	109	135

4.4. Conclusion

I have demonstrated a facile approach to hybridize nanoporous NiCo oxide flakes with graphene sheets. Electrostatic attraction plays a definitive role in compositing the positively charged cyano-bridged CoNi coordination polymer flakes (CoNi-CP) with the negatively charged graphene surfaces. Further, simple thermal treatment converts the graphene wrapped CoNi-CP flakes to Ni-Co oxide/graphene composites without affecting the integrity of the parent graphene sheets. This class of nanoporous graphene based composite architecture shows a high specific capacitance ($\sim 199 \text{ F g}^{-1}$) with good capacitance retention. I expect my strategy will be useful in the future for the synthesis of hybrid structures with dual characters for the application in energy-related systems.

References

- [1] R. R. Salunkhe, Y. V. Kaneti, J. Kim, J. H. Kim, Y. Yamauchi, *Acc. Chem. Res.* **2016**, *49*, 2796–2806.
- [2] Z. Lei, J. Zhang, L. L. Zhang, N. A. Kumar, X. S. Zhao, *Energy Environ. Sci.* **2016**, *9*, 1891–1930.
- [3] R. R. Salunkhe, Y. H. Lee, K. H. Chang, J. M. Li, P. Simon, J. Tang, N. L. Torad, C. C. Hu, Y. Yamauchi, *Chem. Euro. J.* **2014**, *20*, 13838–13852.
- [4] K. N. Wood, R. O’Hayre, S. Pylypenko, *Energy Environ. Sci.* **2014**, *7*, 1212–1249.
- [5] N. A. Kumar, J. B. Baek, *Nanotechnology* **2015**, *26*, 492001.
- [6] F. Du, D. Yu, L. Dai, S. Ganguli, V. Varshney, A. K. Roy, *Chem. Mater* **2011**, *23*, 4810–4816
- [7] P. Tamailarasan, S. Ramaprabhu, *J. Phys. Chem.* **2012**, *116*, 14179–14187.
- [8] N. A. Kumar, J. B. Baek, *Chem. Commun.* **2014**, *50*, 6298–6308.
- [9] N. A. Kumar, H. J. Choi, Y. R. Shin, D. W. Chang, L. Dai, J. B. Baek, *ACS Nano* **2012**, *6*, 1715–1723.
- [10] N. A. Kumar, H. J. Choi, A. Bund, J. B. Baek, Y. T. Jeong, *J. Mater. Chem.* **2012**, *22*, 12268–12274.
- [11] R. S. Kate, S. A. Khalate, R. J. Deokate, *J. Alloys Compd.* **2018**, *734*, 89–111.
- [12] G. Zhang, X. Xiao, B. Li, P. Gu, H. Xue, H. Pang, *J. Mater. Chem. A* **2017**, *5*, 8155–8186.
- [13] X. Li, L. Wang, J. Shi, N. Du, G. He, *ACS Appl. Mater. Inter.* **2016**, *8*, 17276–17283.
- [14] J. Shi, X. Li, G. He, L. Zhang, M. Li, *J. Mater. Chem. A* **2015**, *3*, 20619–20626.
- [15] M. B. Zakaria, M. Hu, M. Pramanik, C. Li, J. Tang, A. Aldalbahi, S. M. Alshehri, V. Malgras and Y. Yamauchi, *Chem. Asian J.* **2015**, *10*, 1541–1545.
- [16] B. H. Toby and R. B. Von Dreele, *J. Appl. Crystallogr.* **2013**, *46*, 544–549.
- [17] M. B. Zakaria, M. Hu, M. Pramanik, C. Li, J. Tang, A. Aldalbahi, S. M. Alshehri, V. Malgras, Y. Yamauchi, *Chem. Asian J.* **2015**, *10*, 1541–1545.

- [18] M. B. Zakaria, V. Malgras, T. Takei, C. Li, Y. Yamauchi, *Chem. Commun.* **2015**, *51*, 16409–16412.
- [19] W. Zhu, K. Liu, X. Sun, X. Wang, Y. Li, L. Cheng, Z. Liu, *ACS Appl. Mater. Inter.* **2015**, *7*, 11575–11582.
- [20] Z. Kartal, A. Ölmez, *Z. Naturforsch* **2005**, *60a*, 537–540.
- [21] Z. Trávníček, R. Zbořil, M. Matiková-Mařarová, B. Drahoš, J. Černák, *Chem. Cent. J.* **2013**, *7*, 7–28.
- [22] A. Ray, I. Bhowmick, W. S. Sheldrick, A. D. Jana and M. Ali, *J. Solid State Chem.* **2009**, *182*, 2608-2612.
- [23] N. J. Robertson, Z. Qin, G. C. Dallinger, E. B. Lobkovsky, S. Lee and G. W. Coates, *Dalton Trans.* **2006**, 5390-5395.
- [24] Y. Hernandez, V. Nicolosi, M. Lotya, F. M. Blighe, Z. Sun, S. De, I. T. McGovern, B. Holland, M. Byrne, Y. K. Gun'Ko, J. J. Boland, P. Niraj, G. Duesberg, S. Krishnamurthy, R. Goodhue, J. Hutchison, V. Scardaci, A. C. Ferrari, J. N. Coleman, *Nat. Nanotechnol.* **2008**, *3*, 563–568.
- [25] M. B. Zakaria, M. Hu, R. R. Salunkhe, M. Pramanik, K. Takai, V. Malgras, S. Choi, S. X. Dou, J. H. Kim, M. Imura, S. Ishihara, Y. Yamauchi, *Chem. Eur. J.* **2015**, *21*, 3605–3612.
- [26] R. Wang, X. Yan, *Sci. Rep.* **2014**, *4*, 3712.
- [27] C. Tang, Z. Tang, H. Gong, *J. Electrochem. Soc.* **2012**, *159*, A538-A547.
- [28] K. Feng, H. Huang, D. Shi, G. Diao, X. Zhang, *J. Mater. Res.* **2018**, *33*, 1167–1178.
- [29] P. Hao, J. Tian, Y. Sang, C. C. Tuan, G. Cui, X. Shi, C. P. Wong, B. Tang, H. Liu, *Nanoscale* **2016**, *8*, 16292–16301.

Chapter 5

Synthesis of Hollow Co–Fe Prussian Blue Analogue Cubes by using Silica Spheres as a Sacrificial Template

5.1. Introduction

Coordination polymers, including porous coordination polymers (PCPs) and metal-organic frameworks (MOFs), have undergone extensive research in recent times. Such studies attract interest in industrial chemistry, materials science, and engineering. The functionality and the regularity of the shapes and sizes of PCPs and MOFs make them useful in separation, storage, catalysis, and so forth.[1–4] Their compositions can be generalized as $A_xM'_y[M''_z(CN)_6]$, where A is an alkali metal cation, M' and M'' are transition metal cations, and the sub- scripts (x, y and z) express non-stoichiometry (or lattice defects), depending also on the valence of the transition metal(s). Their properties can be tuned by selecting the transition-metal cations. When $M'=M''=Fe$, the final composition will be $Fe_4 [Fe(CN)_6]_3 \cdot xH_2O$, which is generally known as Prussian Blue (PB). PB and PB analogues (PBAs) represent a well-known group of coordination polymers (CPs), where cyanide groups act as bridges between the transition metal ions ($M^{2+}-CN-M^{3+}$).[5, 6] Moreover, various PBA nanocubes were synthesized recently in solutions through a controlled crystal growth process.[7] Roy *et al.* demonstrated the formation of mesostructured PB framework using a ligand-assisted templating approach in formamide.[8] Other PBAs with various morphologies (*e.g.* nanowires, nanocubes, nanospheres, and nanotubes) have been reported through different methods such as sonochemical, hydrothermal, electrodeposition, and microwave-assisted methods.[9] Dual-textured PB cubes with nanoporous shells are also reliable electrode materials for sodium-ion storage.[10] Taking advantage of their hybrid nanostructures composed of porous and non-porous domains, dual-textured PB cubes exhibit high reversible capacities, good rate capabilities, stable cyclic performances, and excellent dimensional stabilities even after several charge–discharge cycles, offering new opportunities for the development of robust and high-performance rechargeable sodium-ion batteries.

Although several PB and PBA nanostructures have been re- ported, hollow PBAs have attracted great interests because of their enhanced physical and chemical properties. For example, Maurin-Pasturel *et al.* reported the synthesis of hollow NiFe–PBA nanoparticles using gold nanoparticles as a sacrificial template.[11] By simply dispersing the core–shell

Au@NiFe–PBA in KCN solution, hollow NiFe–PBA could be obtained, because of the intrinsic porosity of the PBA network. In addition, Risset *et al.* demonstrated a facile surfactant-free route to synthesize uniform $\text{Rb}_{0.4}\text{M}_4[\text{Fe}(\text{CN})_6]_{2.8}\cdot 7.2\text{H}_2\text{O}$ (M=Co, Ni) hollow nanoparticles.[12] To the best of my knowledge, to date, only one effective method for the preparation of crystalline hollow PBA nanoparticles by etching with HCl under hydrothermal conditions has been demonstrated.[13] The previous study reported the preparation of hollow PBA cubes by using another PBA sacrificial core followed by removal through a chemical treatment.[14] By investigating the electrochemical performance of solid and hollow CoCo–PBA cubes, it was demonstrated that hollow CoCo–PBA cubes exhibited a higher surface area, which is the significant advantage of a hollow structure for providing more oxidation and reduction reaction sites for better performance in energy storage applications.

For the above nanostructures, a hollow structure is ideal for electrode materials in lithium- and sodium-ion batteries, because the unique nature of a hollow nanostructure can offer a more favorable path for the electrolyte and enlarge the electrochemically active surface area of the electrode materials, thereby improving the electrochemical kinetics. In this chapter, I demonstrate the facile synthesis of hollow CoFe–PBA cubes, using spherical silica cores as sacrificial templates. Recently, silica nanoparticles were used as hard templates, because they possess silanol groups on their surface, which induce the formation reaction of many shells on the surface of silica.[15] Also, it is possible to control the size and the shape of the hollow interiors without consideration of complicated reactions. This method can be applicable to PB and PBA systems for hollow inorganic nanostructures, as shown in this work.

5.2. Experimental Sections

5.2.1. Chemicals

Tetraethyl orthosilicate (TEOS, 99 wt%) and potassium hexacyanoferrate (III) hydrate were purchased from Sigma–Aldrich, USA. Ammonium hydroxide solution (NH_4OH , 25 wt%), hydrofluoric acid (HF, 10wt%), trisodium citrate dihydrate (TSCD), and cobalt (II) chloride anhydrous (CoCl_2) were purchased from Nacalai Tesque, Inc., Japan. All reagents were used without further purification. The spherical silica particles were prepared according to Stçber’s

method. In these procedures, 21 mL of tetraethyl orthosilicate (TEOS, 99 wt%), 9 mL of deionized water, and 245 mL of NH_4OH solution (25 wt%) were added to 225 mL of ethanol and stirred at room temperature for 4h. A white colloidal solution of silica particles was obtained. The silica particles were separated by centrifugation, washed by ethanol for four times, and dried under ambient conditions at room temperature.

5.2.2. Synthesis of Hollow CoFe–PBA

Tetraethyl orthosilicate (TEOS, 99 wt%) and potassium hexacyanoferrate (III) hydrate were purchased from Sigma–Aldrich, USA. Ammonium hydroxide solution (NH_4OH , 25 wt%), hydrofluoric acid (HF, 10wt%), trisodium citrate dihydrate (TSCD), and cobalt (II) chloride anhydrous (CoCl_2) were purchased from Nacalai Tesque, Inc., Japan. All reagents were used without further purification. The spherical silica particles were prepared according to Stçber’s method. In these procedures, 21 mL of tetraethyl orthosilicate (TEOS, 99 wt%), 9 mL of deionized water, and 245 mL of NH_4OH solution (25 wt%) were added to 225 mL of ethanol and stirred at room temperature for 4h. A white colloidal solution of silica particles was obtained. The silica particles were separated by centrifugation, washed by ethanol for four times, and dried under ambient conditions at room temperature.

5.2.3. Synthesis of Hollow CoFe–PBA

The previously prepared spherical silica particles (20 mg) were dispersed in a mixture consisting of cobalt chloride anhydrous (77.9 mg) and TSCD (397.1 mg) dissolved in distilled water (20 mL) to form solution A. At this stage, the surface of the silica particles was decorated with Co ions after interaction with the silanol groups. Meanwhile, potassium hexacyanoferrate (III) hydrate (133 mg) was dissolved in pure water (20 mL) to form clear solution B. Then, solutions A and B were mixed together whilst stirring followed by aging for 4 days. The $\text{SiO}_2@\text{CoFe-PBA}$ precipitate was collected by centrifugation and washing with water and ethanol several times. After drying at room temperature overnight, the SiO_2 cores were removed by etching with HF. $\text{SiO}_2@\text{CoFe-PBA}$ (40 mg) was suspended in 10% HF solution (25 mL) by stirring for 12 h to complete the silica removal. The hollow CoFe–PBA precipitate

was collected by centrifugation and washing with water and ethanol several times, which was dried at room temperature for 24 h.

5.2.4. Structural Characterization Afield-emission

A field-emission scanning electron microscope (FESEM; JEOL JSM- 7000F) and high-resolution transmission electron microscope (HRTEM; JEOL ARM-200F) were employed to characterize the morphology and the nanostructure. X-ray diffraction (XRD; Rigaku RINT 2500X diffractometer) patterns were obtained by using monochromated $\text{Cu}_{K\alpha}$ radiation (40 kV, 40 mA) at a scanning rate of 18 min^{-1} . The XRD data were collected in the 2θ range of $10\text{--}70^\circ$ under ambient conditions. The lattice parameters were refined by the Pawley method, using the GSAS-II software,[16] and the zero shifts of the patterns were corrected with background subtraction. The result of the fitting method was identical to the crystal structure of $\text{K}_2\text{Co}[\text{Fe}(\text{CN})_6]$ (CCDC 28669). Fourier transform infrared spectroscopy (FTIR) of a KBr pressed pellet sample was carried out by using a Thermoscientific Nicolet 4700 instrument, and the data were collected in the range of 500 to 4000 cm^{-1} at room temperature.

5.2.5. Electrochemical Measurements

The slurries were prepared by mixing the active materials (80 wt%) and poly (acrylic acid) and Super-P (10 wt%). The Super-P was used as a conducting agent. The mixer was dissolved in deionized water as a binder (10 wt%) with deionized water. To prepare the working electrodes, the obtained slurries were coated onto Al foil as a current collector. The electrodes were dried at 80°C for 30 min in a convection oven to evaporate the water, and were then heat-treated at 120°C overnight under vacuum. The cells were collected by using CR2032 coin-type half cells with sodium metal used as a counter electrode, glass fiber (GF/F; Whatman) used as a separator, and 0.7 m NaClO_4 dissolved in a mixed solvent of ethylene carbonate (EC) and diethyl carbonate (DEC) (1:1, v/v; Panax Etec Co. Ltd.) used as the electrolyte in an Ar-filled glove box. The cells were galvanostatically charged and discharged at a constant current (CC) within the voltage window of $2.0\text{--}4.0 \text{ V}$ versus Na/Na^+ at 10 mA g^{-1} at room temperature.

5.3. Results and Discussion

The synthetic scheme for the hollow CoFe–PBA nanocubes is shown in **Figure 5-1**. First, the CoFe–PBA grew on the spherical silica particle. After the reaction was complete, the SiO₂@CoFe precipitate was collected by centrifugation and washing with water and ethanol. Finally, the SiO₂ cores were removed by etching, using HF solution to prepare the hollow CoFe–PBA cubes. The morphology and size of the silica spheres, core–shell SiO₂@CoFe–PBA cubes, and hollow CoFe–PBA cubes were investigated by using scanning electron microscopy (SEM) and transmission electron microscopy (TEM) (**Figure 5-2**). Spherical silica particles of around 150 nm in diameter were used as the template (**Figure 5-2a**). After coating with the CoFe–PBA shell, the average particle size became around 200 nm (**Figure 5-2b**), indicating that the shell thickness is around 50 nm. After removal of the silica template, hollow CoFe–PBA cubes were obtained (**Figure 5-2c**). The hollow interior was more than 150 nm in diameter, which was larger than the size of the starting silica particles. This is because the etching agent still works even after the removal of silica particles, resulting in the formation of a larger cavity than expected. **Figure 5-3** shows wide-angle XRD patterns for silica spheres, solid CoFe PBA, core–shell SiO₂@CoFe–PBA cubes, and hollow CoFe–PBA cubes. A broad diffraction peak was noticed from 15 to 30°, which was assigned to silica. The XRD patterns of the core–shell SiO₂@CoFe–PBA cubes and the hollow CoFe–PBA cubes showed the same diffraction patterns of the solid CoFe–PBA, which could be attributed to the face-centered-cubic crystal structure with the Fm3m unit cell. The XRD diffraction peaks of the hollow CoFe–PBA become a little broad, owing to a decrease in the original crystallinity of CoFe–PBAs. However, the crystal structure is preserved even after the removal of the silica cores.

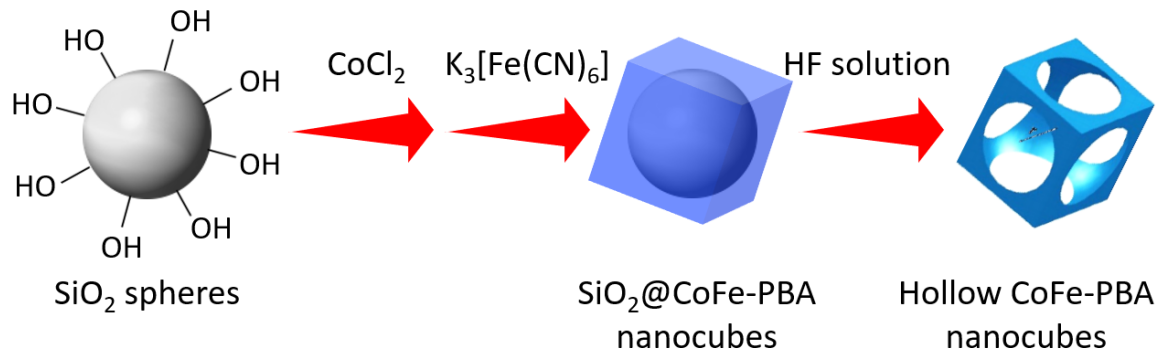


Figure 5-1. Schematic illustration of the formation of hollow CoFe–PBA using silica spheres as sacrificial templates.

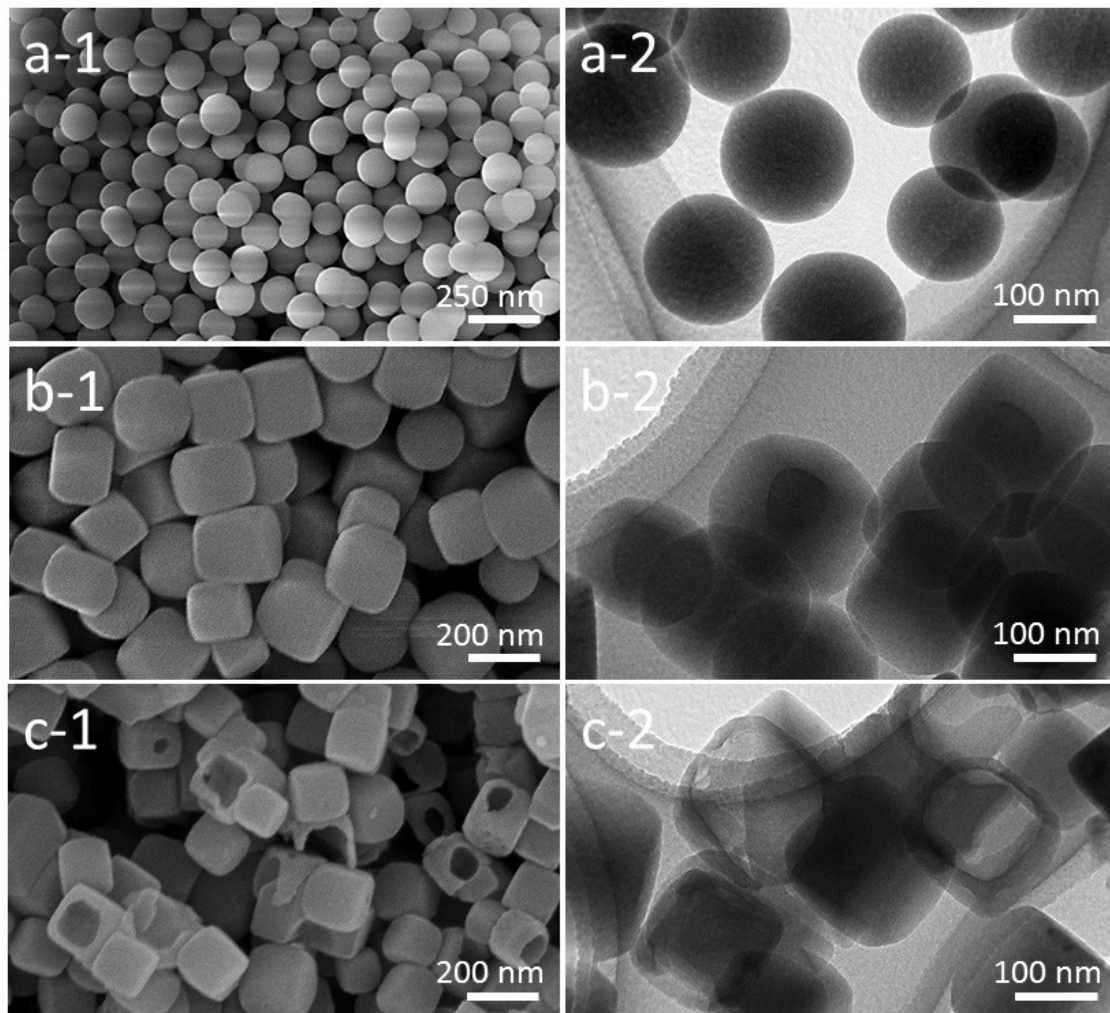


Figure 5-2. SEM (1) and TEM (2) images of a) silica spheres, b) SiO₂@CoFe–PBA, and c) hollow CoFe–PBA cubes.

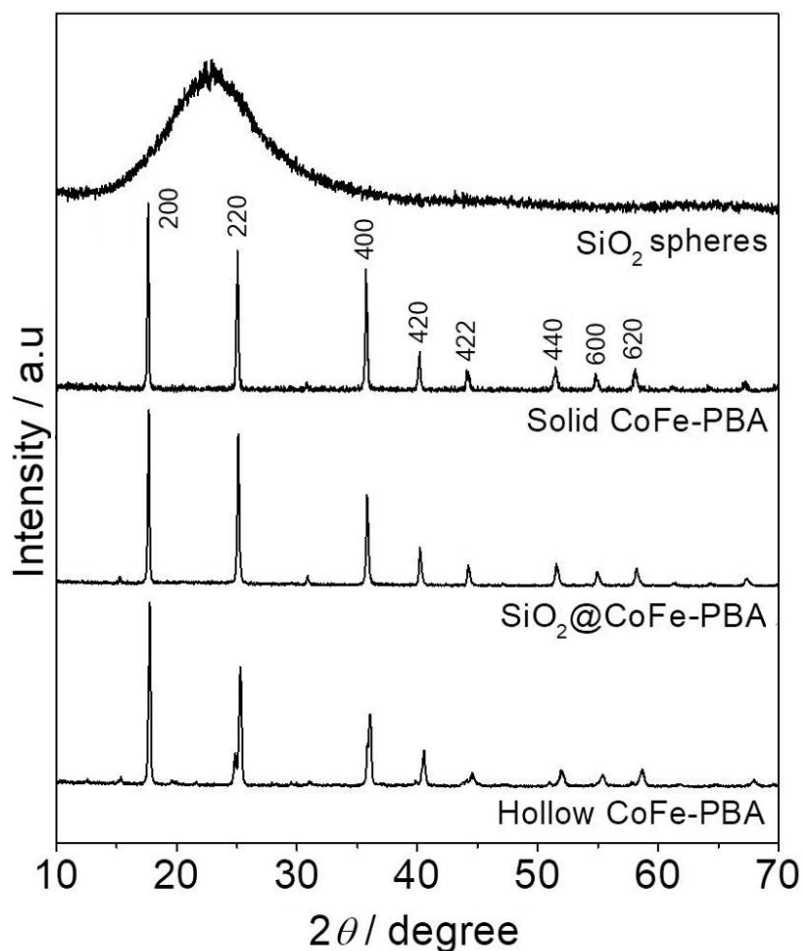


Figure 5-3. Wide-angle XRD diffraction patterns for silica spheres, solid CoFe–PBA, SiO_2 @CoFe–PBA, and hollow CoFe–PBA cubes.

The FTIR spectrum of as-prepared core–shell SiO_2 @CoFe–PBA is shown in **Figure 5-4**. The band at 2114 cm^{-1} could be indexed to the CN stretching ($\text{Co}^{\text{III}}\text{--NC--Fe}^{\text{II}}$), [17] whereas the band at 1110 cm^{-1} could be assigned to the Si–O–Si vibration. [18] **Figures 5-5** and **5-6** show the XRD patterns of as-prepared CoFe–PBA and core–shell SiO_2 @CoFe–PBA. The Pawley fitting of these XRD patterns shows that the structure of each sample is in the same space group. The structural and crystallographic details are provided in **Table 5.1**. These data indicate the successful coating of CoFe–PBA on the silica spheres.

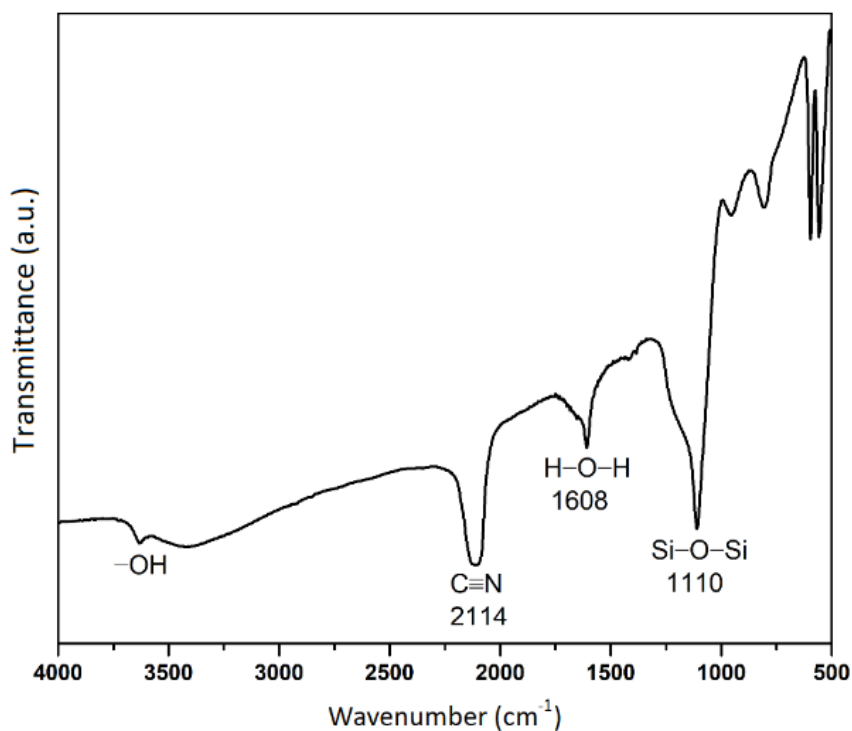


Figure 5-4 FTIR spectrum of SiO₂@CoFe-PBA.

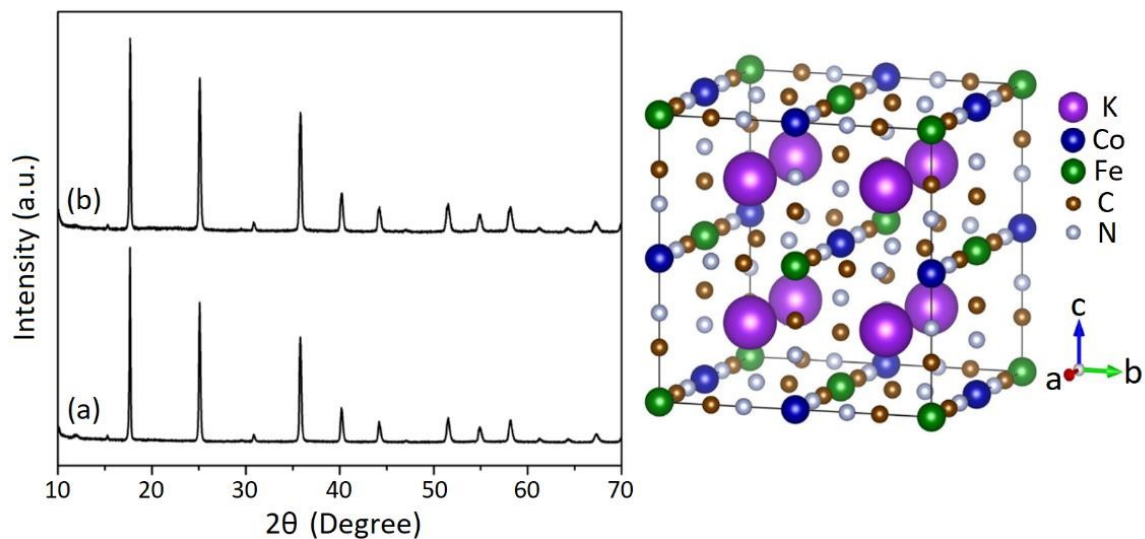


Figure 5-5 XRD patterns of (a) CoFe-PBA and (b) SiO₂@CoFe-PBA. The unit cell of K₂Co[Fe(CN)₆] (CCDC 28669) is also shown (The Co:Fe ratio in the model structure is 1:1.).

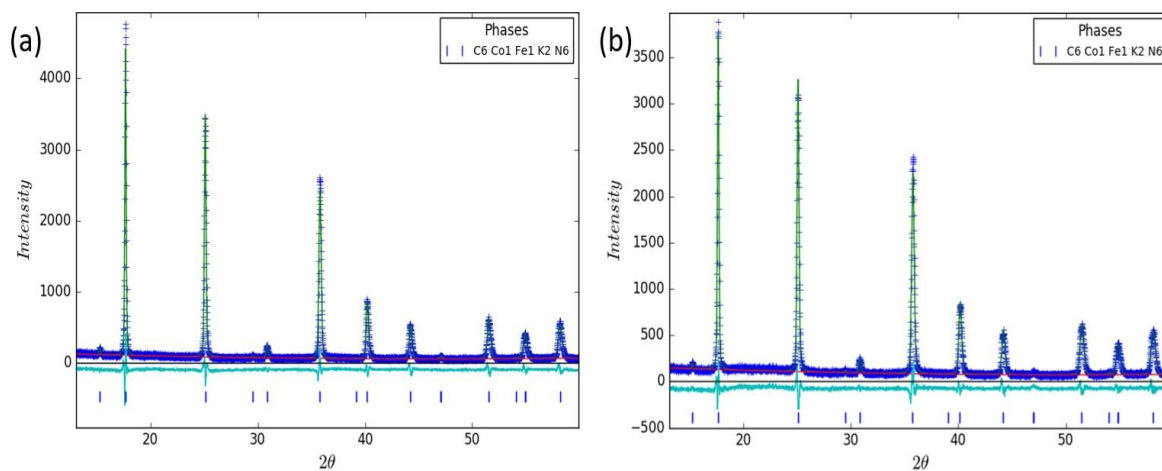


Figure 5-6 XRD patterns and the patterns calculated by the Pawley fitting analysis of (a) CoFe-PBA and (b) SiO₂@CoFe-PBA.

Table 5.1 Lattice constants obtained by the Pawley fitting of XRD data.

	CoFe-PBA	SiO ₂ @CoFe-PBA
Space group	$F\bar{4}5m$	$F\bar{4}5m$
a (Å)	10.0154(4)	10.0363(4)
b (Å)	10.0154(4)	10.0363(4)
c (Å)	10.0154(4)	10.0363(4)
α (°)	90	90
β (°)	90	90
γ (°)	90	90
V (Å ³)	1004.64(12)	1010.91(13)
wR (%)	11.528	10.746
GOF	1.41	1.39

Recently, lithium-ion batteries (LIBs) and sodium-ion batteries (SIBs) with PB and PBAs as electrode materials have been widely explored.[19,20] Owing to the high abundance and suitable redox potential, SIBs are considered possible replacements for LIBs, especially for applications in large energy storage devices.[21] It is widely accepted that the nanostructure of materials holds the key to their electrochemical reactivity.[22, 23] In this context, PB and PBAs offer a solution, because they possess a three-dimensional open framework with large interstitial sites for a high rate of mass transfer to ward alkali cations that can improve their cycle performance at high currents.[19,20] In particular, the hollow structure is known to

improve the electrochemical properties of electrode materials in LIBs and SIBs, as the unique nature of hollow microstructures can offer more favorable pathway for the electrolyte and enlarge the electro-chemically active surface area of electrode materials. Thus, to understand the effect of the nanostructure modification of CoFe–PBA on the electrochemical sodium-ion storage characteristics, solid and hollow CoFe–PBA materials were investigated as cathode materials for SIBs. **Figure 5-7a** shows the voltage profiles of solid and hollow CoFe–PBA cathodes for SIBs. Even though their capacities were relatively low compared to that of other PBA cathodes in previous reports,[24, 25] I clearly found that the hollow nanostructure could significantly improve the sodium-ion storage characteristics of CoFe–PBA cathode materials. Although the solid CoFe–PBA electrode showed just 12.5 mAhg^{-1} in the first cycle, the hollow structured CoFe–PBA electrode showed reversible capacities that were approximately two times higher than the non-treated solid homologue in the same cycle. The inset of **Figure 5-7a** shows the differential capacity plots (DCPs) of solid and hollow CoFe–PBA electrodes for the first cycle. Upon the charging process, the DCP peak of the hollow CoFe–PBA electrode was observed at a lower potential ($3.30 \text{ Vvs. Na/Na}^+$) than that of solid CoFe–PBA ($3.38 \text{ Vvs. Na/Na}^+$). This result combined with the much-improved capacity of hollow CoFe–PBA clearly reveals that nanostructure modification can reduce the over potential of the CoFe–PBA electrode during cycling. Such an improvement in the hollow CoFe–PBA cathode can be explained by the aforementioned nanostructure, which is highly favorable for electrochemical sodium-ion insertion and removal in CoFe–PBA. As shown in **Figure 5-7b**, hollow CoFe–PBA electrode shows fairly stable cycle performance during cycling without significant decrease in the capacity, which is almost double that of the untreated solid CoFe–PBA electrode. This result suggests that the hollow structuring of CoFe–PBA does not have a negative influence on the reliability of repeated sodium-ion insertion and removal process over 100 cycles.

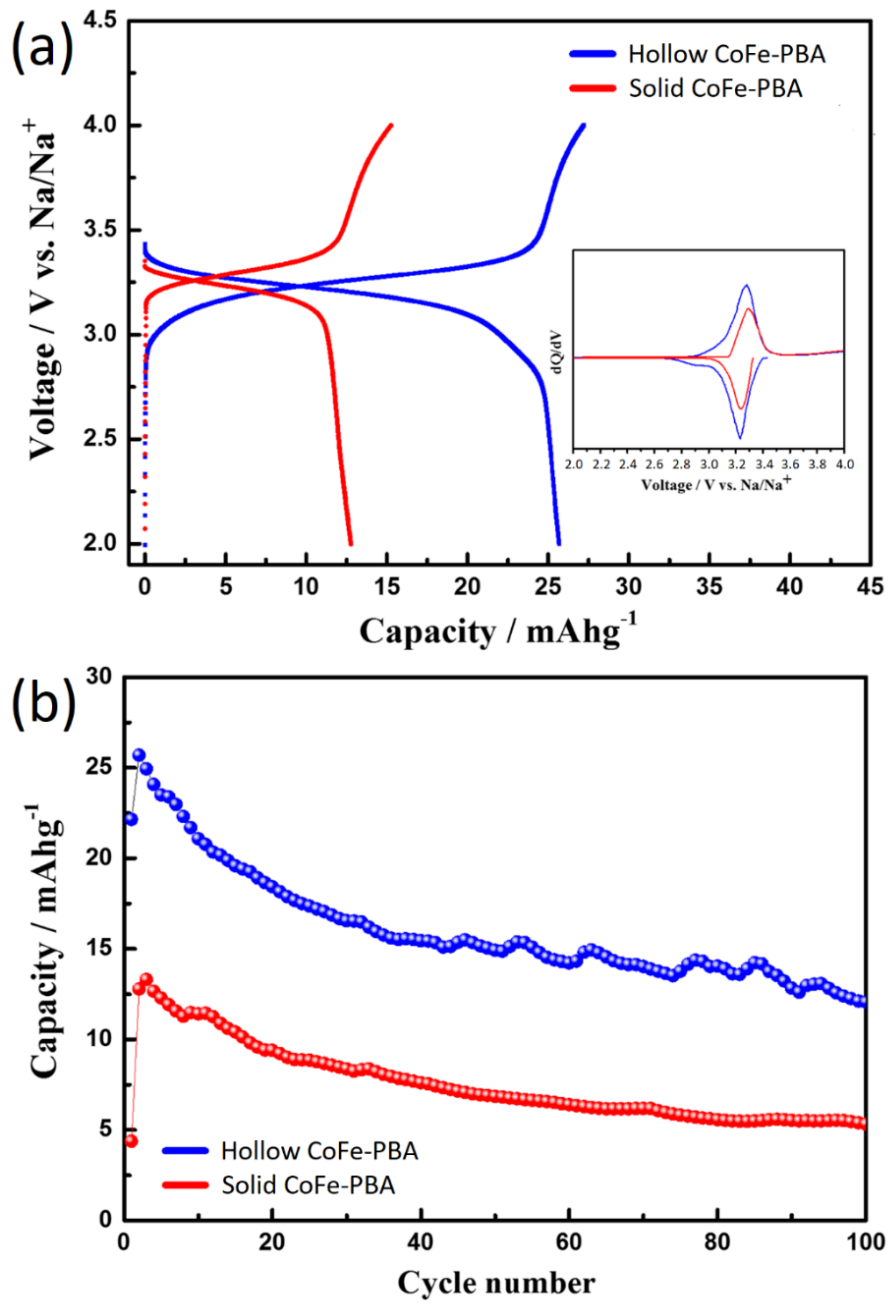


Figure 5-7 (a) Voltage profiles during the initial two cycles and (b) cycle performance of solid and hollow Co-Fe cube.

5.4. Conclusion

I demonstrated the formation of hollow CoFe–PBA nanocubes by using silica spheres as hard templates and examined their feasibility as cathode materials for SIBs. The silanol groups on the surface of the silica spheres reacted with cobalt cations in the first step. Nucleation of CoFe–PBA started simultaneously upon addition of iron cyanide ligands in the second step. After aging overnight, a thin shell of CoFe–PBA was successfully formed on the surface of the silica spheres. Silica cores were then removed by chemical etching, yielding hollow CoFe–PBA nanocubes. The hollow nanostructure of CoFe–PBA nanocubes helps to improve the storage capacity of sodium ions with stable cycle performance compared to the solid CoFe–PBA nanocubes. I strongly believe that my synthetic approach will be useful in the future for the formation of various PB and PBAs with open frame works, high specific surface area, improved storage capacity, and stable cycle performance at high currents for SIBs.

References

- [1] F. Debatin, A. Thomas, A. Kelling, N. Hedin, Z. Bacsik, I. Senkovska, S. Kaskel, M. Junginger, H. Müller, U. Schilde, *Angew.Chem. Int. Ed.* **2010**, *49*,1258–1262; *Angew.Chem.* **2010**, *122*,1280–1284.
- [2] J. Heine, K. Müller-Buschbaum, *Chem. Soc. Rev.* **2013**, *42*,9232–9242.
- [3] Y. B. Huang, J. Liang, X. S. Wang, R. Cao, *Chem. Soc. Rev.* **2017**, *46*,126–157.
- [4] D. Tanaka, A. Henke, K. Albrecht, M. Moeller, K. Nakagawa, S. Kitagawa, *J. Groll, Nat. Chem.* **2010**, *2*,410–416.
- [5] M. B. Zakaria, A. A. Belik, C. H. Liu, H. Y. Hsieh, Y. T. Liao, V. Malgras, Y. Yamauchi, K. C. W. Wu, *Chem.Asian J.* **2015**, *10*,1457–1462.
- [6] S. Adak, L. L. Daemen, M. Hartl, D. Williams, J. Summerhill, H. Nakotte, *J. Solid State Chem.* **2011**, *184*,2854–2861.
- [7] M. Hu, S. Ishihara, K. Ariga, M. Imura, Y. Yamauchi, *Chem. Eur.J.* **2013**, *19*,1882–1885.
- [8] X. Roy, L. K. Thompson, N. Coombs, M. J. MacLachlan, *Angew.Chem.Int. Ed.* **2008**, *47*,511–514; *Angew.Chem.* **2008**, *120*,521–524.

- [9] M. B. Zakaria, T. Chikyow, *Coord.Chem. Rev.* **2017**, 352,328–345.
- [10] D. S. Kim, M. B. Zakaria, M.-S. Park, A. Alowasheer, S. M. Alshehri, Y. Yamauchi, H. Kim, *Electrochim. Acta* **2017**, 240,300–306.
- [11] G. Maurin-Pasturel, J. Long, Y. Guari, F. Godiard, M. G. Willinger, C. Guerin, J. Larionova, *Angew.Chem. Int. Ed.* **2014**, 53,3872–3876; *Angew. Chem.* **2014**, 126,3953–3957.
- [12] O. N. Risset, E. S. Knowles, S. Ma, M. W. Meisel, D. R. Talham, *Chem. Mater.* **2013**, 25,42–47.
- [13] M. Hu, S. Furukawa, R. Ohtani, H. Sukegawa, Y. Nemoto, J. Reboul, S. Kitagawa, Y. Yamauchi, *Angew.Chem. Int. Ed.* **2012**, 51,984–988; *Angew. Chem.* **2012**, 124,1008–1012.
- [14] M. B. Zakaria, M. Hu, M. Imura, R. R. Salunkhe, N. Umezawa, H. Hamoudi, A. A. Belik, Y. Yamauchi, *Chem. Eur.J.* **2014**, 20,17375–17384.
- [15] A. Thomas, F. Goettmann, M. Antonietti, *Chem. Mater.* **2008**, 20,738–755.
- [16] B. H. Toby, R. B. Von Dreele, *J. Appl. Crystallogr.* **2013**, 46,544–549.
- [17] G. Fornasieri, M. Aouadi, P. Durand, P. Beaunier, E. Rivière, A. Bleuzen, *Chem. Commun.* **2010**, 46,8061–8063.
- [18] J. Manokaran, R. Muruganatham, A. Muthukrishnaraj, N. Balasubramanian, *Electrochim. Acta* **2015**, 168,16–24.
- [19] J. Peng, J. Wang, H. Yi, W. J. Hu, Y. Yu, J. Yin, Y. Shen, Y. Liu, J. Luo, Y. Xu, P. Wei, Y. Li, Y. Jin, Y. Ding, L. Miao, J. Jiang, J. Han, Y. Huang, *Adv.Energy Mater.* **2018**, 8,1870048.
- [20] Y. Lu, L. Wang, J. Cheng, J. B. Goodenough, *Chem.Commun.* **2012**, 48, 6544–6546.
- [21] C. Vaalma, D. Buchholz, M. Weil, S. Passerini, *Nat. Rev.Mater.* **2018**, 3, 18013.
- [22] J. Ye, W. Liu, J. Cai, S. Chen, X. Zhao, H. Zhou, L. Qi, *J. Am. Chem. Soc.* **2011**, 133,933–940.
- [23] M. Okubo, E. Hosono, J. Kim, M. Enomoto, N. Kojima, T. Kudo, H. Zhou, I. Honma, *J. Am. Chem. Soc.* **2007**, 129,7444–7452.
- [24] J. Qian, C. Wu, Y. Cao, Z. Ma, Y. Huang, X. Ai, H. Yang, *Adv.Energy Mater.* **2018**, 8,1702619.

[25] X. Bie, K. Kubota, T. Hosaka, K. Chihara, S. Komaba, *J. PowerSources* **2018**, 378,322–330.

Chapter 6-1

Cyano-Bridged Cu-Ni Coordination Polymer Nanoflakes and Their Thermal Conversion to Mixed Cu-Ni Oxides

6-1.1. Introduction

Coordination polymers (CPs) have drawn significant attention because of their recent potential for energy and environmental applications.[1,2] Nanoarchitectures constructed from various molecular building blocks can bring out new chemical and physical properties through the creation of porous frameworks. Recently, one-dimensional (1D) (*e.g.*, nanorods, nanowires),[3] two-dimensional (2D) (*e.g.*, nanosheets, nanoflakes),[4] three-dimensional (3D) nanostructures (*e.g.*, nanocubes)[5] and bulk material[6] have been synthesized under various controlled synthetic conditions. Among these, 2D nanomaterials have attracted the most interest because of their novel physical or chemical properties which are distinct from their bulk counterparts.[7–10] 2D nanostructures possess highly accessible surface area which can enable guest molecules to effectively access the pore surface. Moreover, they exhibit numerous active sites which can boost the catalytic and electrochemical performance and more importantly, assembled 2D nanostructures are highly useful as membrane filters. Previously, ultrasonication-induced exfoliation methods have been used to prepare MOF (metal-organic framework) nanosheets.[7,8] Although exfoliation methods possess some important advantages, they are somewhat inconvenient due to the complicated synthetic procedures and the need for special equipment. Therefore, the development of a facile and convenient method for the large-scale preparation of 2D CPs is highly desired.

Among various CPs, cyano-bridged CPs have attracted increasing scientific interests in various fields, such as gas storage, batteries, catalysis, gas capture and separation, charge transfer, drug delivery, sensing and environmental clean-up.[11–14] Cyanide groups can act as a bridge between metals ions. The controlled thermal treatment of cyano-bridged CPs can lead to the creation of nanoporous hybrid metal oxides. During the thermal treatment of CPs in air, the metallic constituents remain in the frameworks and become oxidized to metal oxides, while the removed -CN- components can generate nanoporosity.[4,5] This method therefore can overcome the limitations of conventional methods (*e.g.*, soft- and hard-templating methods) for the synthesis of nanoporous metals oxides.[15]

In this chapter, I demonstrate the fabrication of a series of 2D cyano-bridged Cu-Ni CP nanoflakes through a controlled crystallization process with the assistance of trisodium citrate dihydrate (TSCD). Following thermal treatment in air, the -CN- constituents present within the Cu-Ni CP nanoflakes are removed and the metals Cu and Ni become oxidized to generate Cu-Ni mixed oxide nanoflakes with nanoporous structures. The effects of pertinent parameters, such as the concentration of TSCD and calcination temperature on the phase composition and morphology of the Cu-Ni CPs and the corresponding Cu-Ni mixed oxide nanoflakes were investigated.

Metal oxides and metal hydroxides have been studied and used for energy storage and conversion.[16–20] Especially, mixed metal oxides are very attractive due to the enhanced capacitance for supercapacitors.[21–25] Here, the electrochemical performance of the Cu-Ni mixed oxide nanoflakes calcined at different temperatures (300–500°C) for supercapacitors was investigated using a three-electrode system and the important parameters were evaluated.

6-1.2. Experimental Sections

6-1.2.1. Chemicals

Potassium tetracyanonickelate hydrate ($K_2[Ni(CN)_4].xH_2O$) was purchased from FUJIFILM Wako Pure Chemical Corporation (Osaka, Japan). Copper nitrate trihydrate ($Cu(NO_3)_2.3H_2O$) and trisodium citrate dehydrate ($Na_3C_6H_5O_7.2H_2O$) were obtained from Nacalai Tesque (Japan). All chemical reagents were used as received without additional purification steps.

6-1.2.2. Synthesis of 2D Cu-Ni CP flakes.

$Cu(NO_3)_2.3H_2O$ and trisodium citrate dehydrate (TSCD) were mixed together in 50 mL of water at room temperature to form a clear solution. In a separate bottle, $K_2[Ni(CN)_4]$ was dissolved in 50 mL water to form another clear solution. Then, the two solutions were mixed under magnetic stirring until the solution became clear and the resulting mixture was aged at room temperature for 24 h. After completion of the reaction, the precipitate was collected by centrifugation. Then, the product was thoroughly washed with water and ethanol for several times. Following drying at ambient temperature, 2D Cu-Ni CP nanoflakes were obtained. The

amount of trisodium citrate dehydrate (TSCD) was varied to prepare Cu-Ni nanoflakes with different size. The sample names are abbreviated as Cu-Ni x where x is the amount of TSCD (g). The detailed quantity of chemicals used for the synthesis is summarized in **Table 6-1.1**.

Table 6-1.1 Synthetic conditions of the various 2D Cu-Ni CPs. Sample

Sample	Cu(NO ₃) ₂ ·3H ₂ O (g)	K ₂ [Ni(CN) ₄] (g)	TSCD (g)	Surface Area (m ² g ⁻¹)
Cu-Ni_0.00	0.120	0.120	0.00	31.54
Cu-Ni_0.15	0.120	0.120	0.15	48.97
Cu-Ni_0.20	0.120	0.120	0.20	47.69
Cu-Ni_0.25	0.120	0.120	0.25	34.43

6-1.2.3. Thermal conversion from 2D Cu-Ni nanoflakes to mixed metal oxides.

The obtained Cu-Ni_{0.20} nanoflakes were used as the precursor and heated from room temperature to the desired temperature with a heating rate of 5°C min⁻¹ in air. After reaching the targeted temperature (300, 400 and 500°C), the samples were annealed for 1 h to complete the thermal decomposition of the Cu-Ni CP nanoflakes and then, they were cooled naturally to room temperature. The samples are labeled as Cu-Ni _{x} _{y} where x is the amount of TSCD (g) and y is the applied calcination temperature.

6-1.2.4. Characterization.

Wide-angle XRD patterns of the samples were collected using a Rigaku RINT 2500X diffractometer with monochromated Cu-K α radiation (40 kV, 40 mA) at a scanning rate of 1° min⁻¹. The parallel beam optics was used, which is the general way to analyse the powder sample. The morphological characterization of the samples was performed using a Hitachi SU8000 scanning electron microscope (SEM) operated at an accelerating voltage of 5 kV. Transmission electron microscopy (TEM) observation was performed using a JEM-2100F TEM system that was operated at 200 kV and equipped with energy-dispersive spectrometer (EDS). The crystal structure of the compound after calcination at 500°C was obtained by the

Pawley method using two starting structure model of CuO and NiO, with the GSAS II program and plotted with zero-shift correction and background subtraction.[26] Thermogravimetric-differential thermal analysis (TG-DTA) of the samples was performed using a Hitachi HT–Seiko Exter 6300 TG/DTA from room temperature to 1000°C under air at a fixed heating rate of 5°C min⁻¹. N₂ adsorption-desorption isotherms of the samples were achieved by employing a Quantachrome Autosorb gas sorption system at 77 K. Fourier transform infrared spectroscopy (FTIR) was used to identify the chemical constituents present on the samples. The samples were mixed with potassium bromide (KBr) and pressed into pellets. The FTIR spectra were collected at room temperature by using the Thermoscientific Nicolet 4700 instrument. UV-vis spectra were collected with the use of V-570 UV-Vis-NIR spectrophotometer made by JASCO.

6-1.2.5. Electrochemical measurements.

The electrochemical measurements were performed by using an electrochemical workstation (CHI 660e, CH Instruments). For the three-electrode measurements, Ag/AgCl and platinum wire were utilized as the reference electrode and counter electrode, respectively. The glassy carbon substrate (1 cm²) was used as the current collector. The working electrode was prepared by coating a slurry containing the active material (1 mg, 85 wt.%), super P (10 wt.%), polyvinylidene fluoride binder (PVDF) (5 wt.%), and N-methyl-2-pyrrolidone on carbon paper as the current collector. The proper amount of slurry was carefully dropped on the glassy carbon electrode (GCE). The coated electrode was dried in a vacuum oven at 80°C for 12 h. All the electrochemical measurements were conducted using 6 MKOH (aq) as the electrolyte. The gravimetric capacitances were calculated from the CV curves by using the following equation:

$$C_g = \frac{1}{ms(V_f - V_i)} \int_{V_i}^{V_f} I(V) dV$$

where ‘C_g’ is gravimetric capacitance (F g⁻¹), ‘s’ is the potential scan rate, ‘V’ is potential window, ‘I’ is current (A), ‘t’ is discharge time (s) and ‘m’ is the mass of active material in gram.

The galvanostatic charge-discharge (GCD) measurements were carried out at varying current densities of 1, 2, 4, 6 and 10 A g⁻¹. The gravimetric capacitances were calculated from the GCD curves via the following equation:

$$C_g = \frac{1 \times \int V dt}{M \times \Delta V^2}$$

where 'C_g' represents the gravimetric capacitance (F g⁻¹), 'ΔV' represents the potential window, 'I' represents the current (A), 't' represents the discharge time (s), and 'M' represents the total mass of active material (g).

6-1.3. Results and Discussion

The morphology of the as-prepared Cu-Ni CP particles was characterized using SEM, as presented in **Figure 6-1.1**. It is clear from this Figure that the concentration of TSCD is critical for controlling the structure and size of the formed 2D CP nanoflakes. Without TSCD, only irregularly-shaped nanoparticles with severe aggregation are obtained. (**Figure 6-1.1a**). In contrast, with increasing amount of the chelating agent, the nanoflake morphology becomes more obvious. It is well known that the particle size of nanoparticles is strongly influenced by the balance between nucleation and crystal growth. Based on the UV-*vis* spectra (**Figure 6-1.2**), it can be observed that following the addition of TSCD, the intensity of the maxima absorption peak of the Cu(NO₃)₂ solution is greatly enhanced and the position of the peak is slightly shifted. These changes are largely caused by the coordination reaction between citrate ions and Cu²⁺ ions [27,28]. The addition of TSCD creates a chelating effect which decelerates the coordination reaction between Cu²⁺ and K₂[Ni(CN)₄], thus leading to the reduction in crystallization speed of the CP particles. Yamauchi group has previously discovered that in the absence of citrate ions, very rapid formation of CP was achieved, and the reaction was terminated within a relatively short time. Thus, by implementing TSCD into the reaction system, the crystallization process of CP was delayed.[29,30] The previous ¹H NMR study demonstrated that citrate anions can stabilize the metal ions (*e.g.*, Ni²⁺) in the solution and the free metal ions released from the citrate complex can slowly react with K₂[Ni(CN)₄] to form the cyano-bridged Ni-Ni CP.[4] In the current reaction system, Cu²⁺ ions are freed in a controlled manner from the Cu-citrate complex and react with [Ni(CN)₄]²⁻ at the beginning of the reaction. This reaction leads to the generation of nuclei which undergo further growth by interacting with the free Cu²⁺ ions and [Ni(CN)₄]²⁻ to form the final Cu-Ni CP. Therefore, with increasing concentration of TSCD, the amount of nuclei generated at the beginning of the

reaction is reduced (**Figure 6-1.1c,d**). As a result, fewer nuclei undergo crystal growth by interacting with $[\text{Ni}(\text{CN})_4]^{2-}$ and Cu-Ni CP nanoflakes with larger sizes are obtained. In contrast, at lower concentrations of TSCD (**Figure 6-1.1a,b**), more free Cu^{2+} ions are available to react with $[\text{Ni}(\text{CN})_4]^{2-}$ immediately. Consequently, there is a greater amount of nuclei which undergo rapid growth at the initial stage of the reaction, leading to smaller-sized nanoflakes, as shown in **Figure 6-1.1a**. TEM images of the Cu-Ni CP synthesized under the typical conditions (Cu-Ni_0.20) are shown in **Figure 6-1.3**. The flake-like morphology is clearly observed over the entire area.

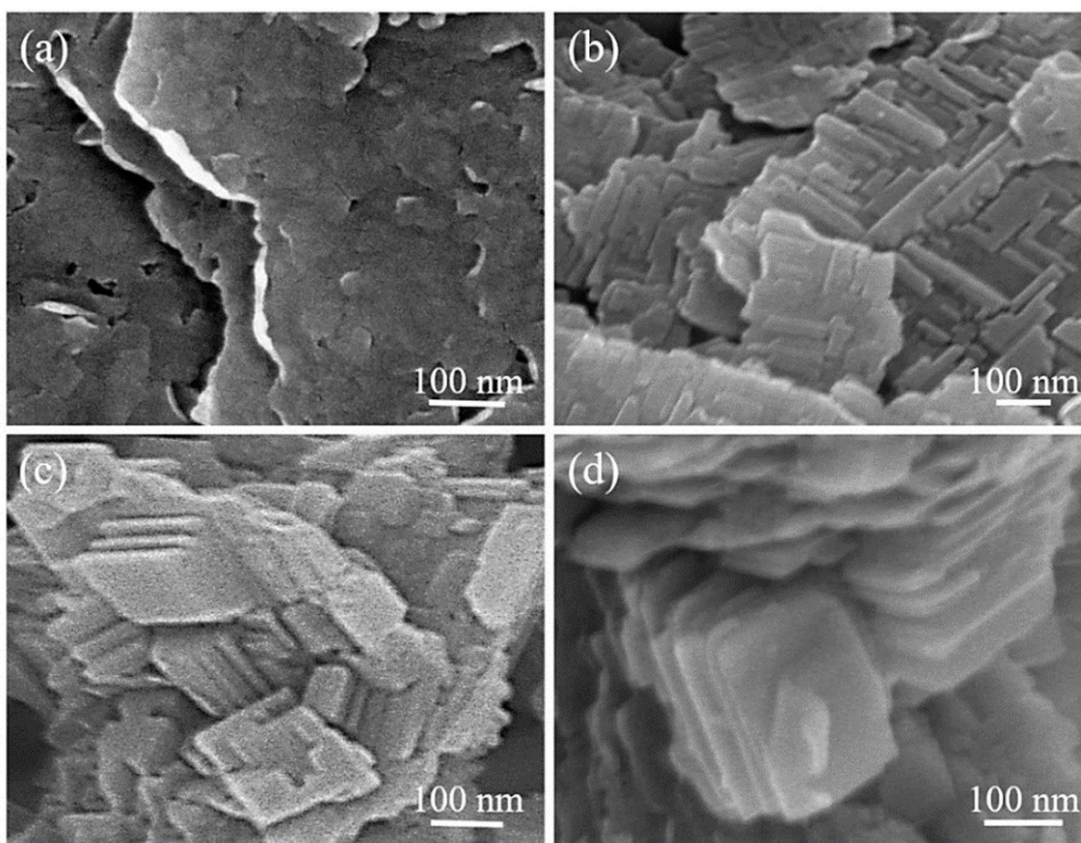


Figure 6-1.1 SEM images of 2D Cu-Ni CPs prepared with different amount of TSCD: (a) Cu-Ni_0.00; (b) Cu-Ni_0.15; (c) Cu-Ni_0.20 and (d) Cu-Ni_0.25).

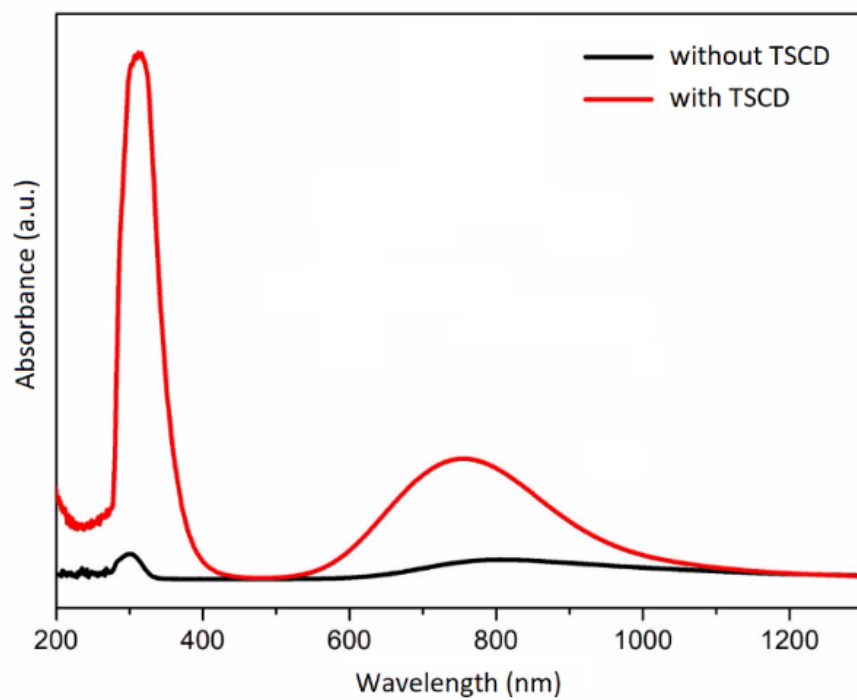


Figure 6-1.2 UV-*vis* spectra of $\text{Cu}(\text{NO}_3)_2$ solution with and without TSCD.

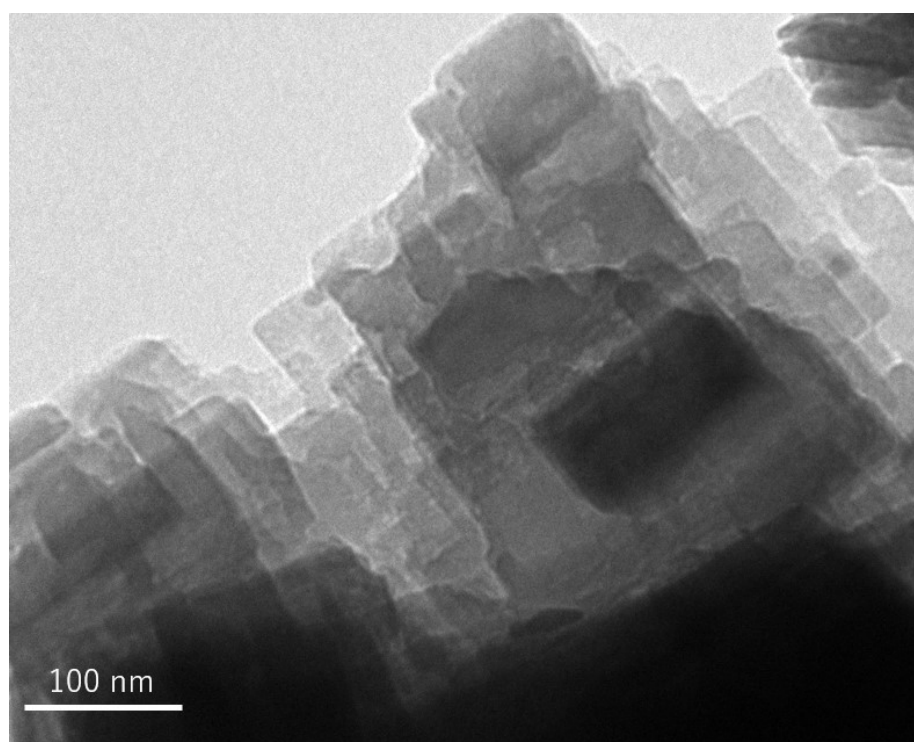


Figure 6-1.3 TEM image of $\text{Cu-Ni}_{0.2}$.

Figure 6-1.4 shows the FTIR spectrum of Cu-Ni_{0.20}, in which the presence of cyano-bridged complexes is identified by the existence of a sharp stretching band (CN) at 2000-2200 cm^{-1} . [31–33] The FTIR spectrum of the $\text{K}_2[\text{Ni}(\text{CN})_4] \cdot x\text{H}_2\text{O}$ shows a sharp stretching vibration (CN) at 2123 cm^{-1} . [34] In the FTIR spectrum of Cu-Ni_{0.20}, there is a shift of the stretching vibration (CN) band to a higher wavenumber of 2170 cm^{-1} . [35,36] This shift is caused by the stringing of the CN bond with other metal ions (Cu-CN-Ni) due to the kinematic effect [36,37]. In addition, the two peaks at 3450 cm^{-1} and 1616 cm^{-1} correspond to the O-H stretching vibration and the H-O-H bending vibration of water existing in the Cu-Ni_{0.20} sample. [31,32,38,39]

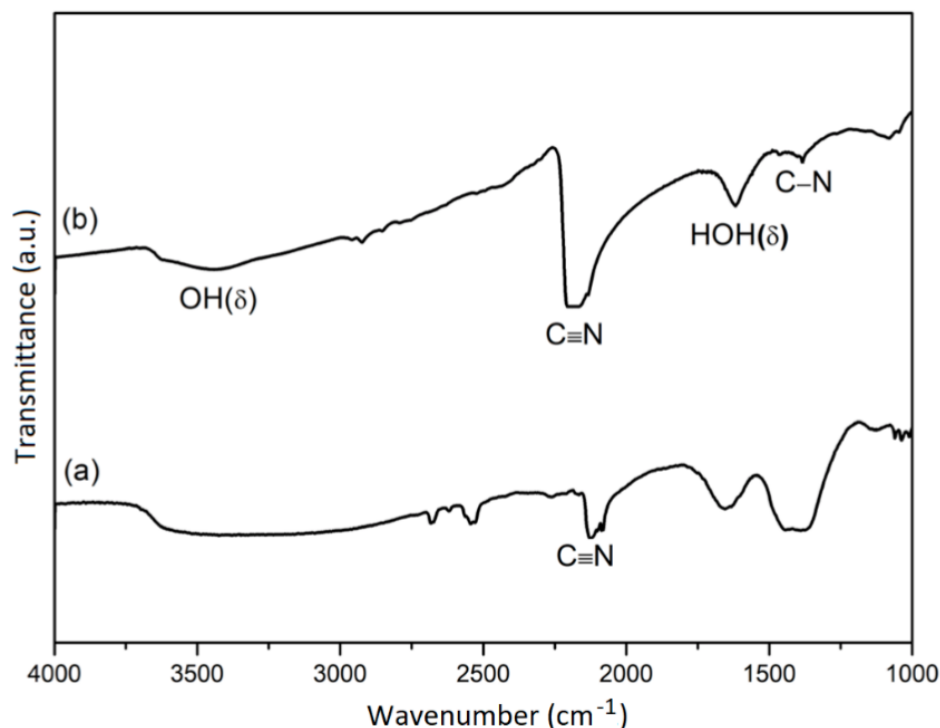


Figure 6-1.4 FTIR spectra of (a) $\text{K}_2\text{Ni}(\text{CN})_4 \cdot \text{H}_2\text{O}$ and (b) Cu-Ni_{0.20}.

In order to investigate the porosity, nitrogen (N_2) adsorption-desorption measurements were performed for all the CPs prepared with different amount of TSCD. Prior to the measurements, all the samples were degassed at 150°C for 24 h. This degassing condition is sufficient for achieving complete removal of water molecules from the Cu-Ni CPs, as will be explained in the later section. The BET surface areas of the Cu-Ni_{0.15} and Cu-Ni_{0.20}

samples are 49.0 and 47.7 m² g⁻¹, respectively, while the surface area of the Cu-Ni sample prepared without TSCD (Cu-Ni_0.00) is the lowest at 31.5 m² g⁻¹. In the case of irregularly shaped particles (Cu-Ni_0.00), N₂ gas cannot easily access the undeveloped pores, thereby leading to a low surface area. By further increasing the amount of TSCD, the surface area of Cu-Ni_0.25 is decreased to 34.4 m² g⁻¹. Thus, the accessibility of N₂ gas to the particle interior varies depending on particle sizes.

The TG-DTA analysis of the typical sample Cu-Ni_0.2 under air atmosphere is shown in **Figure 6-1.5**. A small weight loss at temperatures below 200°C is attributed to the release of water molecules existing in the Cu-Ni CPs. Following this, a clear endothermic reaction occurs at around 350°C and a large weight loss is observed at this stage as -CN- constituents are removed, and the metallic constituents are oxidized in air. In this work, I calcined the CPs at 300°C (minimal), however after reaching the designated temperature, the samples were annealed for 1 h to complete the thermal decomposition of Cu-Ni flakes. This thermal treatment is sufficient to completely remove the -CN- groups present within the CP nanoflakes and no carbon is present in the final product.

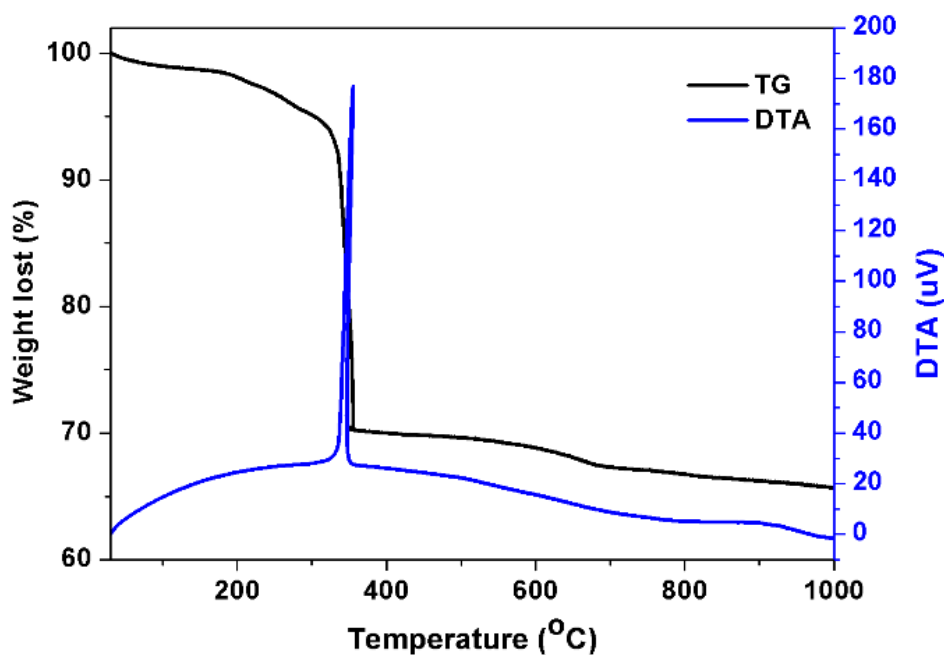


Figure 6-1.5 TG-DTA data of Cu-Ni_0.2. The measurement was carried out in air.

The SEM images of the various nanoporous metal oxide samples derived from the calcination of Cu-Ni_{0.2} CP nanoflakes at different temperatures (300 and 500°C) are shown in **Figure 6-1.6**. The sample calcined at 300°C almost entirely retains the original morphology of the Cu-Ni CP before calcination. However, when the applied calcination temperature is increased, a large structural change occurs through the fusion of several pores/voids via further crystallization of the framework. Wide-angle XRD patterns for the various calcined samples are shown in **Figure 6-1.7 a–c**. The XRD patterns of the samples calcined at 300, 400 and 500°C show no peaks originating from impurities or unoxidized Cu or Ni phase. All the peaks are in agreement with the standard JCPDS cards for CuO (No. 48-1548) and NiO (No. 47-1049). With the increase of applied calcination temperature, the full width at half maximums (FWHMs) are decreased, suggesting that the average crystallite sizes increase. Elemental analysis for the sample calcined at 300°C (Cu-Ni_{0.20_300}) shows that the resulting metal oxide product has similar content of Cu (37.90 at.%) and Ni (37.20 at.%). This ratio is almost similar to the starting composition before calcination, indicating the absence of evaporation of the metallic constituents.

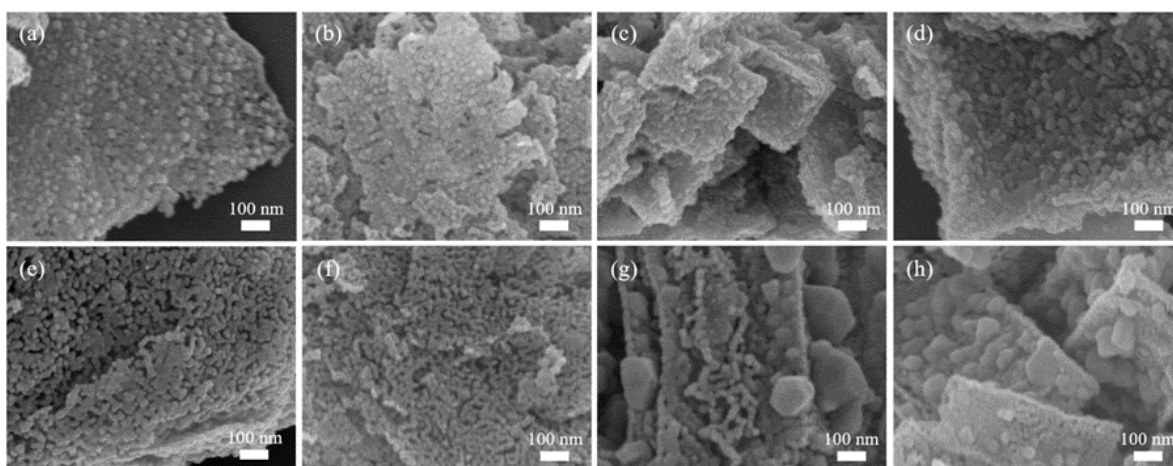


Figure 6-1.6 SEM images of (a) Cu-Ni_{0.00_300}; (b) Cu-Ni_{0.15_300}; (c) Cu-Ni_{0.20_300}; (d) Cu-Ni_{0.25_300}; (e) Cu-Ni_{0.00_500}; (f) Cu-Ni_{0.15_500}; (g) Cu-Ni_{0.20_500} and (h) Cu-Ni_{0.25_500}.

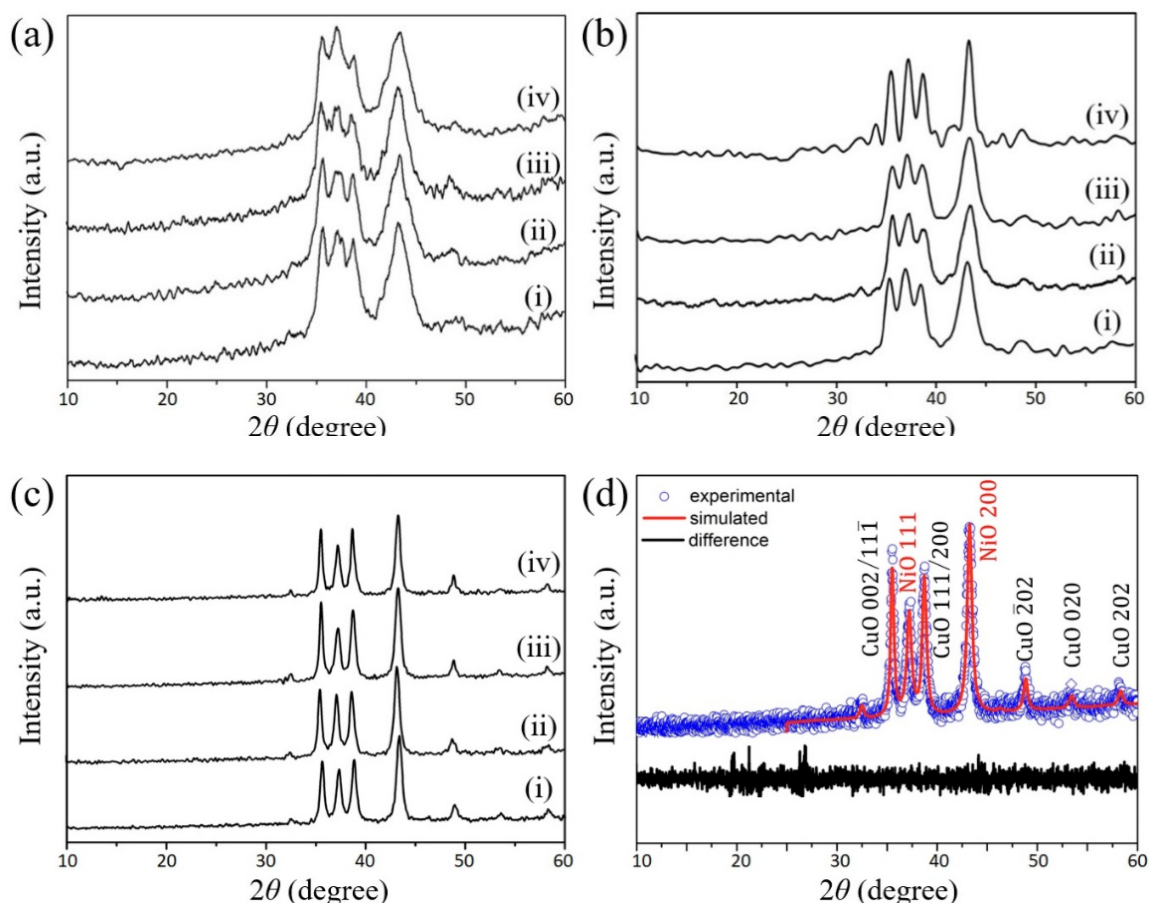


Figure 6-1.7 Wide-angle XRD patterns of the calcined samples at various temperatures ((a) 300°C; (b) 400°C and (c) 500°C) of (i) Cu-Ni_{0.00}, (ii) Cu-Ni_{0.15}, (iii) Cu-Ni_{0.20} and (iv) Cu-Ni_{0.25}; (d) Powder XRD pattern of Cu-Ni_{0.20_500} and refinement by the Pawley method.

After thermal treatment at 300 °C, the sample (Cu-Ni_{0.20_300}) was characterized by TEM (**Figure 6-1.8**). Small crystals with sizes between 5–10 nm aggregate together to form the nanoporous architecture. From the HRTEM image of this sample, clear lattice fringes with respective d-spacing of 0.21 nm and 0.24 nm are observed, which can be indexed to the (111) and (200) planes of NiO crystal, while the d-spacing of 0.25 nm is well matched with the d-spacing of (111) plane of CuO [40,41]. High angle annular dark field scanning transmission electron microscope (HAADF-STEM) images and the corresponding elemental mapping data confirm the flake-like structure and reveal the uniform distribution of the composing elements,

Ni, Cu and O throughout the entire area (**Figure 6-1.9**). These results therefore confirm the successful conversion of the Cu-Ni CPs into nanoporous oxides after calcination.

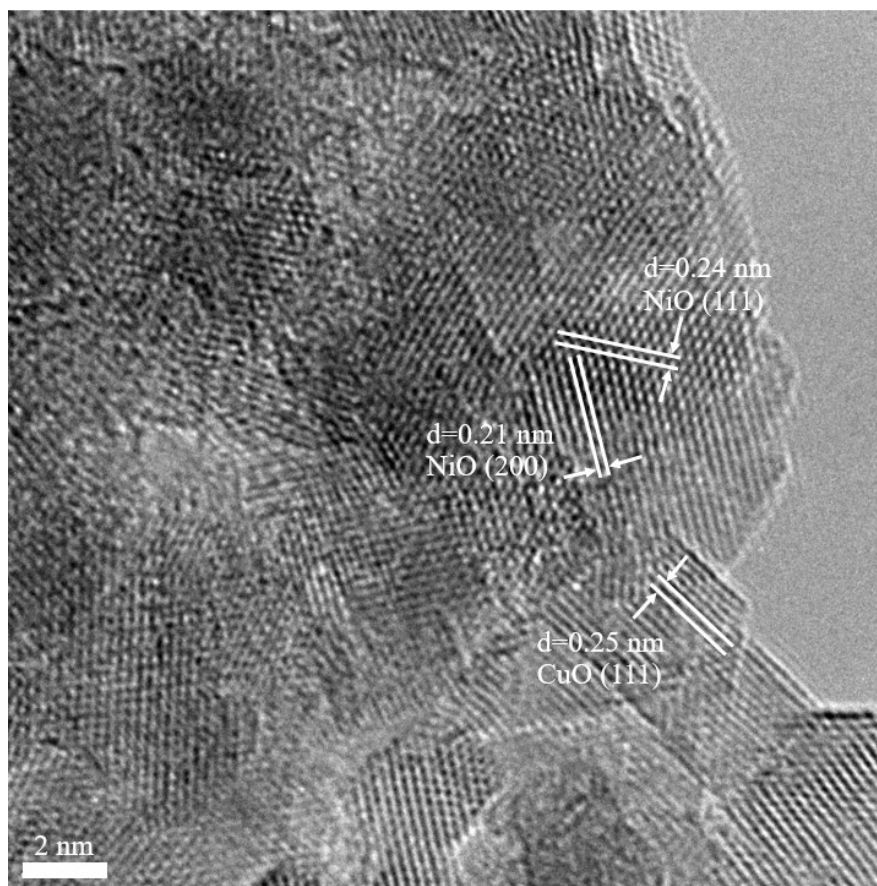


Figure 6-1.8 TEM image of Cu-Ni_{0.2}300.

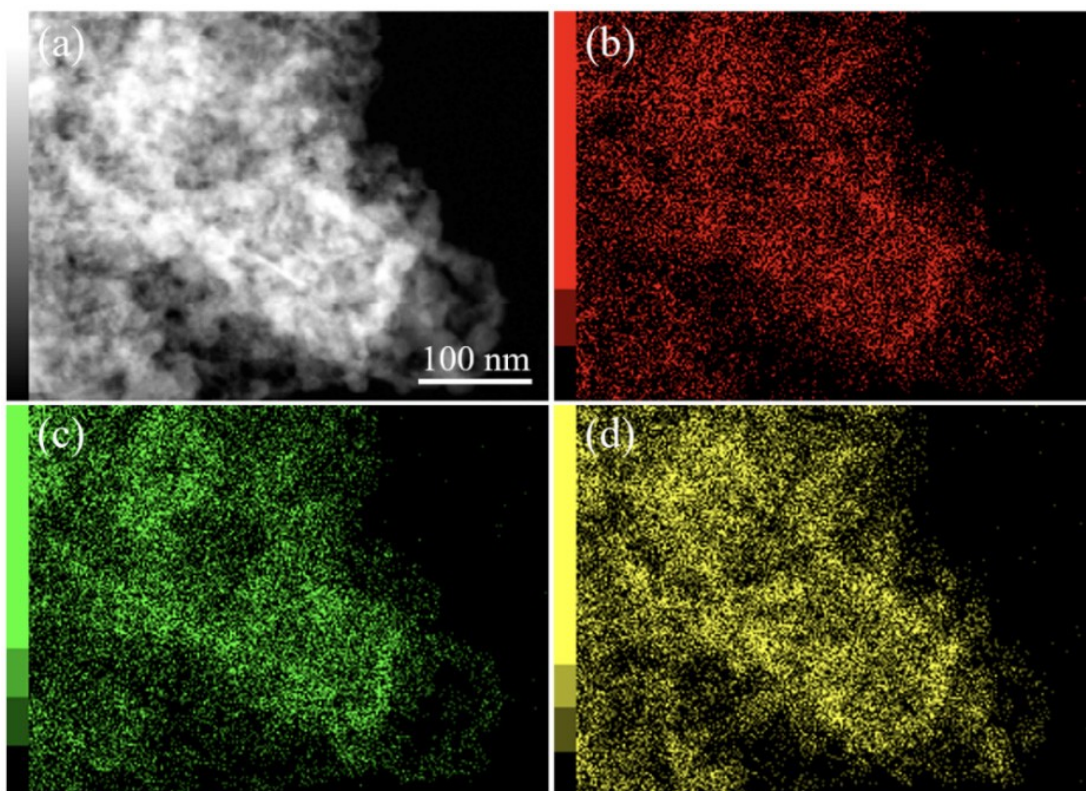


Figure 6-1.9 (a) HAADF-STEM image and (b–d) the corresponding elemental mapping ((b) oxygen, (c) copper, and (d) nickel) images of Cu-Ni_{0.20_300}.

The surface area of the sample calcined at 300°C (Cu-Ni_{0.20_300}) is higher than the other samples calcined at higher temperatures (Cu-Ni_{0.20_400} and Cu-Ni_{0.20_500}). As the applied thermal temperature is increased, the surface area is greatly decreased from 43.1 m² g⁻¹ (Cu-Ni_{0.20_300}) to 11.1 m² g⁻¹ (Cu-Ni_{0.20_400}) and 6.2 m² g⁻¹ (Cu-Ni_{0.20_500}) due to the fusion of pores during the crystallization of the framework. Furthermore, with increasing calcination temperature, larger crystals are observed on the surface of the samples (**Figure 6-1.6g,h**). **Figure 6-1.7d** shows the XRD pattern of Cu-Ni_{0.20_500} and refinement by the Pawley method. Clearly, the presence of two phases (CuO and NiO) are confirmed. The space group of $Fm\bar{3}m$ of NiO structure with lattice constants, $a = 4.178(1)$ Å, $b = 4.178(1)$ Å and $c = 4.178(1)$ Å as well as CuO structure with $C2/c$ space group with lattice parameters, $a = 4.683(7)$ Å, $b = 3.422(6)$ Å and $c = 5.128(8)$ Å, respectively. Finally, the reliability factors are identified as $R_{wp}=29.25\%$ and $R_B=12.32\%$ and $GOF = 1.04$. The results of the structural and crystallographic analyses of the sample Cu-Ni_{0.20_500} are summarized in **Table 6.1-2**.

Table 6.1-2 Crystallographic data for the compound Cu–Ni_0.20_500, obtained by refinement by the Pawley method.

Compound	1	2
Formula	CuO	NiO
Space group	<i>C2/c</i>	<i>Fm3m</i>
<i>a</i> /Å	4.683(7)	4.178(1)
<i>b</i> /Å	3.422(6)	4.178(1)
<i>c</i> /Å	5.128(8)	4.178(1)
α (°)	90.00	90.00
β (°)	99.54	90.00
γ (°)	90.00	90.00
<i>V</i> /Å ³	81.0798	72.9298
<i>wR</i> (%)*	3.2	1.6

It is well-known that transition metal oxides are highly useful for supercapacitor applications due to their redox activity and high specific capacitance.[41,42] To evaluate the electrochemical storage performance of all the Cu-Ni oxide samples, a three-electrode system was used with 6 MKOH as the electrolyte. Cyclic voltammetry (CV) measurements of Cu-Ni_0.20_300, Cu-Ni_0.20_400 and Cu-Ni_0.20_500 were conducted in the potential window of 0–0.5 V which is the well-known potential window of Cu-Ni oxide for supercapacitor application (**Figure 6-1.10a–c**).[41] Based on the CV curves, the specific capacitance values of Cu-Ni_0.20_300, Cu-Ni_0.20_400 and Cu-Ni_0.20_500 at a scan rate of 50 mV s⁻¹ are determined to be 222.6, 149.6, and 134.5 F g⁻¹, respectively (**Figure 6-1.10d**). Among all the samples, Cu-Ni_0.20_300 shows the highest specific capacitance at all scan rates because of its high surface area, although it shows lower capacitance retention at higher scan rates. The sample Cu-Ni_0.20_500 exhibits good capacitance retention of 71%, while the sample Cu-Ni_0.20_300 has poor capacitance retention of 46%. This may be attributed to the higher stability of Cu-Ni oxide composite calcined at higher temperatures. In addition, galvanostatic charge-discharge (GCD) measurements were also carried out for Cu-Ni_0.20_300 at different

current densities. This sample exhibits a specific capacitance of 158 F g^{-1} at a current density of 1 A g^{-1} and displays good stability up to 10 A g^{-1} (Figure 6-1.10e, f).

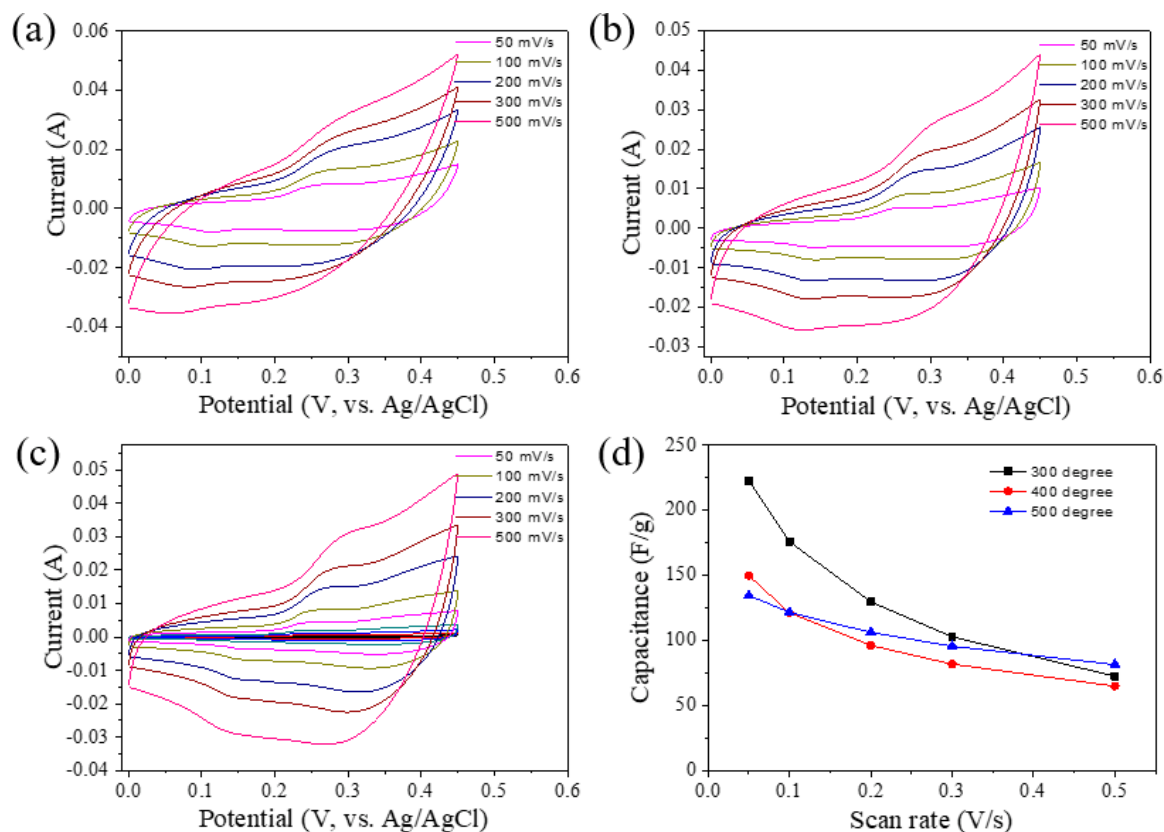


Figure 6-1.10 CV curves of Cu-Ni oxides calcined at (a) 300 °C, (b) 400 °C, and (c) 500 °C at various scan rates ((a) Cu-Ni_0.20_300, (b) Cu-Ni_0.20_400, and (c) Cu-Ni_0.20_500). (d) Specific capacitance versus scan rate plots for all the samples. (e) GCD curves and (f) specific capacitance of Cu-Ni_0.20_300 at different current densities.

6-1.4. Conclusion

I have demonstrated the successful fabrication of 2D Cu-Ni CP nanoflakes via a controlled crystallization process with the assistance of TSCD. It is found that the concentration of TSCD strongly influenced the size and morphology of the resulting Cu-Ni CPs, with higher concentration of TSCD leading to more well-defined and larger-sized nanoflakes due to the reduction in crystallization speed of Cu-Ni CPs. These Cu-Ni CPs were subsequently converted into nanoporous Cu-Ni mixed oxides via thermal treatment in air at 300–500°C and they

showed respectable electrochemical performance for supercapacitors with a maximum specific capacitance 158 F g^{-1} at 1 A g^{-1} and good capacitance retention of 71%. It is expected that the proposed method will be useful for the preparation of other types of 2D and 3D CPs as precursors for the synthesis of various nanoporous metal oxides for energy and environmental applications.

References

- [1] Y. V. Kaneti, S. Dutta, M. S. A. Hossain, M. J. A. Shiddiky, K.-L. Tung, F.-K. Shieh, C.-K. Tsung, K. C. W. Wu, Y. Yamauchi, *Advanced Materials* **2017**, *29*, 1700213.
- [2] Y. V. Kaneti, J. Tang, R. R. Salunkhe, X. Jiang, A. Yu, K. C. W. Wu, Y. Yamauchi, *Advanced Materials* **2017**, *29*, 1604898.
- [3] F. Qu, A. Shi, M. Yang, J. Jiang, G. Shen, R. Yu, *Analytica Chimica Acta* **2007**, *605*, 28-33.
- [4] M. B. Zakaria, M. Hu, M. Pramanik, C. Li, J. Tang, A. Aldalbahi, S. M. Alshehri, V. Malgras, Y. Yamauchi, *Chemistry - An Asian Journal* **2015**, *10*, 1541-1545.
- [5] M. B. Zakaria, M. Hu, M. Imura, R. R. Salunkhe, N. Umezawa, H. Hamoudi, A. A. Belik, Y. Yamauchi, *Chemistry - A European Journal* **2014**, *20*, 17375-17384.
- [6] A. Alowasheer, S. Tominaka, Y. Ide, Y. Yamauchi, Y. Matsushita, *CrystEngComm* **2018**, *20*, 6713-6720.
- [7] Y. Ding, Y. P. Chen, X. Zhang, L. Chen, Z. Dong, H. L. Jiang, H. Xu, H. C. Zhou, *Journal of the American Chemical Society* **2017**, *139*, 9136-9139.
- [8] J. C. Tan, P. J. Saines, E. G. Bithell, A. K. Cheetham, *ACS Nano* **2012**, *6*, 615-621.
- [9] T. Bauer, Z. Zheng, A. Renn, R. Enning, A. Stemmer, J. Sakamoto, A. D. Schlüter, *Angewandte Chemie - International Edition* **2011**, *50*, 7879-7884.
- [10] P. Amo-Ochoa, L. Welte, R. González-Prieto, P. J. Sanz Miguel, C. J. Gómez-García, E. Mateo-Martí, S. Delgado, J. Gómez-Herrero, F. Zamora, *Chemical Communications* **2010**, *46*, 3262-3264.
- [11] J. Nai, J. Zhang, X. W. (David) Lou, *Chem* **2018**, *4*, 1967-1982.

- [12] L. Wang, Y. Han, X. Feng, J. Zhou, P. Qi, B. Wang, *Coordination Chemistry Reviews* **2016**, *307*, 361-381.
- [13] V. Safarifard, A. Morsali, *Coordination Chemistry Reviews* **2015**, *292*, 1-14.
- [14] B. Wang, Y. Han, X. Wang, N. Bahlawane, H. Pan, M. Yan, Y. Jiang, *iScience* **2018**, *3*, 110-133.
- [15] V. Malgras, Q. Ji, Y. Kamachi, T. Mori, F.-K. Shieh, K. C. W. Wu, K. Ariga, Y. Yamauchi, *Bulletin of the Chemical Society of Japan* **2015**, *88*, 1171-1200.
- [16] X. Liu, R. Ma, Y. Bando, T. Sasaki, *Advanced Materials* **2012**, *24*, 2148-2153.
- [17] J. Yan, Z. Fan, W. Sun, G. Ning, T. Wei, Q. Zhang, R. Zhang, L. Zhi, F. Wei, *Advanced Functional Materials* **2012**, *22*, 2632-2641.
- [18] X. Yu, S. Yun, J. S. Yeon, P. Bhattacharya, L. Wang, S. W. Lee, X. Hu, H. S. Park, *Advanced Energy Materials* **2018**, *8*, 1702930.
- [19] O. Diaz-Morales, D. Ferrus-Suspedra, M. T. M. Koper, *Chemical Science* **2016**, *7*, 2639.
- [20] C. Hareli, M. Caspary Toroker, *Journal of Chemical Theory and Computation* **2018**, *14*, 2380-2385.
- [21] R. Wang, X. Yan, *Scientific Reports* **2014**, *4*, 3712.
- [22] T. Y. Wei, C. H. Chen, H. C. Chien, S. Y. Lu, C. C. Hu, *Advanced Materials* **2010**, *22*, 347-351.
- [23] Y. G. Wang, L. Cheng, Y. Y. Xia, *Journal of Power Sources* **2006**, *153*, 191-196.
- [24] L. Q. Mai, F. Yang, Y. L. Zhao, X. Xu, L. Xu, Y. Z. Luo, *Nature Communications* **2011**, *2*, 381.
- [25] C. Yuan, J. Li, L. Hou, X. Zhang, L. Shen, X. W. Lou, *Advanced Functional Materials* **2012**, *22*, 4592-4597.
- [26] B. H. Toby, R. B. Von Dreele, *Journal of Applied Crystallography* **2013**, *46*, 544-549.
- [27] N. C. Li, A. Lindenbaum, J. M. White, *Journal of Inorganic and Nuclear Chemistry* **1959**, *12*, 122-128.
- [28] X. Wu, C. Wu, C. Wei, L. Hu, J. Qian, Y. Cao, X. Ai, J. Wang, H. Yang, *ACS Applied Materials and Interfaces* **2016**, *8*, 5393-5399.

- [29] M. Hu, S. Ishihara, Y. Yamauchi, *Angewandte Chemie International Edition* **2013**, *52*, 1235-1239.
- [30] M. B. Zakaria, M. Hu, Y. Tsujimoto, Y. Sakka, N. Suzuki, Y. Kamachi, M. Imura, S. Ishihara, K. Ariga, Y. Yamauchi, *Chemistry - An Asian Journal* **2014**, *9*, 1511-1514.
- [31] P. Xiong, G. Zeng, L. Zeng, M. Wei, *Dalton Trans.* **2015**, *44*, 16746-16751.
- [32] M. Heibel, G. Kumar, C. Wyse, P. Bukovec, A. B. Bocarsly, *Chemistry of Materials* **1996**, *8*, 1504-1511.
- [33] T. Arun, K. Prakash, R. Kuppusamy, R. J. Joseyphus, *Journal of Physics and Chemistry of Solids* **2013**, *74*, 1761-1768.
- [34] A. A. Lemus-Santana, J. Rodriguez-Hernandez, L. F. Del Castillo, M. Basterrechea, E. Reguera, *Journal of Solid State Chemistry* **2009**, *182*, 757-766.
- [35] L. Hu, P. Zhang, Q. Chen, N. Yan, J. Mei, *Dalton Transactions* **2011**, *40*, 5557-5562.
- [36] R. Vafazadeh, A. Dehghani-Firouzabadi, A. C. Willis, *Acta Chimica Slovenica* **2017**, 686-691.
- [37] D. Türköz, Z. Kartal, S. Bahçeli, *Zeitschrift für Naturforschung A* **2004**, *59*, 523-526.
- [38] D. M. Gil, M. C. Navarro, M. C. Lagarrigue, J. Guimpel, R. E. Carbonio, M. I. Gómez, *Journal of Thermal Analysis and Calorimetry* **2011**, *103*, 889-896.
- [39] L. Huang, X. Ge, S. Dong, *RSC Adv.* **2017**, *7*, 32819-32825.
- [40] S. G. Hosseini, R. Abazari, *RSC Advances* **2015**, *5*, 96777-96784.
- [41] Y. X. Zhang, M. Kuang, J. J. Wang, *CrystEngComm* **2014**, *16*, 492-498.
- [42] M. Huang, F. Li, Y. X. Zhang, B. Li, X. Gao, *Ceramics International* **2014**, *40*, 5533-5538.

Chapter 6-2

In-Situ Formation of Cu-Ni Cyano-Bridged Coordination Polymer on Graphene Oxide Nanosheets and Their Thermal Conversion

6-2.1. Introduction

In the past decade, hybrid nanomaterials have attracted significant interest for various applications, such as catalysts, adsorbents, energy storage devices, and sensors, because of their outstanding properties which combine the advantages of two or more constituents.[1] The layer-by-layer (LbL) approach which relies on the chemical or physical interactions between two materials is a promising method for preparing hybrid materials, as it is simple, versatile, and cost-effective.[2-4] Two-dimensional (2D) graphene oxide (GO) nanosheets have been widely utilized as important host materials for hybridization with other inorganic and organic materials, because they possess several attractive intrinsic properties, including high electrical conductivity and strong mechanical properties.[5-7]

The coordination polymers (CPs) including metal-organic frameworks (MOFs) and porous coordination polymers (PCPs) have gained significant attention for their high surface area, large pore volume, and tunable shape (from 1D to 3D) and composition.[8-11] As a result of these excellent characteristics, they have been investigated for a wide variety of applications, such as energy storage, adsorption, catalysis, sensing and drug delivery.[12,13] Among them, cyano-bridged CPs can serve as highly versatile precursors for the preparation of various nanoporous metal oxides through simple post-synthesis annealing in air.[14-17] In particular, 2D cyano-bridged CPs are interesting because they show many outstanding properties that are not observable in their bulk counterpart.[18-19] Correspondingly, the 2D nanoporous metal oxides derived from these 2D cyano-bridged CPs typically exhibit large accessible surface area to permit guest molecules to effectively access the nanopores or to provide numerous active sites for the adsorption of ions or molecules.

In this chapter, I report the synthesis of a novel hybrid CuCNNi/GO hybrid material consisting of Cu-Ni cyano-bridged CP and GO nanosheets which can be converted into Cu-Ni oxide/graphene composites by simple thermal treatment in air at temperatures between 300-600°C. During the heat treatment, the cyanide group in the original CuCNNi/GO precursor was removed and such removal resulted in the generation of porous Cu-Ni oxide. The Cu-Ni oxide/GO composite calcined at the optimum temperature of 500°C displays a high surface

area of $145 \text{ m}^2 \text{ g}^{-1}$ which is much higher than those of individual Cu-Ni oxide ($11.1 \text{ m}^2 \text{ g}^{-1}$) and GO nanosheets ($34.9 \text{ m}^2 \text{ g}^{-1}$).[6]

6-2.2. Experimental Sections

6-2.2.1. Chemicals

Potassium tetracyanonickelate (II) hydrate ($\text{K}_2[\text{Ni}(\text{CN})_4] \cdot \text{H}_2\text{O}$) was purchased from FUJIFILM Wako Pure Chemical Corp., Japan. Copper (II) nitrate trihydrate ($\text{Cu}(\text{NO}_3)_2 \cdot 3\text{H}_2\text{O}$) and trisodium citrate dihydrate (TSCD) were purchased from Nacalai Tesque, Japan. Nanographite platelets (N008-100-N) with 100 nm thickness was used to prepare graphene oxide (GO) nanosheets (Angestron materials Inc.). Potassium permanganate (KMnO_4), 30% hydrogen peroxide (H_2O_2) solution and sodium nitrate (NaNO_3) were purchased from Kanto Chemicals Co., Inc. All chemical reagents were used without further purification.

6-2.2.2. Synthesis of GO nanosheets.

GO nanosheets were synthesized using a modified Hummer's method.[20] In a typical process, nanographite platelets (0.3 g) and sodium nitrate (0.16 g) were first mixed together, followed by the addition of concentrated sulfuric acid solution (7.67 mL) and the resulting mixture solution was stirred continuously for 1 h. Next, at a temperature lower than 20°C , KMnO_4 (1.0 g) was added gradually into the mixture solution. Then, this solution was heated at 35°C for 2 h followed by the addition of pure water (83 mL) under vigorous stirring. The obtained suspension was subsequently treated with an aqueous 30% H_2O_2 solution (1.67 mL) and the resulting colloidal solution was stored for further synthesis.

6-2.2.3. Synthesis of Cu-Ni cyano-bridged CP.

$\text{Cu}(\text{NO}_3)_2 \cdot 3\text{H}_2\text{O}$ (0.120 g) and TSCD (0.200 g) were mixed together with 50 mL of water at room temperature to form a clear solution. In a separate bottle, $\text{K}_2[\text{Ni}(\text{CN})_4]$ (0.120 g) was dissolved in 50 mL of water to form another clear solution. Then, the two solutions were mixed under magnetic stirring until the solution became clear. The mixture was then aged at room temperature for 24 h. After the reaction was terminated, the solid precipitates were collected by centrifugation and washed for several times with water and ethanol.

6-2.2.3. *In situ* formation of Cu-Ni cyano-bridged CP on GO nanosheets.

In a typical procedure, $\text{Cu}(\text{NO}_3)_2 \cdot 3\text{H}_2\text{O}$ (0.120 g) and TSCD (0.200 g) were dissolved in water (20 mL) to generate a clear solution. This solution was added dropwisely into the GO solution (20 mL, 2 mg mL^{-1}) followed by stirring for 30 min. The obtained mixture was gently mixed with an aqueous solution of $\text{K}_2[\text{Ni}(\text{CN})_4]$ (0.120 g in 20 mL H_2O). The resulting suspension was aged for two days until reaction was completed. The precipitate was isolated by centrifugation. After washing with water and ethanol, the resulting CuCNNi/GO hybrid was dried at room temperature. For the preparation of Cu-Ni oxide/GO composites, the obtained CuCNNi/GO powder was calcined at different temperatures (300, 400, 500 and 600°C) with a heating rate of 1°C min^{-1} for 1 h in the air. The samples were labeled as Cu-Ni oxide/GO_x, where *x* is the applied calcination temperature.

6-2.2.3. Characterization.

The morphological characterization of the samples was performed using a Hitachi SU8000 scanning electron microscope (SEM) operated at an accelerating voltage of 5 kV and a JEOL JEM-2100F transmission electron microscope (TEM) operated at an accelerating voltage of 200 kV. Wide-angle powder X-ray diffraction (XRD) patterns of the samples were obtained with a Rigaku RINT 2500X diffractometer using monochromated Cu $K\alpha$ radiation (40 kV, 40 mA). Nitrogen adsorption-desorption measurements were carried out using a Belsorp-mini II Sorption System at 77 K. The specific surface area and pore size distribution were calculated by the multipoint Brunauer-Emmett-Teller (BET) and Barrett-Joyner-Halenda (BJH) methods, respectively. The Fourier transform infrared spectroscopy (FTIR) measurements were performed in the range of 500 to 4000 cm^{-1} at room temperature (RT) by using a Thermoscientific Nicolet 4700. Thermogravimetric and differential thermal analysis (TG-DTA) were performed simultaneously from RT to 600°C , using a Hitachi HT-Seiko Instrument Exter 6300 TG/DTA in air at a heating rate of 5°C min^{-1} .

6-1.3. Results and Discussion

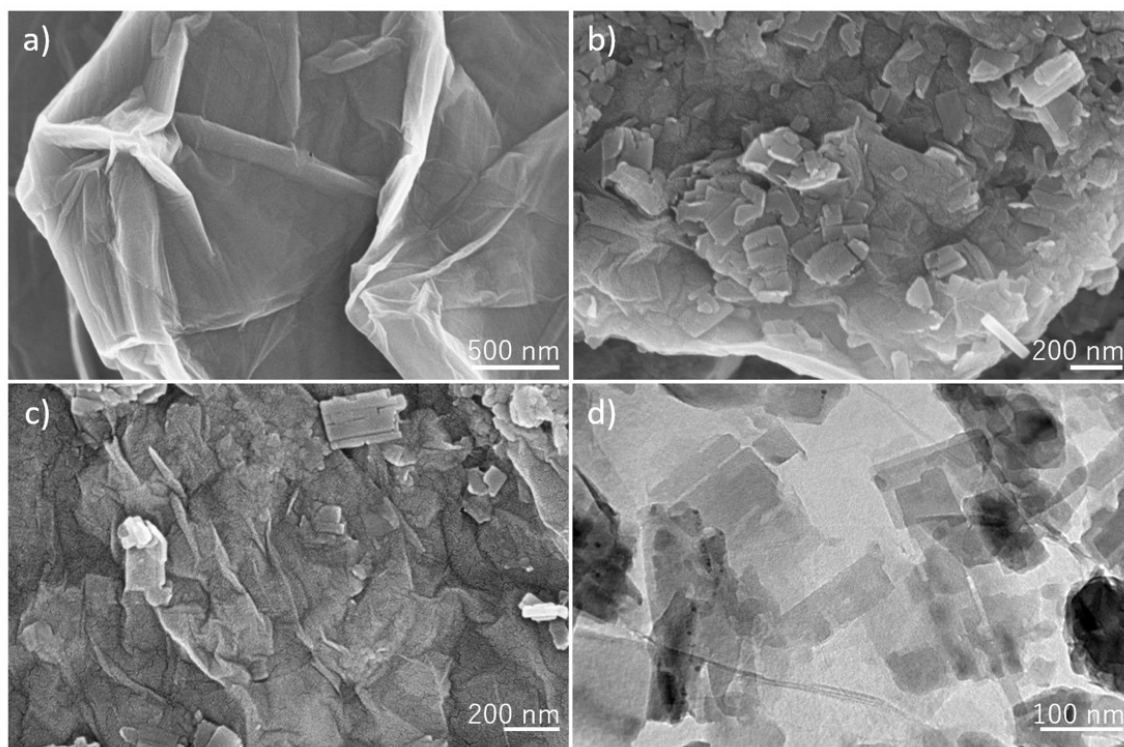


Figure 6-2.1 (a) SEM images of (a) the starting GO nanosheets, (b,c) the as-prepared CuCNNi/GO hybrid. (d) TEM image of as-prepared CuCNNi/GO sample.

The as-prepared GO nanosheets show a typical 2D sheet-like structure, as seen in **Figure 6-2.1a**. The surface of the GO nanosheets is negatively charged, due to the presence of functional groups, such as carboxylic acid and hydroxyl groups.[21,22] These functional groups can serve as bridging sites for interacting with metal cations, such as Cu^{2+} . Following the addition of Cu^{2+} ions to GO nanosheets, the GO surface charge becomes positive. Next, the addition of $[\text{Ni}(\text{CN})_4]^{2-}$ into the above mixture solution initializes the formation and growth of CuCNNi flakes on the GO surface. Finally, the GO nanosheets are wrapped around the CuCNNi flakes (**Figure 6-2.1b-d**).

The cross-sectional TEM image shown in **Figure 6-2.2a** reveals that the CuCNNi flakes uniformly grow on the GO surface and they are encapsulated between the GO nanosheets. Furthermore, the cross-sectional HAADF-STEM image and the corresponding elemental mapping images of C, Ni, and Cu indicate the formation of a well-defined layered architecture

(**Figure 6-2.2**). For comparison, pristine CuCNNi nanoflakes were also prepared without GO nanosheets. The resulting CuCNNi product shows an almost identical flake-like shape as the CuCNNi flakes grown on the GO nanosheets with sizes of around 100-200 nm (**Figure 6-2.3**). FTIR spectra of the resulting CuCNNi/GO sample is show in **Figure 6-2.4**. The C≡N bond from Cu-CN-Ni can be observed at 2186 cm^{-1} . The functional group of C=O in carboxylic acid and carbonyl moieties, C=C, C-OH, and C-O-C of GO sheets can be observed in the hybrid materials, respectively.[23,24]

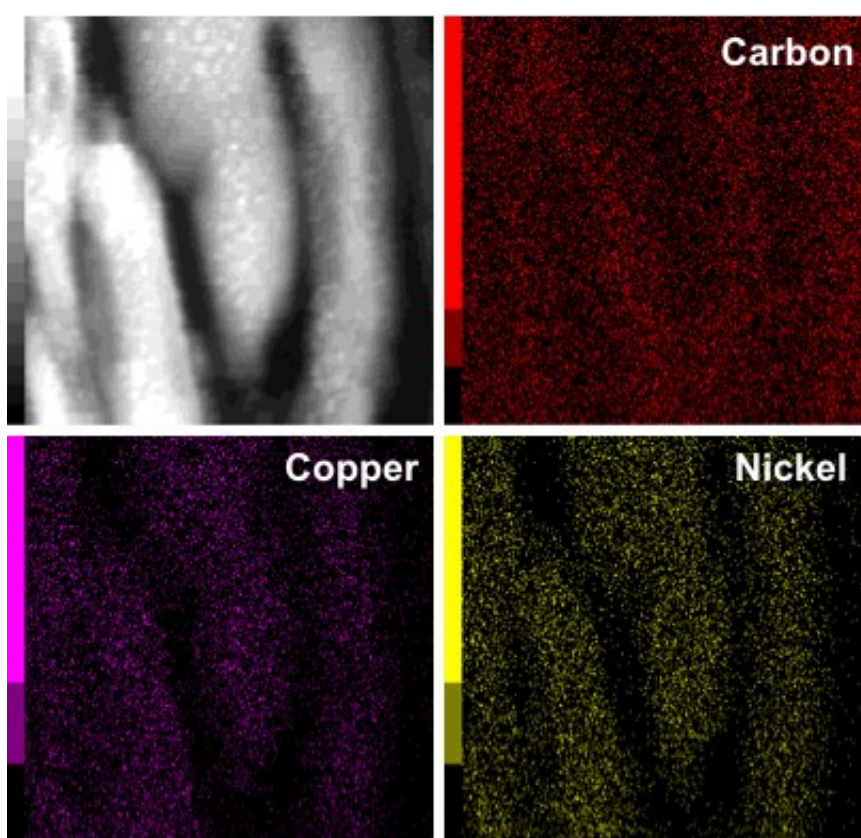


Figure 6-2.2 Cross-sectional HAADF-STEM and the corresponding elemental mapping images (C, Cu, and Ni) of the as-prepared CuCNNi/GO hybrid.

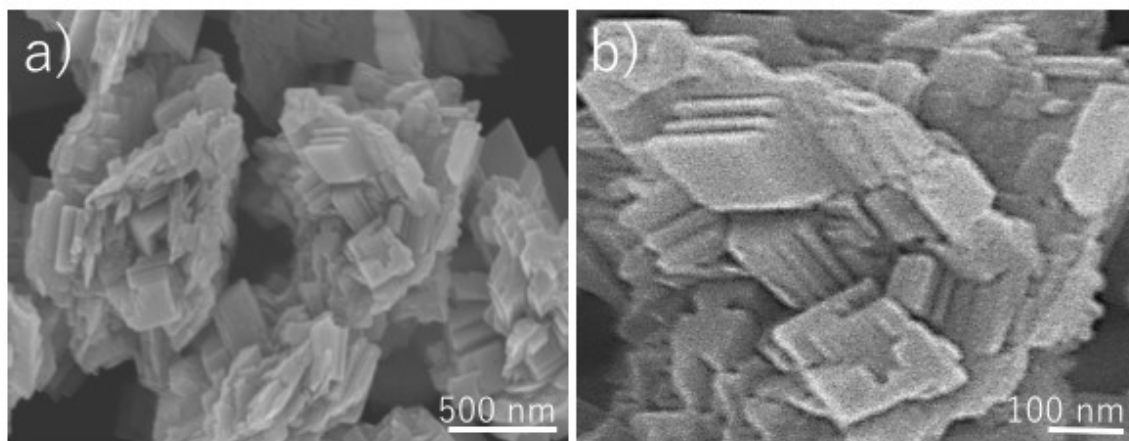


Figure 6-2.3 SEM image of CuCNNi nanoflakes prepared without GO nanosheets.

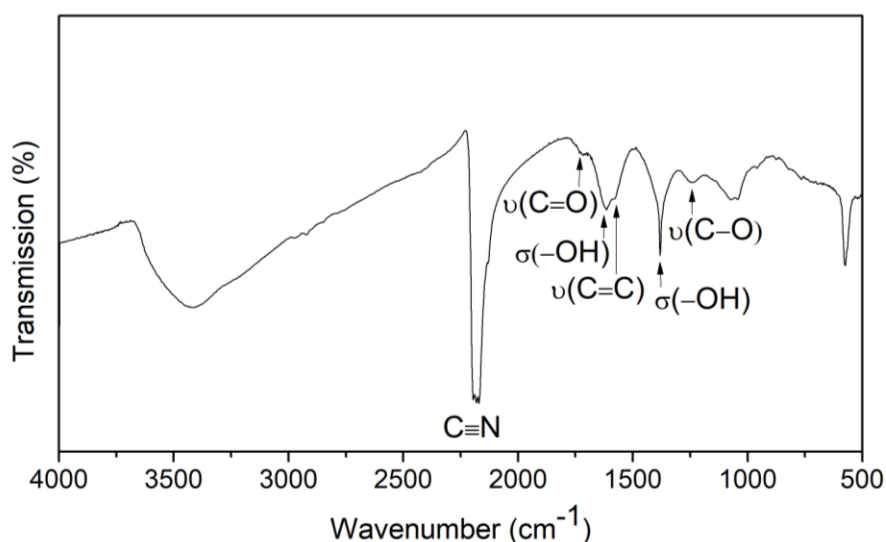


Figure 6-2.4 FTIR spectra of CuCNNi/GO hybrid.

The thermal stability of the GO nanosheets and CuCNNi nanoflakes were studied by TG-DTA under air atmosphere (**Figure 6-2.5**). In the case of GO nanosheets, a sharp peak of DTA curve is confirmed, indicating that a large amount of labile oxygen-containing functional groups (*e.g.*, -COOH and -OH) are removed from the GO surface. While, for the CuCNNi case, a small weight loss is observed until 300°C, which can be attributed to the removal of adsorbed water molecules. At around 350°C, a large weight loss is observable, in which the -CN- group starts to decompose and form the corresponding metal oxide. Until 500°C, the weight losses of the GO and CuCNNi samples are about 50 and 30 %, respectively.

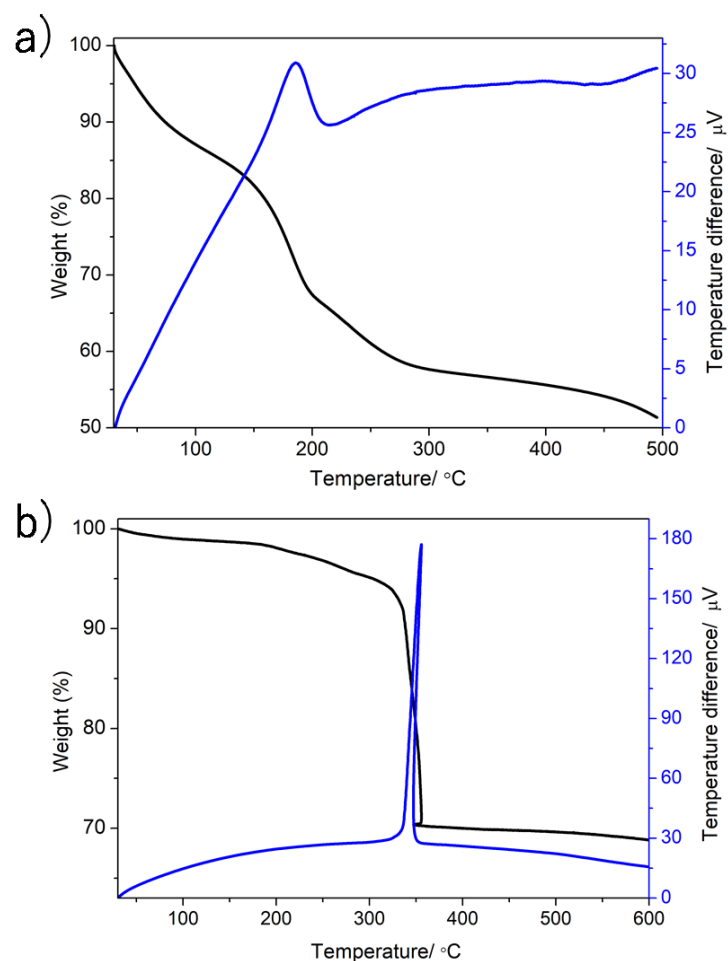


Figure 6-2.5 TG-DTA curves of (a) GO nanosheets and (b) CuCNNi flakes in air.

The thermal conversion of the CuCNNi/GO hybrid into porous Cu-Ni oxide/GO composites was performed in air at various temperatures (300, 400, 500 and 600°C). The samples were labeled as Cu-Ni oxide/GO_ x , where x is the applied calcination temperature. The morphology of the calcined samples was checked by SEM. As shown in **Figure 6-2.6**, the GO nanosheets are preserved after the high-temperature treatment and the 2D Cu-Ni oxide nanoflakes are well-encapsulated within the GO nanosheets.

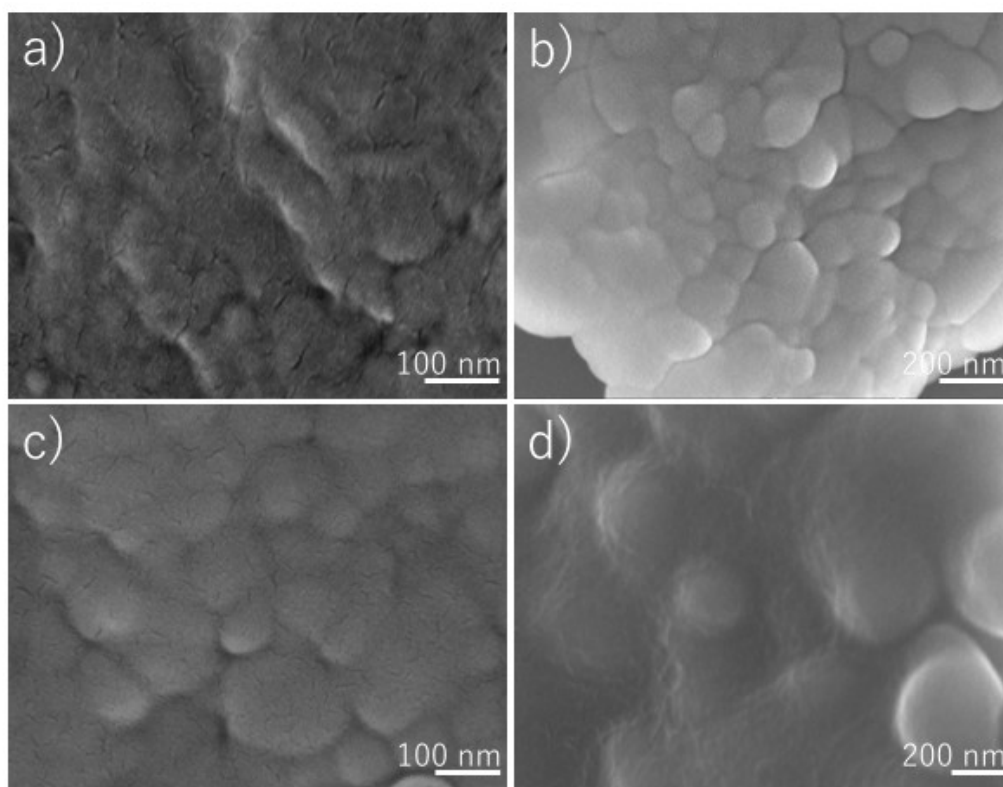


Figure 6-2.6 SEM images of (a) Cu-Ni oxide/GO_300, (b) Cu-Ni oxide/GO_400, (c) Cu-Ni oxide/GO_500, and (d) Cu-Ni oxide/GO_600.

The HAADF-STEM images and the corresponding elemental mapping data of the Cu-Ni oxide/GO composites are shown in **Figure 6-2.7**. The carbon distribution throughout the entire area appears to decrease with the increase of calcination temperature from 300 to 500 °C. However, the elements Cu, Ni, and O are uniformly distributed throughout the entire area. From the ICP elemental analysis, the compositional ratio of Cu:Ni of CuCNNi/GO before the thermal treatment is 1:1 and this ratio is maintained in the Cu-Ni oxide/GO_500 sample. Thus, the compositional ratio of Cu:Ni is not affected by the thermal treatment process. The PXRD patterns of the hybrid materials after calcination at different temperatures are given in **Figure 6-2.8**. The peaks at 35.6, 38.6, 48.8, 53.4 and 58.2° are assigned to (002/11 $\bar{1}$), (111/200), ($\bar{2}$ 02), (020) and (202) peaks of the CuO, and the other peaks at 37.0, 43.3 and 62.7° are assigned to (111), (200) and (220) of the NiO.[25,26] The peak at 26.5° belonging to GO nanosheets becomes weaker and slowly disappears with increasing calcination temperature. The intensities of CuO and NiO diffraction peaks gradually increase at higher temperatures (*e.g.*, 500 and

600°C) due to the increase in their crystallinity.

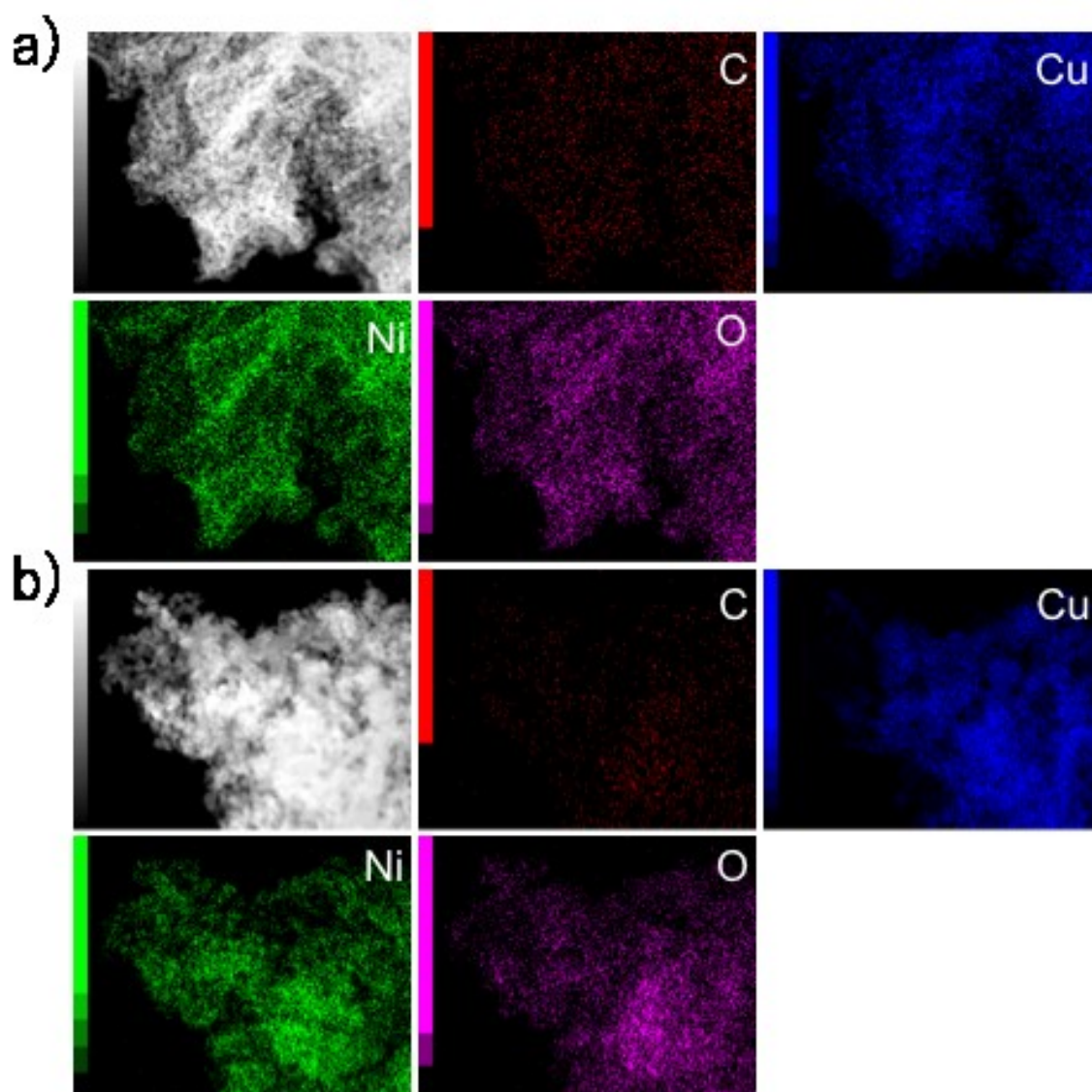


Figure 6-2.7 HAADF-STEM images and the corresponding elemental mapping data (C, Cu, Ni and O) of (a) Cu-Ni oxide/GO_300 and (b) Cu-Ni oxide/GO_500.

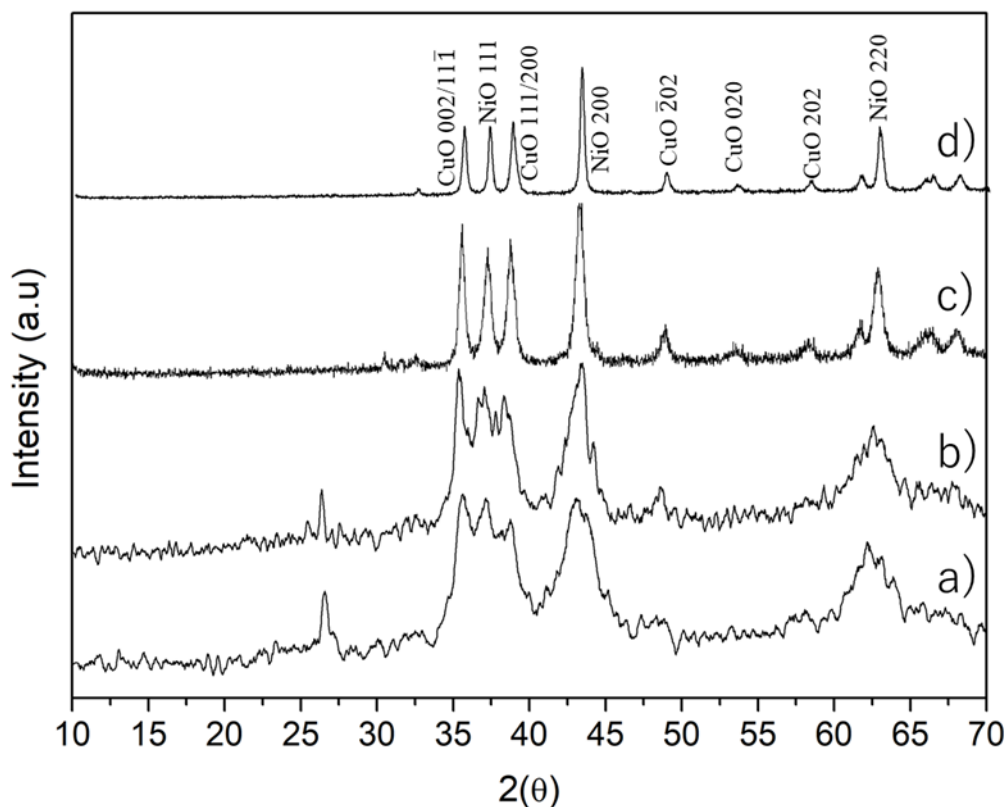


Figure 6-2.8 Wide-angle XRD patterns of (a) Cu-Ni oxide/GO_300, (b) Cu-Ni oxide/GO_400, (c) Cu-Ni oxide/GO_500, and (d) Cu-Ni oxide/GO_600.

The nitrogen (N_2) adsorption-desorption measurements were performed to investigate the porosity of the Cu-Ni oxide/GO composites obtained after thermal treatment (**Figure 6-2.9**). The BET surface area of the Cu-Ni oxide/GO composites initially increases with increasing calcination temperature, reaching an optimum value of $145 \text{ m}^2 \text{ g}^{-1}$ at $500 \text{ }^\circ\text{C}$ (Cu-Ni oxide/GO_500). The FTIR spectrum of Cu-Ni oxide/GO_500 still shows several peaks belonging to the functional groups of GO nanosheets (**Figure 6-2.10**), however the intensity of these peaks becomes weak and the peak assignable to CN units totally disappears. However, the BET specific surface area of the composite rapidly decreases to $20 \text{ m}^2 \text{ g}^{-1}$ when the calcination temperature was raised to $600 \text{ }^\circ\text{C}$, owing to the fusion and crystallization of oxides. In comparison, the pristine Cu-Ni oxide (**Figure 6-2.11**) and GO nanosheets exhibit BET specific surface areas of 11.1 and $34.9 \text{ m}^2 \text{ g}^{-1}$, respectively, indicating the superiority of the Cu-Ni oxide/GO composites. Furthermore, compared to Cu-Ni oxide nanoflakes in **Chapter 6-1**, the addition of GO nanosheets greatly enhances the specific surface area as the GO nanosheets

wrapped around the CuCNNi flakes can prevent the sintering of metal oxides during the thermal treatment.

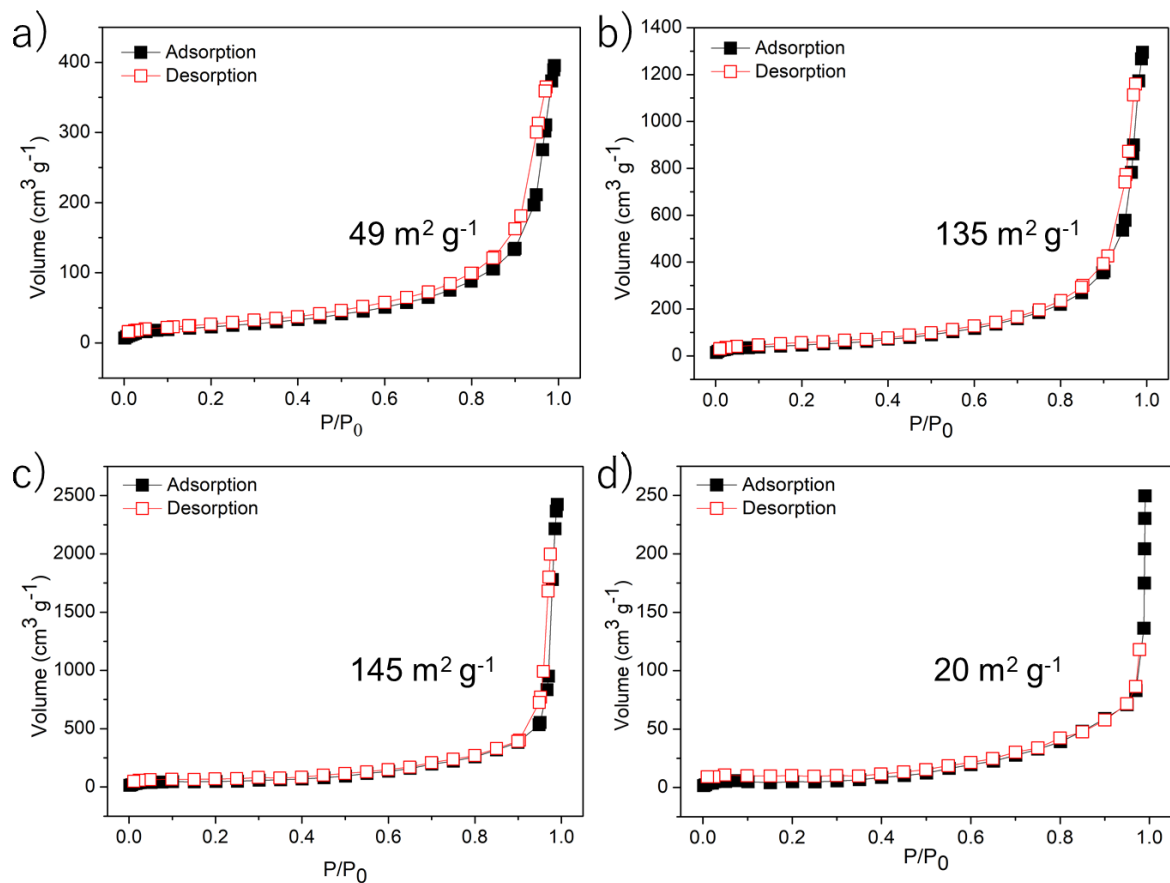


Figure 6-2.9 Nitrogen adsorption-desorption isotherms for Cu-Ni oxide/GO hybrids calcined at (a) 300°C, (b) 400°C, (c) 500°C, and (d) 600°C.

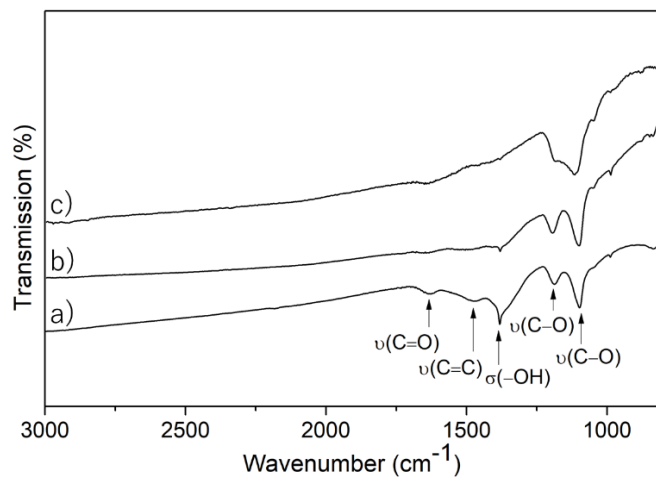


Figure 6-2.10 FTIR spectra of Cu-Ni oxide/GO hybrids calcined at (a) 400°C, (b) 500°C and (c) 600°C.

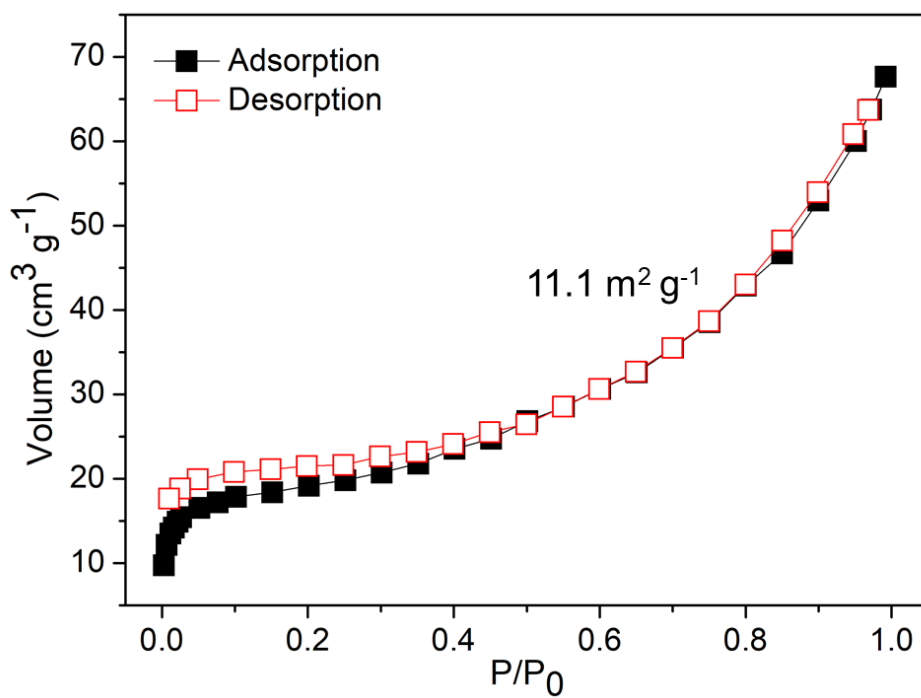


Figure 6-2.11 Nitrogen adsorption-desorption isotherms for Cu-Ni oxide calcined at 300°C.

6-2.4. Conclusion

I have successfully synthesized Cu-Ni cyano-bridged coordination polymer (CuCNNi) nanoflakes on GO nanosheets via a facile approach. In my proposed method, the presence of the positively charged Cu^{2+} ions can promote electrostatic interaction with the GO nanosheets and enable the subsequent formation and growth of the CuCNNi nanoflakes on the GO nanosheets. The thermal treatment of the CuCNNi/GO hybrid at 300-600°C resulted in their conversion to porous Cu-Ni oxide/GO composites. Since the GO nanosheets can prevent the rapid crystallization and fusion of metal oxides during the thermal treatment, I can realize Cu-Ni oxide/GO composite with a high surface area of $150 \text{ m}^2 \text{ g}^{-1}$. This layer-by-layer approach can be extended for the preparation of other CP-derived metal oxide/GO hybrids for a wide variety of functional applications.

References

- [1] M. Faustini, L. Nicole, E. Ruiz-Hitzky, C. Sanchez, *Advanced Functional Materials* **2018**, 28, 1704158-1704188.
- [2] Y. Wang, A. S. Angelatos, F. Caruso, *Chemistry of Materials* **2008**, 20, 848–858.
- [3] M. Li, S. Ishihara, M. Akada, M. Liao, L. Sang, J. P. Hill, V. Krishnan, Y. Ma, K. Ariga, *Journal of the American Chemical Society* **2011**, 133, 7348–7351.
- [4] K. Ariga, Y. Yamauchi, G. Rydzek, Q. Ji, Y. Yonamine, K. C.-W. Wu, J. P. Hill, *Chemistry Letters* **2014**, 43, 36-68.
- [5] M. B. Zakaria, C. Li, Q. Ji, B. Jiang, S. Tominaka, Y. Ide, J. P. Hill, K. Ariga, Y. Yamauchi, *Angewandte Chemie - International Edition* **2016**, 55, 8426–8430.
- [6] S. Tanaka, R. R. Salunkhe, Y. V. Kaneti, V. Malgras, S. M. Alshehri, T. Ahamad, M. B. Zakaria, S. X. Dou, Y. Yamauchi, M. S. A. Hossain, *RSC Advances* **2017**, 7, 33994–33999.
- [7] C. Cho, Y. Song, R. Allen, K. L. Wallace, J. C. Grunlan, *Journal of Materials Chemistry C* **2018**, 6, 2095–2104.
- [8] S. Wannapaiboon, A. Schneemann, I. Hante, M. Tu, K. Epp, A. L. Semrau, C. Sternemann, M. Paulus, S. J. Baxter, G. Kieslich, R. A. Fischer, *Nature Communications*

2019, *10*, 346-35.

[9] H.-C. “Joe” Zhou, S. Kitagawa, *Chem. Soc. Rev.* **2014**, *43*, 5415-5418.

[10] J. Canivet, A. Fateeva, Y. Guo, B. Coasne, D. Farrusseng, *Chem. Soc. Rev.* **2014**, *43*, 5594-5617.

[11] R. Sabouni, H. Kazemian, S. Rohani, *Environmental Science and Pollution Research* **2014**, *21*, 5427-5449.

[12] Y. V. Kaneti, J. Tang, R. R. Salunkhe, X. Jiang, A. Yu, K. C. W. Wu, Y. Yamauchi, *Advanced Materials* **2017**, *29*, 1604898.

[13] C. Wang, Y. V. Kaneti, Y. Bando, J. Lin, C. Liu, J. Li, Y. Yamauchi, *Materials Horizons* **2018**, *5*, 394–407.

[14] S. Tanaka, M. B. Zakaria, Y. V. Kaneti, Y. Jikihara, T. Nakayama, M. Zaman, Y. Bando, M. S. A. Hossain, D. Golberg, Y. Yamauchi, *ChemistrySelect* **2018**, *3*, 13464–13469

[15] M. B. Zakaria, V. Malgras, T. Takei, C. Li, Y. Yamauchi, *Chemical Communications* **2015**, *51*, 16409.

[16] A. Azhar, C. Young, Y. V. Kaneti, Y. Yamauchi, A. Y. Badjah, M. Naushad, M. Habila, S. Wabaidur, *Nanomaterials* **2018**, *12*, 968–980.

[17] M. Hu, A. A. Belik, M. Imura, K. Mibu, Y. Tsujimoto, Y. Yamauchi, *Chemistry of Materials* **2012**, *24*, 2698-2707.

[18] M. Hu, S. Ishihara, Y. Yamauchi, *Angewandte Chemie International Edition* **2013**, *52*, 1235-1239.

[19] M. B. Zakaria, M. Hu, R. R. Salunkhe, M. Pramanik, K. Takai, V. Malgras, S. Choi, S. X. Dou, J. H. Kim, M. Imura, S. Ishihara, Y. Yamauchi, *Chemistry - A European Journal* **2015**, *21*, 3605-3612.

[20] W. S. Hummers, R. E. Offeman, *Journal of the American Chemical Society* **1958**, *80*, 1339.

[21] F. Yang, M. Zhao, B. Zheng, D. Xiao, L. Wu, Y. Guo, *Journal of Materials Chemistry* **2012**, *22*, 25471-25479.

[22] K. Tian, Z. Su, H. Wang, X. Tian, W. Huang, C. Xiao, *Composites Part A: Applied*

Science and Manufacturing **2017**, *94*, 41-49.

[23] J. Lu, Y. Li, S. Li, S. P. Jiang, *Scientific Reports* **2016**, *6*, 21530-21542.

[24] N. Chandrasekaran, S. Sivabalan, A. Prathap, S. Mohan, R. Jagannathan, *RSC Advances* **2014**, *4*, 17879-17883.

[25] R. Zhou, Y. Zheng, D. Hulicova-Jurcakova, S. Z. Qiao, *Journal of Materials Chemistry A* **2013**, *1*, 13179-13185.

[26] F. Liu, X. Wang, J. Hao, S. Han, J. Lian, Q. Jiang, *Scientific Reports* **2017**, *7*, 17709-17719.

Chapter 7

General Conclusions

8.1. Overview of the Achievements

Porous materials based on coordination compounds, including metal-organic frameworks (MOFs) and porous coordination polymers (PCPs), have well-defined pore structures and promising properties. They can efficiently be prepared by conventional and facile coordination methods. Among coordination compounds, Prussian blue (PB) and its analogue (PBA) show high physical/chemical properties and potential as multifunctional platforms for various applications such as information recording, sensing, batteries, biomedicine, imaging, and water purification. The strong relationship between nanoarchitectures and functional properties of PB and PBAs was demonstrated in Chapter 1. In this thesis, I synthesized a various shaped cyano-bridged CPs under strictly controlled crystallization conditions. The tuning of the chemical and physical properties of the PB or PBA-derived materials can be done by controlling the size and morphology of the PB or PBA precursors. In my work, I synthesize various shapes of cyano-bridged CPs from the single crystal to nano- and mesoporous structures. In addition, the structural transformation under humidity control was investigated. Due to the presence of water networks in the two-dimensional (2D) materials the proton conductivity of these materials could be measured. Also, to obtain good quality single crystal, I used a chelating agent to slow down the growth process. In my work, hollow CoFe-PBA nanocubes were also synthesized by using silica spheres as hard templates. Here I used the silica spheres due to the presence of functional silanol group on their surface, which made it is possible to achieve the hollow structure without much complexity. The large interface of this material can be applied for sodium ion-batteries. Also, I prepared NiCo flakes wrapped with graphene (NiCo-CP/G) by electrostatic interaction and successfully converted it to NiCo oxide/G hybrid. The NiCo oxide-graphene hybrid displayed good performance for supercapacitors applications because they possess a high number of active surface sites for the electrochemical reactions. The shape and size change of CuNi CPs were investigated by using trisodium citrate dihydrate (TSCD) as a chelating agent with different amounts. Following thermal treatment in air, the organic cyano group was removed and CuNi oxide was formed. The CuNi oxide products obtained at different thermal treatment

(300, 400 and 500°C) showed respectable electrochemical performance for supercapacitors. The hybrid cyano-bridge CuNi CPs on the surface of graphene oxide (GO) sheets were prepared via *in situ* deposition method and following thermal treatment at high temperatures, CuNi oxide/GO hybrids with high surface areas were obtained, as described in **Figure 7-1**.

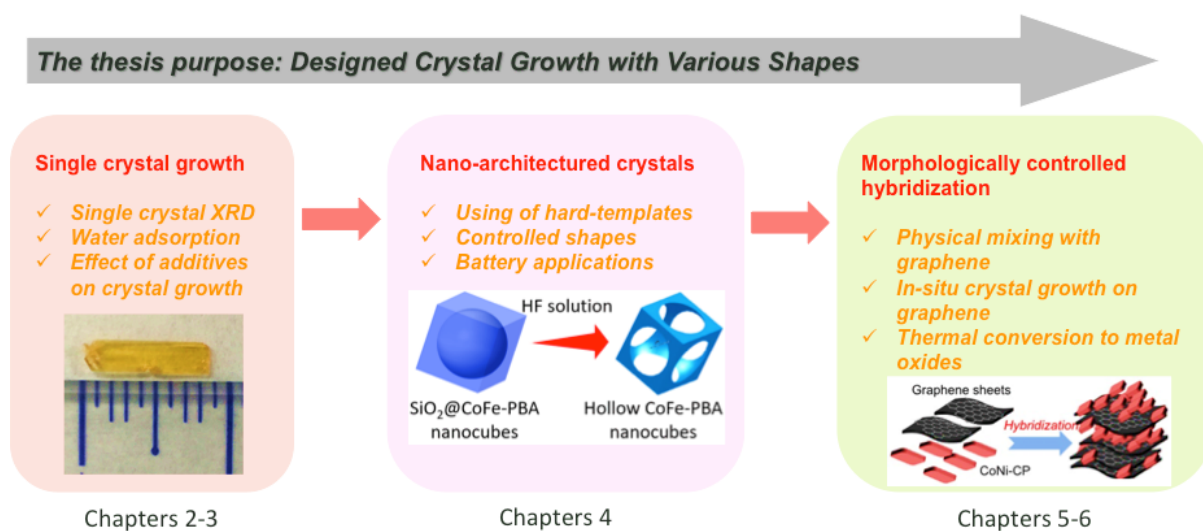


Figure.7-1 Overall projects described in this thesis

(I) Two-dimensional cyano-bridged coordination polymer of $\text{Mn}(\text{H}_2\text{O})_2[\text{Ni}(\text{CN})_4]$: structural analysis and proton conductivity measurements upon dehydration and rehydration (Chapter 2)

$\text{Mn}(\text{H}_2\text{O})_2[\text{Ni}(\text{CN})_4]$ single crystal was grown by a slow diffusion method at low temperatures. Through detailed structural analysis, the as-synthesized crystals of $[\text{Mn}(\text{H}_2\text{O})_2\text{Ni}(\text{CN})_4]\cdot 3\text{H}_2\text{O}$ were transformed into another crystalline phase $[\text{Mn}(\text{H}_2\text{O})_2\text{Ni}(\text{CN})_4]\cdot \text{H}_2\text{O}$ upon dehydration via a topotactic route. The structure of the framework itself changed as the tilt of MnO_6 octahedra changes in response to the change in hydrogen bonds between these water molecules, though the 2D cyano-bridged networks were retained. The water molecules, in particular the hydrogen bonds, played a key role in the structural transformation upon dehydration/hydration in the 2D cyano-bridged CPs, that is, such frameworks are flexible enough to respond to humidity. I investigated the capability for

proton conduction through the hydrogen bonding networks using single crystals at high humidity ratio (100%) which showed low proton conductivity.

(II) Single Crystal Growth of Two-Dimensional Cyano-Bridged Coordination Polymer of $[\text{Co}(\text{H}_2\text{O})_2\text{Ni}(\text{CN})_4] \cdot 4\text{H}_2\text{O}$ Using Trisodium Citrate Dihydrate (Chapter 3)

In this chapter, a single crystal of $\text{Co}(\text{H}_2\text{O})_2\text{Ni}(\text{CN})_4 \cdot 4\text{H}_2\text{O}$ with a very smooth surface was grown by the same method used in **Chapter 2** through a controlled crystallization process with the assistance of TSCD to increase the speed of growth process. The hydrophilicity measurement was investigated by water adsorption/desorption isotherms at room temperature. The pressure at $P/P_0 = 0.91$, the crystal adsorbed absorbs about two water molecules per $[\text{CoNi}(\text{CN})_4]$ unit. This was not in good agreement with the single crystal X-ray diffraction pattern and thermogravimetric analysis/differential thermal analysis (TG-DTA) results which showed a fully hydrated sample containing 5-6 water molecules.

(III) Synthesis of Hollow Co-Fe Prussian Blue Analogue Cubes by using Silica Spheres as a Sacrificial Template (Chapter 4)

This chapter demonstrates the formation of hollow CoFe–PBA nanocubes by using silica spheres as hard templates and examined their feasibility as cathode materials for sodium-ion batteries (SIBs). The silanol groups on the surface of the silica spheres reacted with cobalt cations in the first step. Nucleation of CoFe–PBA started simultaneously upon addition of iron cyanide ligands in the second step. After aging overnight, a thin shell of CoFe–PBA was successfully formed on the surface of the silica spheres. Silica cores were then removed by chemical etching with hydrofluoric acid (HF), yielding hollow CoFe–PBA nanocubes. The hollow nanostructure of CoFe–PBA nanocubes helped to improve the storage capacity of sodium ions with stable cycle performance compared to the solid CoFe–PBA nanocubes.

(IV) Graphene-Wrapped Nanoporous Nickel-Cobalt Oxide Flakes for Electrochemical Supercapacitors (Chapter 5)

This chapter demonstrates a facile approach to hybridize nanoporous NiCo oxide flakes with graphene sheets. Electrostatic attraction played a definitive role in compositing the positively charged cyano-bridged CoNi coordination polymer flakes (CoNi-CP) with the

negatively charged graphene surfaces. Further, simple thermal treatment converted the graphene wrapped CoNi-CP flakes to Ni-Co oxide/graphene composites without affecting the integrity of the parent graphene sheets. This composite showed a high specific capacitance ($\sim 199 \text{ F g}^{-1}$) and a good capacitance retention.

(V) Cyano-Bridged Cu-Ni Coordination Polymer Nanoflakes and Their Thermal Conversion to Mixed Cu-Ni Oxides (Chapter 6)

In first part of this chapter, the successful fabrication of 2D Cu-Ni CPs nanoflakes via a controlled crystallization process with the assistance of TSCD is demonstrated. It is found that the concentration of TSCD strongly influenced the size and morphology of the resulting Cu-Ni CPs, with higher concentration of TSCD leading to more well-defined and larger-sized nanoflakes due to the reduction in crystallization speed of Cu-Ni CPs. These Cu-Ni CPs were subsequently converted into nanoporous Cu-Ni mixed oxides via thermal treatment in air at $300\text{--}500^\circ\text{C}$ and they showed respectable electrochemical performance for supercapacitors with a maximum specific capacitance 158 F g^{-1} at 1 A g^{-1} and good capacitance retention of 71%. It is expected that the proposed method will be useful for the preparation of other types of 2D and 3D CPs as precursors for the synthesis of various nanoporous metal oxides for energy and environmental applications.

In the second part of this chapter, Cu-Ni CPs flakes were successfully hybridized with GO nanosheets. The GO nanosheets served as nucleation sites for the growth of Cu-Ni CPs flakes. After thermal treatment the cyano group in the Cu-Ni CPs was removed and porous CuNi oxide/GO composite was achieved. Since the GO nanosheets could prevent rapid crystallization and fusion of metal oxides during thermal treatment, the surface area of CuNi oxide/GO composite incredible increased from $49 \text{ m}^2 \text{ g}^{-1}$ for the hybrid treated at 300°C to $145 \text{ m}^2 \text{ g}^{-1}$ for the hybrid treated at 500°C .

List of Achievements List

I. Original Papers

1. Synthesis of Hollow Co-Fe Prussian Blue Analogue Cubes by using Silica Spheres as a Sacrificial Template

ChemistryOpen, 2018, 7, 599-603. (Date: August 2018)

Alowasheer Azhar, Mohamed B. Zakaria, El-Zeiny M. Ebeid, Toyohiro Chikyow, Yoshio Bando, Abdulmohsen Ali Alshehri, Yousef Gamaan Alghamdi, Ze-Xing Cai, Nanjundan Ashok Kumar, Jianjian Lin, Hansu Kim and Yusuke Yamauchi

2. Graphene-Wrapped Nanoporous Nickel-Cobalt Oxide Flakes for Electrochemical Supercapacitors

ChemistrySelect, 2018, 3, 8505-8510. (Date: August 2018)

Alowasheer Azhar, Mohamed B. Zakaria, Jianjian Lin, Toyohiro Chikyow, Darren J. Martin, Yousef Gamaan Alghamdi, Abdulmohsen Ali Alshehri, Yoshio Bando, Md. Shahriar A. Hossain, Kevin C.-W. Wu, Nanjundan Ashok Kumar and Yusuke Yamauchi

3. Two-Dimensional Cyano-Bridged Coordination Polymer of $Mn(H_2O)_2[Ni(CN)_4]$: Structural Analysis and Proton Conductivity Measurements upon Dehydration and Rehydration

CrystEngComm, 18, 20, 6713-6720. (Date: September 2018)

Azhar Alowasheer, Satoshi Tominaka, Yusuke Ide, Yusuke Yamauchi and Yoshitaka Matsushita

4. Cyano-Bridged Cu-Ni Coordination Polymer Nanoflakes and Their Thermal Conversion to Mixed Cu-Ni Oxides

Nanomaterials, 2018, 8, 968. (Date: November 2018)

Alowasheeir Azhar, Christine Young, Yusuf Valentino Kaneti, Yusuke Yamauchi, Ahmad Yacine Badjah, Mu Naushad, Mohamed Habila, Saikh Wabaidur, Zeid A. Alothman and Jeonghun Kim

5. Nanoarchitectonics: A New Materials Horizon for Prussian Blue and Its Analogues

Bulletin of the Chemical Society of Japan, under minor revision.

Alowasheeir Azhar, Yucen Li, Zexing Cai, Mohamed Barakat Zakaria, Mostafa Kamal Masud, Md. Shahriar A Hossain, Jeonghun Kim, Wei Zhang, Jong Beom Na, Yusuke Yamauchi, and Ming Hu

6. Dual-Textured Prussian Blue Nanocubes as Sodium Ion Storage Materials

Electrochimica Acta, 2017, 240, 300-306. (Date: April 2017)

Dae Sik Kim, Mohamed B. Zakaria, Min-Sik Park, Azhar Alowasheeir, Saad M. Alshehri, Yusuke Yamauchi and Hansu Kim

7. Three-Dimensional Macroporous Graphitic Carbon for Supercapacitor Application

ChemistrySelect, 2018, 3, 4522-4526. (Date: April 2018)

Rahul R. Salunkhe, Jie Wang, Azhar Alowasheeir, Jianjian Lin, Victor Malgras, Yoshio Bando, Mohamed B. Zakaria, Abdulmohsen Ali Alshehri, Jeonghun Kim, Yusuke Yamauchi and Kevin C. W. Wu

8. Confined Synthesis of Coordination Frameworks inside Double-Network Hydrogel for Fabricating Hydrogel-Based Water Pipes with High Adsorption Capacity for Cesium Ions

Bulletin of the Chemical Society of Japan, 2018, 91, 1357-1363. (Date: June 2018)

Pan Zhao, Wei Zhang, Yusuf Valentino Kaneti, Alowasheeir Azhar, Abdulmohsen Ali Alshehri, Yusuke Yamauchi and Ming Hu

II. Poster Presentations

1. Two-Dimensional Pt/CuO-GO Nanocomposites through Thermal Treatment of Cyano-Bridged Coordination Polymers

The 6th Waseda-NIMS International Symposium (Date: 29 July 2015)

Azhar Alowasheir, Mohamed B. Zakaria, Cuiling Li and Yusuke Yamauchi

Acknowledgment

GOD Thank you for giving me the strength and encouragement especially during all the challenging moments in completing this thesis. I am truly grateful for your exceptional love and grace during this entire journey.

First and foremost, my heartiest gratitude to my supervisors, **Prof. Dr. Yusuke Yamauchi**, for his patience, continuous supervision, guidance, advice, and support in completing this thesis. He is the backbone of this project by giving wonderful suggestions and constructive criticism which gave this study a life. I express my humble gratitude to my supervisor for his willingness to spare me his time and guide me to complete my study. I am happy with the constructive criticism and nice comments from **Prof. Dr. Yoshiyuki Sugahara (Waseda University)**, **Prof. Dr. Turo Asahi (Waseda University)** and **Prof. Dr. Yoshio Bando (NIMS)** for taking much time for reviewing of my thesis and consideration the presentation. Their invaluable comments and academic advices are appreciated which have made me think and learn more deeply about my research. I must express my gratitude to the NIMS members, **Dr. Yusuke Ide**, **Dr. Yoshitaka Matsushita**, and **Dr. Joel Henzie**.

I would like to thank the staff of the International Center at Waseda University for their assistance and their time during my PhD study. I thank all administrative and Namiki Foundry at Research Division for Materials Nanoarchitectonics (MANA), National Institute for Materials Science (NIMS) for their support. I like to thanks **Mr. Kiyotaka Iiyama** and **Mr. Makito Nakatsu**, for facilities teaching and use. I acknowledge the Namiki Foundry staff at MANA/NIMS, especially **Dr. Toshiaki Takei** for his support on TEM measurements, **Miss. Yumiko Sawabe** for her kind support all Time.

Special thanks to my lovely husband **Haidar Albadi**, for his continuous support, encouragement and understanding. He did not complain about our separate life for 10 years and taking a long trip to meet me for short time. Thanks for sharing my wish and believing in me to reach the goal of completing my PhD study. My son **Mujitaba**, who has inspired me with his love and caring, even as his bore the brunt of my moods and absences. I saw in him the innocence of childhood and knew the meaning of motherhood and the meaning of love. A very special appreciation is due to my mother **Mahamoadah Amin-Aldein**, **sisters**, and **brothers** not only for their constant encouragement but also for their patience and understanding throughout. I dedicate this thesis to the soul of my father **Samlan** who taught me the meaning of life.

I also wish to express my heartfelt thanks and appreciation to **Dr. Cuiling Li, Dr. Ming Hu, Dr. Malgras Victor, Dr. Yusuf Valentino Kaneti, Dr. Mohamed Barakat Zakaria Mohamed, Dr. Zexing Cai, Dr. Christine Young,** and **Dr. Jeonghun Kim** for their support, tolerance, fruitful and valuable advice, help, guidance, and encouragement at all stages of my work, and also reviewing critically the manuscripts. Also, I would like to thank my lab seniors, mates, and co-workers, **Dr. Danial Dr. Rahul, Dr. Malay, Dr. Jing Tang, Dr. Jiang Bo, Dr. Mei, Dr. Hamid, Dr. Huayu Qian, Dr. Jie Wang, Dr. Li Yunqi, Dr. Xingtao Xu, Dr. Wang Zhongli, Dr. Bing Ding, Dr. Zhang, Dr. Wael, Dr. Esmail, Dr. Jong Beom Na, Dr. Tomota, Dr. Monika Ostrowsk, Ms. Kimiko Takai, Ms. Naoko Kaneta, Ms. Sakai, Mr. Muhammed Iqbal, Mr. Asep Sugih, Dr. Kamachi, Miss. Yanna, Mr. Tan, Mr. Keni, Mr. Tanaka, Mr. Indra, Mr. Ahmed, Ms. Abeer, Mr. Rafat, Mr. Mohamed Esmat, Mr. Tao Li, Mr. Gilang, Ms. Wulan, Ms. Zhao and Mr. Wei Xia** for their cooperation and assistance during the achievement of this work.

I acknowledge the financial support from the he Custodian of The Two Holy Mosques' Overseas Scholarship Program in Saudi Arabia for twelve years and thank all members in the Saudi Arabia Culture Office and Embassy in Tokyo for their kindness and cooperation during these years. I appreciate the support, kindness, and continuous advice of **Dr. Eng. Essam Bukhary**, who was the head of Saudi Arabia Culture Office until 2015 and supervisor in Saudi Arabia Culture Office **Dr. El-Moamen Abdalla**. I also wish to express my heartfelt thanks and appreciation to my supervisor in Saudi Arabia Culture Office **Ms. Yamamoto** for her support and kindness for four years. Last but not least, I would like thanks **Dr. Mohammed Albori** who took the lead to heaven in the end of last this year.

Finally, a huge thank-you to everyone who has been a part of my life directly or indirectly supported and prayed for me along the way.

Alghar Alowashceir
Waseda University
2019-01-22